

MULTISCALE SIMULATION METHODOLOGY FOR THE FORMING BEHAVIOR OF BIAXIAL WEFT-KNITTED FABRICS

M.Sc. Minh Quang Pham

Geboren am: 03. August 1987 in Ho-Chi-Minh Stadt, Vietnam

DISSERTATION

zur Erlangung des akademischen Grades

DOKTOR INGENIEUR (DR.-ING.)

Erstgutachter

Univ.-Prof. Dr.-Ing. habil. Dipl.-Wirt. Ing. Chokri Cherif

Zweitgutachter

Univ.-Prof. Dr.-Ing. habil. Yordan Kyosev

Eingereicht am: 03.03.2023

Statutory declaration

I declare that I have authored this thesis with the title “Multiscale simulation methodology for the forming behavior of biaxial weft-knitted fabrics” independently, that I have not used other than the declared sources/resources, and that I have explicitly marked all material, which has been quoted either literally or by content from the used sources.

Dresden, 03.03.2023

M.Sc. Minh Quang Pham

Prologue

This thesis originated during my time as research associate at the Institute of Textile Machinery and High Performance Material Technology (ITM), Faculty of Mechanical Science and Engineering, Technische Universität Dresden from 2017 to 2023.

I would like to express my sincerest gratitude to Prof. Cherif for the support and guidance since the master study until the completion of this dissertation at ITM. His constructive feedback and valuable insights help to improve the quality of this work significantly.

I would also like to thank Prof. Kyosev for his acceptance to referee this dissertation.

I am deeply grateful to my team leader Dr. Gereke for providing a stimulating and supportive working environment in the research group "Structure and process simulation" with plenty of room to grow and for his correction of my scientific writing. To the colleagues Ms. Huynh, Mr. Lang and Mr. Annadata, I thank you for the numerous discussion and the mutual support. I would also like to extend my appreciation to the former colleagues Dr. Döbrich and Dr. Hübner for the great works that they have done at ITM, from which I have learned so much.

My thanks also go to the colleagues in other research groups at ITM for the intensive and fruitful collaboration during the years and especially for the willingness to help by the production and testing of textiles and composite. I also thank the students, who wrote their study works under my supervision for the chance to learn from each other.

My research activity at ITM is financed and supported by several sources. The project "Saxon Alliance for Material- and Resource-Efficient Technologies (AMARETO)" (Project No 100291445) is funded by the European Union (European Regional Development Fund) and by the Free State of Saxony. The IGF research project "Verfahrenserweiterung TBV" (18637 BR), "3D-KKP" (19806 BR), and "Komplexe 3D-Schal-Prof-MLG" (20793 BR) of the Forschungsvereinigung Forschungskuratorium Textil e.V. are funded through the AiF within the program for supporting the „Industriellen Gemeinschaftsforschung (IGF)“ from funds of the Federal Ministry For Economic Affairs And Climate Action (BMWK) by a resolution of the German Bundestag. The computation of FEM simulation in this thesis was performed partly on an HPC system at the Center for Information Services and High Performance Computing (ZIH) at TU Dresden. The provided supports from the above-mentioned institutions are acknowledged.

To my family and friends, I thank you for your care and encouragement.

To Ngân, thank you for your love and the life we share.

Zusammenfassung

Trotz der guten Drapierbarkeit ist das Formen von flachen Mehrlagen-Gestricken (MLG) zu 3D-Preforms für schalenartige Faser-Kunststoff-Verbund (FKV) Bauteile immer noch eine Herausforderung, da einige Defekte wie Falten, Gassenbildung oder Faserschäden nicht vollständig vermieden werden können. Daher ist vor der Massenproduktion eine Optimierung erforderlich. Die virtuelle Optimierung des Umformprozesses mit Hilfe von Finite-Element-Methode (FEM) Modellen ist ein attraktiver Ansatz, da die Rechenkosten immer geringer werden. Dazu wurde ein auf Kontinuumsmechanik basierendes Makromodell erfolgreich für MLG implementiert. Der makroskalige Modellierungsansatz bietet angemessene Rechenkosten und kann gängige Defekte wie Faltenbildung vorhersagen. Weitere Defekte wie Faserversatz, ondulierte Fasern, Knicken von Fasern, Faserschädigung und Gassenbildung können jedoch mit dem Makromodell nicht vorhergesagt werden. Da die Komplexität von Bauteilen aus FKV und die Qualitätsanforderungen an die 3D-Preforms zunehmen, sind FEM-Modelle mit höherem Darstellungsgrad erforderlich. Im am weitesten entwickelten mesoskaligen FEM-Modell für MLG verhindert die zu starke Vereinfachung des Strickfadensystems mit Federelementen jedoch die Fähigkeit dieses FEM-Modells, Faserverschiebungen und Gassenbildung bei großer Verformung zu beschreiben, wobei das Gleiten zwischen den Fäden berücksichtigt werden muss. Ziel ist daher die Entwicklung, Validierung und Anwendung eines mesoskaligen FEM-Modells für MLG, um die derzeitigen Einschränkungen zu überwinden.

Es werden neue Modellierungsstrategien für biaxiale MLG auf der Mesoskala entwickelt. Die mechanischen Eigenschaften von MLG werden durch eine Reihe von textilphysikalischen Prüfungen charakterisiert und analysiert, die alle notwendigen Daten für den Aufbau sowie die Validierung der FEM-Modelle liefern. Es sollen zwei Ansätze zur Modellierung des Verstärkungsgarns implementiert und verglichen werden: durch Balken- und durch Schalenelemente. Die validierten Modelle können für die Umformsimulation verwendet werden. Es folgt eine Benchmark-Studie über die Kapazität und Zuverlässigkeit der verfügbaren Makromodelle und der entwickelten Mesomodelle durch Umformsimulation. Als Grundlage für die Benchmark-Studie werden Umformversuche durchgeführt.

Das zweite Ziel der Arbeit ist die Modellierung von FKV auf verschiedenen Skalen. Die Modellierung von FKV auf der Makroebene wird mit den Daten der Faserorientierung durchgeführt, die aus der Umformsimulation gewonnen werden. Eine Mapping-Methode hilft dabei, die vorhergesagte Faserorientierung aus der Umformsimulation von dem MLG

Mesomodell auf das FKV-Makromodell zu übertragen. Um den FKV zu charakterisieren und die Parameter für das FKV Modell vorzubereiten, werden Versuche mit FKV durchgeführt und ausgewertet. Basierend auf dem Mesomodell des MLG wird ein weiteres FKV-Modell vorgeschlagen, wobei Garn und Matrix getrennt modelliert werden. Dieses mesoskalige FKV-Modell enthält auch eine Kontaktformulierung, mit der die Delamination im FKV-Bauteil vorhergesagt werden kann. Prüfungen von Schale-Rippen-Strukturen dienen als Grundlage für die Modellvalidierung. Das validierte Modell wird erfolgreich zur Vorhersage des mechanischen Verhaltens weiterer Schale-Rippen-Strukturen mit unterschiedlicher Höhe und Anordnung der Rippen verwendet.

Kapitel 1 stellt die Einleitung und Problemstellung von dem Thema FKV vor. Kapitel 2 gibt eine Übersicht über Stand-der-Technik von den Hochleistungsfasern, Herstellung von textilen Verstärkungen und Halbzeugen, Fertigung von FKV sowie von Prüftechnik für Textilien und FKV. Zunächst wurden in Kapitel 3 eine Einführung in die Modellierung mit FEM allgemein und Stand-der-Technik der Modellierung von technischen Textilien gegeben. In Kapitel 4 wurden die Zielsetzung und das Forschungsprogramm festgelegt.

Die experimentellen Arbeiten werden in Kapitel 5 vorgestellt. Der erste Schritt ist die Auswahl des Materials und der Konfiguration für die MLG. Sowohl das Ausgangsmaterial als auch die produzierten MLG sollten systematisch getestet werden. Als Referenz wird auch ein Leinwandgewebe in die Prüfprogramme aufgenommen. Neben der Charakterisierung von textilen Flächengebilden sollen auch deren gleichwertige FKV geprüft werden. Das erste Ziel des Forschungsprogramms wird in Kapitel 6 erreicht, wobei verschiedene Ansätze zur Modellierung von MLG vorgestellt und validiert werden. Die entwickelten und validierten FEM-Modelle werden für die Benchmark-Studie der Umformsimulation in Kapitel 7 verwendet. Kapitel 8 befasst sich mit der Modellierung von FKV in verschiedenen Skalen. Zunächst wird das Mapping-Verfahren vorgestellt. Es wird ein Mapping für ein schalenförmiges T-Napf-Bauteil durchgeführt. Die Strukturanalyse für das T-Napf-Bauteil erfolgt für übliche Lastfälle. Zweitens wird ein mesoskaliges FEM-Modell für MLG-verstärkte FKV vorgeschlagen. Dieses Modell wird auf der Grundlage der Prüfdaten aus Kapitel 5 validiert. Das validierte Modell wird dann zur Vorhersage des mechanischen Verhaltens eines Schale-Rippen-FKV-Bauteils unter Biegebelastung verwendet.

Kapitel 9 gibt eine Zusammenfassung von den Forschungsergebnissen und Vorschlägen für mögliche weitere Forschungen rund um dem Thema MLG als Verstärkung für FKV. Die Kombination von vorhandenen Makro- und Mesomodellen in einer einzigen Simulation kann die Berechnungskosten senken, ohne die Vorhersagenfähigkeiten des Modells kompromittiert zu werden.

Contents

Statutory declaration.....	I
Prologue.....	II
Zusammenfassung.....	III
Contents.....	V
Symbols and abbreviations.....	IX
Latin Symbols.....	IX
Greek Symbols.....	X
Indices.....	X
Mathematical symbols and operators.....	XI
Abbreviations.....	XI
1 Introduction.....	1
2 State of technology and research.....	5
2.1 Fiber-reinforced plastics.....	5
2.2 Selected high performance fibers.....	7
2.2.1 Glass fiber (GF).....	8
2.2.2 Carbon fiber (CF).....	9
2.2.3 Hybrid yarns.....	11
2.3 Fiber-matrix interface and matrix materials.....	11
2.3.1 Fiber-matrix interface.....	11
2.3.2 Matrix materials.....	12
2.4 FRP production process.....	14
2.5 Forming behavior of textile reinforcement.....	17
2.6 Selected textile semi-finished products.....	22
2.6.1 Woven fabrics.....	22
2.6.2 Warp-knitted fabrics.....	25
2.6.3 Weft-knitted fabrics.....	26
2.7 Test methods for textile material and FRP.....	35
2.7.1 Fiber tests.....	35

2.7.2	Yarn tests	36
2.7.3	Fabric tests.....	37
2.7.4	FRP tests	44
3	Modelling of textile structures and FRP	46
3.1	Overview	46
3.2	Basis of FEM	47
3.3	FEM models for textile structures.....	55
3.4	Modelling of FRP	61
3.5	Summary.....	69
4	Objectives and research program	70
4.1	Motivation.....	70
4.2	Specification of the research program.....	70
4.2.1	Objectives.....	70
4.2.2	Research program	71
5	Analysis of the structural behavior of biaxial weft-knitted fabrics and their FRP	72
5.1	Systematic test planning	72
5.1.1	Material selection and textile production	72
5.1.2	Testing plan	75
5.2	Fiber and yarn tests	75
5.2.1	Fiber tests.....	75
5.2.2	Yarn tests	76
5.3	Fabric tests	79
5.3.1	Tensile.....	80
5.3.2	Bending	84
5.3.3	In-plane shear.....	86
5.3.4	Friction.....	91
5.3.5	Yarn pull-out test	93
5.4	FRP production and testing.....	94
5.4.1	Production of FRP	95

5.4.2	Fiber volume content	101
5.4.3	Tensile test of FRP.....	102
5.4.4	Four-point bending test of FRP	107
5.4.5	Interlaminar shear strength (ILSS)	110
5.4.6	Three-point bending test of T-shaped FRP	113
5.5	Summary.....	116
6	Development and validation of BWKF models	117
6.1	Macro-scale model	117
6.2	Meso-scale model.....	124
6.2.1	Beam element model.....	124
6.2.2	Shell element model.....	130
6.3	Validation of FEM models.....	134
6.3.1	Tensile behavior.....	134
6.3.2	Bending behavior.....	139
6.3.3	Shear behavior	140
6.3.4	Friction.....	145
6.4	Summary.....	147
7	Simulation of forming process.....	148
7.1	Fabric forming with hemisphere tools.....	148
7.1.1	Experiment.....	148
7.1.2	Simulation	150
7.1.3	Influence of fabric configuration on forming behavior of BWKF.....	154
7.2	Fabric forming with L-profile shape tools.....	164
7.2.1	Experiment.....	164
7.2.2	Simulation	167
7.3	Simulative development of T-cup forming tools	177
7.4	Computational cost.....	179
7.5	Summary.....	179
8	Modelling of FRP made from BWKF	180

8.1	Macroscale FRP model.....	180
8.1.1	Mapping method	180
8.1.2	Validation of composite model.....	184
8.1.3	Investigation of the influence of yarn orientation on FRP properties	185
8.2	Mesoscale FRP model	188
8.2.1	Shell-rib structures as stiffened element	188
8.2.2	Modelling of FRP	190
8.2.3	Validation of the FRP model	192
8.3	Numerical structural analysis of further shell-rib FRP variants.....	198
8.4	Summary.....	201
9	Conclusion and outlook	202
10	References.....	206
	List of figures.....	250
	List of tables.....	259

Symbols and abbreviations

LATIN SYMBOLS

symbol	significance	SI-unit
E	Elasticity modulus / Young's modulus	N/mm ²
G	Shear modulus	N/mm ²
A	Area	mm ²
F	Force	N
F	Force vector	N
f	Fiber volume content	%
m	Weight	g
M	Fiber weight content	%
v	volume	cm ³
F	Force matrix	N
K	Stiffness matrix	N/mm
U	Displacement vector	mm
U	Velocity vector	mm/s
U	Acceleration vector	mm/s ²
C	Viscosity matrix	N*s/mm
M	Mass matrix	g
t	time	s
Δt	time step	s
l	characteristic length of the element	mm
c	speed of sound	mm/s
μ	Coulomb coefficient of friction	-
B	Bending stiffness	N/mm ²
B	Bending stiffness of textile according to DIN 53362	cN*cm ²
I	Moment of inertia	g*mm ²
L	Length of the picture frame side	mm
d	Displacement of tensile test machine	mm
b	Width of specimen	mm

h	Thickness of specimen	mm
E	Green-Lagrangian strain tensor	-
S	2 nd Piola-Kirchhoff stress tensor	N/mm ²
F	Deformation gradient	-
I	Identity matrix	-
J	Determinant of the deformation gradient F	-
B	Bending stiffness matrix	N/mm ²

GREEK SYMBOLS

symbol	significance	SI-unit
σ	Stress	N/mm ²
ε	Strain	-
ρ	Material density	g/cm ³
β, γ	Newmark constant	-
ν	Poisson's ratio	-
φ	Shear angle	rad
θ	Picture frame angle	rad
τ	Interlaminar shear strength according to EN ISO 14130	N/mm ²
λ	Fraction of thickness in laminate formulation	-
ξ, η, ζ	Parametric coordinate of Hughes-Liu beam	-

INDICES

$ $	fiber direction
\perp	transverse to fiber direction
P	value calculated by Puck theory

MATHEMATICAL SYMBOLS AND OPERATORS

π Archimedes' constant, Ludolphian number, $\pi = 3.14159$

ABBREVIATIONS

1D	One dimensional
2D	Two dimensional
3D	Three dimensional
AR	Aramid fiber
ASTM	American Society for Testing and Materials
BWKF	Biaxial Weft-Knitted Fabrics
CAD	Computer-aided design
CF	Carbon fiber
CFRP	Carbon fiber reinforced polymers
CNT	Carbon nanotube
CoF	Coefficient of Friction
CTL	Composite Laminate Theories
DIN	German Institute for Standardization
DOF	Degree of freedom
DTS	Domain Superposition Technique
EN	European Standards (Europäische Norm)
EP	Epoxy
FE/FEM	Finite element / Finite element method
FKV	Faser-Kunststoff-Verbund, the German term for FRP
FRP	Fiber-reinforced polymers/plastic
GF	Glass fiber
GFRP	Glass fiber reinforced polymers
HM CFRP	High modulus carbon fiber-reinforced plastic

HS CFRP	High strength carbon fiber-reinforced plastic
ILSS	Interlaminar shear strength
ISO	International Organization for Standardization
KFRP	Kevlar fiber-reinforced plastic
LCM	Liquid composite molding
MLG	MehrLagenGestricke, the German term for MWKF
MWKF	Multilayer reinforced weft-knitted fabrics
NCF	Non-crimp fabric
PA	Polyamide
PMC	Polymer matrix composites
RTM	Resin transfer molding
SCD	Stitch cam depth
SL	Stitch length
UD	Uni directional
VARI	Vacuum assisted resin infusion
VARTM	Vacuum assisted resin transfer molding
W	Woven fabrics

1 Introduction

Throughout the history of humanity, learning to harness and use of natural resources has always been a survival skill. The efficiency of using natural resources represents the level of progress of a civilization. Consequently, the improvement of material for working tools and structures is inevitable. Material science was formed and assisted by the natural sciences such as physics, chemistry and mathematics. Nowadays, material science is an interdisciplinary study supported by a wide spectrum of science and engineering disciplines.

Phase of material (or state of matter) is defined by Ehlers and Potter [1] in Encyclopedia Britannica as *“chemically and physically uniform or homogeneous quantity of matter that can be separated mechanically from a nonhomogeneous mixture and that may consist of a single substance or a mixture of substances”*. According to Soboyejo [2], the mechanical properties of materials can be modified by two methods: intrinsic and extrinsic modification. The intrinsic modification is about the change of the internal structure of a given material phase, namely the arrangement and bonding of atoms, ions and molecules. For example, the material can be modified by minor alloying [3], heat treatment [4], plasma treatment [5], laser treatment [6]. Material system created by this method is quite diverse due to the great possibility of elemental combination, provided their interface can be maximized on the atomic scale. The iteration of modification for a given system is however restricted due to the intrinsic limits. As the result of this limitation, most material systems developed by intrinsic modification are homogenous and have limited array of properties. This limitation can be overcome by using the second approach, in which additional (external) phases are introduced into the material system. This extrinsic modification opens the possibility for additional array of properties of the material system to be engineered. For example, strength of a “host” material (also known as “matrix”) can be reinforced by a second material, which has higher strength than the intrinsic limit of the matrix. Material system developed by extrinsic modification is the mixture of two or more phases and well known with the name “composite material”. This is rather a general definition for composite material and valid for both natural material system (exist in nature such as hemi-cellulose fibers in a matrix of lignin) and synthetic system (man-made material such as steel-reinforced concrete or fiber-reinforced plastics) [2]. Somewhere in between of the two approaches, there is the so-called “two-phase alloy”, where each element of the material system stays in distinct phases and their interface is minimized [7].

Both of the mentioned approaches have been intensively researched to extend the limitation of the materials or to engineer their properties for a specific application. In

comparison with the classical metallic materials, fiber composites or fiber-reinforced polymers/plastics (FRP) have significant lower mass density (except Beryllium). In the recent development of structural material, lightweight is an important criterion. The light material supports the realization of lightweight design principle, which helps to save structural weight and to improve the efficiency of mechanical systems and structures by reducing overall energy consumption as well as CO₂ emission. For example, there has been more and more structural parts of various means of transport use of carbon fiber reinforced polymers (CFRP) instead of metal. Klein [8] estimated that a mass saving of 100 kg in a passenger car results in a reduction in fuel consumption of 0.5 l fuel per 100 km and a 12 g/km reduction in CO₂ emissions. For the aviation industry, Steinegger stated that a reduction in weight of an airplane by 1 kg saves ~0.02 to 0.03 kg of fuel per 1000 km [9]. At the other hand, lightweight material enables the construction of many renewable energy harnessing system such as wind power plants. Namely, rotor blades of wind power plants cannot reach their desirable dimensions without glass fiber reinforced polymers (GFRP) [10].

However, such saving of weight comes at an additional cost for lightweight construction. As the saving rates and their benefit vary from industry to industry, the accepted additional expense for lightweight construction is also different (Figure 1-1). Current solutions usually represent a compromise between technical and economic aspects [8]. The application of FRP in aviation and aerospace has been always under heavily research and development [11–15]. Great effort has also been put into expanding the use of this class of material among other industries such as civil engineering [16,17], production machine [18], testing machine [19], wind energy [20–24], automobile [25–27], ship building [28,29], rail vehicles [30], etc. They altogether have been forming a small industry sector with great growth potential [31,32]. Reducing production cost and improving the mechanical performance are two main concerns in the research and development. Other needs of research and development are about a new fiber/ matrix, new initial precursor material forms, complex geometry of part, multi-functionality, enhancement of a specific physical properties [33]. Material cost of the high-performance fiber-reinforcement alone are generally higher than the classical metallic material. Additionally, the production chain of FRP involves many processing steps, which means higher labor cost and greater risk of faulty products. Palmer [34] estimated the cost components for manufacture of a carbon reinforced composite 8' x 20' aircraft blade stiffened panels (Figure 1-2) by various fabrication processes as shown in Figure 1-3. The high labor cost of hand layup can be avoided by application of automated tape layup or stitching process.

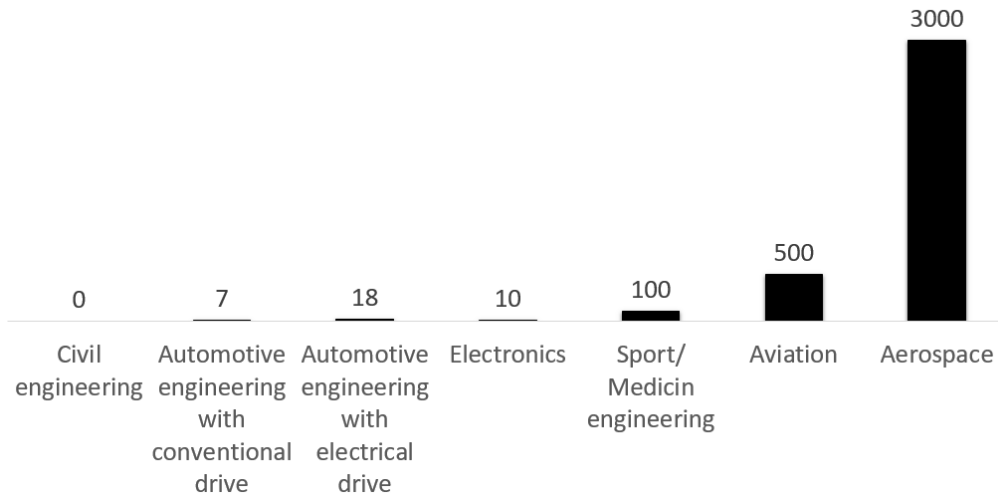


Figure 1-1: Industry accepted additional cost for lightweight construction in € per kilogram according to Klein [8]

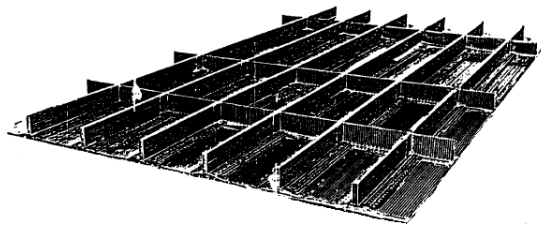


Figure 1-2: Design of a composite 8' x 20' aircraft blade stiffened panels [34]

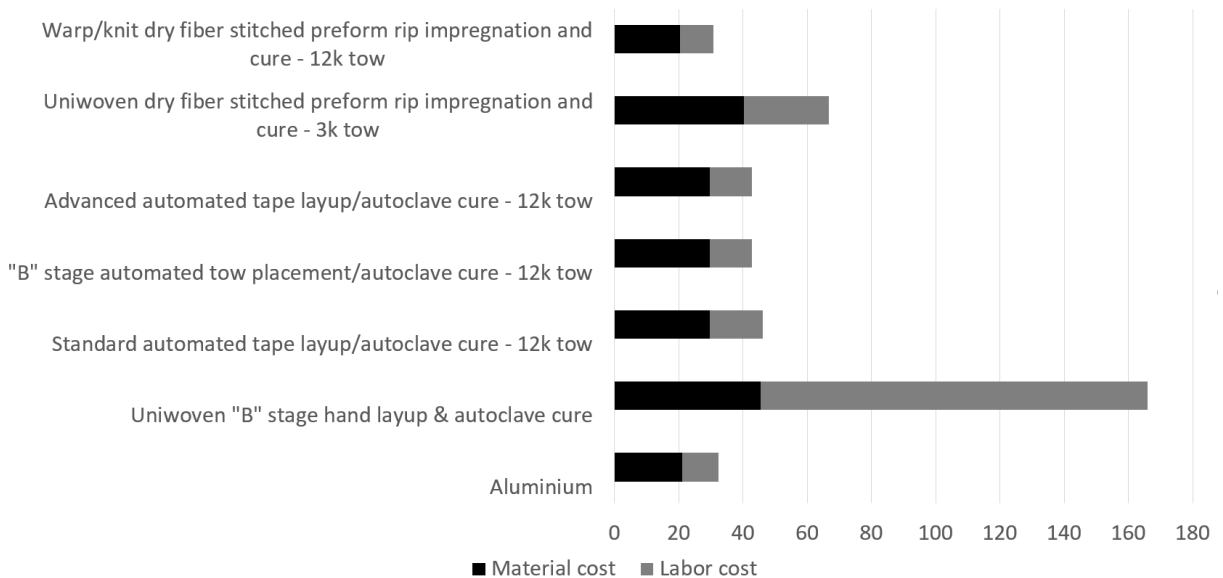


Figure 1-3: Estimated cost summary for a composite 8' x 20' aircraft blade stiffened panels by various fabrication processes (in thousand USD) [34]

The production of FRP for industrial application is a long and complicated process chain, where damage and defects can occur at any stage. Hence, each process in the chain should be optimized before mass production. The process optimization is often cost intensive due to the trial-and-error method. To avoid this, the numerical approach would be an attractive solution. A virtual process chain can help to reduce development time and improve the quality of FRP, as well as avoid unnecessary over dimensioning. Furthermore, the development of new forming and fabrication methods could also be encouraged. Comprehension of the forming behavior of textiles and successful modelling of these forming behaviors are the prerequisite for the virtual process chain. In the recent development, multilayer reinforced weft-knitted fabrics (MWKF) arise as a potential fiber reinforcement structure with good formability [35–38]. Biaxial weft-knitted fabrics (BWKF) is multilayer reinforced weft-knitted fabrics with yarn reinforcement in 0° and 90° direction. To compensate for the low productivity, the weft-knitting technique offers great flexibility in the development of new methods for producing complex 3D preforms for FRP with high automation potential, thus the process becomes faster with reduced labor [35–37]. A virtual process chain based on numerical models of BWKF would help to reduce costs and accelerate the optimization of forming process, as well as the development of new production technique with weft-knitting machine and thus spread the application of this textile reinforcing structure in the practical production of FRP. The effort in this thesis is put into creating numerical models of BWKF for forming process as well as models for further structural analysis of the FRP made from BWKF. With suitable models, the forming process can be optimized faster for the production. Useful information of yarn orientation can also be provided, which would be eventually used for FRP structural analysis. With the support of the virtual process chain, the use of BWKF in the industry would be expanded in the course of time, as the expense is reduced.

2 State of technology and research

2.1 Fiber-reinforced plastics

Fiber-reinforced plastics (FRPs) belong to the material class “composite” with at least two phases. Some authors also use the term “fiber-reinforced polymers” or “polymer matrix composites” (PMCs) [38] to mention this kind of material. The matrix is normally a thermoset or a thermoplastic polymer. Fiber reinforcement plays the role of the external phase, which has significantly higher stiffness and strength than the intrinsic limit of the matrix material. Composite parts made of FRP have significant lower weight with the same or enhanced mechanical properties in comparison to metallic parts. Another advantage of FRP is the corrosion resistance, which would eventually lead to extended durability and less maintenance requirement, thus reduce the overall lifetime costs [33]. Bunsell [39] compares some of the metallic materials with FRPs as shown in Table 2-1. FRPs are preferentially manufactured based on a thermoset matrix (more than 75% of all the composites) due to the ease of manufacturing, higher thermal stability, excellent fatigue strength, and good fiber to matrix adhesion [40]. FRP based on a thermoplastic matrix are attracting growing interest because of unlimited storage, semi-products delivered ready for use, thermal formability, fast consolidation, and environmental friendliness. Thermoplastic composites can be made from fully impregnated organic sheets or partially impregnated composite fabrics using polymer powders, solvent impregnation, dipping or coating with molten matrix, coating with films or nonwoven fabrics, and insertion of thermoplastic yarns or hybrid yarns made of reinforcement fibers and thermoplastic fibers [41]. The mechanical behavior of FRP is anisotropic, namely dependent on the orientation of the fiber reinforcement, which is true for tensile and shear behavior as well as contraction coefficient. Consequently, design of FRP part requires good understanding of working condition of the FRP part, namely the load cases that the part must withstand. So that reasonable decision on placement/location/type/quantity of fiber in the part can be made. To assure the actually produced FRP part meets the expectation that set by the designer, understanding of the FRP production process is required.

FRP is brittle and has significant lower break elongation than metal. FRP fails immediately when its strain reaches the break elongation within elastic strain area, while metal undergoes a plastic deformation after yielding before catastrophic failure. A comparison between tensile behavior of FRP and metal is shown in Figure 2-1.

Table 2-1: Typical properties of some metallic materials and FRPs according to Bunsell [39]

Material	Mass density (g/cm ³)	Young's modulus (GPa)	Specific modulus (GPa*cm ³ /g)
<i>Metallic materials</i>			
Steel	7.9	210	25.3
Aluminum	2.7	76	28
Titanium	4.5	116	25.7
Beryllium	1.8	289	161
Copper	8.9	110	12.4
Nickel	8.8	21	2.4
Tungsten	19.6	400	20.4
<i>Fiber-reinforced plastic</i>			
Glass fiber-reinforced plastic (GFRP)	2.08	45	16
Kevlar fiber-reinforced plastic (KFRP)	1.43	83	58
High strength carbon fiber-reinforced plastic (HS CFRP)	1.64	143-179	87-109
High modulus carbon fiber-reinforced plastic (HM CFRP)	1.85	500	270

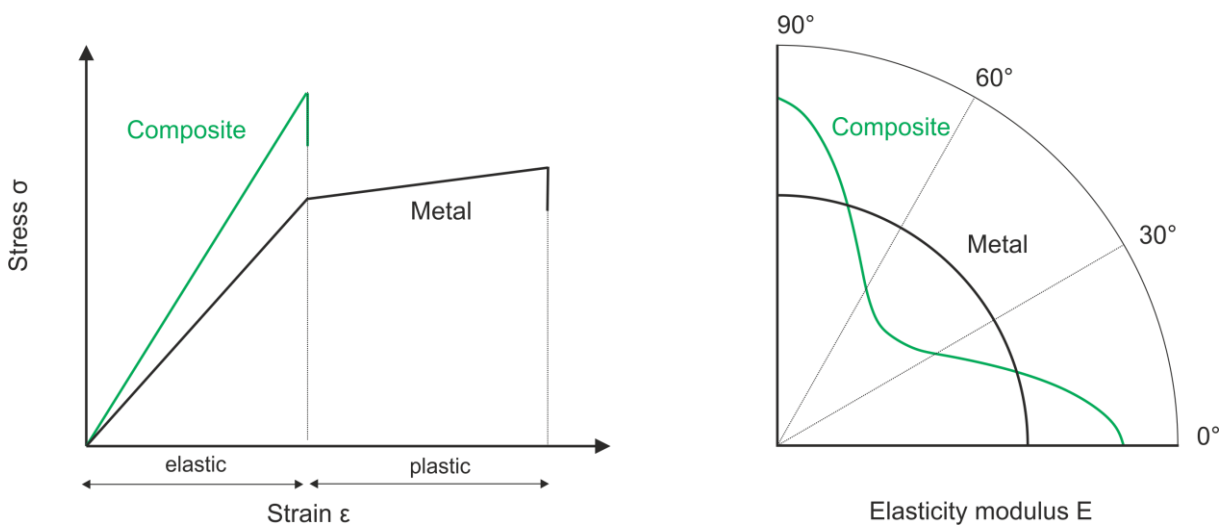


Figure 2-1: Tensile behavior of biaxial reinforced FRP vs. metal

2.2 Selected high performance fibers

Reinforcement fibers can be classified into some main categories: high performance fiber, high strength fiber, metal fiber and natural fiber [42]. High performance fibers are with exceptional high level of physical and chemical properties and used in application where the requirement of mechanical performance and endurance are extreme. Glass fiber (GF), carbon fiber (CF) and aramid fiber (AR) belong to the high-performance fibers group. High strength material is used in applications with moderate requirement, which can be synthetic fiber (e.g., polyester PES, polyamide PA, polyethylene PE) or inorganic origin natural fiber (e.g., ceramics fiber, basalt fiber). Metal fiber can be made from steel, aluminum, copper, tin, zinc, nickel, titanium and their alloys in continuous or staple form. The use of metal fiber can add functionality (in case of shape memory alloys SMA [43–45]) or improve fracture toughness of composite [46]. Some organic origin natural fibers such as flax or sisal are used to produce composite for relatively low mechanical load components [42]. An overview of typical reinforcing fiber is given by Bunsell [39], as shown in Table 2-2. In this section, selected high performance fibers are introduced.

Table 2-2: Overview of typical reinforcing fiber given by Bunsell [39]

Fiber	Mass density (g/cm ³)	Young's modulus (GPa)	Specific modulus (GPa*cm ³ /g)
<i>High performance fiber</i>			
Glass	2.5	72	27.6
Carbon (high strength – H.S.)	1.8	295	164
Carbon (ultra-high modulus – H.M.)	2.16	830	384
Kevlar (para-aramid)	1.45	135	93
<i>High strength fiber</i>			
Polyester PES	1.38	15	10.8
Nylon (PA 6.6)	1.15	5	3.3
Dyneema polyethylene PE	0.96	117	122
<i>Natural fiber</i>			
Flax	1.53	65	43

2.2.1 Glass fiber (GF)

Commercial continuous glass fibers are produced by various melt spinning methods and with a wide range of composition [47]. Silicon dioxide SiO_2 is the main composition of high-performance glass fiber and can be found in nature in sand or quartz. Depending on the type of glass and application, further ingredients can be added to the production process of glass fiber: limestone (calcium carbonate), colemanite (borate mineral), kaolin (kaolinite), boron, aluminum oxides, calcium and magnesium oxides [42,47]. Wallenberger [47] increased the environmental and energy-friendliness of E-glass production by varying the compositions. As reinforcement, high performance GF have a wide spectrum of application across different industries: defense (vehicle armor, small arms protective insert (SAPI) plates), aerospace (rotor blades, cargo liners, interior panels), manufacturing industrial (pressure vessels, wind generator blades), automotive (cords and belts, muffler fill), marine (boat hulls), and sport equipment [48]. GF can also be used as insulation and in electrical/electronic application such as optical signal carrier and printed circuit board (PCB) [49]. Freudenberg [42] gives an overview of typical glass fibers used in various application as shown in Table 2-3. Further details of these typical glass fibers can be found in [42]. In comparison to CF, GF is cheaper but their tensile stiffness is significantly lower. The elongation is absolute linear elastic; thus, any non-linear behavior appears on yarn and textile fabrics can be traced back to their structural undulation/ crimp. GF is dominant and growth driver of the composite sector and predicted to contribute more than 90 % of the composite market worldwide in the period from 2020-2025 [50].

The strength of brittle fibers such as GF and carbon fiber (CF) increases, when the fiber diameter decreases. This phenomenon can be explained by the fact that the probability of defect occurrences (e.g. cracks, notches, slitting, stages) is proportional to volume of fiber, thus also diameter and length of fibers, which can be accurately described by the Weibull probability distribution [39]. The Weibull distribution also explains the reason why the strength of yarn is lower than the collective sum of all individual fibers in its bundle, besides the fact that the fibers not loaded at the same time in the typical tensile test. With the help of a Finite Element (FE) model in combination with the Weibull probability distribution developed by Döbrich, tensile behavior of yarn can be predicted, once the characteristics of the fiber are known [51]. Care should be taken in the design and production of parts working under constant load, as creep contributes a significant elongation growth to glass fiber in the long time. Mechanical properties of glass fiber can be altered under extreme short-term or permanent temperature loads. When used as reinforcement for concrete, their loading capacity is lost under fire stresses and thus leads

to structural failure [52]. It is worth to mention that glass fibers with a high portion of alkali oxides in their composition such as R- and S-glass are sensitive to water. They can lose significant strength when exposed in long time to humidity or dipped in water as well as acidic and basic media [53].

Table 2-3: Overview of typical glass fiber by Freudenberg [42]

Type	Description	Application
E-glass	Aluminum borosilicate glass with less than 2 % alkali oxides	General plastic reinforcement and electrical applications, most common glass fiber type
AR glass	Alkali-containing glass with an increased level of zirconium oxide, alkali resistance	Concrete reinforcement
R glass	Aluminosilicate glass with added calcium and magnesium oxide	High mechanical requirements even at high temperatures
S glass	Aluminosilicate glass with added magnesium oxide	High mechanical requirements even at high temperatures
Silicate	High SiO ₂ mass content ratio (>99.9 %)	Very high temperature resistance
M glass	Beryllium—containing glass	High Young's modulus, used for the highest mechanical requirements

2.2.2 Carbon fiber (CF)

Carbon can form many allotropes, depending on the arrangement of the C atoms in the molecules. Some of the well-known allotropes are amorphous carbon, diamond, graphite, carbon nanotube (CNT) [54]. Amorphous carbon has no crystalline and can be found in coal. Diamond has eight C atoms in a unit cell formed as a face-centered cubic crystal structure. Graphite consists of multiple planes, where the unit cell is a hexagonal ring of six C atoms horizontally arranged in each plane without any bondings between these planes. In CNT, the hexagonal ring of six C atoms is cylindrically arranged into tube form. CNT has exceptional stiffness and strength but the research to use carbon nanotube to produce nanocomposites, which can compete with normal FRP, has not been succeeded after more than three decades [55] due to the so called “agglomeration” phenomenon [56,57]. Current research concentrates on using of CNT to enhance the interface between CF and matrix in FRP [58].

Fibrous carbon material consists of bondings between the graphite planes. If these bondings are not orientated in an identifiable direction, the material is called isotropic fibers [42]. Isotropic fibers have low strength and are barely suitable for composite application. When the graphite planes are parallel to the fiber axis and the bonding is perpendicular to fiber axis, the material is called anisotropic fibers, which have high strength and can be used as reinforcement for composites. Hereafter, the abbreviation CF is used to mention about anisotropic fibers. CF can be produced in the form of carbon filaments from two raw materials: PAN and pitch.

The production technique of CF from PAN was firstly invented in the middle of 1960s [59]. PAN is the precursor for the production of CF and produced by solvent spinning methods. The production of PAN is a chain of multiple processes: steam cracking of crude oil [60] to get propylene, ammoxidation of propylene to get acrylonitrile [61], and finally polymerization of acrylonitrile by solvent spinning methods [42,62] to get PAN fiber. Alternatively, production of some intermediate products such as propylene [63] and acrylonitrile [64] can be carried out via green chemistry route, where renewable biomass instead of crude oil is used. To become CF, PAN fiber must undergo three further processing stages with different temperature: oxidation (200-300°C), carbonization (1200-2200°C) and graphitization (2400-3000°C). By the production of PAN-based CF, oxidation helps the ring formation of the PAN chain molecules. By carbonization, all other atoms except C are removed from the molecule structure, and thus form the hexagonal ring unit cell. Graphitization is necessary by production of high modulus CF, where it improves the alignment and orientation of crystalline region in the fiber. Depend upon the processing temperature, CF with different strength and modulus can be produced [42]. Fiber surface treatment, sizing, coating follow if necessary.

Pitch are a mixture of thousands of aromatic hydrocarbons with 3-8 fused ring produced by distillation of carbon based products such as plant, crude oil and coal [65,66]. Mesophase pitch is thermotropic crystal produced by polymerizing pitch. Mesophase pitch is brought into continuous form by melt spinning. Thereafter, the same three heat treatment stages as by PAN-based CF production are carried out. There is a small difference: oxidation by the production of pitch-based CF helps the cross-linking between molecules to make the material infusible. Varying of temperature during the three heat treatment stages is also resulting in pitch-based CF with different strength and modulus.

In comparison to GF, CF has significant lower elongation growth caused by creep in the long time as well as better resistance against heat, water, basic and acidic media. Being a brittle material, the strength of CF is also subjected to Weibull probability distribution as GF [39], i.e. inversely proportional to volume of the fiber. CF has also a wide spectrum of

application across the industries from aerospace to sport equipment as GF, but due to its high cost, the volume is significantly lower than GF [50].

2.2.3 Hybrid yarns

Hybrid yarns with at least one reinforcing fiber and one matrix fiber, have several advantages. Since the reinforcing fiber and the thermoplastic matrix components are combined within one hybrid yarn, the flowing distance of the thermoplastic polymer matrix to the reinforcing fibers is significantly reduced. Hence, the cycle time is reduced and the impregnation quality is improved. The thermoplastic polymer matrix can be blended with the reinforcing fiber into the hybrid yarn by several techniques. Folding and wrapping two (or more) parallel yarns into one spool is fast and simple but result in bad blending rate and homogeneity. In twisting method, at least two yarns are twisted around each other. This method has a negative effect on the tensile strength of fibers that are sensitive to transverse force, such as glass or carbon [67]. The mixing is not particularly homogeneous, with negative consequences for the quality of the impregnation of the reinforcing fibers when the thermoplastic portion is melted. In wrapping method, the matrix fiber is wrapped around the reinforcing fiber, thus the damaging of reinforcing fiber is less severe but the mixing is not improved. Online melt spinning technology [68] can produce hybrid yarn with no twisting of the filaments, and good mixing is ensured. GF/PP hybrid yarn produced by this method is commercialized under the name Twintex [69]. In commingling technology [70], the reinforcing fiber and matrix fiber are bonded together by means of air blasts. This results in better mixing of the filaments, which has a positive effect on the quality of the impregnation of the reinforcing fibers by the thermoplastic melt in the bonding process, but, like twisting, also damages the fibers that are sensitive to transverse force.

2.3 Fiber-matrix interface and matrix materials

2.3.1 Fiber-matrix interface

Sizing and coating help to protect the finished fiber from external influencing factors, e.g. mechanical, heat, radiation (e.g. UV); or bring functionality to fiber, e.g. conductive by silver coating [71,72]; as well as to change the surface energy and wettability to enhance the fiber-matrix interface for further processing steps to produce thermoset or thermoplastic composite. Silane coupling agent is a popular sizing material for GF, while sizing material for CF often contains epoxy (EP) and polyurethane [73]. Fiber surface treatment, e.g. plasma treatment [74] or oxy-fluorination [75], is another option for fiber-matrix interface modification, and can be used depending on the type of high

performance fiber and end product application [76]. Recent research of using carbon nanoparticle to improve the fiber-matrix interface of FRP also shows positive results [58].

A good interface can assure the load transfer between fiber and matrix and affect many criteria of composite such as tensile strength, toughness, and shear strength. An extensive review of interfaces in multicomponent materials is given by Pukánszky [77]. The author argued that an excessively strong bond between fiber and matrix results in rigid composite with low energy absorption capacity. Ehrenstein also suggested that fiber-matrix debonding (or detaching) process is an effective mechanism for energy dissipation [78]. By engineering the fiber matrix interface, the energy absorption of FRP can be improved [79]. Therefore, rather than setting perfect adhesion as target, the composite designer should consider the use case of the component and decide a reasonable fiber-matrix interface requirement. This interface design principle applies for any pair of reinforcement/ matrix.

Test methods to characterize the fiber-matrix interface have been established such as fiber fragmentation test [80], single fiber pull-out [81], single fiber push-out [82], single fiber push-in [83] and interlaminar shear strength (ILSS) [84]. The characterization and influence of relevant factors on interface between high performance fiber and matrix have also been intensively researched, e.g. GF/thermoset [85,86], GF/thermoplastic [87,88], CF/thermoplastic [89,90], AR/thermoset [91].

2.3.2 Matrix materials

Matrix has many functions in composite: fixation and protection of the reinforcing fiber from transverse/ compression loads and other external influences, e.g., humidity, chemical, heat and radiation; taking and distribution of the external load to reinforcing fiber. Depending on the applications, metal [92], ceramics [93], elastomer [94] or cement [95] can be used as matrix; further details can be found in the cited literatures. For the production of FRP, there are two main groups of matrix material: thermoset and thermoplastics. Thermoset and thermoplastic have their own advantages and disadvantages, when compared with each other. Table 2-4 shows some qualitative assessment of the both matrix material on some important criteria. Each thermoplastics type has their advantage and disadvantage. Choice of thermoplastics for production of FRP should be referenced to compatibility with used fiber; the requirement of part under certain working condition such as strength, stiffness, toughness, thermal resistance, abrasion resistance, chemical resistance; as well as their availability and price on the market.

For the production of FRP, thermoset matrix are available in form of liquid, namely reactive cross-linking matrix resins, including epoxy resin (EP), vinyl ester resins, vinyl ester-urethane hybrid resin, unsaturated polyester resins, phenol resins [73]. These resins can be used directly during the consolidation process, e.g., by one of various methods in the liquid composite molding (LCM) family, or to produce semi-finished thermoset prepregs [96].

Beside film, powder and melt, thermoplastic matrix is available in the form of continuous filaments, which enables the integration into reinforcing yarn to create hybrid yarns as presented in 2.2.3. Thermoplastic matrix is quite diversified; some examples of thermoplastics are polypropylene (PP), polyamides (PA), polyester (PES), polyether sulfone (PSU), polyphenylene sulfide (PPS), polyetherimide (PEI), poly ether ether ketone (PEEK) [42,97]. Thermoplastic matrix can be used directly in the production of composite part, e.g., injection molding, or in the production of semi-finished products such as thermoplastic prepregs (ogano sheet) or hybrid yarn. Typically, extreme high pressure is needed in the consolidation process for thermoplastic, because of their high viscosity. Application of hybrid garn helps to reduce this partly, as the fiber and matrix component are well mixed into each other, where the flow distance of thermoplastics after melting is significant reduced.

Properties of the matrix materials can be further modified or enhanced as necessary by adding substance such as thixotropic agents (to change viscosity), pigments and colorants, fire retardants, suppressants (to block evaporation), UV inhibitors and stabilizers, conductive additives, release agents (to control or eliminate of adhesion) [50].

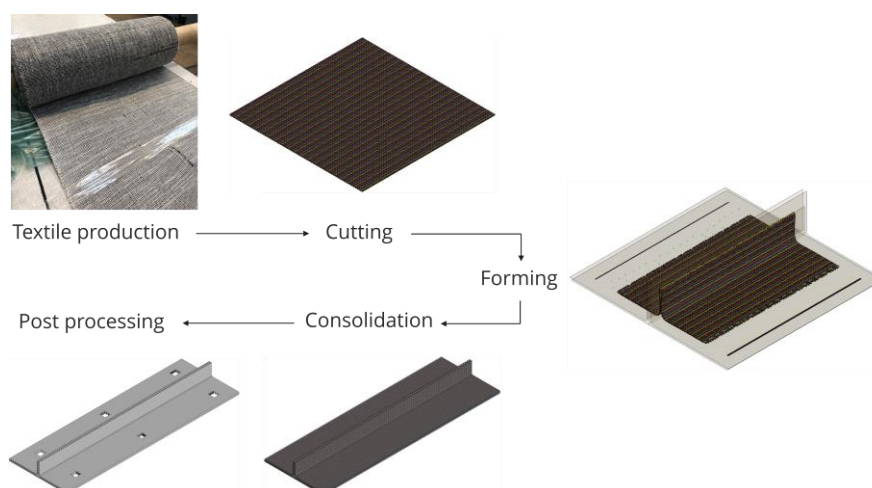
In a multi-step production process, binder can be used during the preforming 2D flat textile to 3D preform [98]. Binder help to fix and maintain position of yarn in each layer as well as of 3D preform overall shape during the transport from preforming station to consolidation station. Binder can be liquid, solid or integrated into textile as yarn. Care should be taken by choosing a suitable binder for each type of matrix.

Table 2-4: Qualitative comparison between thermoset and thermoplastic matrix

Criteria	Thermoset	Thermoplastic
Viscosity/ Flow resistance	low	high
Required pressure for consolidation	low	high-extreme high
Consolidation time	long	short
Fracture property	brittle	ductile
Impact strength/ Toughness	low	high
Hardness	high	low
Temperature resistance	high	low-high
Weld/ Repair/ Recycle	not possible	possible
Storage of semi-products	limited time by cold storage	unlimited time
Curing chemistry	required	no

2.4 FRP production process

The FRP production process can be summarized as shown in Figure 2-2. These steps can be carried out continuously or in a multi stage manner depending on the specification of the production process.

**Figure 2-2: FRP production process with "multi-step" forming**

The reinforcement forming often involves the forming of the fiber material into 3D preform. The forming process can be carried out by "one-step" or "multi-step" forming

methods. In the “one-step” forming process, the input fiber material can be directly and automatically shaped into 3D semi-products. Representative examples for the “one-step” forming method are fiber resin spraying (also called spray layup) [99], injection molding [100], pull-winding [101,102], filament winding [103,104], braiding [105–109], fiber placement techniques [110,111] (including automated tape laying ATL [112], automated fiber placement AFP [112,113], tailored fiber placement TFP [114–116], fiber patch preforming FPP [117] and 3D printing technique [118,119]). Fiber resin spraying and injection molding can only be applied for short fiber based input material. Pull-winding technique can be combined with pultrusion technique to produce of structural profile with constant cross-section and defined orientation for continuous fiber [102]. Classical filament winding has limited use for axially symmetrical convex part [120]. Minsch developed a novel robotized 3D filament winding technique for load optimized three dimensional framework structures [103].

In a “multi-step” forming process, the fiber material must be firstly brought into 2D flat semi-products by various classical textile production techniques such as weaving [121–123], weft-knitting [124–126], warp-knitting [127], nonwoven [128,129]. Textile is produced with great length and wrapped in roll. Thereafter, the flat textiles can be cut into necessary dimension and transformed into 3D preforms manually, e.g. hand layup or prepreg layup, which also means high costs and low productivity; or automatically by draping [130–132] or ready-made technologies [133]. In order to reduce the labor cost of the FRP production and to improve the quality of composite parts, recent research and development focusses on establishing “one-step” preform production process with classical textile manufacturing technique, e.g. direct manufacturing of spherical 3D preform with weaving technique [134], complex 3D nodal preform with weaving technique [135], integrally woven pressure actuated cellular structures [136], complex 3D net-shape preform with weft-knitting technique [37], 3D near net-shape preform with multiaxial warp-knitting technique [137].

In the next step, the 3D fiber semi-products go into the consolidation process, where the merging with the matrix material takes place. Depending on the types of matrix various infiltration and consolidation procedures are available. Suitable for both thermoset and thermoplastics matrix, there are injection molding [100,138], compression molding (CM) [139], continuous compression molding (CCM) [101], pultrusion [102], thermoforming (also called **thermopressing**, hot stamping or sheet forming) [33,140–142], autoclave [143].

Specialized for thermoset matrix, there are **resin transfer molding (RTM)** [144], and its variations in the liquid composite molding (LCM) family (e.g., vacuum assisted resin

transfer molding (VARTM) [145], **vacuum assisted resin infusion (VARI)** [146], compression resin transfer molding (CRTM) [147], Seemann's composite resin infusion molding process (SCRIMP), vacuum induced preform relaxation (VIPR), fast remotely actuated channeling (FASTRAC), structural reaction injection molding (S-RIM), co-injection resin transfer molding (CIRTM), resin infusion between double flexible tooling (RIDFT), Light RTM (LRTM)), and resin film infusion (RFI) [148]. Joule heating [149,150] is a method specialized for thermoplastic matrix and only applicable for fiber with electrical conductivity.

RTM was adopted to enable the production of FRP with continuous fiber, where the required mechanical performance cannot be achieved with short fiber. Although some thermoplastic with low viscosity were introduced, due to the high cost of equipment for thermoplastic resin transfer, where very high injection pressure is required, the most used matrix in resin transfer molding is thermoset [144]. Dry or partially impregnated flat fabrics or 3D preforms are firstly placed on the mold cavity. The resin is drawn from a reservoir then transferred into the free space between the upper and the lower molds or between a single side mold and vacuum bag (in case of VARTM) with the help of pressure or vacuum. The cured part is taken out for further necessary processing (e.g., tempering). Variations of RTM in the LCM family are improved with further modification to overcome disadvantages such as slow infusion time, deformation of preform, non-uniform fiber volume, high tooling cost [144].

Post processing involves drilling, cutting, sawing, machining, sanding to get the part to its final shape/ configuration [151,152]. Care should be taken, otherwise the mechanical performance of the composite part can be reduced.

Aside from the used fiber and matrix material, Advani and Hsiao [33] expressed that the production process of FRP also plays an important role on the mechanical performance of the part. Defects and damage can occur at various states of the manufacturing process of FRP, e.g.:

- by preforming: fiber misalignment, wavy fibers, buckling of fibers, damaged fibers, wrinkle formation, gap formation,
- by consolidation: consolidation degree, voids, foreign bodies, incorrect fiber volume due to insufficient or excess resin, bonding defects, ply cracking, delamination, fracture, fiber exposure, inhomogeneous fiber matrix distribution, weld line, warpage/ residual stress, blister, sink mark, oxidation/ degradation

are just a few examples of more than 130 different types of possible defects [153–157]. Defects on 3D preforms can decrease the mechanical performance of the final FRP [158]. For example, according to Vallons [159], just **5° fiber off-axis angle would lead to 20%**

reduction of FRP tensile strength. Bagherpour [160] gave more detail on the loss of tensile strength of FRP in dependence of angle between fibers and stress as shown in Figure 2-3. In the production process with consolidation technique such as RTM, VARI, and thermopressing, the flat textile can be formed into 3D preform at dry condition in a separate step with forming tools or just with the consolidation tools. Thus, the forming of textile from 2D to 3D should be optimized before mass production to minimized defects on 3D preforms. To serve that purpose, good understanding of the forming behavior of textile reinforcement is required.

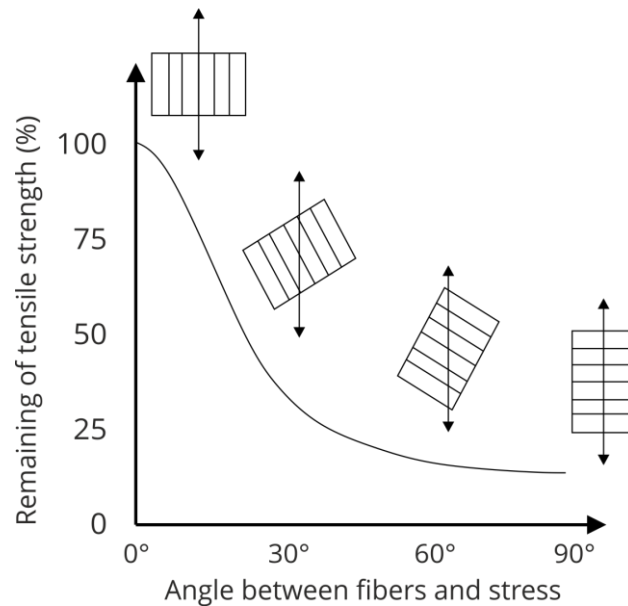


Figure 2-3: Loss of tensile strength in dependence of angle between fibers and stress (adapted from Bagherpour [160])

2.5 Forming behavior of textile reinforcement

The formability (or drapability) of a certain textile reinforcement structure is the ability of the flat reinforcement to be formed into 3D shape without significant defects as mentioned above, e.g., without wrinkle formation as definition of Hörsting [161]. The forming ability of dry fabrics in general is limited, thus, forming of 3D preforms without defects is challenging. The fiber itself has naturally certain influence on the overall drapability of the textile reinforcement, but the configurations of the structure such as type of fabrics, type of binding, number of layer and their order in structure are the key factors. In general, the deformation behavior of textile reinforcement is complicated but it can be broken down into different fiber deformation mechanisms [162] (Figure 2-4):

- compaction of fiber tow
- inter-fiber shear: rotation of fiber within the unit cell

- inter-fiber slip: translation of fiber relative to their neighbors
- fiber buckling: bending of fiber induced by in-plane compression, which leads to wrinkle (out-of-plane) or waviness (in-plane)
- fiber extension: strain of fiber induced by in-plane tension, only significant when elastic modulus is low and break elongation is great

In warp and weft-knitting fabrics, as the stitch yarn present, follow additional mechanisms can also be counted:

- stitch tension
- frictional stitch sliding
- interaction between stitch yarn and reinforcing yarn

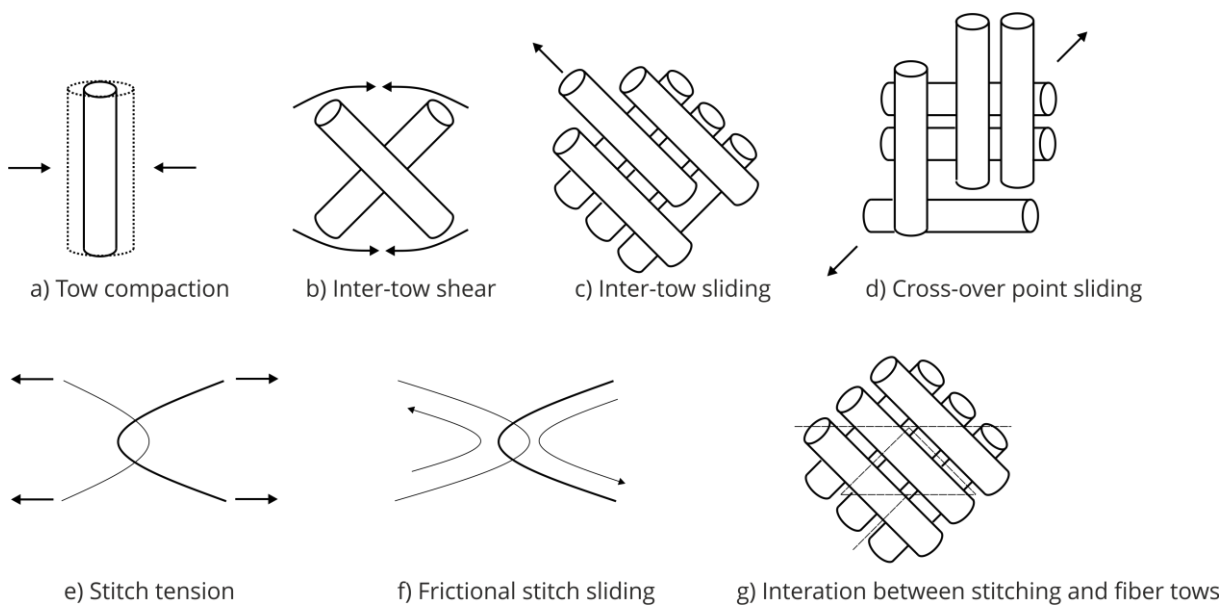


Figure 2-4: Illustrations of fiber deformation mechanisms (adapted from Creech and Pickett [163])

The inter-fiber shear and fiber buckling mechanisms are dominant by woven fabrics, where the yarn systems are interlocked and the relative movement of neighboring yarn is difficult. For other structures such as reinforced weft- and warp-knitted fabrics, inter-fiber slip can be more significant and gap formation can be seen more often.

A quantitative measurement of these deformation mechanisms is challenging. For soft fabrics in the garment industry, determination of drapability including drape coefficient according to the standard DIN EN ISO 9073 is used, where round specimens with different diameters are clamped by an round tools, and fall freely under their own weight (Figure 2-5).

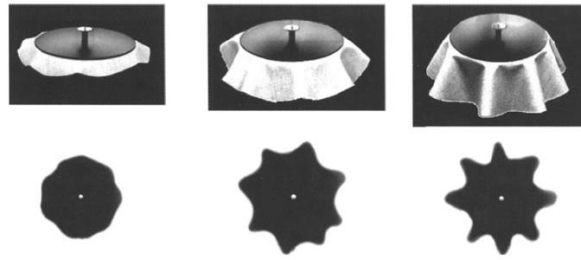


Figure 2-5: Drapability test according to DIN EN ISO 9073

There is no standard for measuring the drapability of fabrics made from high performance fiber. Instead, drapability is considered as the sum of individual fiber deformation mechanisms, of which only the following can be quantitatively measured: tensile, shearing and bending. With the help of tensile test, the structural fiber straightening and extension can be measured. Except of UD non-crimp fabrics (NCF), most of the reinforcing textile structure have a certain degree of crimping and shows non-linear tensile behavior at the initial strain. The test of shear resistance such as picture frame test (also called trellis frame) or bias extension test [164] can help to measure the resistance of textile structure against shearing deformation. The bending tests (such as cantilever, or 2-point-bending test) help to measure the bending stiffness. While cantilever is popular for relative soft fabrics, it is hard to apply test very stiff fabrics such as multi-layer woven. That is when 2-point-bending test should be used [165].

The interaction between the named fiber deformation mechanisms is significant in some cases, e.g., change on tensile behavior of warp yarn system, while weft yarn system under tension [166] (and vice versa), or increase of in-plane tension leads to change of shear behavior [157] (Figure 2-6). Depending on scale of view, certain fiber deformation mechanisms can be named differently. For example, during bending, relative motion between layers can also be observed (as in Figure 2-7). On the micro- or mesoscale, this relative motion between layers can be seen as sliding. On the macro scale, it can be considered as shear deformation.

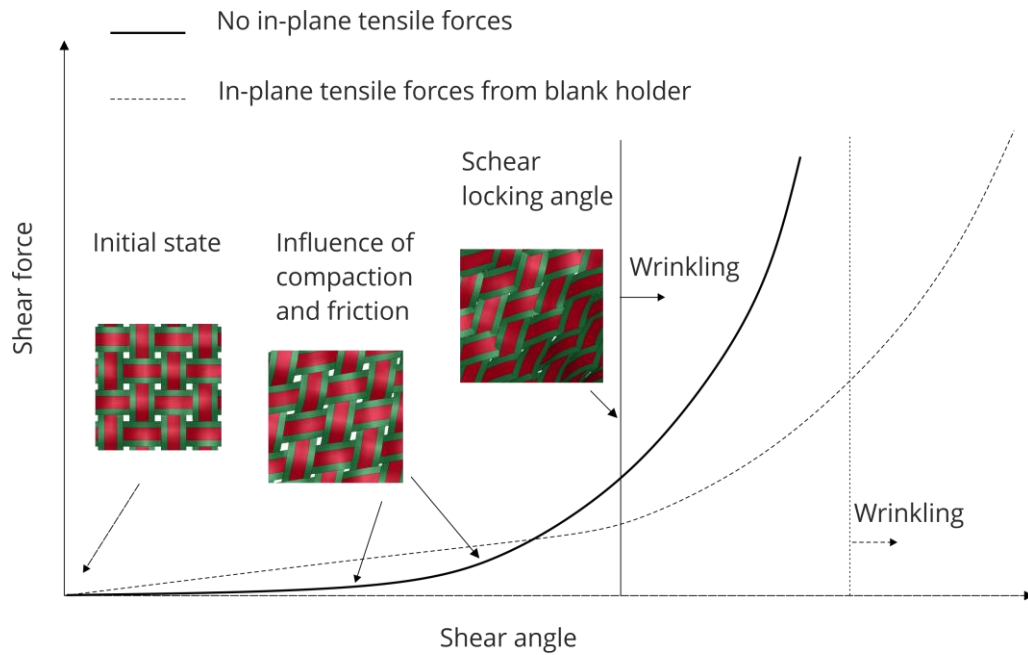


Figure 2-6: Influence of in-plane tensile stress on shear behavior (adapted from Thor [157])

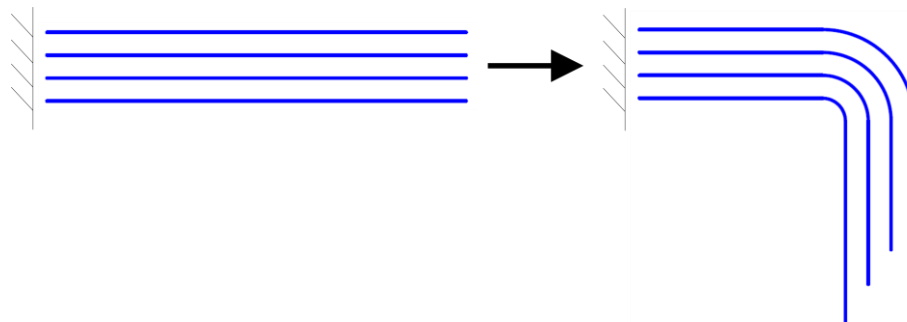


Figure 2-7: Sliding between fiber layers during textile bending

The complexity of the surface geometry can be classified from flat, single curvature, double curvature to free form as shown in Figure 2-8.

Forming test apparatus with different geometries have been used by researchers around the world, e.g., conical [167], double dome [168], tetrahedral [169] and L-shape [170], and most of them belong to the doubly-curve surface class. The L-shape forming tools is free form surface. As an effort to quantitative assess the forming ability of reinforcing textile, the company Saertex GmbH & Co. KG built the Saerdrape forming test machine, which can measure the force-displacement-curve, while forming textile with spherical stamp and blank holder under defined pressure. On basis of the working principle of Saerdrape, the Textechno Drapetest machine comes with the improvement of complex digital image

analysis system and laser triangulation sensor, [171] which can quantify the position and direction of fiber as well as dimension/size of wrinkles and gaps.

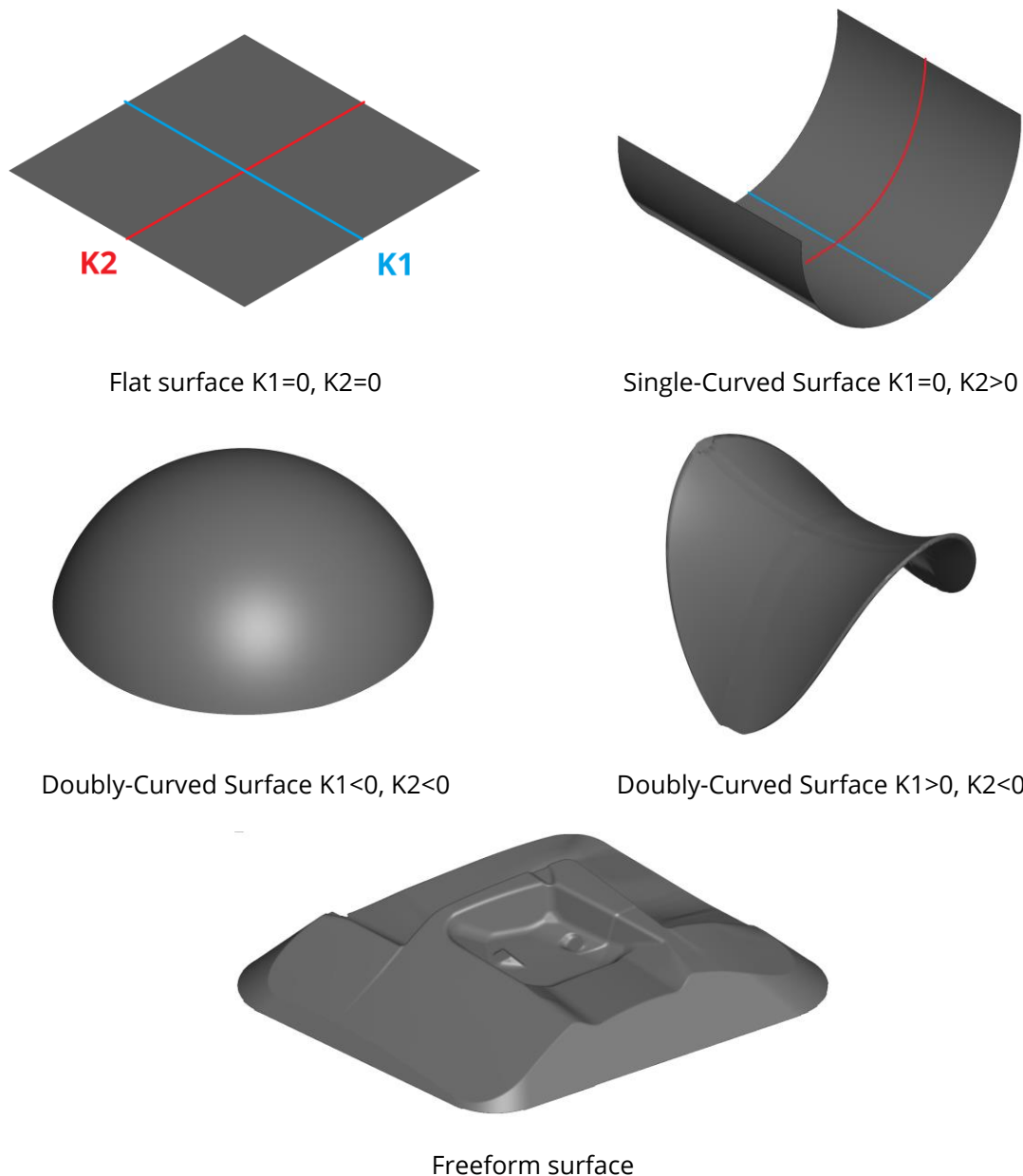


Figure 2-8: Surface typology and principal curvature (adapted from Mansoori [172])

In the production of thin-walled doubly curved composite part, the forming of 3D preform is especially important. Friedrich et al. reported that the wrinkle in glass fabric preforms can be suppressed by suitable clamping stress on flange area [173]. The clamping stress can be realized by hydraulic, pneumatic, electric actuator or magnetic clamp [174]. It is challenging to choose an appropriate clamping stress. At high clamping stress, fiber can be damaged or fabric can be torn due to the friction induced in-plane tensile stress [175], while insufficient clamping stress cannot suppress the wrinkle as well as the in-

plane and out-of-plane waviness (buckling) on the preforms [141,176]. Nosrat Nezami et al. [131] reported that the forming tool geometry and forming process parameters can be adapted and actively controlled in order to manipulate the magnitude, direction, and distribution of the friction induced in-plane stress in order to suppress the forming defects or to reach a load path optimized fiber orientation without damaging the fiber. Therefore, the forming process should be optimized before serial production, which costs time and material due to the trial-and-error method. By changing the geometry of forming tools, e.g., lead-time and manufacturing costs of the new tools are considerably increased. To reduce these costs, a numerical approach can be helpful, e.g. the load distribution of clamps can be virtually optimized [177]. Thanks to the advantage of information technologies, computing cost has been becoming always cheaper. That would make a digital twin process chain more competitive to the traditional trial-and-error method. A good virtual process chain requires good understanding of the forming behavior of textile, and good modelling strategy to assure the plausibility and applicability of the numerical model.

2.6 Selected textile semi-finished products

2.6.1 Woven fabrics

The first hand woven fabric can be traced back to more than 7000 years ago [122,178]. Hammesfahr patented the first glass woven fabrics in the USA in 1880 [179], which consists of silk and glass fiber, but this kind of fabric was not used as reinforcement. First woven glass fabrics were used as reinforcement for composite boat in 1937 and car body in 1945 [180]. First carbon woven fabrics was introduced in 1974 [181]. Weaving is a well-established processing technique with great progress in the recent decades in general as well as for the production of 2D and 3D preform for FRP.

Weaving machine can be categorized based on its shed formation system (tappet weaving machine, dobby weaving machine and Jacquard machine) or weft insertion principle (shuttle, projectile, jet, rapier, ribbon needle, circular, wave-shed, shed course) [122]. Out of these categories, there are special weaving machines for 2D polar (spiral) fabrics [178], 3D polar fabrics, multiaxial woven fabric, fully interlaced 3D woven structure [182]. Processing of high-performance fibers such as GF and CF with minimum fiber damage is challenging, as they are brittle and sensitive to transverse force. For this reason, the production of woven fabrics from high performance fibers is preferred to use rapier weaving machine [123,183].

Distinguished from other fabric structures, woven fabrics consist at least of two yarn systems, which are interlaced into each other due to the weaving process. The yarn system parallel to production direction is called warp yarn. Shaft is the machine element, which carries the warp yarn and translates in the vertical direction during the weaving process. The shaft position during the insertion of weft yarn in the perpendicular direction will decide that warp yarn lays over or under the weft yarn.

The weave pattern of single layer woven fabric is the representation of the arrangement of warp and weft yarn in a unit cell, which repeats itself as groups of warp yarn in different shafts are controlled simultaneously. The weave pattern has significant influence on the various criteria of fabrics such as permeability, mass per unit area, thickness, crimp, tear resistance and forming behavior including: tensile, shear, bending and slippage resistance [122,165].

Weave pattern of single layer woven fabric is described by a color-coded grid of square, where colored square is the position, the warp yarn lays over the weft yarn. Basic weave patterns of single layer woven fabric can be categorized in the following group: plain, twill, satin. The derivation and combination of the basic weave pattern result in an enormous amount of possible weave patterns. Jacquard weave pattern can only be realized on a Jacquard weaving machine, where every single warp yarn can be controlled independently [122]. Figure 2-9 shows an example of plain weave from GF 1200 tex: weave pattern, fabric appearance and cross-section.

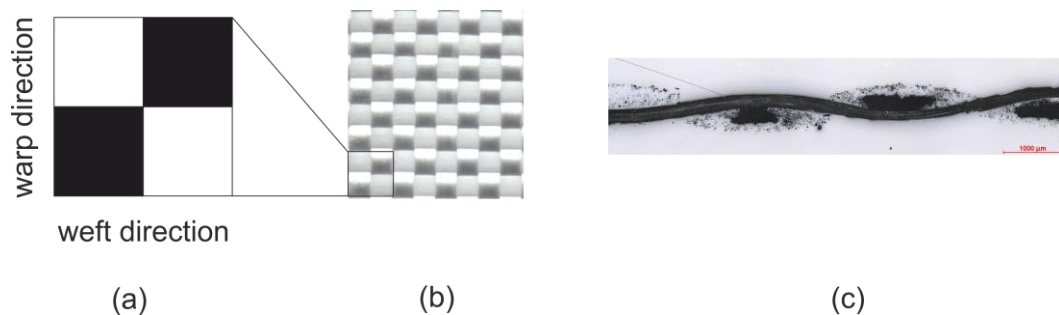


Figure 2-9: Plain woven glass fabric from GF 1200 tex: a) weave pattern, b) fabric appearance and c) cross-section

The coding of multi-layer weave patterns is more complicated, as multi-layer woven fabrics consist of multiple warp and weft yarn systems. Multi-layer woven fabrics are diverse. Some selected basic weave types can be named as the following: orthogonal (ORT), diagonal/angle interlock (AI) and layer-to-layer (LTL). Depend upon the yarn path, each type of multi-layer weave can be further divided into smaller groups with different weave patterns, e.g. ORT plain, ORT twill, ORT satin [123]. Figure 2-10 shows an example

of a multi-layer woven fabric made from GF 2400 tex with four weft yarns in a row: weave pattern, 3D illustration by TexGen, top appearance and cross-section in the warp direction. The color-coded grid square is made of two columns (k1-k2) representing warp yarns, and eight rows (s1-s8) representing weft yarns in the corresponding position. If the warp yarn lays above the weft yarn, the square is colored; otherwise, it is left blank.

With a sophisticated weave pattern design, weaving technique can produce tube joint [184,185], carrier profile [122], space fabric [183], pressure actuated cellular structures [136]. Open-Reed-Weaving (ORW) [122] is a new technology, which allows to insert additional yarns into the woven fabric with arbitrary path. ORW is suitable for functional integration of woven fabric and their FRP such as sensor [186] or actuator [44]. For production of grid structure reinforcement in form of non-crimp fabric with application in civil engineering, modifications were made to available Leno weaving technology [187], which enables processing of high performance fibers with limited damage and makes weaving now competitive with warp-knitting technique in this sector. The research and development of woven fabric reinforcements carry on, in which direct manufacturing of complex preforms for FRP is an important goal.

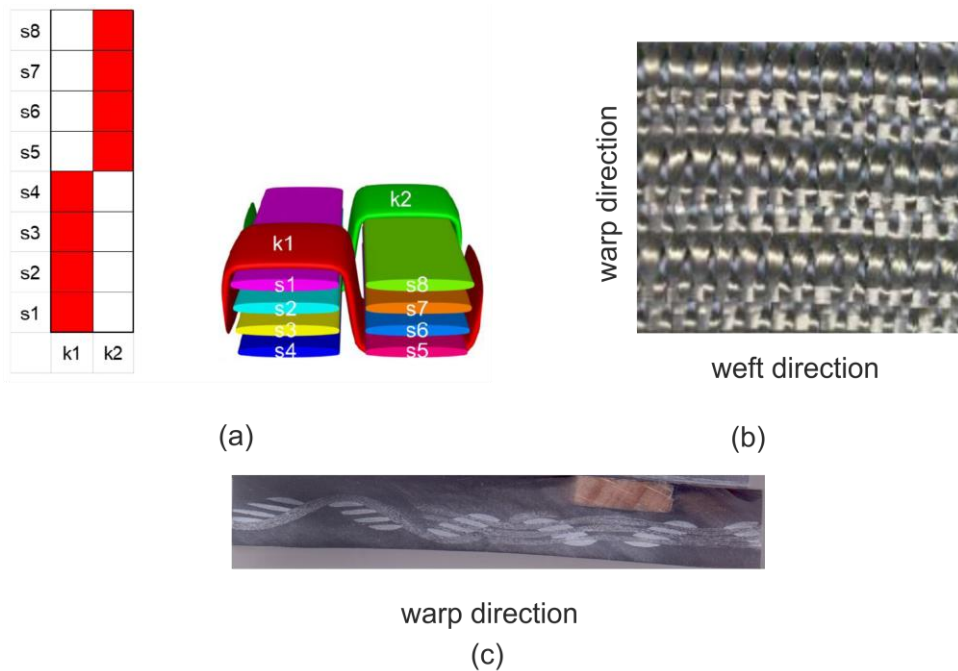


Figure 2-10: ORT plain weave: a) weave pattern and 3D illustration by TexGen, b) top appearance, c) cross-section in the warp direction

2.6.2 Warp-knitted fabrics

The knitting technique is divided into two large groups, where the direction of yarn path, as well as stitch formation is distinguished: weft knitting across the production direction and warp knitting along the production direction. Figure 2-11 shows the comparison of stitch structure and stitch formation with bearded needle between weft- and warp-knitting. Warp-knitting technique is one of the most productive textile production methods but less flexible in comparison to other textile production methods. The stitch of warp-knitted fabrics is formed along the production direction by intermeshing the warp yarns into the previous formed stitch. Needle bars control the warp yarn movements. In general, the warp knitting technique can be further divided into two groups, depending on the quantity of needle bars: right-left (RL) and right-right (RR). A full list a machine types of each group can be found in [127]. Production of reinforcement for FRP is based on the following machine types: RL weft insertion, RL stitch-bonding machine and RR double-needle bar raschel machine. Distinguished from classical warp-knitted products, the reinforcement for FRP requires additional reinforcing yarn system besides the warp-stitching yarn. The fineness of warp-stitching yarn in most cases is significantly lower than the reinforcing yarns. The most common reinforcing type is in the warp direction (0°), which results in unidirectional non-crimp fabrics (UD-NCF) [188]. Biaxial NCF has additional reinforcing yarns in the transverse direction (90°). As state of the art, multi-axial NCF has reinforcing yarns in four directions: 0° , 90° , and $\pm 45^\circ$. The quantity, direction and sequence of reinforcing yarn layer in the NCF structure are configurable, which enables a great diversity construction of NCF. An example is shown in Figure 2-12. The warp yarns normally come directly from spools through the guiding system into the knitting zone. Reinforcing yarns in other directions must be firstly fixed on a yarn transportation system, before being fed into the knitting zone, where the warp-knitting stitch is formed that fixes the reinforcing yarns all together. In recent development, Tsai suggested a new concept as “double-double” composite laminate [189], in which the variation of the reinforcing yarn orientation is more than the four standard angles and varies gradually within the stack of composite laminate. Such laminate structure improves various criteria of the composite performance. An implementation of the double-double composite laminate with warp-knitting technique would reduce the production cost and enable the use of this structure in the industries.

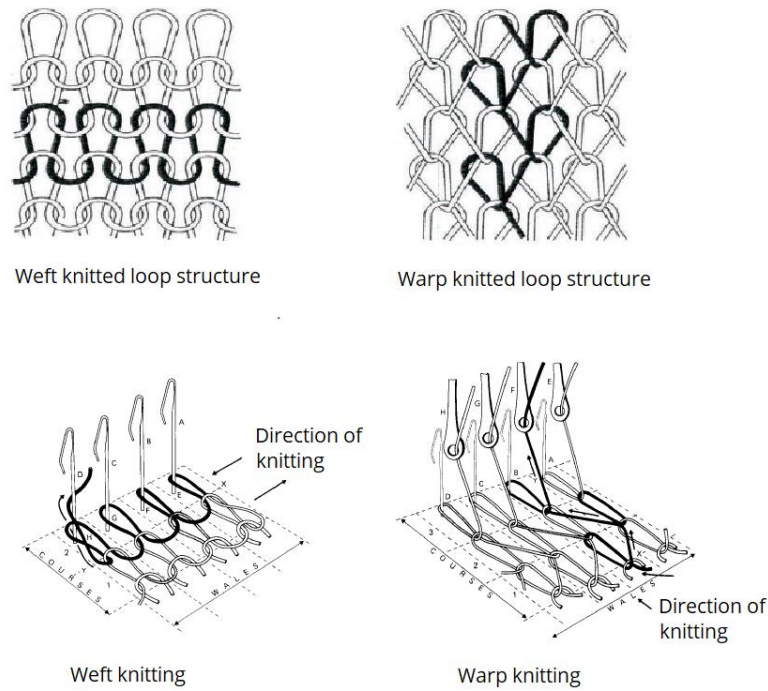


Figure 2-11: Comparison of loop structure and loop formation with bearded needle between weft and warp knitting according to Spencer [190]

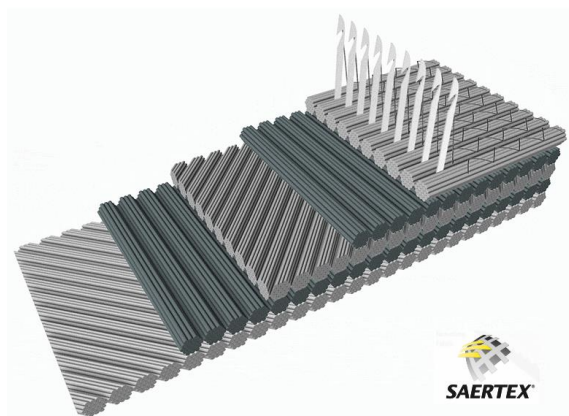


Figure 2-12: An example of non-crimp fabrics construction (© SAERTEX GmbH & Co.KG)

2.6.3 Weft-knitted fabrics

In contrary to warp knitting, new stitch of weft-knitted fabrics is created across the production direction by intermeshing the newly fed stitching yarn into the previous formed stitch (Figure 2-13). Thus, the weft-knitted fabric is formed progressively row by row. Weft-knitted fabrics were originally handcrafting products. Since the invention of stock hand frame by William Lee in the 16th century [125,191], the production of weft-fabrics has been mechanized, and thus the productivity was significantly improved.

Further improvements have been made afterwards, e.g. double needle bed by Jedediah Strutt in 1758 [190], circular loom by Frenchman Decroix and Marc Isambard Brunel in the period 1798-1816, latch needle by Matthew Townsend in 1847. Based on the foundation of the named improvements, the first knitting machine was created and patented by William Lamb in 1863 [192]. In recent developments, the weft-knitting machine has been upgraded with many features such as computer controller (also called Jacquard), computer-aided design (CAD) system support, fully fashioning (also called shape knitting), stitch pressing-down devices, multi-gauge technique, advanced take-down system and needle bed racking [125,193].

Weft-knitting machines can be categorized by different criteria: needle bed geometry (flat or circular), type of needle (latch needle, compound needle and bearded needle), needle automation grade (Jacquard or non-Jacquard), type of cylinder (only applicable for circular knitting machine: single or double cylinder), and type of binding type (single jersey, double jersey, rib, purl, interlock, single truck, multi truck, socks) [194]. Latch needles and compound needles can be individually moved, thus they are suitable for high grade of automation, while bearded needles are jointly moved.

The stitch formation with bearded needle in weft and warp direction are shown in Figure 2-11 and explained in [190]. Stitch forming with compound needle is similar to latch needle with the only difference: the sliding latch of compound needle is actively controlled. Additionally, the production of fabrics in this thesis is based on a knitting machine with latch needle, thus only the stitch formation with latch needle is explained in more detail. Figure 2-13b shows the stitch formation with latch needle on a knitting machine with cam system. The latch needles are rested on the needle bed and fixed between the trick walls, so that they can only translate in one direction along the trick wall. The translational movement of the needle is strictly controlled by the free space between the clearing cam, guard cam, stitch cam and upthrow cam, where the needle butt slides along. Five needles in the Figure 2-13b demonstrate the formation process of one stitch systematically:

- The latch needle 1 is in the rest position, while it holds the old loop inside its hook and the latch is closed. The needle butt is positioned at the start of the cam.
- The needle 2 starts rising as its butt is lifted up by the clearing cam, whereas the guard cam limits the movement. Due to the contact with the old loop, the latch opens and the old loop slides out of the hook.
- The needle 3 is at the highest position of the clearing cam, which also means the old loop is now completely away from the latch. New yarn is fed into the hook by the yarn feeder.

- The needle 4 starts descending as its butt slides down the clearing cam. This is limited by the stitch cam. The old loop now slides up, touches the latch and closes it, while the new yarn is already inside the hook.
- The needle 5 continues descending, normally at a depth lower than the rest position, as its hook now pulls the newly fed yarn into the old loop, also called knock-over, and forms a new loop. After that, the needle is moved up a bit by the upthrow cam to the standard rest position. The cycle repeats itself for the next stitch.

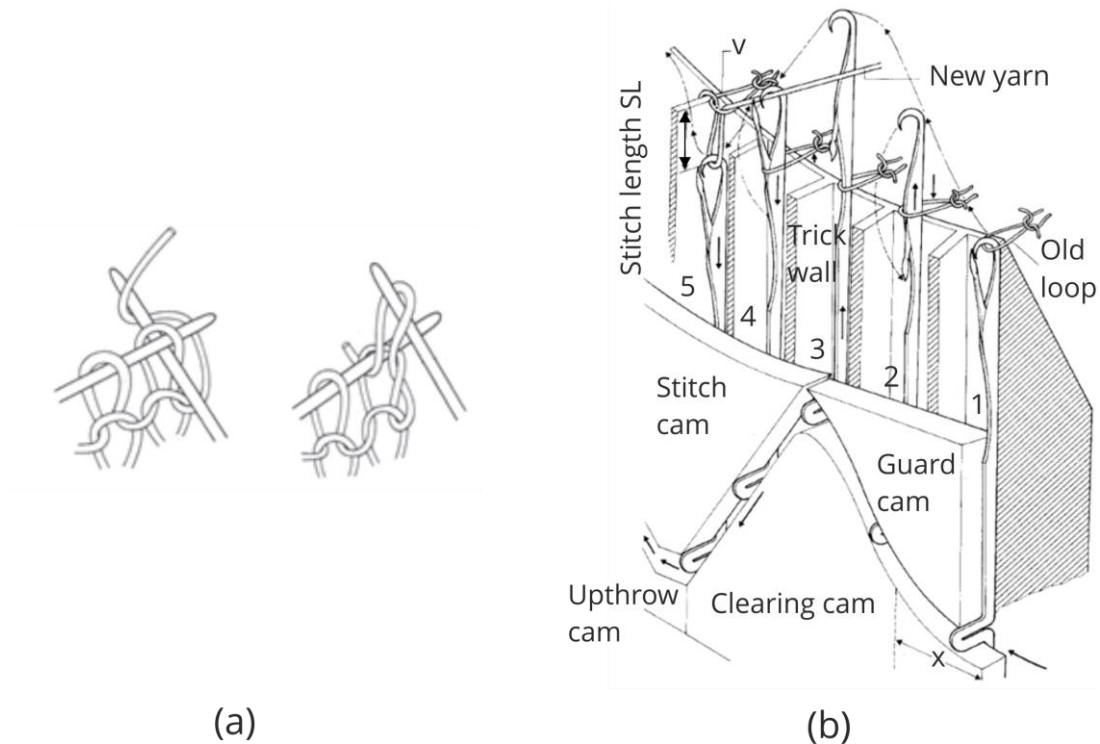


Figure 2-13: Single jersey stitch formation by hand knitting using: (a) pins and (b) by knitting machine with latch needle and cam according to Spencer [190]

That is the formation of standard knit loop, where the needle receives a new loop and knocks over the old loop of the last knitting cycle (Figure 2-14a). When the needle receives a new loop without knock-over, i.e., holding two loops at the same time on a row, it is a tuck knit (Figure 2-14b). Tuck stitch is formed, when the needle is left standing at its highest position in a knitting cycle, where it can receive a new loop but does not knock over the old loop. Float stitch (Figure 2-14c) is formed, when the needle is left standing at its rest position, holding the old loop without receiving the new loop or knocking over. The formation of tuck stitch and float stitch requires certain needle to be left out standing during a knitting cycle at a desired position. That was already possible with manual knitting machines, where the operator must deactivate and activate the needle selector

by hand. Advanced knitting machines are equipped with electronic needle selection system, which allows to program complicated knitting patterns [195]. There are also more complicated stitch formation techniques: i.e., transfer of a loop from one to another needle on the same needle bed or on the opposite needle bed. Besides the visual effects, such transfer is the foundation of fully-fashioned technique, where the whole knitwear can be produced as one piece in one-step. Structure of weft-knitted fabric has significant influence on the mechanical behavior, e.g., the tensile behavior in weft direction as shown in Figure 2-15.

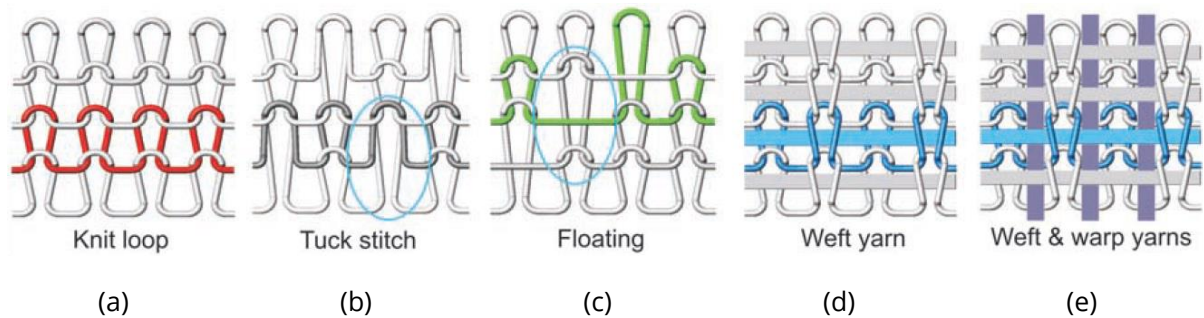


Figure 2-14: Structural element by flat knitting according to Abounaim [193]

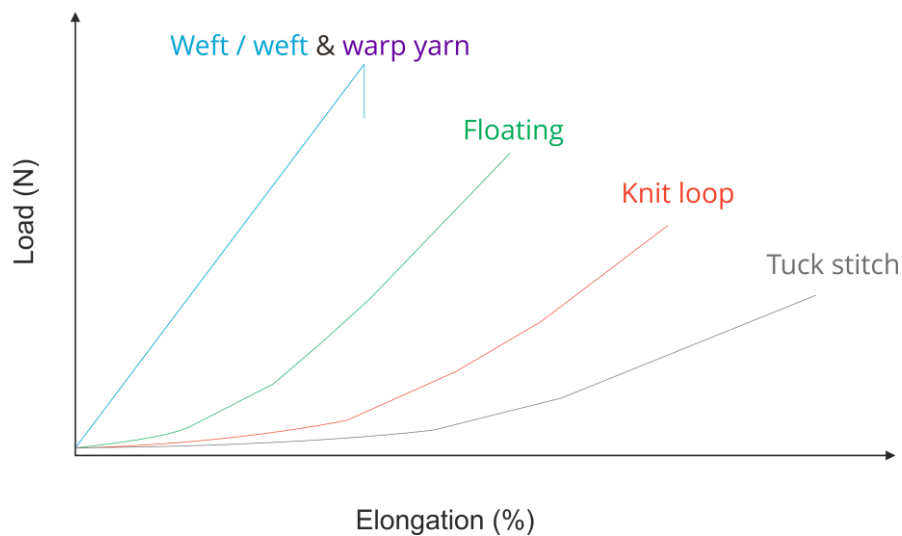


Figure 2-15: Dependence of tensile behavior on structure of BWKF (in weft direction) according to Trümper [125]

Unreinforced weft-knitted fabrics, with only stitching yarn system from high performance fibers can be used as reinforcement for FRP [196,197] as they showed good formability from 2D into deeply curved geometries. FRP made from unreinforced weft-knitted fabrics have good impact strength and fracture toughness [198–203]. However, without the straight reinforcing fibers, they are lacking of tensile strength and stiffness [204–206]. de

Araújo et al. [207] believed that the main reason is due to the non-linear behavior of unreinforced knitted structure under tensile loading. Damage of fiber during knitting process should also contribute partly to the phenomenon, as the high performance fiber must undergo bending load, which is especially dangerous in the case of brittle and sensitive fiber such as CF and GF [208,209]. Significant damage of fibers is caused while forming tuck stitch (Figure 2-14b) [210]. Rudd suggested that introduction of floating stitch (Figure 2-14c) into structure would improve the mechanical performance [205]. Other researchers suggested that integration of fully straightened yarn is more effective as crimps are reduced [211]. The work of Abounaim confirmed this suggestion for the case of straight yarn in the weft direction [204].

The integration of straight yarns into weft-knitted fabrics in cross production direction (90°) can be realized by weft inlay (Figure 2-14d), where a separate feeder carries the inlay yarn. This feeder moves and feeds the inlay yarn into the structure at a period, where no needles move, so that the inlay yarn is not formed into loop. When the inlay yarn has been completely fed, loop formation process is started, and the stitching yarn embraces the inlay yarn into the knitted structure. The location and length of inlay yarn can be arbitrary defined along the width of the knitted fabrics. For reinforcement, length of inlay yarn is normally equal to fabric width. The inlay yarn integration technique can also be used for adding functional components such as sensor or actuator yarn/network into knitted structure. Integration of straight fiber in production direction (0°) (Figure 2-14e) is more challenging, as additional yarn feeders and guide for warp yarns, and suitable binding type of stitching yarn are required. Such modification can be made on standard V-bed flat knitting machine (Figure 2-16) [212–214]. That leads to the creation of multilayer weft knitted fabrics – MWKF or MLG (abbreviation of the German term “MehrLagenGestricke”). With reinforcing yarn in both warp and weft direction, structure is also called by some authors with the name “multilayer-connected biaxial weft knit” (MBWK) [215–217]. Hasani gave a good review on state of the art of **biaxial weft-knitted fabrics (BWKF)** [215]. In this work, the term BWKF is used. With one stitching yarn system, BWKF can have from two to eleven reinforcing layers [213,218,219]. While the production of BWKF with asymmetric configuration needs only needle on one needle bed (Figure 2-16), symmetric configuration requires needles on both needle beds (Figure 2-17a & b). The tensile strength and stiffness of FRP made from BWKF is significantly improved with the present straight yarn system in warp and weft direction [216]. By changing the binding of knitting system, the mechanical performance of FRP made from BWKF such as tensile, three-point bending, and three-point bending impact can be improved [217]. When high performance fiber is used as stitching yarn, additional reinforcing effects in the thickness direction (z-

direction) can also be realized, which would help to minimize the risk of failure of FRP due to delamination.

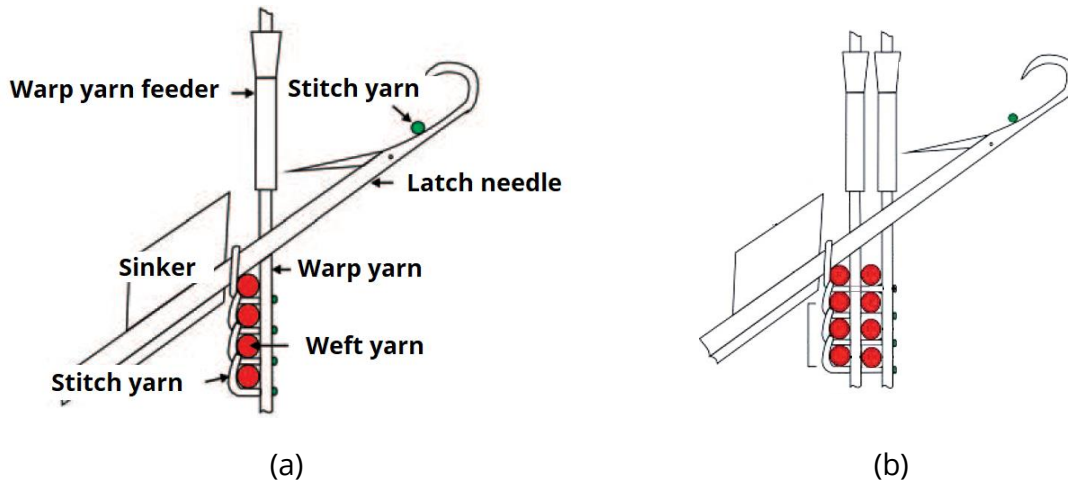


Figure 2-16: Construction of the knitting zone of: (a) asymmetric 2- and (b) 4-layer BWKF [193]

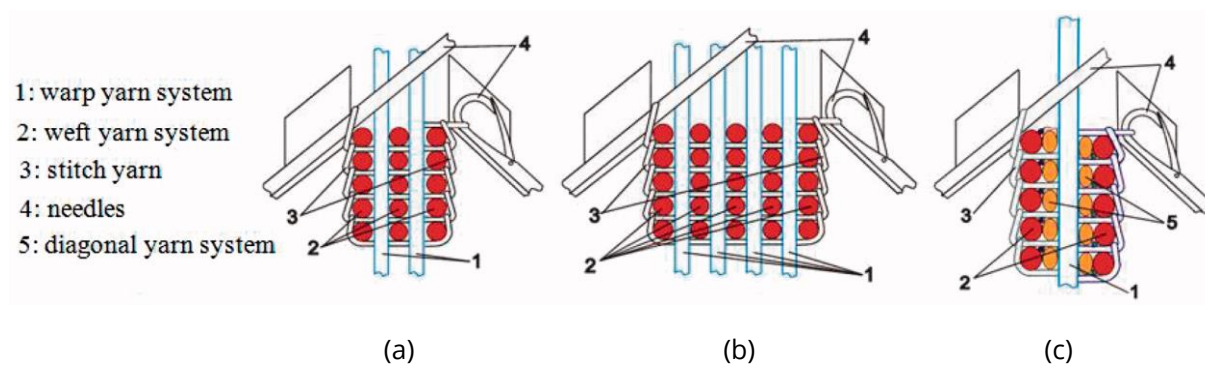


Figure 2-17: Construction of the knitting zone of: (a) symmetric 5-, (b) 9-layer BWKF and (c) symmetric 5-layer MWKF [219]

On the basis of the working principle of BWKF production technique, many further knitting techniques for direct forming of 3D preforms have been developed:

- production of fully fashioned near-net shape BWKF preforms by varying stitch number, stitch length and stitch pattern in both warp and weft direction, e.g. cuboid, sphere, spirally circular disk (Figure 2-18) [218],
- production of 3D spacer BWKF preforms with warp and weft reinforcement on each side and with the fully fashioned technique in combination with needle parking technique (Figure 2-19) [124,193,204,220],
- production of MWKF (Figure 2-20c) [125],
- production of complex 2D/3D BWKF preforms with the help of computer-aided design (CAD) software, which transforms the target 3D geometries to 2D cut

pattern (Figure 2-21) [36,219], and with active segmented take-down system [221,222],

- production of tubular (with constant or variable cross-section) and net-shaped 3D skin-stringer BWKF (with constant or variable height) preforms (Figure 2-23) [37]

Co-woven-knitted (CWK) biaxial fabrics is a special combination of weft-knitting and classical weaving technique, where the standard construction is the same as BWKF but the warp and weft yarn are interwoven with each other [223,224]. FRP made from CWK shows plastic failure under tensile load instead of brittle as BWKF reinforced FRP.

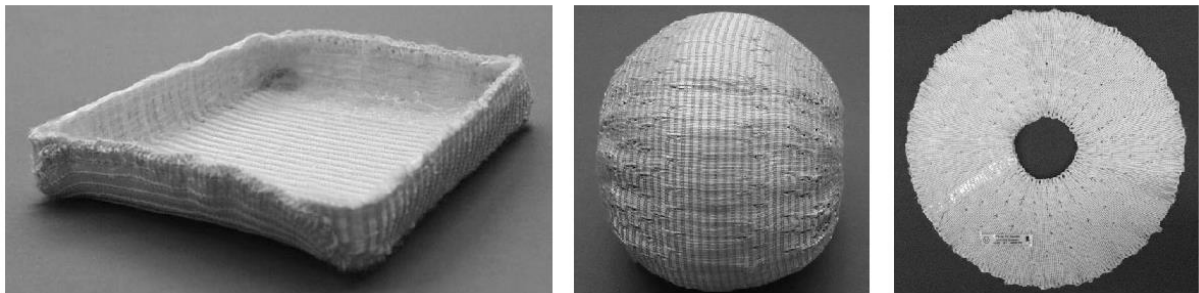


Figure 2-18: Fully fashioned near-net shape BWKF preforms [218]

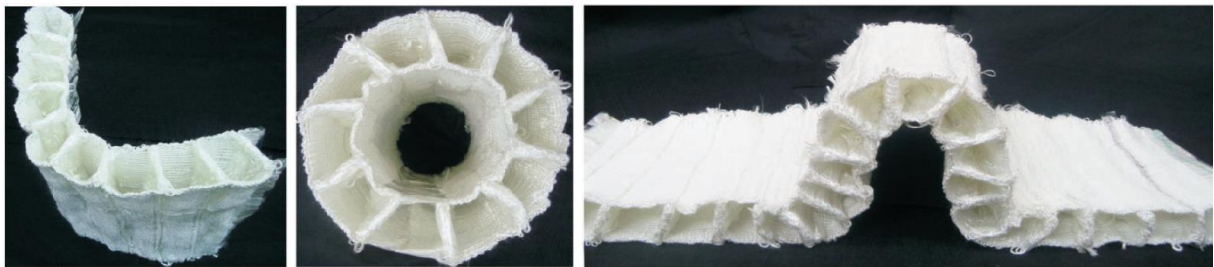


Figure 2-19: 3D spacer BWKF preforms [193]

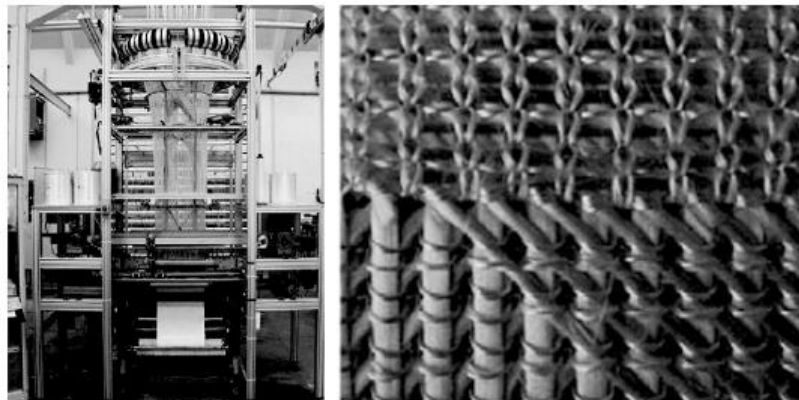


Figure 2-20: MWKF knitting machine and the orientation of the reinforcing yarns in MWKF [125]



Figure 2-21: 3D complex BWKF preform of a truck corner connection [219]

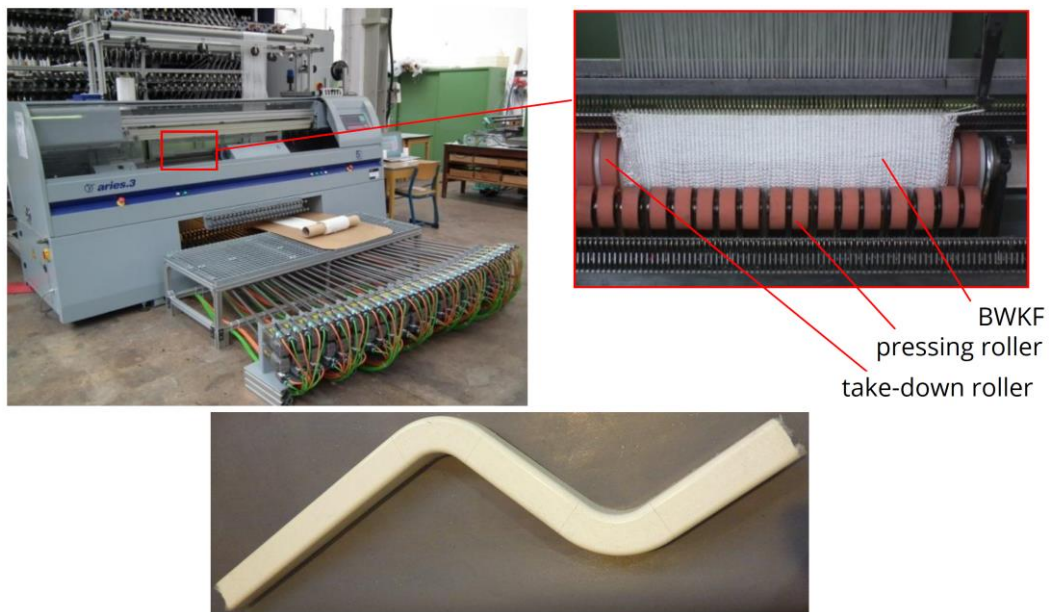


Figure 2-22: Production of 3D BWKF preforms for cabin carrier on flat knitting machine with active segmented take-down system [222]



Figure 2-23: Tubular and shell-rib BWKF preforms [37]

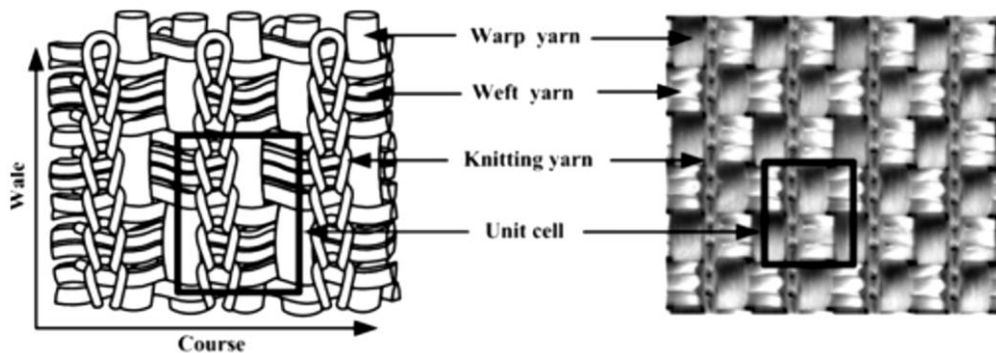


Figure 2-24: Structural geometry and surface of CWK fabric [223]

Flat BWKF also offers an excellent formability into complex shapes for composite reinforcement [225]. By configuration of the stitch length (SL), the shear behavior of BWKF can be accurately tailored. Namely, the control of the shear force-shear angle-curves and the critical shear angle (φ_{SL}) are possible as shown in Figure 2-25. However, the wide spread of BWKF in the industries is prevented by existing disadvantages, which should be improved in further development: low productivity, long preparation and set-up time, especially for the warp yarn feeding system. The first commercial weft-knitting machine with biaxial yarn insertion is introduced at JEC World 2022 (Paris, France) and Techtexil exhibition 2022 (Frankfurt, Germany) by the knitting machine producer Shima Seiki Mfg., Ltd. (Wakayama, Japan).

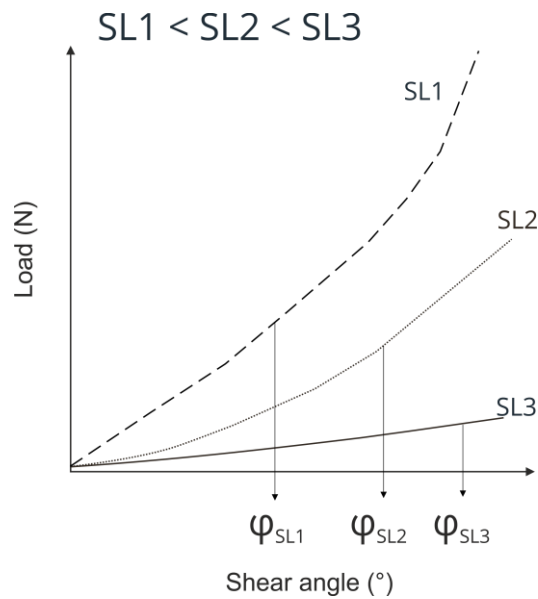


Figure 2-25: Dependence of shear behavior of BWKF on stitch length according to Trümper [125]

2.7 Test methods for textile material and FRP

2.7.1 Fiber tests

Fiber is defined as linear structure that can be processed into textile. Fiber is significant long in relation to its cross-section, which is true for both continuous as well as staple fiber. GF and CF are high-performance continuous fiber. The test methods fineness and diameter of fiber are well standardized such as DIN 60905-1 (Tex system), DIN 60910 (conversion tables), DIN EN ISO 1973 (gravimetric and vibration method), DIN EN ISO 10306 (air flow method), ISO 2403 (micronaire value), DIN 65571-1 (calculation method), DIN 65571-2 (longitudinal projection method), DIN 65571-3 (transverse micro-section), ISO 1888 (glass fiber diameter). The test methods for fiber length are also diverse and well established: DIN 53805 (definition), DIN 53806 (comb staple method), DIN 53808-1 (measuring of individual fibers), ASTM D 1447 (photoelectric measurement), ASTM D 5867 (cotton fiber). Test methods for mechanical properties of fiber such as tensile strength and tensile strain (DIN EN ISO 5079, DIN ISO 3060, ASTM D 1445, DIN 53843-2) and elasticity (DIN EN 15930) are also available.

The vibration method according to the standard DIN EN ISO 1973 is explained in details as it will be used later to test fiber in this work. The testing principle is presented in Figure 2-26. The fiber with the length L is clamped at both ends. A pre-tension force F_v is applied, before fiber is set into vibration. Resonant frequency is applied, and the vibration amplitude is measured. The measuring method of vibration amplitude varies between

test machine manufactures. The fiber test machine Vibromat ME of Textechno Mönchengladbach uses optical sensor to record the maximum amplitude, while the resonant frequency f varies in a defined range. The fiber test machine Vibroskop of Lenzing Instrument keeps using a constant frequency, and changes the fiber length L until the maximum amplitude recorded. Despite of the measuring method, the linear density Tt is calculated with the Equation (2-1):

$$Tt = \frac{F_v}{4 \cdot f^2 \cdot L^2} \quad (2-1)$$

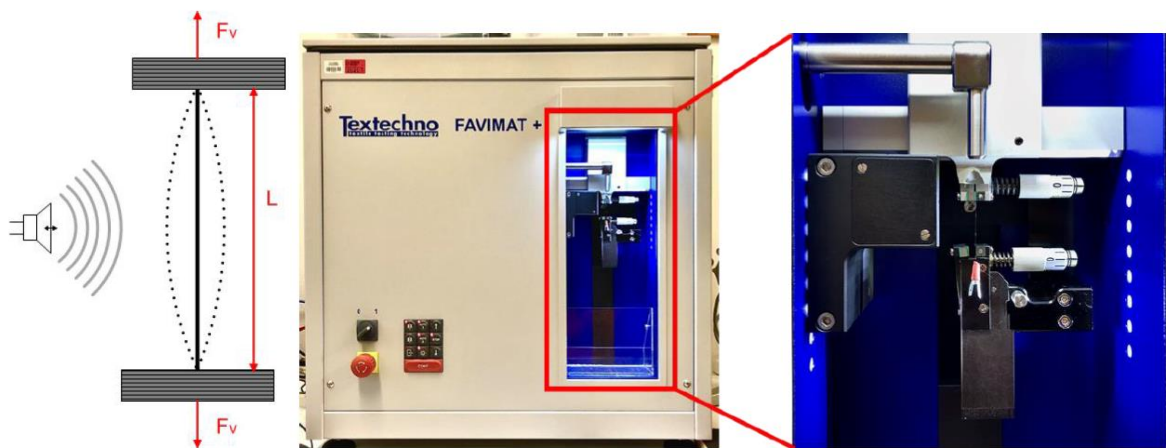


Figure 2-26: Testing principle of vibration method and the FAVIMAT+ test machine

2.7.2 Yarn tests

Most tests for yarn are standardized. The fineness of yarn can be measured according to the available standards: DIN 60900-2 (Tex system), DIN EN ISO 2060 (skein method), DIN 53830-3 (short length method), DIN EN ISO 1889 (reinforcement yarns). Yarn twist can be test according to DIN EN ISO 2061 (counting method), DIN EN ISO 1890 (reinforcement yarns), ASTM D 1422 (untwist-retwist method). The mechanical properties of yarns can be tested with available standards: DIN 53815 (definition), DIN EN ISO 2062 (single-end breaking force and elongation at break using constant rate of extension), DIN 53842-1 (knot tensile test), DIN 53843-1 (loop tensile test), DIN EN ISO 10618 (tensile properties of resin-impregnated yarn), DIN EN ISO 9163 (tensile strength of impregnated rovings), DIN EN 12562 (para-aramid), DIN 65382 (tensile test of impregnated yarn), ISO 3341 (breaking force and breaking elongation of textile glass), DIN 53835-1 (elastic behavior), DIN 53835-2 (repeated application of tensile load between constant extension limits), DIN 53835 (single application of tensile load between constant extension limits), DIN 53835-4 (single

application of tensile load between constant force limits). Unevenness of yarns can be tested by capacitance method as established in the standard ISO 16549 or ASTM D 1425. The tests for friction between yarn and solid (ASTM D 3108) or between yarn and yarn (ASTM D 3412) are available. The crimp of yarn can be tested by the standard DIN EN 14621.

2.7.3 Fabric tests

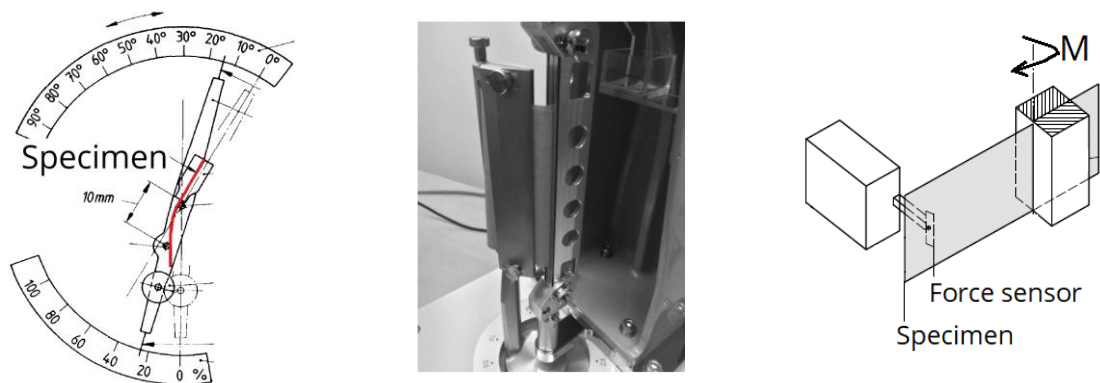
Many tests of fabric are already well standardized such as: length and width (DIN EN 1773 and ISO 5025), thickness (DIN EN ISO 5084 and ISO 4603), compression (DIN 53885), yarn density (DIN EN 1049-2), stitch length (DIN EN 14970), stitching yarn quantity (DIN EN 14971), DIN 53852 (yarn length ratios in fabrics), area density of fabrics (DIN EN 12127, DIN EN ISO 10352, DIN EN 2329, DIN EN 2557)

Tensile test

The mechanical properties of fabrics such as tensile behavior can be tested by stripe tensile test (DIN EN ISO 13934-1), grab method (DIN EN ISO 13934-2); tear properties by ballistic pendulum method (DIN EN ISO 13937-1), single tear method (DIN EN ISO 13937-2 and DIN EN ISO 13937-3), double tear test (DIN EN ISO 13937-4), trapezoid test (DIN 53859-5); elastic behavior by DIN 53835-13 (single application of tensile load between constant extension limits), DIN 53835-14 (single strain between two force limits).

Bending test

There are different methods to assess the bending behavior of fabrics. They can be divided into two groups: deformation-controlled method and gravitational method. With the deformation-controlled method, one or both ends of the fabrics are clamped, and actively bended by test apparatus, where the deformation (normally rotating angle) is pre-defined and controlled. The reaction force is recorded by sensor for evaluation. Representative for this group are Schlenker method (DIN 53864), Kawabata (KES-F2) as shown in Figure 2-27.



Schlenker method according to DIN 53864 Kawabata method © KATO TECH CO., LTD. (KES-FB2-S Pure Bending Tester) ISO 2493-1 Paper and board - Determination of bending resistance

Figure 2-27: Deformation controlled test methods for bending stiffness

With the gravitational method, no external load is used and the specimen is bent by its own weight. The deformation of the fabric is recorded for evaluation. According to Plaut [226], the methods within this group can be further divided into smaller groups:

- cantilever test,
- loop test (with specimen in different shapes: heart loop as in the standard ASTM D1388-18 Option B, hanging ring loop, hanging pear loop,
- fold test (including free fold and clamped fold),
- wrinkle test (including standing wrinkle test and hanging wrinkle test),
- and standing ring.

Plaut suggested formulas to calculate the bending stiffness from these gravitational tests [226]. Information on literature of these gravitational tests can also be found in the work of Plaut [226]. Generally, gravitational method is suitable for measuring bending stiffness of relative soft fabrics, namely, if their overhang length in the cantilever test according to DIN 53362 is still relative short. For very thick, i.e. very stiff, fabrics extreme long specimen is required for the gravitational method. Therefore, application of the deformation-controlled method makes more sense. Hübner used 2-point bending test, which is a combination of Schlenker method (DIN 53864) with ISO 2493-1 for his study of multilayer woven fabrics [165].

In-plane shear test

Orawattanasrikul [225] distinguished the difference between simple shear and pure shear as shown in Figure 2-28. Suppose that an arbitrary square unit cell of textile structure with

side length “a” is deformed with shear angle φ . Simple shear deformation results from relative motions of the fibers within the layers with fiber elongation, namely $A_S C_S = a / \cos \varphi$. Despite of small fiber elongation ΔL , due to great Young’s modulus of high performance fibers, tensile force will contribute mainly to the recorded force on the measurement device.

Pure shear is deformation without fiber elongation ($A_P C_P = AC = a$). “Trellis effect” is the twist at the binding points (of any kind of fabrics), which can also be consider a form of pure shear. The area of the deformed unit cell after simple shear is reserved, where $Area_S = a^2$, but the area of the unit cell after pure shear is reduced, namely $Area_P = a^2 \cos \varphi$. This reduction of area thus leads to compaction of yarn in the same layer. When the shear locking angle is reached, “all the yarns are in contact and compressed the force increases rapidly” [158], this compaction contributes to the formation of wrinkles (see illustration in Figure 2-6 by Thor [157]). In detail, pure shear deformation involves rotating, sliding and compacting of yarn with their neighbors.

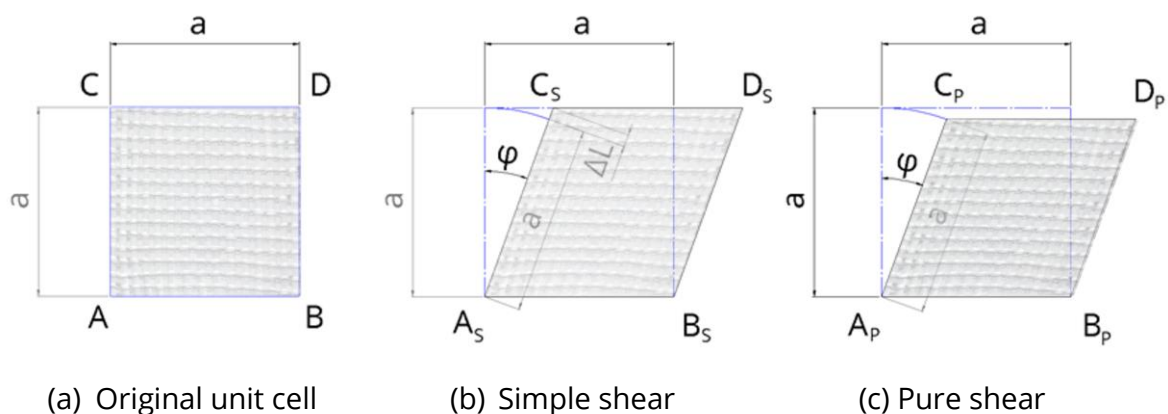


Figure 2-28: Schematic of shear principle adapted from Orwattanasrikul [225]

There is no general standard for measuring the shear behavior of fabrics. Many different testing methods and devices for shear resistance have been developed, which can be classified into the following working principles (Figure 2-29):

- **Rotation:** ITADRAPE2 [161], ITADRAPE3 [227], ITADRAPE4 [228]
- **Circular translation:** Dreby (as cited in [229]), Treloar (as cited in [161]), TEXPROOF (NAISS GmbH), picture-frame-test family (e.g., Culpin [230], ITADRAPE1 [161,227], Stumpf [231], Lomov [232], Orwattanasrikul [225] and Nezami [170])
- **Translation:** Mörner und Eegolofson (as cited in [233]), Kawabata KES-F [234],
- **Tension:** bias-tension [235], and biaxial-tension (by Kawabata [236], Chen [237])
- **Torsion:** El-Messiry [238]

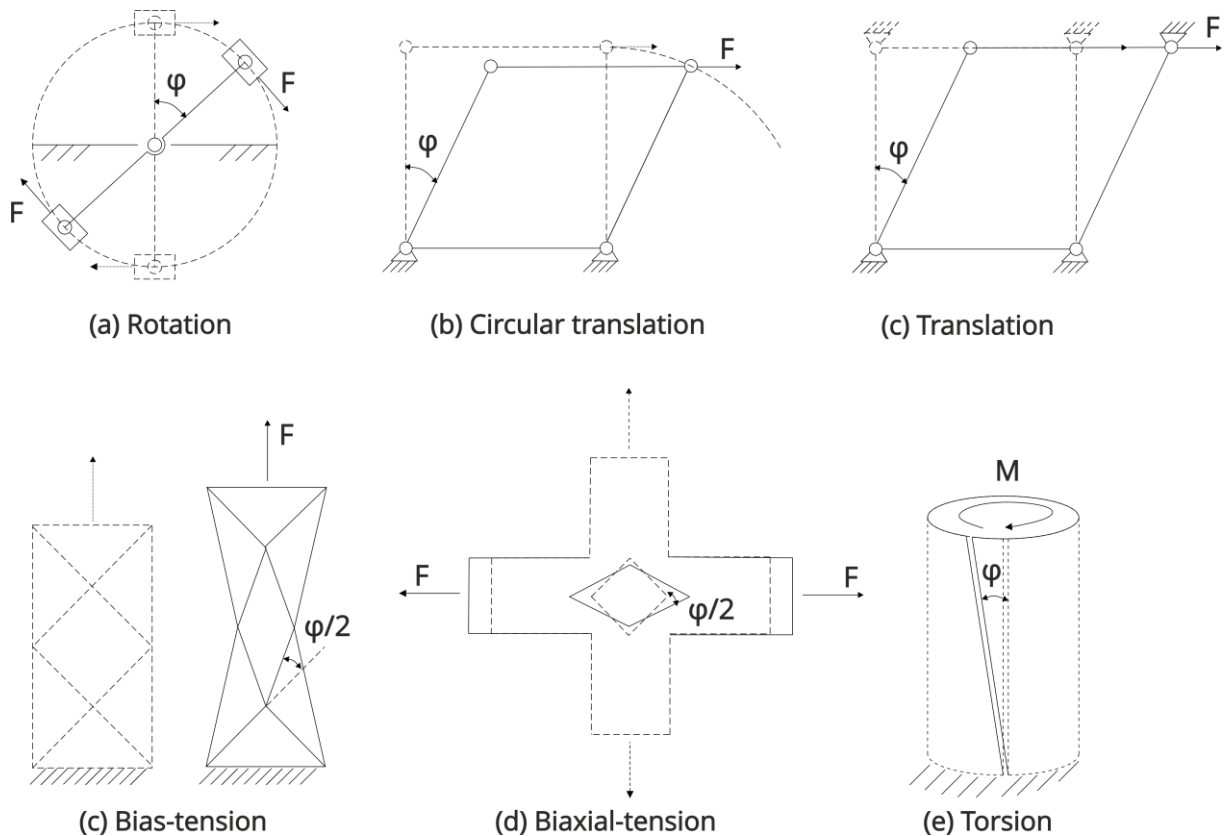


Figure 2-29: Simple illustration of test principles for shear behavior of fabrics (adapted from Orawattanasrikul [225] with supplement)

In general, shear angle and shear force can be measured independently or together as shear force – shear angle – curve. As every test method has its own goal, one or both of the shear force / shear angle are measured. Mörner/Eegolofson method measures reaction force at one bearing of the textile clamps (see illustration in [225]), while the textile is loaded under constant mono-axial pre-tension and external shear load. Treloar method is similar to Mörner/Eegolofson method but with low magnitude of load, and shear angle is also recorded. KES-F method [234] as well as the biaxial tension method [236] of Kawabata aim to measure shear stiffness, and shear hysteresis at small shear angle. Kawabata KES-F method works similar to Mörner/Eegolofson but the shear force is recorded instead of the reaction force of one bearing. The biaxial tensile shear method of Chen [237] also aims to measure shear stiffness, and shear hysteresis at small shear angle, but this method is specialized for coated fabrics (textile membranes). The difference of the biaxial tension shear test between Chen and Kawabata are as follows. Firstly, despite both tests use specimen of cross shape, the specimen of Kawabata has reinforcing yarn parallel to the edge of the specimen, while the specimen of Chen is cut in diagonal direction. Secondly, Kawabata clamps 3 of 4 ends of the specimen, and pulls one end cyclically in one direction, while Chen clamps all 4 ends and pulls each pair of ends

cyclically in both direction. By twisting a thin cylinder of fabrics, the torsion method of El-Messiry can measure shear stiffness and shear hysteresis at larger shear strain. Method by Dreby aims to detect the critical shear angle, namely when the wrinkle touches the contact bar. Similarly, TEXPROOF (generation 2004) measures the shear angle, when the wrinkles reach 3 mm high.

Stumpf did not aim to measure the critical shear angle, but the shear force – shear angle curves. Other researchers also pursued that goal with the rotation methods, picture-frame-test family and the bias-tension method. The critical shear angle can be estimated by using intersection point of two tangential lines of the shear force – shear angle curves, or at 5 % increase of the shear force in the shear force – shear angle – curve in comparison with the tangential line. For some type of fabrics (such as multiaxial NCF), the shear force – shear angle curves can be linear, thus, these two estimation methods are difficult to apply. In that case, use of optical sensor device such as laser [239] during the shear test can help to determine the critical shear angle objectively.

Bias-tension is an in-direct method to measure shear resistance of fabrics. The test specimen is cut in diagonal direction ($\pm 45^\circ$) and clamped into the tensile machine. Under tensile load, areas of the specimen are sheared with different shear angle (Figure 2-29c) and the shear angle as well as shear force must be calculated from displacement/ tensile force [164].

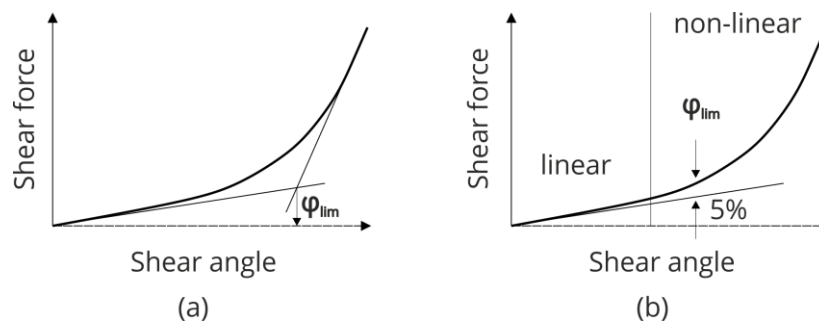


Figure 2-30: Estimation method for critical shear angle according to: (a) Souter [240] and (b) Cherif [227] - Zhu [241] (adapted from Rothe [239])

The shear resistance measurement of uni- and biaxial textile can be carried out by most the named methods. Measurement of multiaxial reinforced textile requires special device such as the ITADRAPE [227,228]. Picture-frame can be used for textile with multiaxial reinforcing fabrics with maximum three reinforcing yarn systems in 0° (or 90°) and $\pm 45^\circ$, where the 0° (or 90°) reinforcing yarn must be oriented horizontally during the test. Among numerous testing method for shear behavior of fabrics, the picture-frame-test is most suitable for the analysis for the biaxial BWKF as it meets the following requirements:

- pure shear of the textile
- measurement the at large shear deformation
- record of shear force – shear angle curves, which will be used as input data for FEM model

Friction test

The importance of friction has been explained in 2.5, as it decides the magnitude of the in-plane friction-induced tension of fabric during forming process. The friction between fabric and forming tool, as well as between layers of fabrics have been the concern of many research [242–253], which are including dry fabric, thermoset infiltrated fabric as well as heated thermoplastic fabric with molten matrix. Friction between any materials is a complicated phenomenon. When fiber material is involved, it becomes even more complicated. Many factors have an influence on the friction, where one or both partners are fiber: type of fiber, type of contact (sliding or rolling), velocity of contact, contact pressure between participating partners, deformation type of contact partners (elastic or plastic), moisture, and temperature. Roughness of tool surface influences the friction coefficient between fiber and tool [254]. Bowden and Young [255] generalized the law of friction as Equation (2-2), with F_R as the friction force and F_N as the normal load; k and n are curve fitting parameters for non-linear, normal load dependent friction. Depending on the nature of contact, n can have a value in the range from $2/3$ to 1 as shown in Table 2-5.

$$F_R = k \cdot F_N^n \quad (2-2)$$

Table 2-5: Value of n for each type of contact

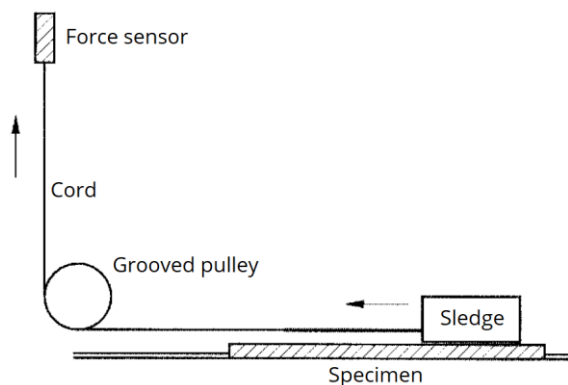
Type of contact	Plastic	Pure elastic	Elastic-plastic
n value	1	$\frac{2}{3}$	$\frac{2}{3}$ to 1

In case of plastic deformation $n=1$, the Equation (2-2) becomes Coulomb law of friction, which can be rewritten as Equation (2-3), with μ as the friction coefficient (CoF). Howell discovered that, CoF is higher at low contact pressure [256].

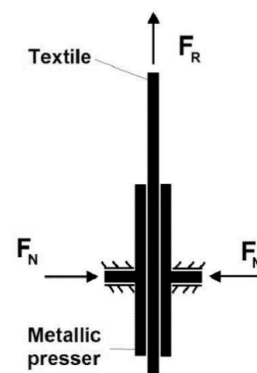
$$F_R = \mu \cdot F_N \quad (2-3)$$

There are different methods for testing of friction between fabric and metal surface. Depending on the requirement, a suitable method can be chosen and applied. For dry

fabric, under relative low pressure, at room temperature, the method of DIN EN 14882 (Rubber or plastic coated fabrics - Determination of the static and dynamic coefficient of friction) can be used (Figure 2-31a), where the normal load is realized by the weight of the sliding sledge. When greater normal pressure is necessary, the pull-out test principle of ten Thije [247,257] can be applied (Figure 2-31b). The free end of the specimen should be longer than the intended pull-out length so that the pressure of metallic presser on textile remains constant. The pull-out test has different implementation in which the normal load is realized differently: by spring load, by weight load or by external force from one side or both sides of fabrics [258]. Lin used a Bohlin CVOR200 rheometer to test fabric-tool friction of viscous textile composites [259]. When high temperature test condition is necessary, the whole set-up can be put into a temperature chamber; or test tool and textile can be heated up with thermal elements such as electric or infrared heaters. An overview of different test set-ups for the measurement of dynamic friction between thermoplastic fabric and metal surface and a benchmark study under defined test conditions (velocity, pressure, temperature) were given by Sachs [258], where the maximum of normal pressure is 0.16 MPa. Sachs concluded that for dry fabric, *“the friction behavior is fairly well described with the Amontons-Coulomb model, which states that the CoF is independent of the sliding velocity and normal force”*.



(a) DIN EN 14882



(b) Pull-out test principle



(c) Pull-out test with biaxial tensile machine

Figure 2-31: Some test principles of fabric/metal surface friction

2.7.4 FRP tests

Fiber volume content

Fiber volume content is an important indicator for the mechanical properties of FRP [514]. There are many factors that can influence the fiber volume content: lay-up/ thickness of textile preform, defects in the textile preform such as gap formation or fiber damage, FRP production process parameters, defect in the composite FRP such as void, etc. Therefore, the fiber volume content might vary locally within a composite part. There are many methods to measure the fiber volume content, such as acid digestion [515], optical microscopy-based techniques [515,516], resin burning-off method [517]. The fiber volume content is normally from 50% to 65%, max. 70%. FRP with less or greater fiber volume content than these limits shows decrease of the mechanical properties [515,517,518]. When the resin burning-off method according to method A of the standard DIN EN ISO 1172 or DIN EN ISO 3451-1 is used, the initial weight m_{FRP} and the rest weight of the specimen m_F after the burning-off are used to calculate the fiber weight content M_F in % as the following

$$M_F = \frac{m_F}{m_{FRP}} \quad (2-4)$$

$$m_M = m_{FRP} - m_F \quad (2-5)$$

The fiber volume content V_F can be calculated according to their definition, based on the volume of fiber v_F and the volume of FRP v_{FRP} as the following:

$$f = \frac{v_F}{v_{FRP}} \quad (2-6)$$

According to the definition of material density, we have

$$\rho = \frac{m}{v} \quad (2-7)$$

with ρ is material density, m is weight and v is volume. As the density of fiber ρ_F and matrix ρ_M (see Table 5-2 and Table 5-12) as well as their weight m_F and m_M in the specimen are known, their volume v_F and v_M can be calculated by Equation (2-7). Thus, also the volume of the FRP can be found, assume that no voids occur:

$$v_{FRP} = v_F + v_M \quad (2-8)$$

The fiber volume content f is finally calculated by the Equation (2-6) as all necessary parameters are found.

Mechanical tests of FRP

The mechanical performance of FRP can be tested at different levels: coupon and element level (small specimen/part) for material data of FRP, component and structural level (large part to full-scale structure) for structural characteristics. The tests can be static or dynamic, single cycle or cyclic (fatigue testing). There are more than 150 testing standards that dedicate to different aspects of the FRP, e.g., tensile (for UD FRP such as ISO 527-5, EN 2561, ASTM D 3039, DIN 65378, and for multidirectional FRP such as ISO 527-4, ASTM D 3039), open hole (ASTM D 5766) and filled hole tensile (ASTM D 6742), compression after impact (ISO 18352, ASTM D 7137, DIN 65561), interlaminar shear strength (ISO 14130, EN 2377, EN 2563, ASTM D 2344), lap shear (EN 2243-1, EN 2243-6, DIN 65148), in-plane shear (ISO 14129, ASTM D 3518), rail shear (V-notched ASTM D 7078), V-notch beam shear (Iosipescu ASTM D 5379), bearing strength (ASTM D 5961, DIN 65562), fracture mechanics (Double Cantilever Beam ISO 15024, ASTM D 5528 for Mode I crack opening; End Notch Flexure ASTM D 7905, ISO 15114 or ASTM D 6671 for Mode II in-plane shear; and Mode III out-of-plane shear), impact (Notched Izod ASTM D256, ISO 180), hardness (ISO 7619-1, ASTM D2240 and ISO 868), creep (ISO 899-1, ISO 899-2, and ASTM D2990), plain compression (end-loading method such as ISO 14126 method 2, ASTM D 695, DIN 65375; shear loading such as ISO 14126 method 1, ASTM D 3410 or combined method such as ISO 14126 method 2, ASTM D 6641), open hole and filled hole compression (ASTM D 6484, ASTM D 6742), flexural (ISO 14125, EN 2562, ASTM D 7264), fatigue (ASTM D3479). Depend upon the need, suitable tests are chosen and carried out.

3 Modelling of textile structures and FRP

3.1 Overview

Simulation is the effort to replicate a phenomenon (physical or social system) under controlled conditions for analysis and prediction purpose. Simulation can be done with or without a computer [260]. Without the computer, there are destructive simulation such as crash test, drop test, impact test, or non-destructive simulation such as wind tunnel and wave channel (Figure 3-1). Due to the advance of information technology, computers are becoming faster and cheaper [261]. That makes simulations with the help of computer more and more attractive. A computer simulation is based on the mathematical model of the phenomenon, which is processed on the computer. According to Veit [260], they can be divided into smaller groups such as technical simulation (Finite Element Method FEM, Computational Fluid Dynamics CFD, Fluid-Structure Interaction FSI), biological simulation (neural net, evolution) and sociological simulation (e.g. model of COVID-19 spreading in Germany [262]). Figure 3-1 shows the Wood versus Waves experiment by Deltares to demonstrate the protective function of trees under extreme wave. A Fluid-Structure Interaction (FSI) simulation would replace this experiment.

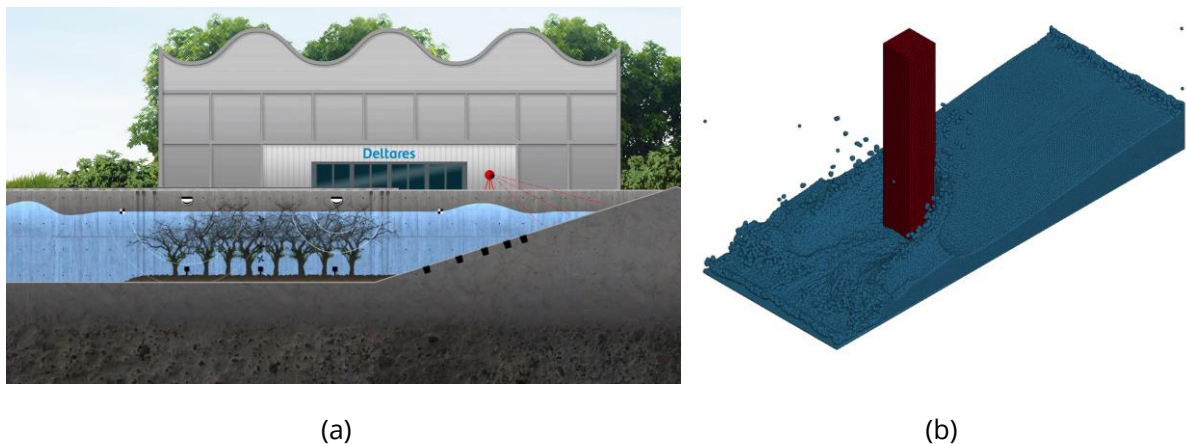


Figure 3-1: (a) Wood versus Waves experiment by Deltares and (b) Fluid-Structure Interaction simulation with LS-DYNA

First numerical approaches for the forming of textile structures are based on simple kinematic models (also called fish net or pin-jointed net methods) [104,181,263]. The kinematic method helps to predict the fiber orientation of the flat textile after it is transformed into the 3D preform regardless of the influence of external loads and sequence of stacking of multiple plies. Kinematic model has been implemented in many commercial software such as PAM-QUICKFORM (ESI), DesignConcept 3D (Lectra), FiberSIM

(Siemens AG), ExactFlat (Tri-D Technologies Inc.), and Composite Part Design (Dassault Systèmes). Figure 3-2 shows the analysis result of kinematic model with ExactFlat, where the black area is predicted to be with high risk of wrinkle.

In computer graphic science, animation of clothing is carried out mainly by particle collision detection method, which is fast and can run in real-time, but this method is not suitable for other applications due to its simplicity [264,265]. Comprehensive [266] and progressive [267] drape models are membrane stress based, where tension and compression deformation are taken into account. However, as the trellis-like shear and bending are neglected, the forming behavior of textile cannot be completely described. Additionally, the influence of forming tools cannot be taken into account. To overcome such disadvantages, Finite-Element-Method (FEM) models are necessary.

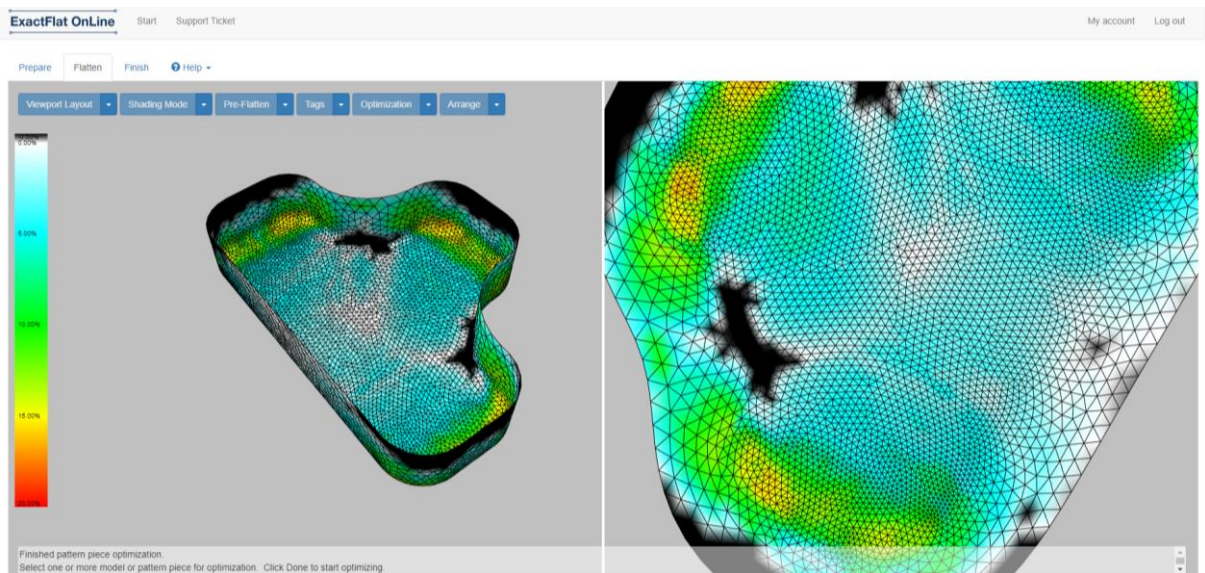


Figure 3-2: Kinematic analysis of a thin-walled T-cup component with ExactFlat

3.2 Basis of FEM

Kyosev explained the basics of FEM and relevant applications in textile technology [268]. In branches of physics such as mechanics, thermodynamics, acoustics, electromagnetics, most phenomena can be mathematically described by multi variable equations. Derivative in mathematics is defined as the rate of change of a certain function, e.g., speed is the derivative of distance with respect to time, and acceleration is derivative of speed with respect to time. Partial derivative is derivative with respect to a certain independent variable, e.g., one of the directions in a certain defined coordinate system in 2D or 3D. An accurate description of natural phenomena often involves such partial derivatives. The used multi variable equations in that case are called partial differential equations (PDE).

Solving such PDE is required, when some variables are already known or defined and the remaining variables should be found. An analytical approach is generally not possible; thus, FEM comes as a promising alternative. FEM divides the investigated body into small elements with a finite size. The elements contain nodes, where the analytical solution for the PDE is available. A mutual node of two or more neighbor elements (also called shared node) has the same value, when it is evaluated in one of these neighbor elements. The original PDEs are broken down into a set of equations, which describe the state of each node at a certain known/ defined conditions (also called boundary conditions) with or without respect of time. This set of equations are normally represented in matrix form (Figure 3-3). Considered the investigated body is ideal linear elastics according to Hooke's law, and undergoes static loading without velocity and acceleration, the matrix equation is as the follows:

$$\mathbf{K} \cdot \mathbf{U} = \mathbf{F} \quad (3-1)$$

where \mathbf{K} is the stiffness matrix, \mathbf{U} is displacement vector, and \mathbf{F} is the vector of external loads. The product of \mathbf{K} and \mathbf{U} is the internal elastic force. The Equation (3-1) describes the equilibrium state of the investigated body. In a more general case [268], the Equation (3-1) can be expanded to:

$$\mathbf{K} \cdot \mathbf{U} + \mathbf{C} \cdot \dot{\mathbf{U}} + \mathbf{M} \cdot \ddot{\mathbf{U}} = \mathbf{F} \quad (3-2)$$

where $\dot{\mathbf{U}}$ is the derivative of displacement with respect to time, thus velocity. Moreover, $\ddot{\mathbf{U}}$ is the derivative of velocity with respect to time, thus acceleration. \mathbf{C} is the viscosity matrix and the product of \mathbf{C} and $\dot{\mathbf{U}}$ describes the internal viscous force. \mathbf{M} is the mass of the investigated body and the product of \mathbf{M} and $\ddot{\mathbf{U}}$ describes the force of inertia. The Equation (3-2) can be further expanded if necessary, e.g. for thermal loading or vibration [269].

Solving this set of equations leads to an approximate solution for the PDE, which is acceptable in most engineering applications. Due to the advance of computational mechanics and information technology, nowadays FEM software can be responsible for all steps from dividing the investigated body into elements (meshing) to solving and presenting the calculated results. Some representatives of FEM software are PAM-CRASH (ESI), LS-DYNA and ANSYS (both belong to Ansys, Inc.), Simcenter Nastran (Siemens AG), Abaqus (Dassault Systèmes) and Z88 (Prof. Dr.-Ing. Frank Rieg of University of Bayreuth).

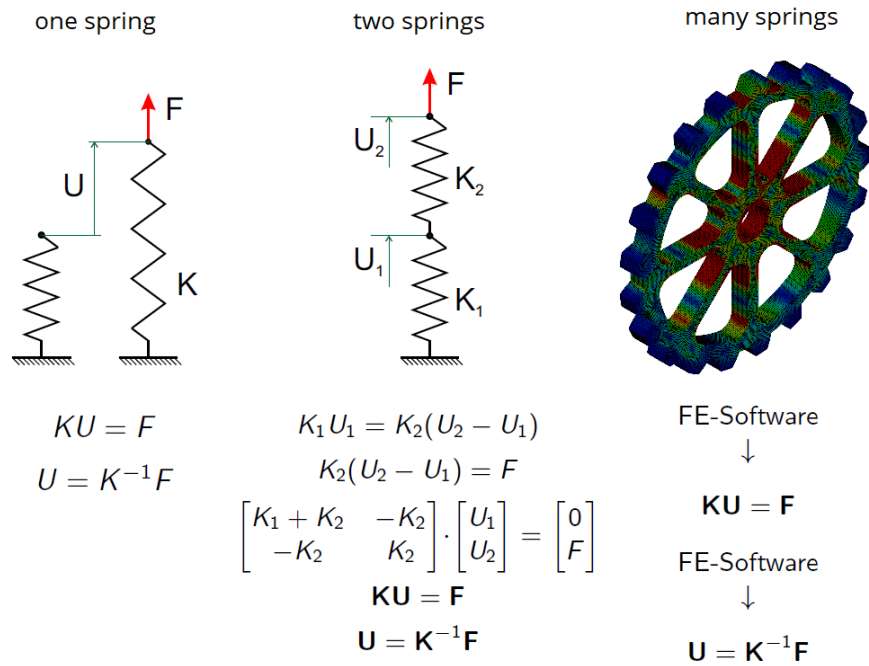


Figure 3-3: FEM explanation for simple static case (Equation (3-1)) by T. Gereke

Continuum elements

The investigated body must be broken into smaller parts. One start point of this step is the geometrical model generated by Computer-Aided-Design (CAD) software. The CAD model is meshed into elements and nodes, which define a calculation domain for the PDE. Depending on the definition method of the coordinate system, continuum element can be labelled as Lagrangian or Eulerian meshes [270]. Nodes in Lagrangian meshes are fixed to the investigated body and deformed with it, while nodes in Eulerian meshes are rather a reference frame. In general, there are three types of continuum element: 1D-, 2D- and 3D-continua. The displacement of any arbitrary point on the element is approximated by chosen function, which is called shape function, once the displacement of the nodes on the element are known [269]. The shape function can be linear (first-order), quadratic (second-order), cubic (third-order) or higher order. Linear 1-D continua have two nodes. Higher order 1-D continua have more nodes. Figure 3-4 shows a linear 1D-continua with two nodes ($i=1, 2$), where each node has maximum 6 degrees of freedom (DOF). Translation in x -, y - and z -directions and rotation around x -, y - and z -directions are denoted u and v , respectively. Depending on the DOF, 1D-continua can be divided into rod, truss and beam elements (Table 3-1). Rod is the simplest form of 1D-continua with only response to tensile stress along the length axis. In truss elements, stresses in the transverse direction are transferred as well. Beam element has the most DOF, where bending and torsion moments are described additionally. 1D-continua are used, where

the deformation is in one direction, which is significantly greater than the two others, e.g., yarn deformation under tension load. Every software has its own implementation of each type of elements. Derivatives of the basic elements with enhanced formulation for fast calculation as well as better stability are available.

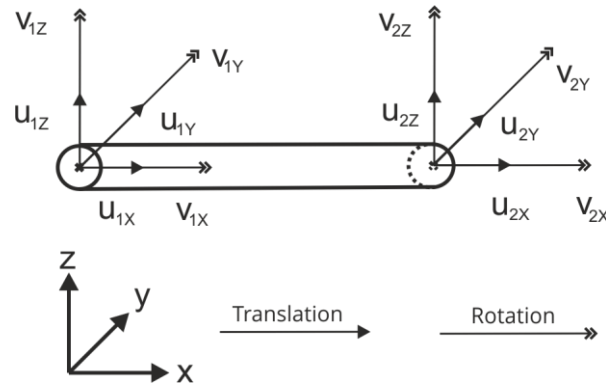


Figure 3-4: A two nodes 1D-continua with 6 DOF of each node

Table 3-1: Overview of basic 1D-continua with different DOF

1D-continua	u_x	u_y	u_z	v_x	v_y	v_z
Rod	✓	-	-	-	-	-
Truss	✓	✓	✓	-	-	-
Beam	✓	✓	✓	✓	✓	✓

Linear 2D-continua have three or four nodes. Higher order 2D-continua can have more nodes, e.g., 6 or 8 nodes for quadratic shape function, and more for cubic shape function [269]. Figure 3-5 shows a linear 2D-continua with four nodes ($i=1, 2, 3, 4$) and each node has maximum 6 DOF. There are three basic types of 2D-continua: membrane, bending plate and shell. Membrane is specialized to treat in-plane load (in x and y direction), while bending plate is for out-of-plane load. Shell element is a combination of membrane and bending plate. 2D-continua are used in case the deformation in two directions is significantly higher than the third direction (also called thickness direction), e.g., deformation of flat textile by preforming.

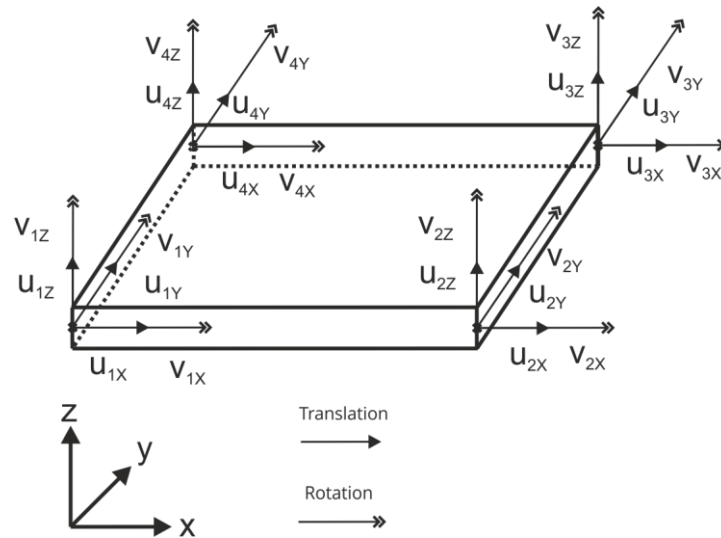


Figure 3-5: A four nodes 2D-continua with six DOF at each node

Table 3-2: Overview of basic 2D-continua with different DOF

2D-continua	u_x	u_y	u_z	v_x	v_y	v_z
Membrane	✓	✓	-	-	-	✓
Bending plate	-	-	✓	✓	✓	-
Shell	✓	✓	✓	✓	✓	✓

3D-continua are used, when deformation in all directions is significant, e.g., deformation of composite part with thick wall. There are three typical types of 3D-continua: tetrahedron (4 nodes with linear shape function), pentahedron (6 nodes with linear shape function) and hexahedron (8 nodes with linear shape function) as shown in Figure 3-6. Higher order 3D-continua have more nodes [269].

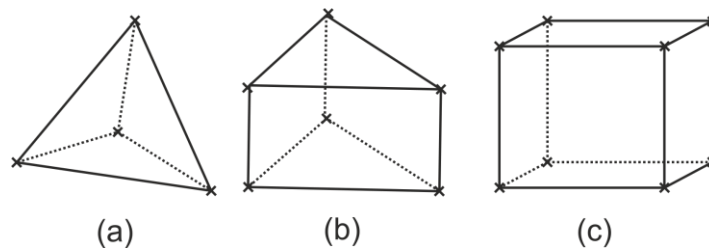


Figure 3-6: Typical 3D-continua: (a) tetrahedron, (b) pentahedron and (c) hexahedron

In a recent trend of research and development, Isogeometric Analysis (IGA) is an alternative method of bridging between CAD and FEM software, where the B-Spline, Non-

uniform rational B-Spline (NURBS) and T-Spline are used as basic mathematical description for line, surface and volume in the CAD models [271,272]. With such CAD database, the analysis can be carried out directly without meshing. IGA has been deployed in some commercial software such as LS-DYNA [273].

Implicit and explicit analysis

There are two methods to solve dynamic equations such as Equation (3-2): implicit and explicit method. In the implicit scheme (as known as Newmark method [274]), a constant mean acceleration \ddot{U} is assumed between two time steps. The displacement U and velocity \dot{U} of the next step can be written as follows:

$$\mathbf{U}_{t+\Delta t} = \mathbf{U}_t + \Delta t \dot{\mathbf{U}}_t + \left(\frac{1}{2} - \beta\right) \Delta t^2 \ddot{\mathbf{U}}_t + \beta \Delta t^2 \ddot{\mathbf{U}}_{t+\Delta t} \quad (3-3)$$

$$\dot{\mathbf{U}}_{t+\Delta t} = \dot{\mathbf{U}}_t + \Delta t(1 - \gamma) \ddot{\mathbf{U}}_t + \gamma \Delta t \ddot{\mathbf{U}}_{t+\Delta t} \quad (3-4)$$

where t is the current time point and Δt is the time step size. While γ and β are two constant parameters, which can be chosen freely. For the stability as well as accuracy of the computation, commonly chosen for these parameters are $\gamma = \frac{1}{2}$ and $\beta = \frac{1}{4}$. The Equation (3-2) now becomes

$$\mathbf{K} \cdot \mathbf{U}_{t+\Delta t} + \mathbf{C} \cdot \dot{\mathbf{U}}_{t+\Delta t} + \mathbf{M} \cdot \ddot{\mathbf{U}}_{t+\Delta t} = \mathbf{F}_{t+\Delta t} \quad (3-5)$$

The Equation (3-5) always has a solution for linear problems, in other words, unconditionally converges, and gives answer to the equilibrium state of the investigated body at the next time step $t+\Delta t$. However, for highly nonlinear problems, there could be no convergence and no solution can be found. Time step size can be chosen theoretically arbitrary. However, in practice, the time step must be adjusted to the expected level of stability and accuracy. Direct solvers, which are based on Gauss methods, or iterative solver can be used [269]. Direct solvers require the decomposition of the matrix before solving; thus, it is memory intensive. Iterative solvers require normally less memory. The computing time depends on the number of nodes/ elements in model. The implicit method is suitable for static and quasi-static problems, where few non-linear phenomena are involved. There are several causes of nonlinearities: large deformation, nonlinear geometry, nonlinear material behavior, nonlinear boundary condition and complex contact formulation [275]. In modelling of textiles and forming simulations, most of these criteria are met.

The solution for problems with high nonlinearities is the explicit scheme. In most cases, the central difference method is used [270], which involves finding solution at the current time step t . The Equation (3-2) is written as

$$\mathbf{K} \cdot \mathbf{U}_t + \mathbf{C} \cdot \dot{\mathbf{U}}_t + \mathbf{M} \cdot \ddot{\mathbf{U}}_t = \mathbf{F}_t \quad (3-6)$$

The velocity $\dot{\mathbf{U}}$ and acceleration $\ddot{\mathbf{U}}$ of the current step are formulated by displacement \mathbf{U} of previous, current and next time step:

$$\dot{\mathbf{U}}_t = \frac{1}{2\Delta t} (\mathbf{U}_t - \mathbf{U}_{t-\Delta t}) \quad (3-7)$$

$$\ddot{\mathbf{U}}_t = \frac{1}{\Delta t^2} (\mathbf{U}_{t-\Delta t} - 2\mathbf{U}_t + \mathbf{U}_{t+\Delta t}) \quad (3-8)$$

Hence, the Equation (3-6) can be written as

$$\left(\frac{1}{\Delta t^2} \mathbf{M} + \frac{1}{2\Delta t} \mathbf{C} \right) \mathbf{U}_{t+\Delta t} = \mathbf{F}_t - \left(\mathbf{K} - \frac{2}{\Delta t^2} \mathbf{M} \right) \mathbf{U}_t - \left(\frac{1}{\Delta t^2} \mathbf{M} - \frac{1}{2\Delta t} \mathbf{C} \right) \mathbf{U}_{t-\Delta t} \quad (3-9)$$

Solving the Equation (3-9) gives answer to the equilibrium state of the time step $t+\Delta t$. The explicit method converges conditionally, namely the time step should be smaller than the time that is required for a stress wave to propagate through an element (as known as the critical time step or stable time step). In practice, the time step of the whole model is defined by the smallest element. The critical time step is given by the Courant condition [270] as follows

$$\Delta t_{crit} = \min \frac{l}{c} = \min \left(l \sqrt{\frac{\rho}{E}} \right) \quad (3-10)$$

$$c = \sqrt{\frac{E}{\rho}} \quad (3-11)$$

with Δt_{crit} is the critical time step, l is the characteristic length of the element, c is the speed of sound, E is the elastic modulus and ρ is mass density. As the time step size is limited, the computation with the explicit scheme is slow and CPU intensive. By computational operation, only inverting of the element matrix is required, thus less memory intensive in comparison to implicit analysis. To save computational resource by explicit analysis, some methods have been adopted in practice:

- Mass scaling: artificially increase mass density ρ , which increases critical time step
- Elasticity modulus scaling: artificially decrease of elasticity modulus E , which also increases critical time step
- Use elements with coarse mesh: increase of l , thus increase the critical time step
- Speed scaling: artificially increase of velocity/ acceleration, which reduce the overall investigated time, thus less steps are needed to be calculated

Care should be taken, when any of the named method above is applied. Abuse of these “necessary evils” would eventually lead to unacceptable results.

Contact formulation

Practical prototype testing and manufacturing applications involve interaction of multiple working components; thus, modelling of such systems requires a reasonable description of the contact between participating parties. An example is the interaction between blank holder and stamp with textile during forming process. The first step of contact formulation is the definition of possible contact position at the element and node level. While some basic FEM software requires an exact definition of contact nodes, advanced FEM software can search the whole model and detect the possible contact position by contact search algorithms, e.g., bucket-sort. Fundamentally, contact can happen in normal or in tangential direction of the contact position. For the normal contact, a function of penetration is necessary. While in tangential contact, the relative velocity and displacement of the node at the contact position is required. On top of that, constitutive equation of the contact surface, variational equations and its discretization, as well as special algorithms are deciding components of a success contact formulation [275]. When two surfaces participate the contact, one can be denoted as slave surface and the other as master surface. By the mathematical formulation of the function of penetration, the distance of every node on the slave surface to the master surface is calculated. If the slave and master surfaces can exchange their role to each other without changing the result, it is called symmetric contact, otherwise it is an asymmetric contact. Relative velocity and displacement of nodes are also measured in the same manner. These data are next passed to the constitutive equation of the contact surface to calculate the contact force. The constitutive equations for normal contact calculate the contact force from penetration depth in a manner similar to Hooke’s law. In simple words, a spring is placed between the contact nodes, which has the tendency of pushing these two contact nodes far away from each other. How the stiffness of this spring (as known as contact stiffness) is calculated varies from algorithm to algorithm. In case of tangential contact, sliding force is calculated on the basis of Coulomb friction law, where the transition between static to dynamic friction (also called stick-slip phenomenon) is treated with different frictional

constitutive equations [275]. In practical software environment, for example LS-DYNA, further constraints can be set on contact such as sliding only (penetration excluded), tied (fixed node to another surface/node), tiebreak (fixed but decoupling at certain condition allowed), and one-way (only penetration from specific slave node are checked with master surface, penetration of node on master surface on slave surface are ignored) [276].

3.3 FEM models for textile structures

Many FEM models have been developed to simulate the mechanical behavior of textile fabrics. These models are potentially suitable for various purposes. They can be used to predict the influence of textile production parameters on textile structure, mechanical performance of the composite component, properties of textile under ballistic impact, and to virtually optimize the forming process of 3D preforms.

The draping ability of textile fabrics made of continuous yarns varies over a wide spectrum, from structure to structure and from material to material. This also applies to their FEM models. Some literature sources give a comprehensive review on the state of the art of FEM models [158,277,278]. Table 3-3 give an overview of representative numerical models of selected textile structure in various scales, where some geometrical models (GM) are also included. Principally, any geometrical model with clear mathematical description for the yarn path in structure can be used to generate meso/micro FEM model.

In general, FEM models can be divided into three groups based on their length scale: macro-, meso- and micro-scale models as shown in Figure 3-7 (for short: macro, meso and micro models). The macro models describe textiles on the fabric level. They are based on continuum mechanics, with the assumption that any textile structure regardless of their construction can be considered as continuous mass without any kind of separation. Macro models require the least computational cost as in most case only shell elements are used. Therefore, they have been widely used for simulation of the forming process of 3D preforms for bulky components.

In principle, the important mechanical properties of the fabrics that have a significant influence on the draping ability, including tensile, bending and shear behavior should be taken into account. Lacking of bending would prevent the model to predict wrinkle formation accurately. Compression behavior of textile and fiber dispersion are rarely considered. Under complicated forming conditions, such as high temperature or velocity, additional features such as rate dependent and temperature dependent properties can be required.

The challenge of using macro model is the requirement of special mechanical material law to describe the behavior of the textile structure. The first requirement is the non-linearity of tensile and shear behavior. Additionally, description of the bending stiffness is also difficult. The bending stiffness B of fibrous material cannot be calculated from the tensile elastic modulus E and the area moment of inertia I with the classical formula:

$$B = E \cdot I \quad (3-12)$$

Actual bending stiffness of textile material is significantly lower than the value computed with the Equation (3-12). Textile reinforcement may undergo great deformation while transforming from 2D to 3D shape. The material model must be able to describe the state of textile structure under large strain, large in-plane shear angles and large bending deformation [279]. Standard continuum mechanics of Cauchy cannot describe the possibility of slippage between fibers and the bending stiffness [280]. Hence, other approaches are necessary. Textile is considered as continuous medium. The mechanical properties of the real material are homogenized with the help of experiment as well as numerical test simulation. There have been many solutions suggested by research around the world. Some selected approaches are presented below.

Each proposed implementation is unique and tends to meet a certain set of requirements, e.g., anisotropic material with temperature dependent by Hsiao and Kikuchi [281], modelling in-plane shear with temperature and shear rate dependent by Harrison et al. [282], shear model computed with equilibrium equation combining friction and compaction laws by Liu et al. [245], shell finite element with transverse stress by Soulat et al. [283], model for correct computation of bending behavior by Liang et al. [284], decoupling bending and in-plane stiffness for their correct description by Döbrich et al. [285], hybrid model of membrane and shell element by Nishi [286], elastic theory combined with uniaxial continuum theory for bending behavior by Wang et al. [287], bending behavior with time-temperature dependent by Alshahrani and Hojjati [288], combination of linear elastic fiber and shear thinning power law for matrix material by Sachs and Akkermann [289], use of virtual coating element [290], strain smoothing technique [291], Dahl's friction model for inelastic bending behavior [292]. Further information on models for shear behavior of dry textile can be found in the review paper of Syerko [293].

The material laws developed for textile composite forming can be classified into three groups: hypoelastic, hyperelastic and second gradient material models [278]. Hypoelastic material model uses constitutive equation, which is independent of finite strain measures

(except linearized case) [294]. Hyperelastic material model uses constitutive equation, which describes material as ideal elastic, and the stress-strain relationship is dependent on strain energy density function. Detailed comparison and explanation of hypoelastic and hyperelastic materials can be found in [295,296]. Second gradient material model has further modifications of the constitutive equation. For example, by adding the kinematical descriptors for displacement field, the model can describe the in-plane shear transition zone between areas under different shear deformation modes [297]. Different bending stiffness in the warp and weft direction, yarn slippage can also be taken in account, when the strain energy is defined as a function of strain and rate of strain [298].

Computation of complex macro model requires additional numerical technique and element technology to achieve correct and stable results. One of the critical points is the locking of finite element. It can be intra-ply shear locking [299], or tension locking [300–302], when 2D elements are used. Hourglassing is another concern, and should also be dealt with [303,304]. The same issue can also happen to 3D elements [165,290].

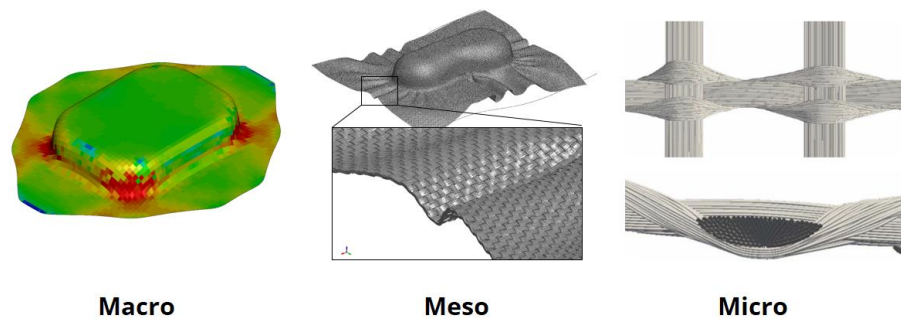


Figure 3-7: Multi-scale modelling of textile structures

As the geometry of the composite components becomes increasingly complicated, a higher grade of representation is required. Meso and micro models describe the textile structure as their actual configuration with discrete yarn/fiber components, which can move independently from each other. The meso models describe textile on the yarn level. They have sufficient representation degree at a reasonable computational cost. Meso models use a single chain of beam elements [305], a stripe [306] or a tube [307] of shell elements or solid elements [307–311] to represent one yarn. As computational costs drop over time, models with higher grade of representation are more and more favorable. With meso models, further defects such as fiber misalignment, fiber damage, yarn slippage and gap formation can be predicted. As the yarn orientation can be predicted, its influence [312] on the mechanical properties of 3D components can also be analyzed without producing and testing the actual prototype [313]. Many textile structures can be modelled on the meso-scale as volume models with available software such as TexGen [314], WiseTex [315] and TexMind [316]. Nevertheless, due to high computing costs, meso-scale

models with solid elements are presently not feasible for large scale simulation such as forming process. Thus, to keep computing costs at a reasonable level, only beam and shell elements should be used and a corresponding modelling strategy for textile structures with beam and shell elements is necessary. Naturally, correct description of mechanical properties such as tensile, bending, and shear behavior are still important requirement for meso model [165].

Micro models describe textiles on the fiber level. They are the most realistic and complex, where every single yarn is described as a bundle of multiple filaments (normally by beam elements, or combination of truss and beam elements as in [317]), and the relative movement between these filaments is possible. Thus, they are involving extremely high computational costs. Micro models are especially suitable for the investigation of textile structural physical behavior, when the properties of the fiber are known. Simulation with micro model is normally limited within the size of one or several unit-cells. Döbrich [166] investigated the tensile, shear and bending behavior of woven fabric with simulation within unicell. The quantity of beam for modelling a yarn, show great influence on the simulation results [318,319]. Thompson [320,321] used high fidelity micro-scale model of 2D woven to predict the compression behavior and possible defects.

Semi-discrete approach is a compromise solution between macro and meso models, where stress tensor is not used. The mechanical behavior of textile such as tension, in-plane shear and bending are directly defined in the unit cell based on the experimental data. Such models show good performance for forming simulation of 2D [169,322] and 3D [323] woven fabrics.

The in-plane tensile stress, which is induced by friction between textile and blank holder during the forming process, has a significant influence on the preform quality. Therefore, sufficient contact formulation is necessary within the FEM model. Friction coefficient for this contact formulation should also be validated. Some literature source have tackled this problem along with the textile model [324–327]. In the meso and micro models, the friction between yarns in textile, as well as between filaments in yarn should also be taken into account.

Table 3-3: Overview of representative FEM models of selected textile structures

Textile	Macro-scale	Meso-scale	Micro-scale
Woven	Hübner [328], Boisse [132], Garnich [329], Wang [287], Wriggers [302], Auricchio [330], Peng [331], Xue [332], Cao [333], Lee [334], Zhang [335], Chen [336], Erol [337], ten Thije [338], Khan [168]	Erol [339], Tran [340], Naouar [308], Wilfayeau [341], Pinkos [342], Nilakantan [343], Grujicic [344], Zeng [345], Vidal-Sallé [346], Lomov [347], Wang [348], Lin [349], Tabiei [350,351]	Döbrich [166], Yang [352], Russcher [353], Durville [354]
Braided	none	Hans [355], Pickett [356], Gereke [357], Wang [358], Shanahan [359], Barry [360], Kyosev [361] (GM)	Vu [362], Ghaedsharaf [363], Zhou [364]
Warp-knitted	Dörr [365], Schirmaier [188], Bardl [366], Yu [367], Chen [336], Mallach [368]	Cherif [227], Orlik [369], Kyosev [370,371], Robitaille [372] (GM)	Colin [373]
Weft-knitted	Döbrich [285,374] (BWKF)	de Araújo [305,310], Ru [375], Kyosev [371] (BWKF), Maron [376] (BWKF)	Duhovic [196,377]

Limitation of available models for BWKF

In recent state of development, the FRP is widely spread across many industries; there are more and more needs to produce FRP parts with complex geometries. Producing textile 3D preforms for complex FRP parts shows great challenge. With the help of FEM model, the optimization of process parameters and forming tools can be accelerated. For high quality FRP part, defects on preform should be minimized as much as possible. That leads to the needs to use FEM model with higher grade of description. Macro models can only predict some defects of 3D preform such as wrinkle formation or textile damaged. There is lack of the ability to describe further defects such as fiber misalignment, wavy fibers,

buckling of fibers, damaged fibers and gap formation. While many meso scale FEM models are developed for woven, braided and warp-knitted fabrics, only a few are available for weft-knitted fabrics (Table 3-3).

And the available models are limited in some aspects. The models of de Araújo [305,310] and Ru [375] are only developed for plain weft-knitted fabric, which is without warp and weft reinforcement. The topological model of Kyosev [371] can describe BWKF with warp and weft reinforcement at relaxation state and under shear loading pretty well (Figure 3-8). However, this model assume that warp and weft reinforcement remain straight and the interaction between them with the tensioned stitching yarn is not considered. The mathematical description of yarn path can be used to create FEM model, but the crimp of reinforcing yarn systems will not be taken into account. Thus, the non-linearity of tensile behavior of BWKF cannot be described.

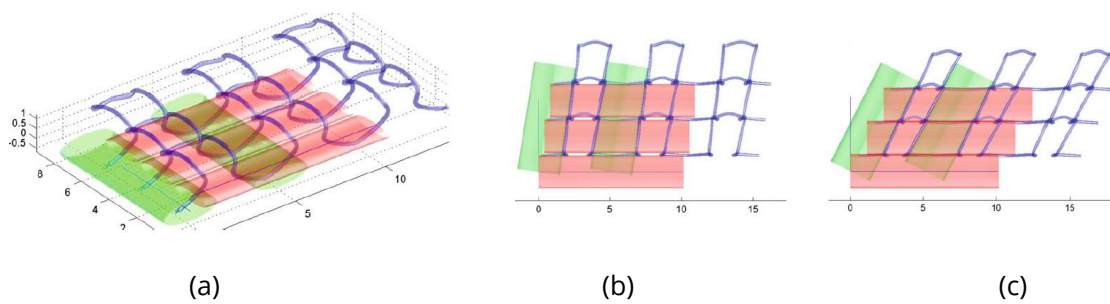


Figure 3-8: Topological model of BWKF by Kyosev [371], implemented in Matlab: (a) Relaxation state, (b) Shear state and (c) Jammed state (© Kyosev)

The meso FEM model of Maron [376] uses shell element to describe reinforcing yarn, and simple spring element for stitching yarn (Figure 3-9). As the interaction between reinforcing and stitching yarn systems is taken into account, the non-linear tensile behavior of BWKF can be described better. However, as the stitching yarn is over simplified with spring elements, which are simple connected with each other at one node at the middle, no relative movement between them is possible. That would to limitation of the model, when description of fiber misalignment and gap formation are necessary. Namely, sliding of stitching yarn must be modelled.

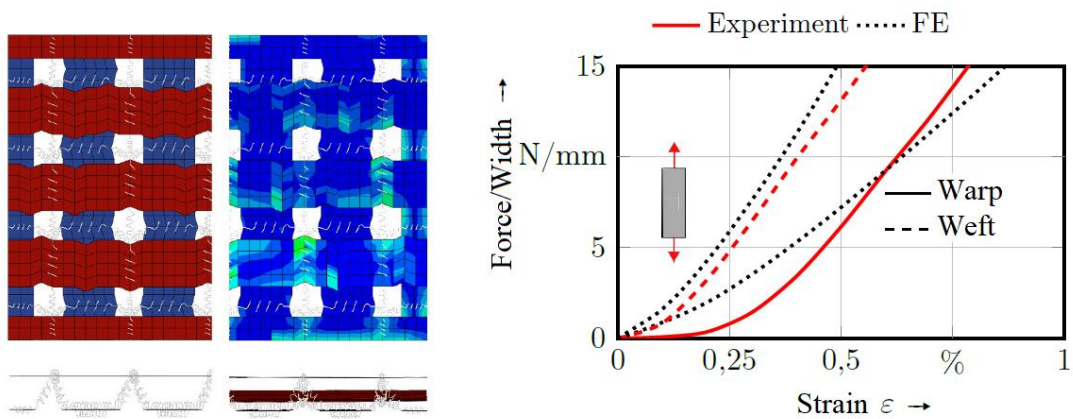


Figure 3-9: Meso FEM model of BWKF by Macron [376] and its description of non-linear tensile behavior of BWKF

3.4 Modelling of FRP

Fundamentals of FRP mechanics

The mechanical characteristic of FRP is anisotropic and distinguished from isotropic material such as metal. The fiber reinforcement plays a decisive role of the mechanical performance of FRP. Due its significant high stiffness and strength in comparison to the matrix material, fiber is the load-carrying component, but it can only transfer load along its main axis direction. Thus, the fiber orientation has a significant influence on the performance of the FRP part under a certain load scenario. Failure of FRP is complex, which can be initiated by fiber break, matrix break, debonding between fiber/matrix, or combination of these, depend on what kind of load is dominant, and that eventually leads to different failure modes [378] (Figure 3-10). The elastic modulus of FRP depends on fiber volume content. The break elongation is strongly varied according to the load direction. When the load is along the fiber, most of the load can be transferred to the fiber, and the composite is broken, when the fiber is broken. When the load is transverse to the fiber, the break elongation of the composite is reduced significantly, thus the strength of composite is also reduced (Figure 3-11).

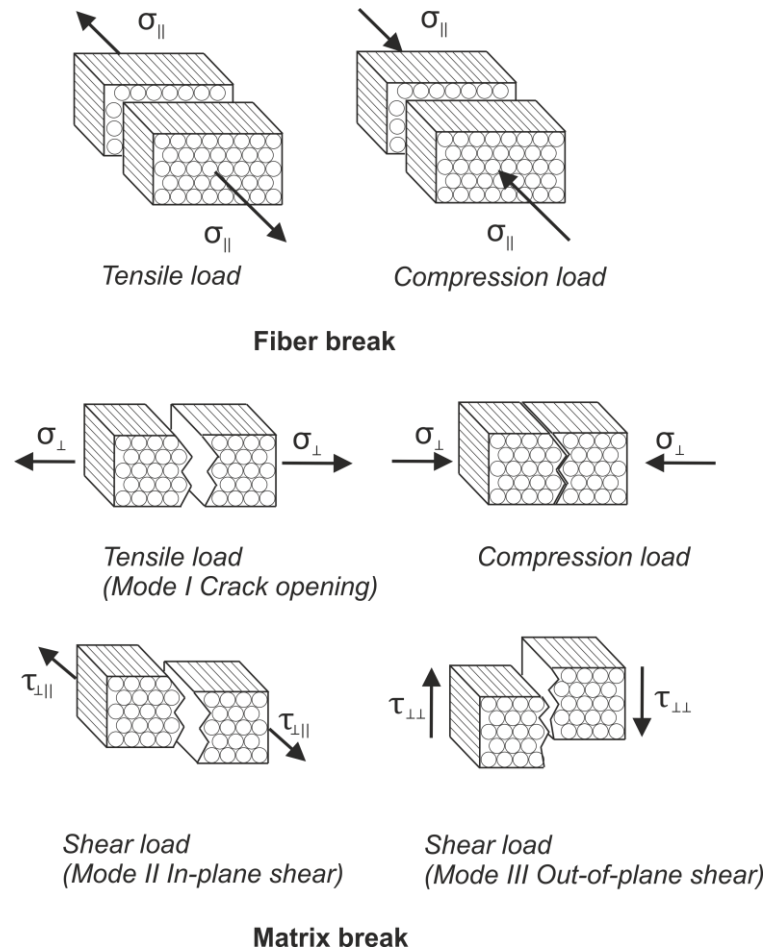


Figure 3-10: Typical failure modes of FRP adapted from AVK [378] with modification

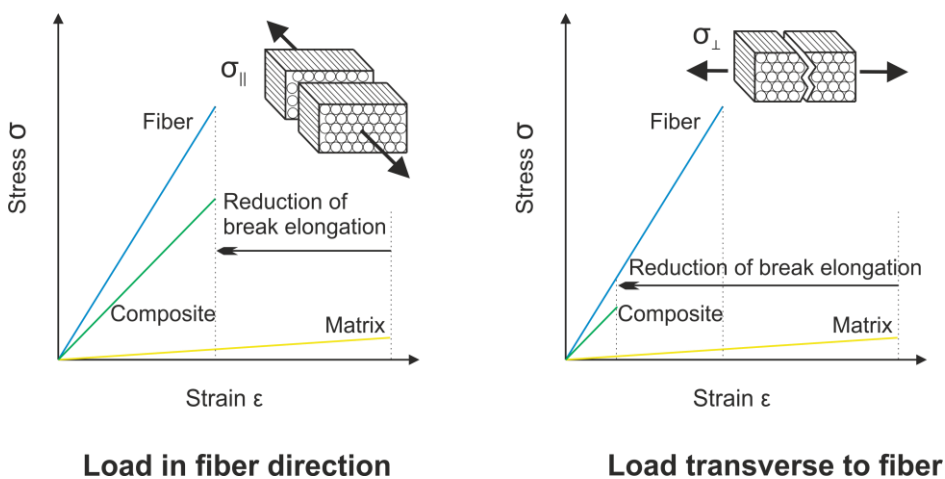


Figure 3-11: Qualitative stress-strain diagram of a single layer UD composite according to AVK [378]

The stiffness of the FRP depends on the fiber volume content f , which is calculated by Equation (2-6) as presented in section 2.7.4. The engineering constants of single layer UD

composite can be calculated in some load cases with simple rule of mixtures and fundamental understanding of FRP mechanics [165,379,380]:

$$E_{||} = fE_{F||} + (1 - f)E_M \quad (3-13)$$

$$E_{\perp} = \frac{E_{F\perp}E_M}{(1 - f)E_{F\perp} + fE_M} \quad (3-14)$$

$$G_{\perp||} = \frac{G_F G_M}{(1 - f)G_{F\perp} + fG_M} \quad (3-15)$$

$$\nu_{\perp||} = f\nu_{F\perp||} + (1 - f)\nu_M \quad (3-16)$$

$$\nu_{||\perp} = \nu_{\perp||} \frac{E_{\perp}}{E_{||}} \quad (3-17)$$

E, G and ν are the Young's modulus, shear modulus and Poisson's ratio of composite, respectively. The symbol $||$ and \perp denote direction of fiber and transverse to fiber. The equations from (3-13) to (3-17) give good agreement with experimental measurement of elastic modulus in the fiber direction and Poisson's ratio. However, there are differences of elastic modulus in transverse direction and shear modulus.

In practice, composite parts are built up from multiple layers of reinforcement. These thin layers are termed lamina and built up the composite laminate. The laminate structure can contain layers of reinforcement with fiber orientation in one direction (unidirectional laminate) or in different directions (multidirectional laminate). The lay-ups of fiber reinforcement are usually symmetric to reduce thermal stresses during curing. Multidirectional laminate can help the composite to withstand different loading scenarios. To describe the mechanical properties of such composite laminate, some semi-empirical equations have been suggested to give a better approximation, e.g. Puck [381] equations as the following

$$E_M^* = \frac{E_M}{1 - \nu_M^2} \quad (3-18)$$

$$E_{\perp}^P = \frac{E_M^*(1 + 0.85f^2)}{f \frac{E_M^*}{E_{F\perp}} + (1 - f)^{1.25}} \quad (3-19)$$

$$G_{\perp}^P = \frac{G_M(1 + 0.6\sqrt{f})}{f \frac{G_M}{G_F} + (1 - f)^{1.25}} \quad (3-20)$$

The superscript P denoted value calculated by Puck theory. E_M^* is the intermediate variable calculated from Young's modulus of matrix and Poisson's ratio of matrix.

Composite Laminate Theories

The first two-dimensional classical theory of plates was proposed by Kirchhoff [382] and later developed further by Love [383] and Timoshenko [384]. Based on the classical Kirchhoff-Love theory of plates, the classical laminate theory (CLT) has been developed to predict the properties of thin composite laminate in reference to fiber orientation of each layer [378,385,386]. CLT has the following assumptions:

- the normal to the center plane before deformation remains straight and normal to the plane after deformation, or in other words, there is no shear deformation in the thickness direction, i.e., no relative translation between layers
- small in-plane strain
- ideal bonding between layers
- linear elastic material behavior

The material constants of fiber for calculation of strength are defined in the fiber coordinate system. When analysing with CLT, stress and strength of every layer are calculated separately, which requires a transformation from fiber coordinates to laminate coordinates. The thickness and lay-ups of the reinforcing layer are also taken into account. The complete procedure of CLT has been explained in various literatures, e.g. [165]. CLT has been implemented in common software such as eLAMX². However, due to the assumptions listed above, CLT is not suitable for analysis of thick composite laminates under complex loading cases such as bending, torsion, and uniaxial tension. Hence, further composite laminate theories are developed. First-order shear deformation theories (FSDT) of Mindlin [387] and Reissner [388] consider shear deformation and rotary inertia effects. FSDT is also known as Mindlin-Reissner plate theory. The results obtained by FSDT are only accurate for very thin plates, as it is assumed that shear stress is constant along the thickness direction, which is not true, because shear stress should be zero at free surfaces. Hence, a correction factor for shear stress is necessary. Bhaskar and Varadan [389] as well as Roufaeil [390] introduced new computation techniques to tackle with the shear stress correction without increasing the order and complexity of the formulation.

One step ahead is the Higher Order Shear Deformation Theory (HSDT), with the assumption of nonlinear stress variation through the thickness [391]. Within the HSDT group, many researchers have contributed to improvement such as analysis of interlaminar normal stress by Whitney [392] and Pagano [393], boundary layer theory by Tang [394], perturbation solution for interlaminar stresses by Hsu and Herakovich [395], approximate elasticity solutions for interlaminar stresses by Pipes [396], and analysis of stress singularities by Wang and Choi [397]. Despite this improvement, HSDT can only be

applied for relatively thin composite laminate. For thicker composite laminates, further enhancements have been made continuously, such as higher-order transverse shear stress function by Ambartsumyan [398], parabolic distribution of the transverse shear strains by Reddy [399], analysis of buckling by Matsunaga [400]. Detailed list of contribution to HSDT theory can be found in [401].

Trigonometric shear deformation plate theory (TSDPT) such as Touratier [402] and Stein [403] used trigonometric series to describe the shear stress function. When a hyperbolic function is involved, it is called hyperbolic shear deformation theory, such as Soldatos [404] and Ramalingeswara Rao [405].

The above theories consider the composite laminate as one medium, or better known as equivalent single layer (ESL). Layerwise Theory (LT) considers the composite laminate as a set of multiple layers (thin lamina), where the mechanical response in the thickness direction can be predicted efficiently. A review of historical development of LT is given by Carrera, where theories in this group are called zig-zag theories [406]. Some representatives of this group are Pagano [407], Reddy [408], Plagianakos [409], Noor [410], Barbero [411], Heyliger [412], Averill and Yip [413]. These theories are based on kinematic assumptions for the displacement in the thickness direction. Better description for thick composites and sandwich structures are possible thanks to these theories. However, as the 3D equilibrium equations with multiple variables have to be solved, the computational costs are increased significantly.

Failure theories

Due to the composite laminate theories, different stress states in the composite laminate under certain working conditions can be predicted. The combination of these stress states would eventually lead to failure of the composite laminate. Composite laminates have more complicated failure modes compared to a single UD lamina. Failure can be initiated by fiber and matrix breaks, or debonding of fiber-matrix interface, thus leads to inter-fiber failure mode such as delamination, which occur at the boundary between the reinforcing layers. As the quantity of reinforcing layer increases and the composite laminate becomes thicker, stress and strain in the thickness direction must also be taken into account. Composite laminate can also fail due to fatigue, where the structure is slowly damaged as micro-cracking occurs and spreads progressively. Many failure criteria for composite laminate have been developed. They include lamina based and non-lamina based theories. According to Hinton et al. [414] and Daniel [415], the lamina-based failure theories could be divided into the following groups:

- *Limit or non-interactive failure theories* including maximum stress of Zinoviev [416], maximum strain of Bogetti [417]. When any stress or strain of the lamina in a certain direction crosses the allowable limit, the first failure is initiated. Hart-Smith introduced a 2D version of maximum strain and truncated maximum strain failure theory [418].
- *Interactive failure theories* are derivatives from Hill's theories for yielding of metals with update for anisotropy and load dependent (i.e., tensile or compressive) strength. Representative theories of this group are the Tsai-Hill [419] and the Tsai-Wu [420] criteria.
- *Partially interactive or failure mode based theories*, where failure modes are specified, and each failure mode is described by a unique equation within the theory. The interaction between the failure mechanisms may also be taken into account. This type of theory can provide prediction about strength, strain to failure and mode of failure. Representative theories of this group are Puck [381], Hashin-Rotem [421,422] and Cuntze [423]. Sun [424] proposed an empirical modified version of Hashin-Rotem's theory.
- *Damage mechanics* is the analytical approach for the description of initiation and evolution of damage, where failure is considered as a process instead of a catastrophic event. Representative theories of this group are McCartney [425]

Some theories use a combination approach, where multiple theories are utilized in their framework, e.g. Edge (maximum stress and interactive failure) [426]. According to Hinton et al. [414], the non-lamina based failure theories group includes:

- Micromechanics based theories: Chamis (implemented in ICAN and CODSTRAN programs) [427,428], Daniel (strain rate effects) [429], Huang [430], Mayes and Hansen [431]
- Strain energy based failure theory: Wolfe and Butalia [432], Doudican [433]
- Dissipated Energy Density (DED) by Mast [434]
- Continuum Damage Mechanics (CDM) models: Li [435], Talreja [436]

Simple method such as the ten-percent rule of Hart-Smith [437,438] is also useful, as it helps to preliminarily estimate the dimensions of fibrous composite structures. Post failure degradation model (PFDM) can be included in the analysis or not. Without the PFDM, the composite laminate is considered failed immediately when the first failure is initiated, which is also called First Ply Failure (FPF), e.g., Hart-Smith theories. With the PFDM, the computation process is iterative, as any failed ply will be considered, and certain properties of the composite laminate will be degraded for the next calculation step, until the ultimate failure occurs, thus it is called Progressive Ply Failure (PPF). The properties

can be degraded abruptly as in Tsai, Wolfe, Sun, Chamis, Bogetti, Huang and Mayes or gradually as in Cuntze, Puck, Edge, Rotem, Zinoviev, McCartney.

Hinton et al. [414] introduced the worldwide failure exercise (WWFE), which is a global scale collaboration effort to benchmark the performance of 19 leading failure theories, to assess the maturity of these theories, and to gain further insight of the mechanical behavior of composite laminate under 14 different test cases (with variation of loading scenarios, material and lay-up sequence). The conclusion of WWFE is rather unexpected: the predictive capabilities judged against test data are not reliable [439]. There is no universal theory, which can be applied under any circumstance. However, in a well understood design situation, a suitable failure theory can be chosen [440]. Recommendation for designer and researcher have also been given [441]. Talreja [439] commented further on the results of WWFE, that *"homogenizing the two constituents removes the possibility of analyzing the failure and thereby determining the conditions of criticality"*. He suggested that the multi-scale modelling approach should be the future trend, where fiber and matrix failures are calculated independently by the FEM model based on known failure mechanisms and validated by experimental data.

Multi-scale numerical models for textile-reinforced FRP

Composite laminate theories and failure theories have been widely implemented into FEM software, where the composite laminate is treated as continuum and can be modelled by shell and solid elements. They can be classified as macro-scale models. FRP with any type of textile reinforcement can be modelled with the macro-scale scheme, as the geometric configuration of fiber in the structure is not considered. The prerequisite is that the constitutive law is adapted to the respective textile structure.

Due to the advance of computational micromechanics, new approaches have been suggested, where fiber and matrix are modelled separately, and mostly within a Representative Volume Element (RVE) [442] or Representative Unit Cell (RUC) [443]. While RVE is based on statistical homogeneity, RUC refers to the periodic microstructure. Such models can be classified as micro-scale. RVE and RUC approaches can be used to predict the failure mechanism of FRP under different load cases, e.g., longitudinal tension [444,445], transverse compression and longitudinal shear [446], transverse tension and out-of-plane shear [447], or to investigate the fiber-matrix interface properties on the in-plane shear deformation [448]. Micro-scale models for UD composite have been suggested by many authors [445]. Döbrich [166,449] and Liu [450] proposed micro FE models for woven composites, where the fiber is modelled with beam elements.

The fiber component can be modelled at the yarn level with finite elements, which are clearly separated from the matrix component, and then they can be classified as meso-scale. Meso-scale models of many different textile reinforced FRP can be generated by geometric modelling software such as TexGen [314], WiseTex [451,452], and transferred directly to FEM software for calculation. As the computation is still limited, most of the meso-scale simulations of FRP are carried out within the RUC. The predicted results from high detailed models can be transferred to macro-scale models for structural analysis. Few authors carried out the structural analysis of FRP on the meso-scale, e.g. Hübner [306]. Interface elements are introduced into meso-scale model to describe the progressive failure due to delamination [453–456]. Table 3-4 shows an overview of FEM models for selected textile reinforced FRP at the macro and meso-scales.

In recent development, combination of multiple models of different scales into one-single computing process brings advantages in comparison of using these models separately. One representative of this approach is the FE² method [457].

Table 3-4: Overview of FEM models of FRP made from selected textile structures

	Macro-scale	Meso-scale
Woven	Tabiei [458], Whitcomb [459], Woo [460], Fujita [461], Raju [462], Ishikawa [463], Hahn [464], Zhang [465], Naik [466], Soykasap [467]	Hübner [306], Stig [307,468], Lomov [451], Wang [469], Le Page [470], LLorca [442], Barbero [471], Daggumati [472], Yu [473], Cox [474,475]
Braided	Cichosz [476], Blinzler [477], Vinot [478],	Li [479], Zhang [480], Pickett [356], Liu [481], Gholami [482], Gu [483], Dhimole [484], Li [485], Zheng [486], Kun [487], Yamamoto [488], Song [489,490], Fang [491]
Warp-knitted	Mattsson [492]	Drapier [493], Yin [494], Carvelli [495], Ferreira [496], González [497], Mikhaluk [498],
Weft-knitted	Haasemann [499]	Ravandi [500], Ionesi [501], Hamedi [502], Haasemann [503]

3.5 Summary

The research and development of FRP production technique has a long history and a wide diversification. As part of material science, research on FRP production is supported by a wide spectrum of disciplines from chemistry, physics, mathematics, mechanical engineering, automation/mechatronics, information technology, computational mechanics, textile technology to industrial engineering. Technological and economical improvements on different aspects have been made continuously and that trend carries on. Among them, in the trend of digitalization, the use of numerical method is more and more widely spread, and gets involved in different steps of FRP production. Two of the important models are textile model and FRP model. The textile model supports the development of reinforcement architecture. The FRP model helps in the structural analysis, namely, the behavior of FRP part under certain loading conditions. Virtual models reduce time and cost of development, as the actual prototype must not be produced repeatedly. Because of their usefulness, numerical models has been continuously developed. The later generation of models always delivers more advanced feature, or overcomes disadvantage of the last generation. The effort put in this thesis concentrates on numerical model of BWKF and the FRP made from them. FEM models for both BWKF and their FRP should be developed on the meso-scale, which bring significant advantage in comparison to the available macro-scale model. Meso-scale model of BWKF should allow the description of yarn sliding, gap formation as well as fiber damage. Meso-scale of FRP should allow the separate damage criteria for fiber and matrix, as well as delamination.

4 Objectives and research program

4.1 Motivation

Despite of good formability, forming of flat BWKF into 3D preforms for shell-like composite part is still challenging, namely some defects such as wrinkles, gap formation, or damage of fiber cannot be totally avoided. Thus, optimization is required before mass production. Virtual forming process optimization with FEM models is an attractive approach as the computational cost has always been cheaper. As state of the art, macro-scale model based on continuum mechanics has been implemented for BWKF successfully by Döbrich [285,374]. The macro-scale modelling approach offers reasonable computational costs and can predict common defect such as wrinkle formation. However, further defects such as fiber misalignment, wavy fibers, buckling of fibers, damaged fibers, and gap formation cannot be predicted with macro-model. As the complexity of composite part and quality requirement of the 3D preform increases, FEM models with higher grade of details is necessary. The most advanced meso FEM model for BWKF is the one by Macron [376]. But the over simplified of stitching yarn system with spring element prevents the ability of this FEM model to described fiber misalignment and gap formation by extreme deformation, where the sliding between stitching yarn must be taken into account. A further meso FEM model for BWKF should be developed to overcome the present limitation.

4.2 Specification of the research program

4.2.1 Objectives

New modelling strategies for biaxial BWKF at meso-scale will be developed. The mechanical properties of BWKF are characterized by a series of textile physical tests, which provide all necessary data for the setup as well as validation of the FEM models. Two approaches for modelling of reinforcing yarn should be implemented: by beam and by shell elements. The validated models can be used for forming simulation. A benchmarking study on the capacity and reliability of available macro-scale model with the developed meso-scale models by forming simulation follow. Experiments of forming should be carried out in order to serve as foundation for the benchmarking study.

The second objective of the thesis is modelling of FRP at different scales. The macro-scale FRP modelling is carried out with the data of fiber orientation, which is gained from the forming simulation. A mapping method can help to transfer the predicted fiber orientation of meso-scale forming simulation to macro-scale FRP model. Tests of FRP have

to be carried out to characterize the composite and prepare parameter for the composite model. A further meso-scale for BWKF reinforced FRP will be suggested, where yarn and matrix are modelled separately. This meso-scale FRP model is also included an interface element, which helps to predict the delamination failure of the composite part. Tests of T-rib composite part serve as foundation for model validation. The validated model will be used to predict the mechanical behavior of the T-rib composite with different height of the rib.

4.2.2 Research program

The first step is selection of material and configuration for the BWKF. The input material as well as the produced BWKF should be tested systematically. As reference, a plain-woven fabric is also included in the testing programs. Along with the characterization of textile fabrics, their equivalent FRP should also be tested. The experimental works are presented in Chapter 5. The first objective of the research program is realized in Chapter 6, where various approaches of modelling for BWKF will be presented and validated. The developed and validated FEM models will be used for the benchmarking study of forming simulation in Chapter 7. Chapter 8 is about modelling of FRP at different scales. Firstly, the mapping procedure is introduced. Mapping for demonstration shell-like composite part will be carried out. The structural analysis for the demonstration composite part under some common loading cases will be presented. Secondly, a meso FEM model for BWKF reinforced FRP is proposed. This model should be validated based on the test data from Chapter 5. The validated model is then used to predict the mechanical behavior of T shape rib-stiffened FRP composite part under bending load.

5 Analysis of the structural behavior of biaxial weft-knitted fabrics and their FRP

5.1 Systematic test planning

5.1.1 Material selection and textile production

Biaxial weft-knitted fabrics (BWKF) can be produced with various configurations and machine parameters. According to the work of Orawattanasrikul [225], stitch length (SL) and yarn density influence the forming behavior of BWKF. Additionally, the layer configuration of reinforcement layers in fabrics also play an important role. The type of reinforcing yarn and stitching yarn have certain influence. To prepare the input parameter for modelling as well as validation, a limited quantity of BWKF variants with the configuration as in Table 5-1 are chosen for the textile physical testing plan. Only asymmetric 2-layer and 4-layer BWKF with one stitching yarn system are used for the investigations. Figure 5-1 shows an overview of surface appearance and cross-section of 2-layer BWKF that were produced from different materials. A plain-woven fabric is also tested and used as a reference to compare to BWKF. GF and hybrid commingling yarn CF/PA 6.6 are used as the reinforcing yarn. 2-layer BWKF made from hybrid commingling yarns CF/PA are produced with two different settings of weft density. Zanoaga suggested that, the yarn density has an influence on the mechanical properties of FRP later [504].

GF has the fineness of 1200 tex and is produced by P-D Glasseiden GmbH Oschatz (Oschatz, Germany) with the commercial name DR199 EC17-1200-350. Textiles made from this type of GF can be used to produce FRP with thermoset matrix by any consolidation method in the LCM family.

The carbon fiber is Tenax-E HTA40 E13 3K 200 tex of the manufacturer Teijin Carbon Europe GmbH (Wuppertal, Germany). The polyamide 6.6 is AICK062 with 94 tex and constituted from 140 filaments (f140) (Polyamide 6.6 High Tenacity, hereafter for short PA 6.6) of the manufacturer W. Barnet GmbH & Co. KG (Aachen, Germany). The commingling hybrid yarns were manufactured on an air jet texturing machine Stähle RMT-D (Stähle-Eltex GmbH, Germany) according to [70] with the following process parameters: overfeed of CF 2%, overfeed of PA 6.6 3.5% and air pressure 3.5 MPa. The output hybrid yarn has a fineness of about 300 tex. BWKF made from hybrid commingling yarn CF/PA 6.6 can be consolidated by thermoforming technique, as the matrix PA 6.6 has already been mixed into yarn with CF. This yarn architecture helps to shorten the cycle time of consolidation and improves the quality of the composite part as the flow distance of matrix to fiber

material is significantly reduced. The actual reinforcing yarn is folded from four CF/PA 6.6 hybrid yarns.

BWKF are manufactured on a modified flatbed weft-knitting machine Aries 3D of the manufacturer Steiger Participations Sa. (Vionnaz, Switzerland). For the production of BWKF from GF 1200 tex, only GF 68 tex x 2 is used for stitching yarn. This glass fiber has the commercial name FZP084 EC-9 68 X 2 S150 1383 and is provided by Culimeta GmbH & Co. KG (Bersenbrück, Germany). While in the production of BWKF with hybrid commingling yarn CF/PA 6.6, stitching yarn is folded yarn of GF 2 x 68 tex with PA 6.6 94 tex. The plain-woven (for short W GF) fabric is fabricated on a rapier-weaving machine of the company Lindauer DORNIER GmbH (Lindau, Germany).

A special variant called “BWKF GF integral 4-layer” is produced as reinforcement for the T-shaped FRP, but not included in the textile or composite testing program. The BWKF GF integral 4-layer is produced as flat textile out of the weft-knitting machine Aries 3D, and manually formed into 3D preform with the principle shown in Figure 5-2. The BWKF integral structure is the result of the research effort to produce the reinforcement from BWKF faster and with continuous running yarn, even for FRP with complex shell-rib geometries. More details on the production technique of BWKF GF integral 4-layer can be found in [37].

Table 5-1: Fabric configurations

Type of textile	Biaxial weft-knitted fabric					Plain woven fabric
Variant	BWKF GF 2-layer	BWKF GF 4-layer	BWKF CF/PA 2-layer V1	BWKF CF/PA 2-layer V2	BWKF CF/PA 4-layer	W GF
Reinforcing yarn	GF 1200 tex		CF/PA 6.6 (300 tex x 4)			GF 1200 tex
Stitching yarn	GF (68 tex x 2)		GF (68 tex x 2) / PA 6.6 (94 tex)			not used
Warp yarn density (yarn/100 mm)	28	57	28	28	57	40
Weft yarn density (yarn/100 mm)	28	57	28	41	57	40

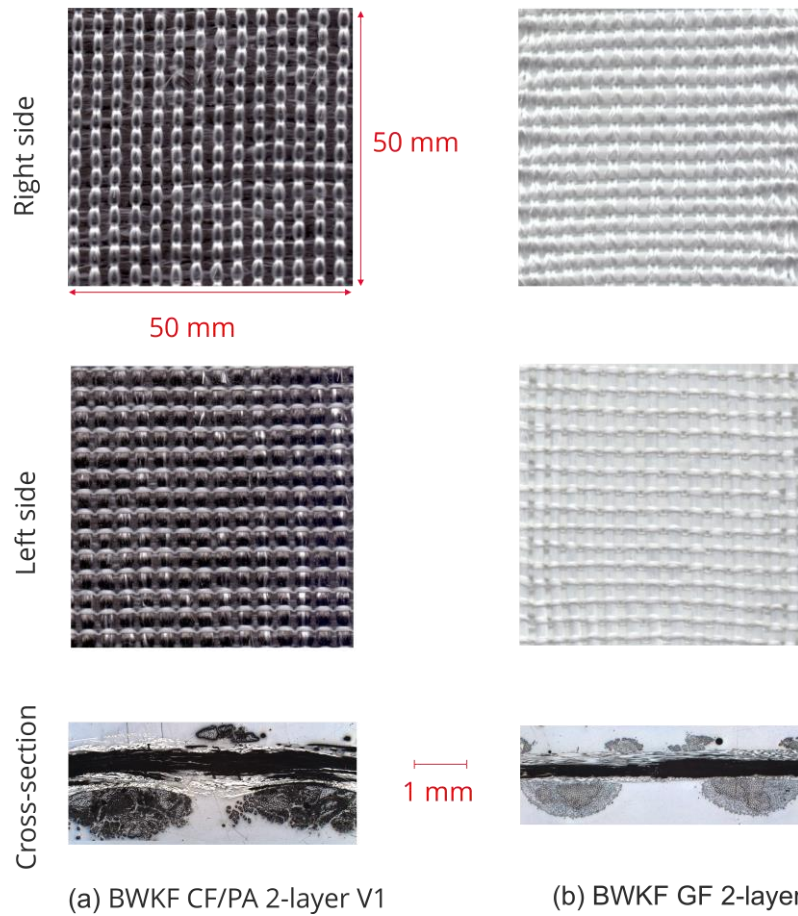


Figure 5-1: Overview of the representative fabrics and their cross-sections (microscopy photos along warp direction): (a) BWKF CF/PA 2-layer V1 and (b) BWKF GF 2-layer

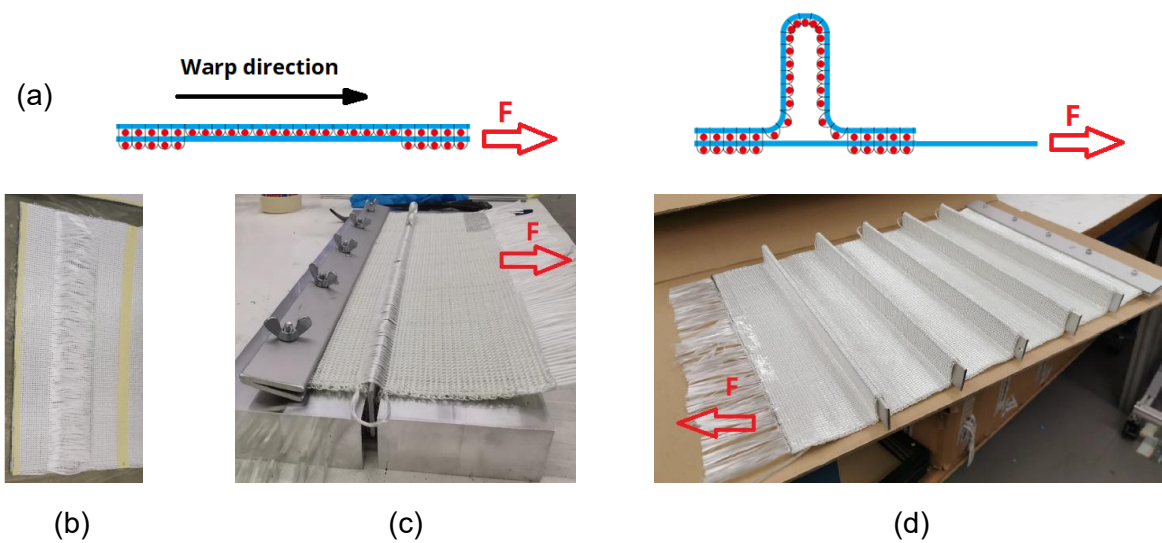


Figure 5-2: Preforming of integral BWKF from 2D to 3D: a) illustration of the principle, b) flat fabric, c) clamp and yarn pull out and d) 3D integral BWKF

5.1.2 Testing plan

Fibers and yarns are the basic building blocks of textile structures. Understanding their mechanical properties provides a solid foundation for the modelling of textile structures. For that reason, tensile test of fiber and yarn are included in the testing plan.

Basis values of BWKF such as stitch length, thickness, and area density are tested according to available standard. Based on the understanding of forming behavior of textile presented in 2.5, the following mechanical properties of BWKF are investigated: tensile, shear, bending behaviors and friction between fabrics and tools. Friction tests are used to investigate the interaction between fabric and tools during forming process. Same tests are carried out for the plain woven fabric. For more understanding of the sliding of yarn in textile structure, yarn pull-out test is included.

FRP made from some selected BWKF from the textile-testing program are tested to prepare input data as well as for validation of the FRP model. To prepare the necessary parameter for the FRP modelling, the following tests are included in the testing plan: tensile, 4-point bending, ILSS. For T-shaped rib-stiffened FRP, 3-point bending tests are carried out to measure their bending stiffness and strength.

Tests are further explained in following subsections.

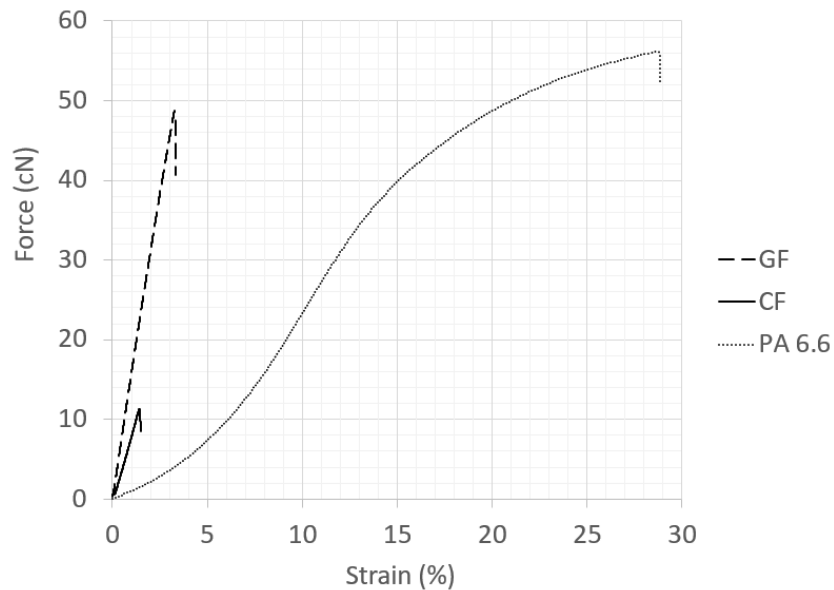
5.2 Fiber and yarn tests

5.2.1 Fiber tests

GF, CF and PA 6.6 fiber are tested on a FAVIMAT test machine of Textechno Mönchengladbach, which has the function of tensile testing on the same specimen, after its linear density is measured with vibration method. The test results are presented in Table 5-2 and Figure 5-3. While the high performance fibers show linear elastic behavior, the thermoplastic fiber PA 6.6 show non-linear elastic-plastic behavior. The break elongation of PA 6.6 is one order greater than GF and CF.

Table 5-2: Test results of GF, CF and PA 6.6 fiber (deviation)

Parameter	GF	CF	PA 6.6
Fineness (dtex)	5.7 (1.1)	0.6 (0.1)	7.2 (0.9)
Density (g/cm ³)	2.52 [42]	1.76 (specification)	1.14 [42]
Filament diameter (μm)	17.1 (1.6)	6.8 (0.3)	28 (1.8)
Tensile strength (MPa)	1816 (248)	3262 (655)	886 (54)
Specific tensile strength, axial (MPa cm ³ /g)	726	1853	770
Initial modulus (cN/tex)	2745 (66)	13294 (1080)	537 (53)
Elongation at break (%)	2.9 (0.6)	1.6 (0.3)	27 (3)

**Figure 5-3: Force-strain-curve of fiber tensile test (average value)**

5.2.2 Yarn tests

Tensile behavior of high-performance yarns is tested on a tensile testing machine Zwick Z100 (Zwick GmbH & Co. KG, Ulm, Germany) according to the standard ISO 3341, where the strain is measured by an optical extensometer. The distance between two clamps is 500 mm. A pre-tension of 0.5 cN/tex is applied on the yarn. The Young's modulus is measured in defined strain ranges as shown in Table 5-3. The thermoplastic yarn PA 6.6

is tested on a Zwick 2.5kN tensile test machine according to the standard DIN EN ISO 2062, where strain is measured via displacement of the traverse. Table 5-3 gives an overview of the test results of the homogeneous yarns. Similar to the fiber behaviors, the high performance yarns show linear-elastic behavior and the thermoplastic yarns show non-linear elastic-plastic behavior as shown in Figure 5-4. The strain range is chosen for each type of fiber such that Young's modulus is determined in the linear range of the curve.

Table 5-3: Homogeneous yarn properties given as mean value (standard deviation)

Parameter		GF 68 tex x 2	GF 1200 tex	CF 200 tex	PA 6.6 94 tex
Young's modulus (GPa)	modulus	71.9 (6.4)	51.4 (2.3)	207 (15)	3.6 (0.2)
Strain range for determination of Young's modulus (%)	range for determination of	0.05-0.25	0.3-0.5	0.25-0.35	0.15-0.3
Fracture strain (%)		2.69 (0.14)	1.8 (0.1)	0.9 (0.1)	24.8 (1.7)
Breaking force (N)		96.4 (5.32)	574 (21)	183 (13)	67.3 (2.7)

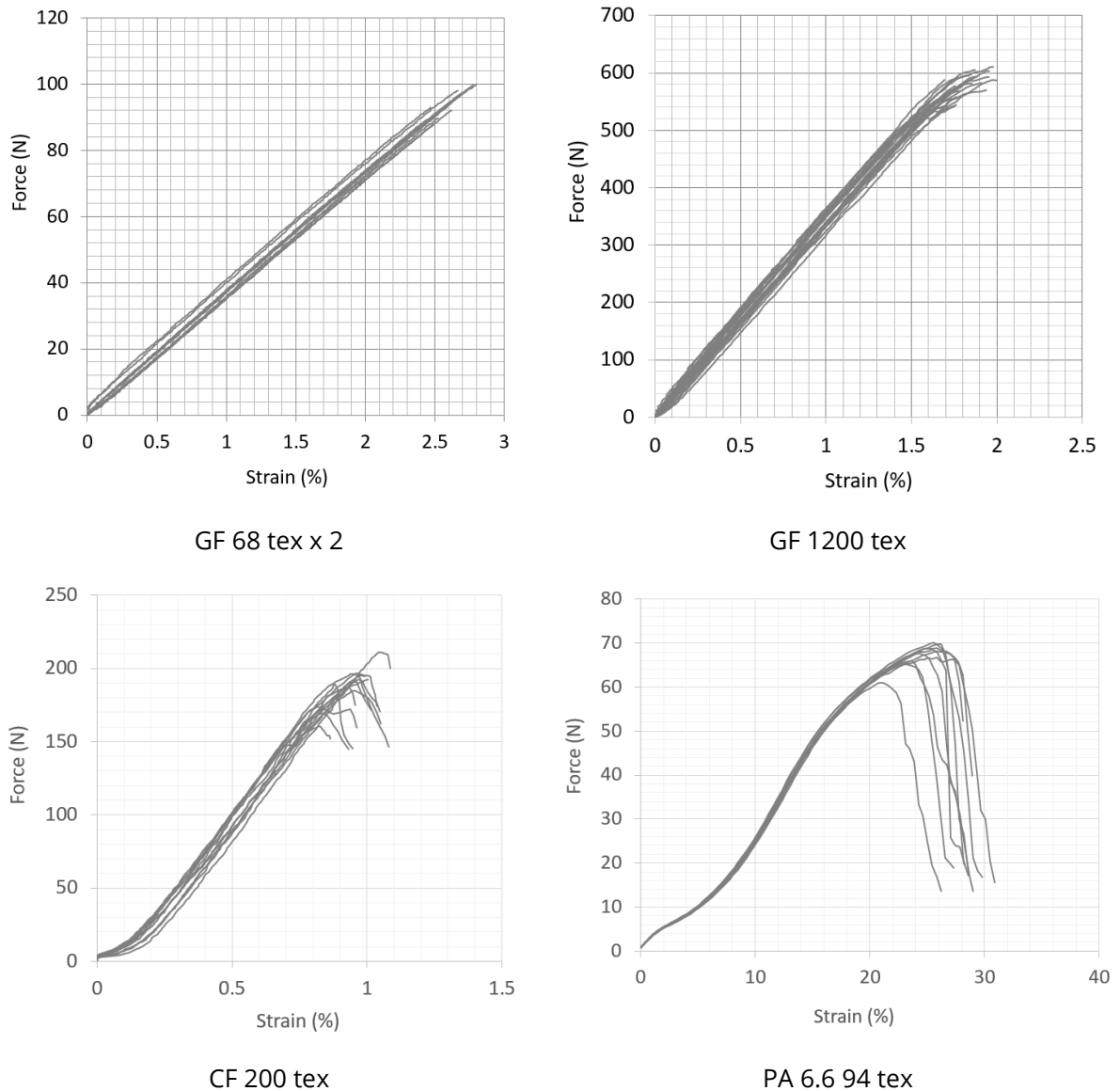
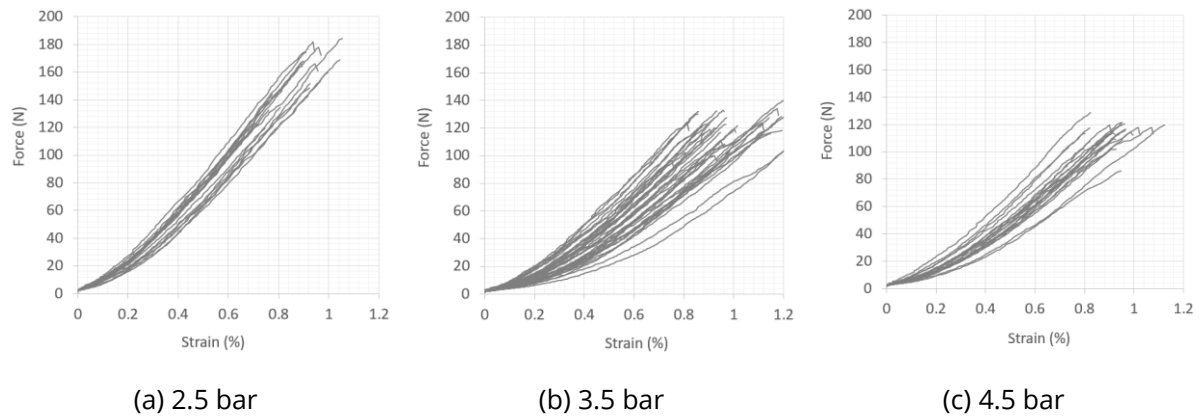


Figure 5-4: Force-strain-curves of homogeneous yarns

The produced commingling hybrid yarns CF/PA 6.6 300 were produced under different air jet pressure and are tested in order to determine the damage that is caused by the air jet texture process (cf. Table 5-4). In general, hybrid yarn CF/PA 6.6 shows great non-linear elastic behavior at the start. This non-linearity belongs to the structural strain, as both CF and PA 6.6 fibers are overfed into the air jet chamber. Additionally, they are twisted and entangled by the air vortex. Under different air jet pressure, different rate of yarn damage can be quantitatively assessed by the maximum tensile force. Experimental data shows that the higher air jet pressure leads to higher yarn damage. Both strength and stiffness of yarn decline, when the air jet pressure increases.

Table 5-4: Hybrid yarn properties given as mean value (standard deviation)

Parameter	CF/PA 6.6 300 tex		
Air jet pressure (MPa)	2.5	3.5	4.5
Young's modulus (GPa)	97 (14)	59 (18)	63 (12)
Strain range for determination of Young's modulus (%)	0.25-0.35	0.25-0.35	0.25-0.35
Fracture strain (%)	0.9 (0.1)	1.0 (0.2)	0.9 (0.1)
Breaking force (N)	155 (18.9)	120 (10.9)	115 (8.9)

**Figure 5-5: Tensile force-strain-curves of commingling CF/PA 6.6 hybrid yarns produced by different air jet pressure**

5.3 Fabric tests

Basic values of fabrics are tested according to available standards. The thickness is measured according to the standard DIN EN ISO 5084, where the fabric is put under a pressure of 1 kPa. The area mass density is measured according to the standard DIN EN 12127, where a specimen of fabric with an area of $A=100 \text{ cm}^2$ is cut out and its mass m is weighed by a digital laboratory scale. The area mass density (ρ_A in g/m^2) is then calculated as follows:

$$\rho_A = \frac{m}{A} \quad (5-1)$$

The stitch length of stitching yarn the knitted fabrics is determined according to the standard DIN EN 14970. Results of these basic values are shown in Table 5-5.

Table 5-5: Basic properties of fabrics given as mean value (standard deviation)

Type of textile	Reinforced weft-knitted fabric					Plain woven fabric
Variant	BWKF GF 2-layer	BWKF GF 4-layer	BWKF CF/PA 2-layer V1	BWKF CF/PA 2-layer V2	BWKF CF/PA 4-layer	W GF
Thickness (mm)	1.6 (0.03)	2.4 (0.04)	2.2 (0.1)	2.6 (0.2)	3.6 (0.1)	0.85 (0.01)
Areal density (g/m ²)	1027 (34)	1722 (44)	824 (46)	1199 (29)	1656 (45)	955 (15)
Stitch length (mm)	13.6 (0.6)	16.8 (0.5)	14.4 (0.5)	13.4 (0.5)	19.5 (1)	-

Diverse mechanical properties of the fabrics, which play important role on the forming ability, are tested, including: tensile, bending, shear. Additional relevant tests are friction between fabrics and tools, and single yarn pull-out test. The test method and result are presented in the following sections accordingly.

5.3.1 Tensile

Tensile tests of the fabrics are carried out on a tensile testing machine Zwick Z100 (Figure 5-6) and according to the standard DIN EN ISO 13934-1. The test specimen is 300 x 50 mm², the distance between two clamps is 200 mm, and the test speed is 20 mm/min. Strain of the fabrics during the test is measured by an optical measuring device. The clamping pressure is set at maximal 80 bar to prevent the slippage of fabrics out of the clamps. Because high-performance fibers as GF and CF are sensitive to transverse force, higher clamping pressure would cause breakage at the clamp position, which should be avoided.



Figure 5-6: Tensile test of BWKF CF/PA 2-layer V1 on a Zwick Z100 machine

An overview of the tensile test results of fabrics is given in Table 5-6. The test results illustrate a non-linear tensile behavior in the warp and weft directions of all fabrics as shown in Figure 5-7 (BWKF GF), Figure 5-8 (BWKF CF/PA), Figure 5-9 (W GF). The non-linearity in tensile behavior of the plain woven fabric is purely caused by structural waviness/crimp of yarn. The non-linearity in tensile behavior of weft-knitted fabric is partially caused by the non-linear tensile behavior of the reinforcing yarns as tested above. In addition, reinforcing yarns have a certain degree of waviness due to interaction with the stitching yarn system. This also contributes to the non-linear tensile behavior of the fabrics. The tensile strength and fracture strain of most fabrics in both directions do not exhibit a great difference.

In principle, textile structures with similar warp and weft reinforcement density should have the same strength in both warp and weft direction. Some variants show noticeable difference of tensile strength between warp and weft direction. BWKF CF/PA V2 2-layer has higher density of reinforcing yarn in weft direction, thus, higher tensile strength in weft direction is logical. It is not clear, what causes the difference of strength in warp and weft direction in BWKF GF 2-layer and BWKF CF/PA 4-layer. A possible explanation for such phenomenon is the weft yarn is strongly damaged during the knitting process.

Table 5-6: Overview of the tensile test results of fabrics

Variant	Reinforced weft-knitted fabric										Plain woven fabric	
	BWKF GF 2-layer		BWKF GF 4-layer		BWKF CF/PA 2-layer V1		BWKF CF/PA 2-layer V2		BWKF CF/PA 4-layer		W GF	GF
Direction	Warp	Weft	Warp	Weft	Warp	Weft	Warp	Weft	Warp	Weft	Warp	Weft
Max. tensile force (N)	6744 (573)	4649 (418)	13247 (575)	13556 (856)	5820 (461)	5744 (354)	5800 (367)	7332 (380)	12600 (809)	9230 (986)	10350 (347)	9820 (652)
Fracture strain (%)	1.8 (0.2)	1.9 (0.2)	1.6 (0.1)	1.6 (0.4)	1.6 (0.3)	1.6 (0.2)	1.6 (0.1)	1.6 (0.2)	1.4 (0.2)	1.6 (0.2)	3.5 (0.2)	2.9 (0.2)

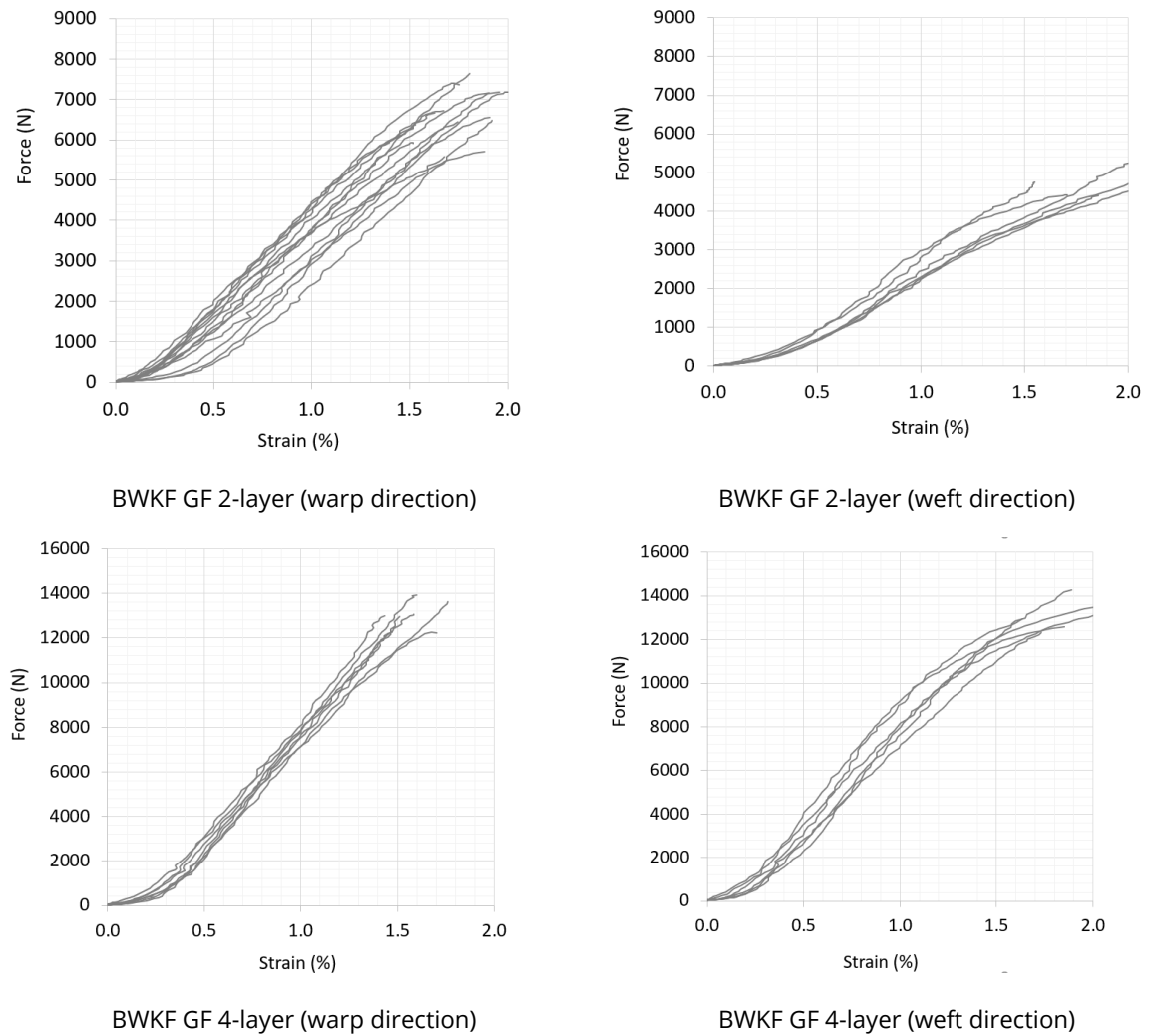


Figure 5-7: Force-strain curves of textile stripe tensile tests for BWKF GF 2-layer and 4-layer

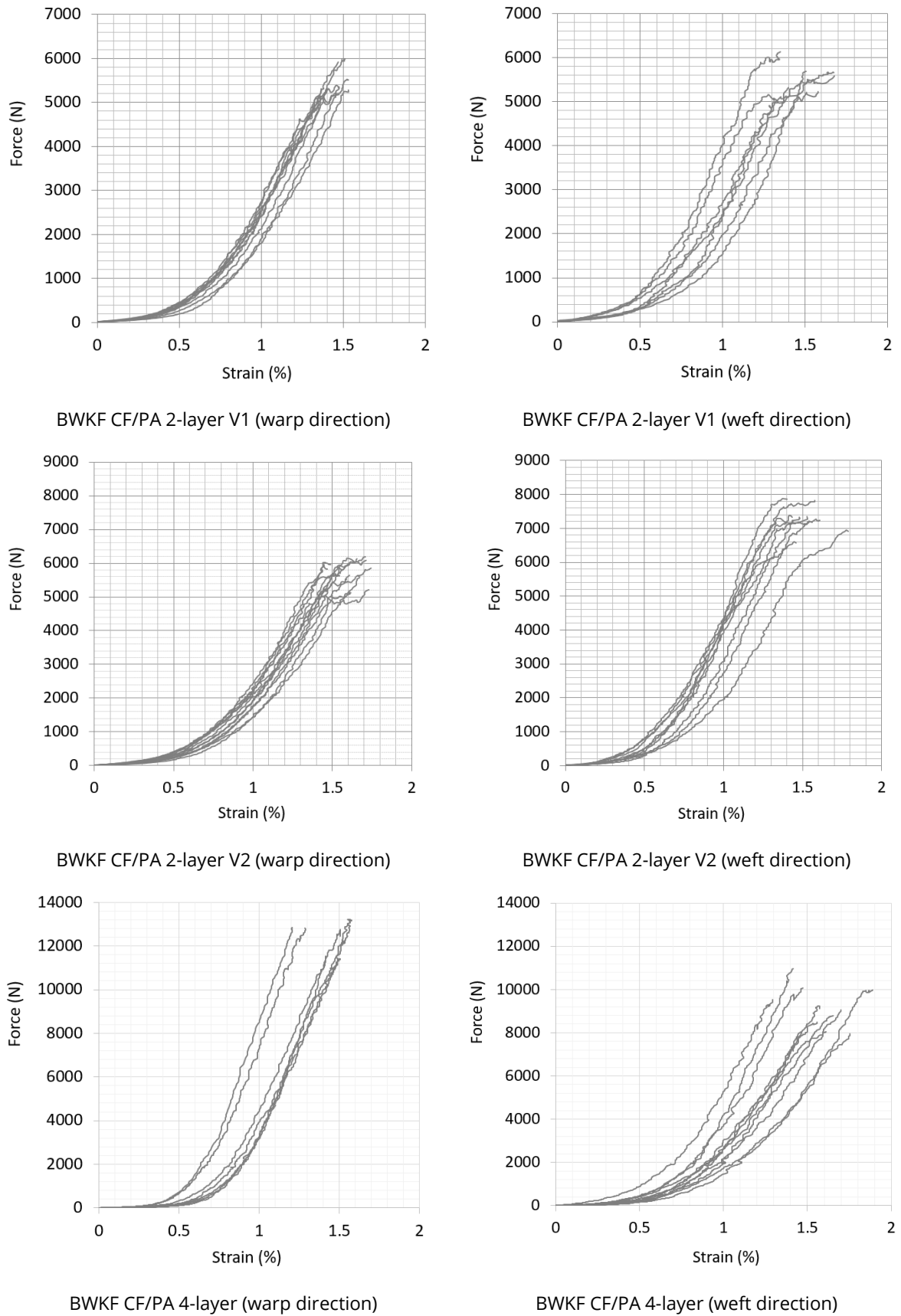


Figure 5-8: Force-strain curves of textile stripe tensile tests for BWKF CF/PA 2-layer (V1 & V2) and 4-layer

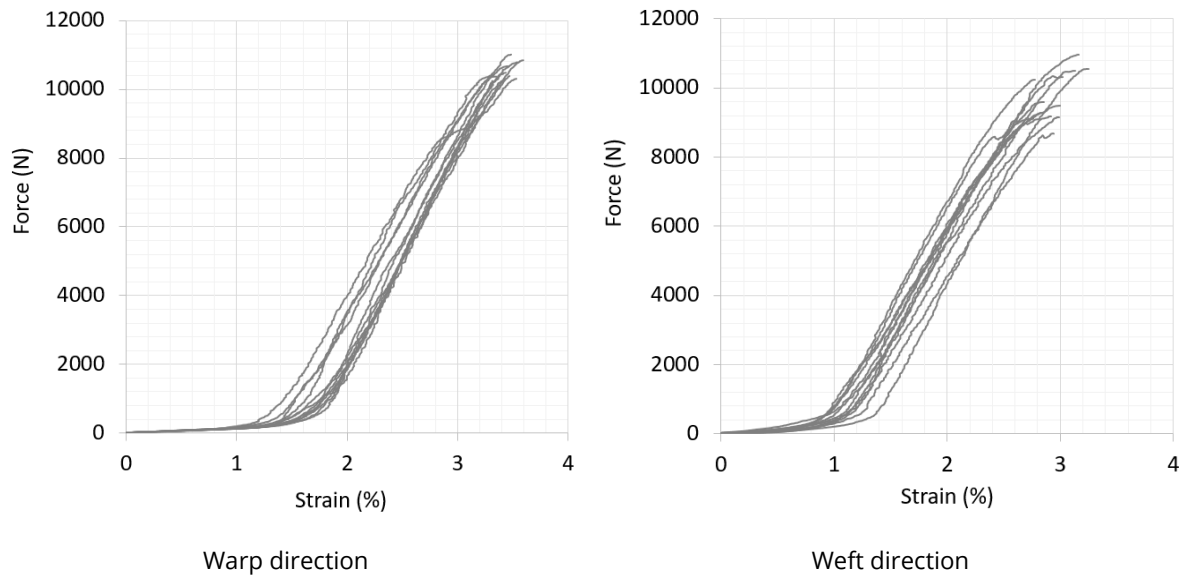


Figure 5-9: Force-strain curves of textile stripe tensile tests for plain-woven fabrics W GF

5.3.2 Bending

Since the fabrics are not very stiff (overhang length less than 300 mm), the out of plane bending stiffness of the fabrics is measured on a cantilever bending test machine ACPM 200 of the company Cetex (Chemnitz, Germany) according to the standard DIN 53362 (Figure 5-10). As the whole test process is automated, the test result is objective and deviation caused by test person is reduced to a minimum.

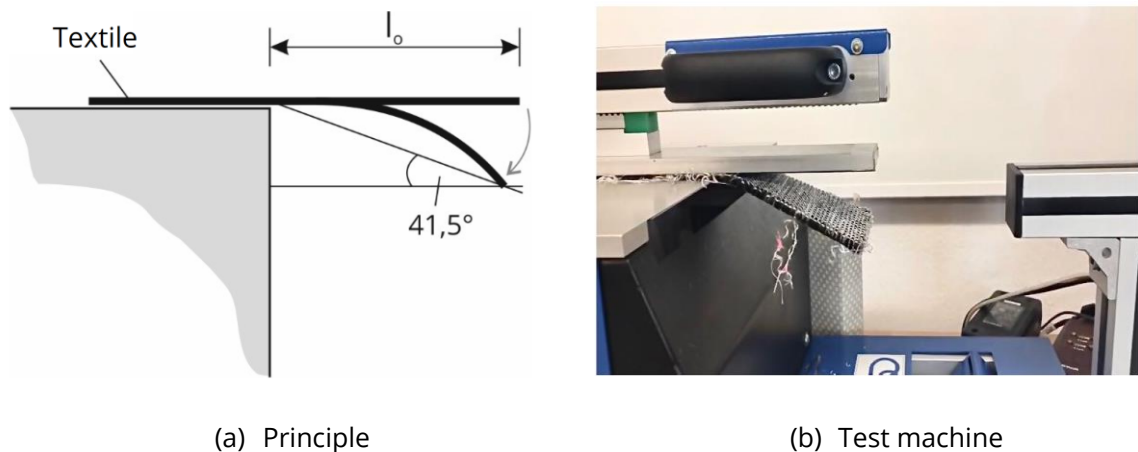


Figure 5-10: Cantilever test principle according to DIN 53362 and the test machine ACPM 200

The standard DIN 53362 for cantilever test has a pre-defined deformation state of the fabric, namely when it touches the reference plane with an angle of 41.5°. The fabric is pushed slowly out of the edge to reach the defined deformation state and then overhang

length at that state of deformation is recorded for evaluation. The 41.5° reference plane is monitored by a row of laser sensors. The overhang length is recorded and the cantilever bending stiffness is calculated according to [505] as

$$B = \frac{mg}{l} \left(\frac{l_0}{2}\right)^3 \quad (5-2)$$

where B (cN*cm²) is the bending stiffness, m (g) is the mass of the textile stripe, g (cm/s²) is the gravitational acceleration, l (cm) is the total length of the textile stripe, and l₀ (cm) is the overhang length. Thus, only a single value of bending stiffness is determined for one direction, while the bending stiffness of fabrics made from high performance material tends to decrease with increasing curvature [506]. Harrison et al. [507] found, however, that a constant value of bending stiffness is sufficient for further investigations.

Due to the asymmetric nature of the fiber architecture in the thickness direction, bending stiffness of textile such as NCF, BWKF is direction and side dependent. That means significant difference between bending stiffness in warp and weft direction can be observed. In Table 5-7, the test results confirmed this phenomenon for BWKF. The BWKF variants with 4-layer of reinforcing yarn show significant higher bending stiffness in comparison with the 2-layer variants. The BWKF CF/PA 2-layer V2 with increased reinforcing yarn density in weft direction, also shows distinctly higher bending stiffness in comparison with BWKF CF/PA 2-layer V1. But the plain-woven fabrics has symmetric binding, thus, the difference is not great. The same statement can be true, by comparison the bending stiffness between the left side and right side of certain fabric. However, the test results show no significant difference bending stiffness between two sides of the fabrics in this thesis. Therefore, just one bending stiffness value for both sides of the fabrics will be used for modelling.

Table 5-7: Test results of cantilever test (deviation)

Variant	Biaxial reinforced weft-knitted fabric										Plain woven fabric	
	BWKf GF 2-layer		BWKf GF 4-layer		BWKf CF/PA 2-layer V1		BWKf CF/PA 2-layer V2		BWKf CF/PA 4-layer		W GF	
Direction	Warp	Weft	Warp	Weft	Warp	Weft	Warp	Weft	Warp	Weft	Warp	Weft
Overhang length (mm)	179 (14)	146 (8)	244 (10)	252 (5)	171 (51)	151 (15)	178 (14)	194 (8)	249 (6)	235 (8)	150 (7)	143 (4)
Cantilever bending stiffness $\times 10^5$ (cNcm ²)	3.6	2.0	15.8	17.4	2.5	1.7	4.1	5.4	15.7	13.2	2.0	1.7

5.3.3 In-plane shear

Picture-frame-test

The picture frame developed by Orawattanasrikul [225] was used to test the shear behavior of all fabrics. The special construction of this picture frame, in which rows of needles are used instead of clamps, helps to avoid yarn bending at fixing position, and thus, improves the accuracy of the recorded shear force. By picture frame without such special needle clamping system, the difference between frame shear and local fabric shear can be up to 2° [232]. The picture-frame test works with circular translation principle, but the picture frame is fixed at one corner and pulled at the opposite corner (Figure 5-11), instead of being fixed at two neighboring corners as shown in Figure 2-29. The picture frame has the dimension of 200 x 200 mm² and is attached to a Zwick 2.5 kN tensile test machine. The test specimen has the size of 300 x 300 mm², with reinforcing yarn parallel to the side of the frame.

The pulling force F (N) of the frame is measured by load sensor with a maximum capacity of 500 N. The displacement d (mm) of the crosshead, i.e the upper corner of the frame, is recorded. The shear angle φ (rad) and shear force F_s (N) are calculated according to [158] with the following equations:

$$\varphi = \frac{\pi}{2} - 2\arccos\left(\frac{\sqrt{2}L + d}{2L}\right) \quad (5-3)$$

$$\theta = \frac{\pi}{2} - \varphi \quad (5-4)$$

$$F_s = F \cdot \cos \frac{\theta}{2} \quad (5-5)$$

where L (mm) is the picture frame side length (200 mm in the used frame), and θ (rad) is the angle between two side of the frame.

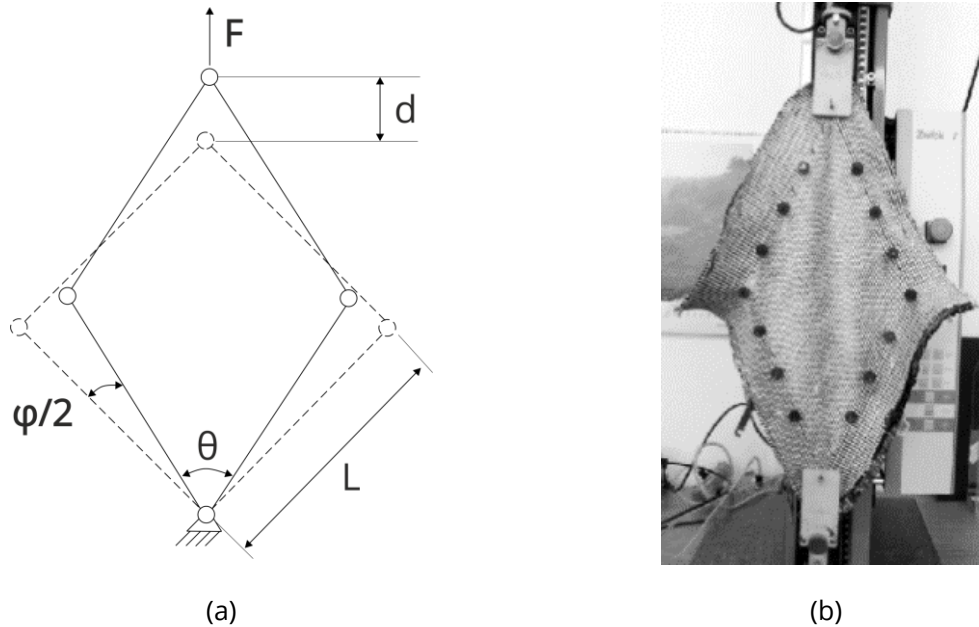


Figure 5-11: (a) Working principle of picture-frame-test and (b) Test of biaxial BWKF CF/PA 2-layer V1 on Zwick 2.5kN tensile test machine

A scanner Artec Eva 3D of the company Artec3D (Luxembourg City, Luxembourg) is used to capture the wrinkle formation on the textile specimen during the picture frame test. Specimens of plain woven fabric and biaxial BWKF CF/PA 2-layer V1 are scanned.

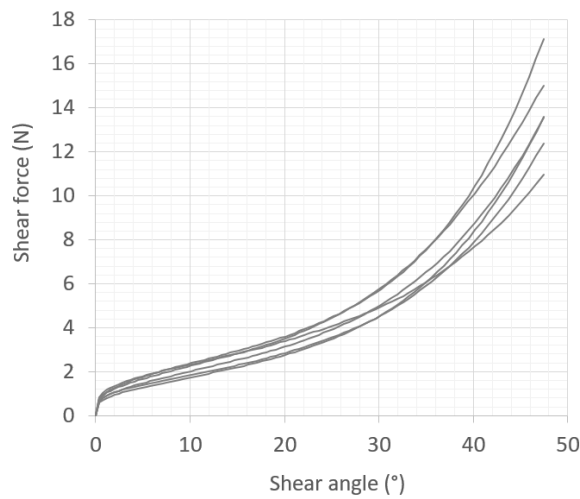
All fabrics are characterized by non-linear shear behavior according to the test results. Initially, friction between yarns increases the shear force, which is then followed by lateral compression of the yarns [158]. The rapid increase of the shear force indicates that the yarns are fully compressed and will soon be laterally incompressible [232]. As a quantitative criterion, critical shear angle is used to indicate this shear limit [508]. Based on the method of Souter [240], the critical shear angle of all fabrics are estimated as shown in Table 5-8. Consequently, wrinkles are expected to occur by further shear loading after the locking angle as the incompressible yarns are pushed out of the plane. The scan results provided in Figure 5-15 show several wrinkles on fabrics under large shear deformation. However, this shear behavior is not solely responsible for the wrinkle formation as the tensile and bending stiffness of the fabric also have certain influences [509].

The estimated critical shear angle of all fabrics are within the range of 32°-36°. The shear force – shear angle – curves of some fabrics shows good repetition, with limited deviation between specimens, such as BWKF GF 2-layer, BWKF GF 4-layer and BWKF CF/PA 4-layer. The others show wider range between specimens and the most scatter measurement happened for plain woven fabrics. The reason of such great deviation is due to the instability of yarn tension of fabrics during production. Especially the woven fabrics, where tension of yarn in both warp and weft direction swing strongly under high production speed [510]. Such phenomenon has less impact on BWKF, as the production speed is significantly slower. Most distorted test results of BWKF happened for BWKF CF/PA 2-layer V2, where the density of weft reinforcing yarn is increased, thus, there is risk of instability. Additionally, unexpected fabric deformation or misalignment of the test specimen can happen during the preparation and clamping of the specimen into the frame. That would lead to tension of fabric in frame and affect the test results [164].

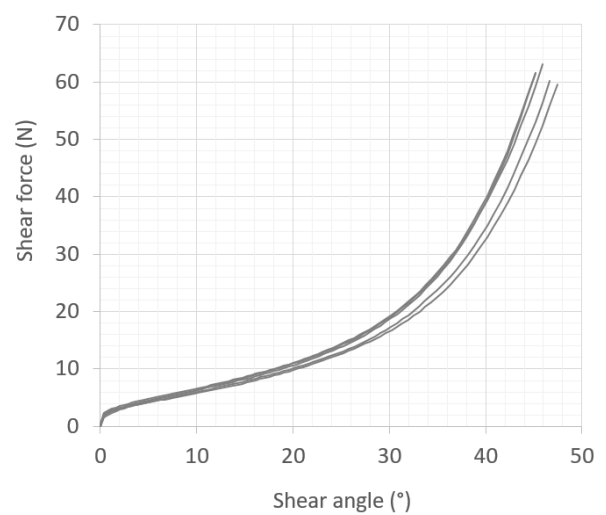
Some more remarks can be given here: there is a proportional relation between shear resistance and density of reinforcing yarn in BWKF structure. 2-layer BWKF have generally lower shear force than 4-layer. Increasing of weft density also leads to noticeable increase of shear force in BWKF CF/PA 2-layer V2. Another factor that could affect the shear resistance: the compaction of reinforcing yarn. GF 1200 tex is multifilament and produced from melt-spinning, where yarn is pulled out and stretched at high temperature and high speed, thus the yarn is compacted. In contrary, the commingling CF/PA 6.6 hybrid garn produced by air-jet texture machine, where two type of filament yarn are opened, mixed. Thus, their original compaction is no longer maintained. Cross-section of BWKF GF 2-layer and BWKF CF/PA 2-layer V1 can be found in Figure 5-1. Without compaction, the yarn tends to have greater interaction with their neighbor, prevent their sliding, and reach the incompressible state faster. The test results of picture frame test show the symmetry of shear behavior of BWKF, despite of the asymmetric nature of the stitching yarn path in fabrics.

Table 5-8: Estimated critical shear angle of fabrics

Variant	Biaxial reinforced weft-knitted fabric					Plain woven fabric
	BWKF GF 2-layer	BWKF GF 4-layer	BWKF CF/PA V1 2-layer	BWKF CF/PA V2 2-layer	BWKF CF/PA 4-layer	W GF
Estimated critical shear angle (°)	36	34	34	32	34	34
Shear force min-max (N)	11-17	60-64	16-35	15-55	80-108	85-210



(a) BWKF GF 2-layer



(b) BWKF GF 4-layer

Figure 5-12: Shear force - shear angle curves of (a) BWKF GF 2-layer and (b) BWKF GF 4-layer

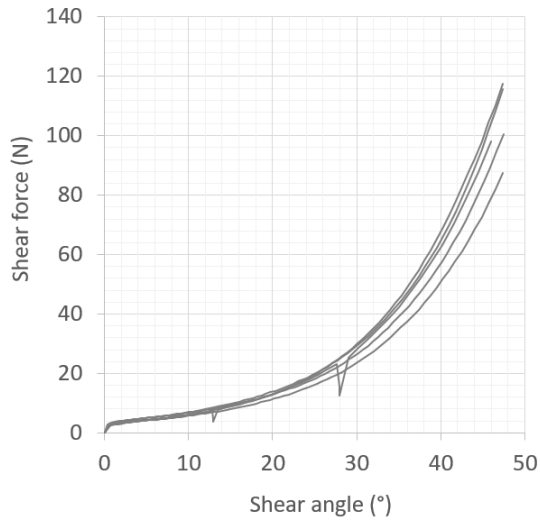
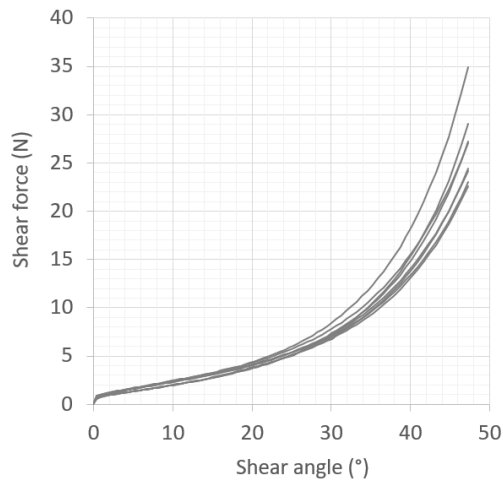
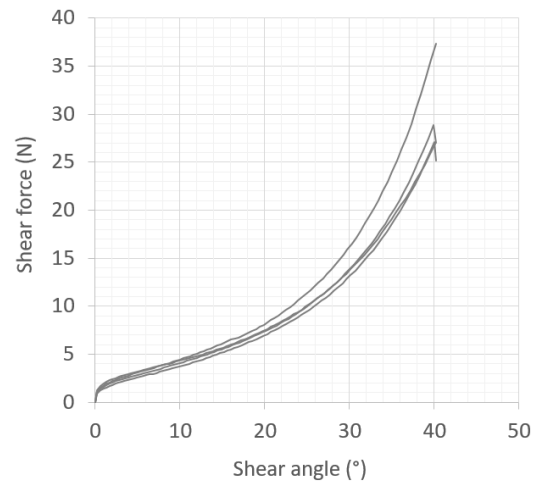


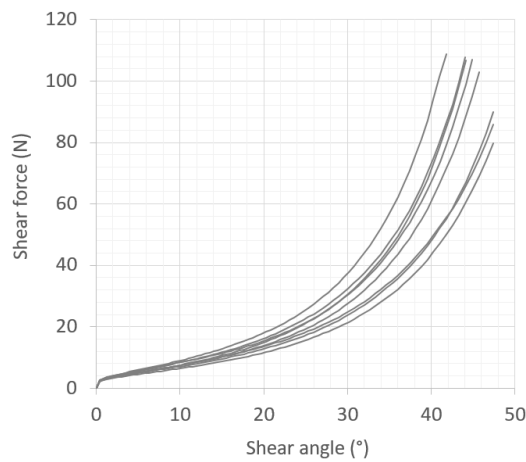
Figure 5-13: Shear force - shear angle curves of plain-woven fabrics W GF



(a) BWKF CF/PA 2-layer V1



(b) BWKF CF/PA 2-layer V2



(c) BWKF CF/PA 4-layer

Figure 5-14: Shear force - shear angle curves of BWKF CF/PA: (a) 2-layer V1, (b) 2-layer V2 and (c) 4-layer

Some scanned results are exemplary shown in Figure 5-15, where the out-of-plane displacement of fabrics are color coded, and the wrinkle formation is visible. The specimens are scanned during the picture frame test at 30, 60 and 90 mm of frame displacement, which are equivalent to 13°, 28° and 47.5° of shear angle. On each specimen, at least 3 wrinkles can be seen, where their out-of-plane deformation on each side is more than 10 mm.

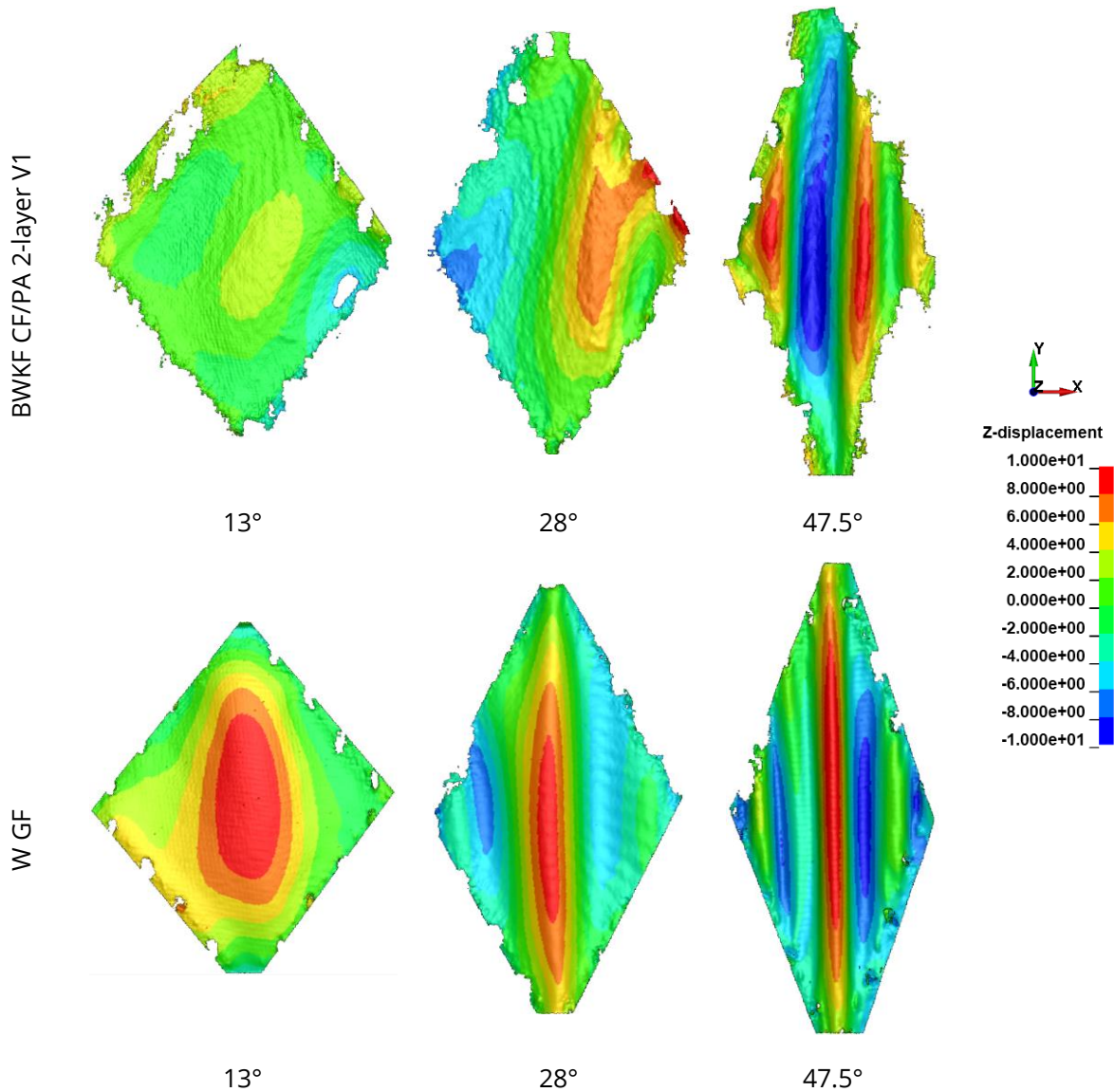


Figure 5-15: Scan data of wrinkle formation at different shear angles during the picture frame test of BWKF CF/PA 2-layer V1 and W GF

5.3.4 Friction

The pull-out test principle was used to test some variants of fabrics in this work. The tests were carried out with a biaxial tensile test machine of Zwick at ITM. As forming of dry

fabric at room temperature is the main concern of this work, no heater was used. The fabric stripe ($300 \times 50 \text{ mm}^2$) is pressed between a couple of metallic plates ($150 \times 50 \text{ mm}^2$) under a defined normal force F_N (within the range from 0.25 MPa to 1.4 MPa) and one end is pulled out with the velocity of 50 mm/min (Figure 2-31c). At least 50 mm of fabric is left out at the free end. The metallic plates are made of high-alloy steel 1.2379. The pull force F_R is recorded and used to calculate the friction coefficient as the following, as the external normal loads F_N are applied from both sides of the fabrics:

$$\mu = \frac{F_R}{2 \cdot F_N} \quad (5-6)$$

The results (Figure 5-16) show a relatively constant pull force during the tests of plain woven W GF (at 0.25 MPa normal pressure), BWKF GF 2-layer (at 0.37 MPa normal pressure) and BWKF CF/PA 2-layer V1 (at 0.36 MPa normal pressure). There is minor difference between static and kinetic friction and the force-displacement curves reach the steady state shortly after the test starts. The influence of normal load on friction coefficient is noticeable, as suggested by Howell, but not significant within the tested range of normal load (Figure 5-17). Thus, the average value of friction coefficient at different normal loads can be used to represent for the friction behavior as shown in Table 5-9. This agrees with the conclusion of Sachs in the benchmarking study [258]. The CoF of W GF is a little lower than the CoF of BWKF GF 2-layer, although they are both made of GF 1200 tex. That suggests the geometry configuration, i.e., the face appearance of textile, has an influence on the friction behavior.

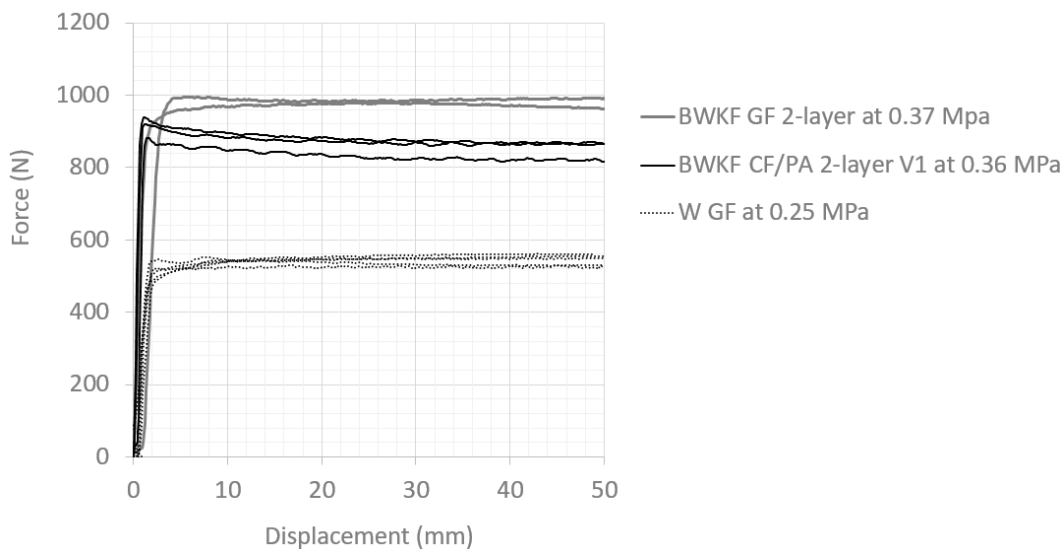


Figure 5-16: Force-displacement curve during friction test of fabrics at defined normal pressure

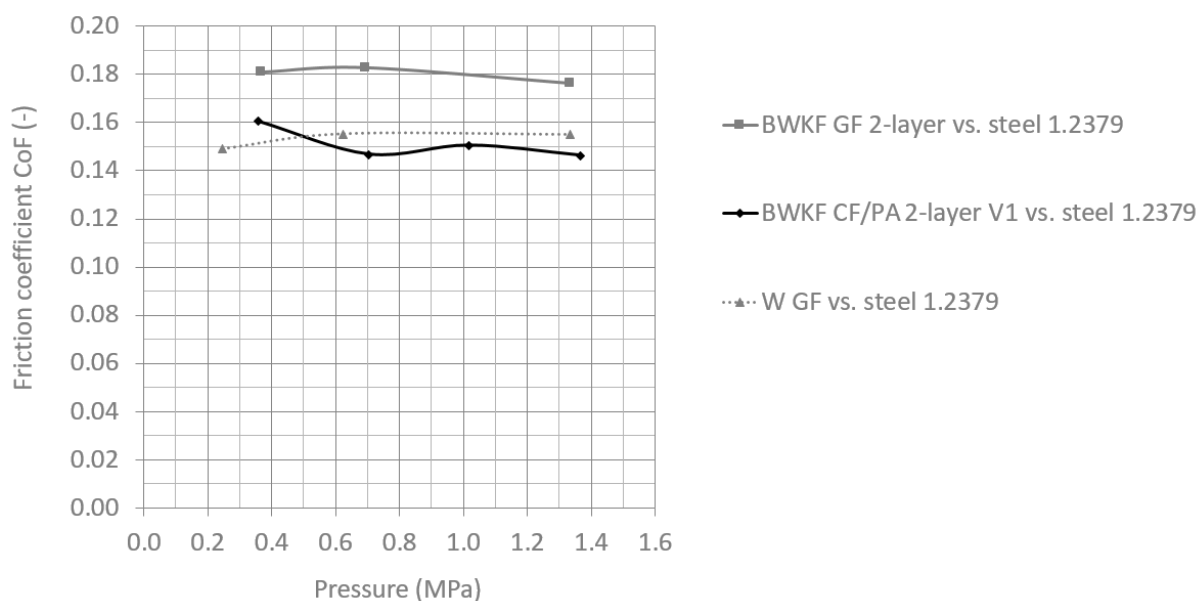


Figure 5-17: Friction coefficient CoF of fabrics under different pressure

Table 5-9: Average of friction coefficient CoF under different normal loads

Fabrics	BWKF GF 2-layer	BWKF CF/PA 2-layer V1	W GF
Friction coefficient CoF (-)	0.18	0.15	0.15

5.3.5 Yarn pull-out test

This test is about pulling one single reinforcing yarn from the textile structure with the aim to measure the resistance of the yarn to sliding in the textile structure. In other words, the influence of the interaction of a yarn with other yarns in the local neighborhood on their relative movement is investigated. A stripe of fabric with the dimension of 200 x 50 mm² is used. About 50 mm length of one end of the specimen is clamped with one single yarn excluded from clamping in the center. At the other end, the excluded single yarn is clamped and pulled out as shown in Figure 5-18. The pull-force and displacement of the pulled yarn are recorded for evaluation. The test is carried out for BWKF CF/PA 2-layer V1 and V2 in both warp and weft direction. The test results are shown in Figure 5-18. The shape of the force-displacement-curves show a similar pattern: the force reaches its maximum value shortly after the start of the test and declines gradually until the end. The yarn is first retained in the fabric leading to the high force. After the pull-out force overcomes the static friction, the yarn starts to slide out of the fabric. Due to dynamic friction and a reduced contact surface between the yarn and its neighbor yarns, the pull force declines. While a clear distinction between warp and weft direction can be seen in

the pull-out force-displacement-curves of BWKF CF/PA 2-layer V1, less differences are found for BWKF CF/PA 2-layer V2.

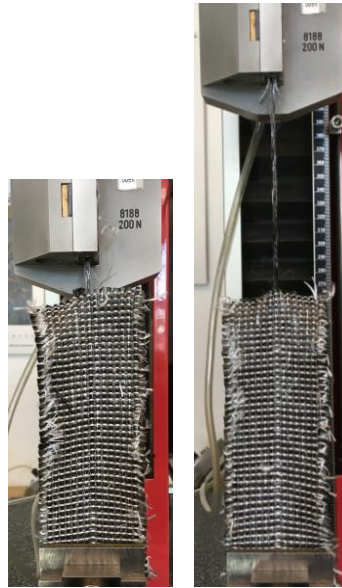
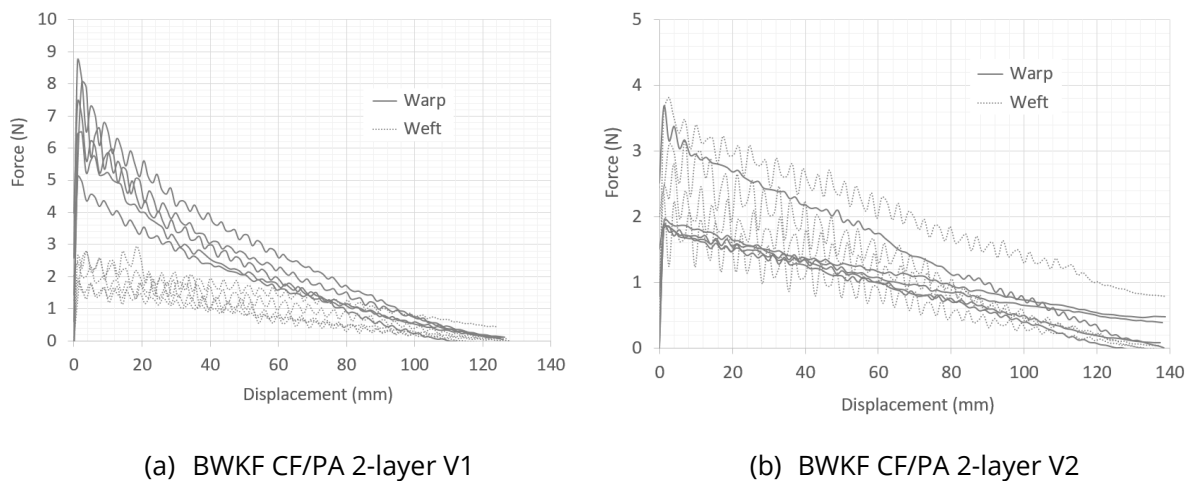


Figure 5-18: Yarn pull-out test for BWKF CF/PA 2-layer V1 in warp direction



(a) BWKF CF/PA 2-layer V1

(b) BWKF CF/PA 2-layer V2

Figure 5-19: Force-displace-curves of yarn pull-out test

5.4 FRP production and testing

The following FRP specimens were available for the tests: thermoplastic UD FRP made of hybrid commingling yarn CF/PA 6.6, thermoplastic FRP made of BWKF CF/PA 2-layer V1 and thermoset FRP made of BWKF GF at coupon level. All thermoplastic FRP coupon specimen and the T cup thin-walled thermoplastic FRP were produced by thermo-pressing method on a COLLIN P300 PV laboratory press (Dr. Collin GmbH, Germany). The

thermoset coupon specimen were produced by vacuum assisted resin transfer molding (VARTM) process. The T-shaped thermoset FRP samples are produced with vacuum assisted resin infusion (VARI) process.

5.4.1 Production of FRP

Thermo-pressing

At the very early state of research project AMARETO, three variants of commingling hybrid yarn were produced from CF and PA 6.6 under three different air pressure setting: 2.5, 3.5 and 4.5 bar. These hybrid yarns were used to produce FRP-UD test specimen for tensile test. For the convenience, the FRP-UD are named according to their air pressure setting as the following: FRP-UD2.5, FRP-UD3.5 and FRP-UD4.5. The tensile test of FRP-UD aimed to investigate the influence of air pressure during comingling process on strength and stiffness of FRP. Based on the test results, an optimal air pressure should be selected for the production of all commingling hybrid yarn CF/PA 6.6 in the framework of research project AMARETO. The hybrid yarn is warped into a square frame by a warping machine of Industrielle Wickeltechnik (IWT) GmbH, Germany. The consolidating the warped hybrid commingling CF/PA 6.6 yarn on the frame with the parameter as shown in Table 5-10. Vacuum is activated during the whole consolidation process. The parameter was adopted from the work of Hasan et al. [70], in which the hybrid yarn with the same composition (CF and PA 6.6) was used.

Table 5-10: Parameter of the COLLIN P300 PV laboratory press for the production of UD FRP according to Hasan [70]

Process step	1	2	3	4	5
Duration (s)	60	1740	600	600	1740
Temperature (°C)	30	320	320	320	30
Heating up and cooling down rate (K/min)	-	10	-	-	10
Pressure (MPa)	0.03	0.5	0.5	7.3	7.3

BWKF CF/PA 2-layer V1 is used for the thermo-pressing process to produce FRP coupon test specimen. This variant has a symmetric lay-up of $[(0^\circ/90^\circ)_2]_s$, and for the convenience, it is named FRP-C0. The FRP plate has thermo-pressed with the parameters as shown in Table 5-11. Vacuum is also used here. The specimen have a thickness about 2.48 mm.

Table 5-11: Parameter for FRP test specimen production from BWKF CF/PA 2-layer V1 according to D. Rabe

Process step	1	2	3	4	5
Duration (s)	60	1800	600	900	1900
Temperature (°C)	30	330	330	330	30
Heating up and cooling down rate (K/min)	-	10	-	-	10
Pressure (MPa)	10	10	10	155	155

The consolidation with T-cup thin-walled thermoplastic FRP is carried out with the consolidation tools that developed in framework of the research project AMARETO. The consolidation tools has been firstly developed and tested on the laboratory press (RUCKS Maschinenbau GmbH, Germany) at ILK, TU Dresden as shown in Figure 5-20. The T cup forming tools is after that installed on the COLLIN P300 PV laboratory press at ITM and used to produced T-cup thin-walled part, as demonstrator for the project AMARETO with BWKF CF/PA 2-layer V1. The process parameter is as shown in Figure 5-21. The successfully produced part is shown in Figure 5-22, which has an average thickness about 0.62 mm.

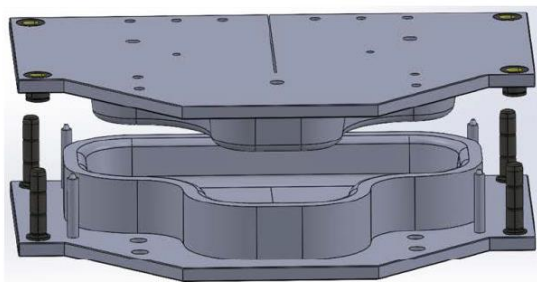


Figure 5-20: CAD model of T-cup shell-like forming tools and the installation of the developed tools on a RUCKS laboratory press at ILK © D. Weck

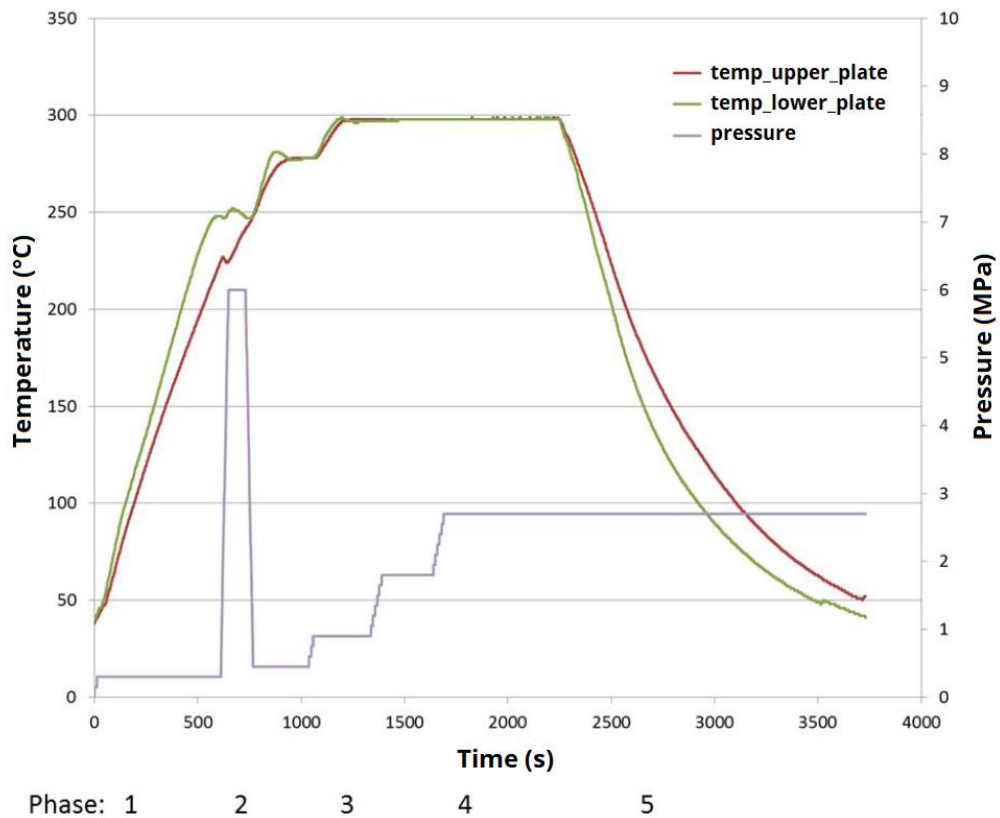


Figure 5-21: Parameter for thermo-pressing of T cup thin-walled composite part on the COLLIN P300 PV laboratory press © D. Weck

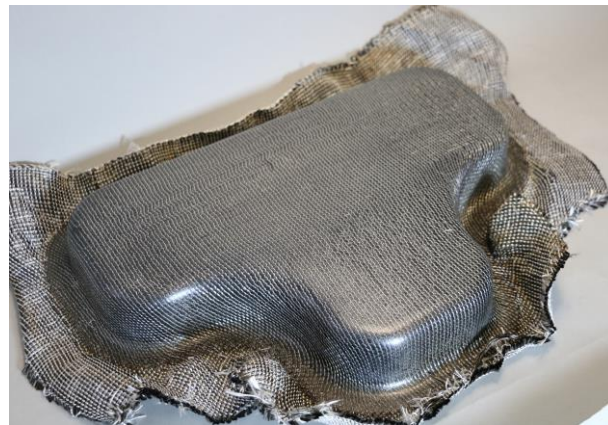


Figure 5-22: T cup thin-walled composite part produced from BWKF CF/PA 2-layer V1

Resin-infusion

Three variants of BWKF were chosen for manufacturing and testing: BWKF GF 2-layer (0°/90°), a BWKF GF 4-layer asymmetric (0°/90°/0°/90°), and an integral 4-layer BWKF (see Figure 5-2). The BWKF GF 2-layer and the BWKF GF 4-layer asymmetric are used for textile physical tests and production of FRP specimens for coupon level tests. Those FRP

specimens are manufactured with three configurations of 2- and 4-layer fabrics, FRP-C1, FRP-C2, and FRP-C3, as shown in Table 5-13. The integral 4-layer BWKF is used as preform for T-shaped FRP samples only.

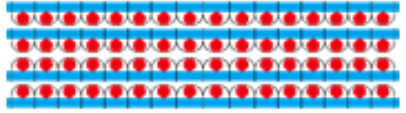
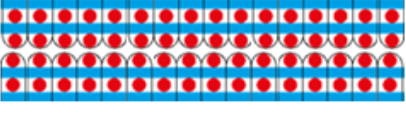
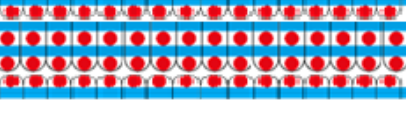
A vacuum assisted resin transfer molding (VARTM) process is carried out for the consolidation of the coupon level FRP samples, which exhibit a flat shape. A mixture of RIMR 135 epoxy resin and RIMH 137 hardener of Hexion Specialty Chemicals (Stuttgart, Germany) is used as the reaction resin. Table 5-12 provides the material properties of the unreinforced epoxy matrix as given by the producer.

Table 5-12: Material properties of unreinforced epoxy matrix given by Hexion Specialty Chemicals

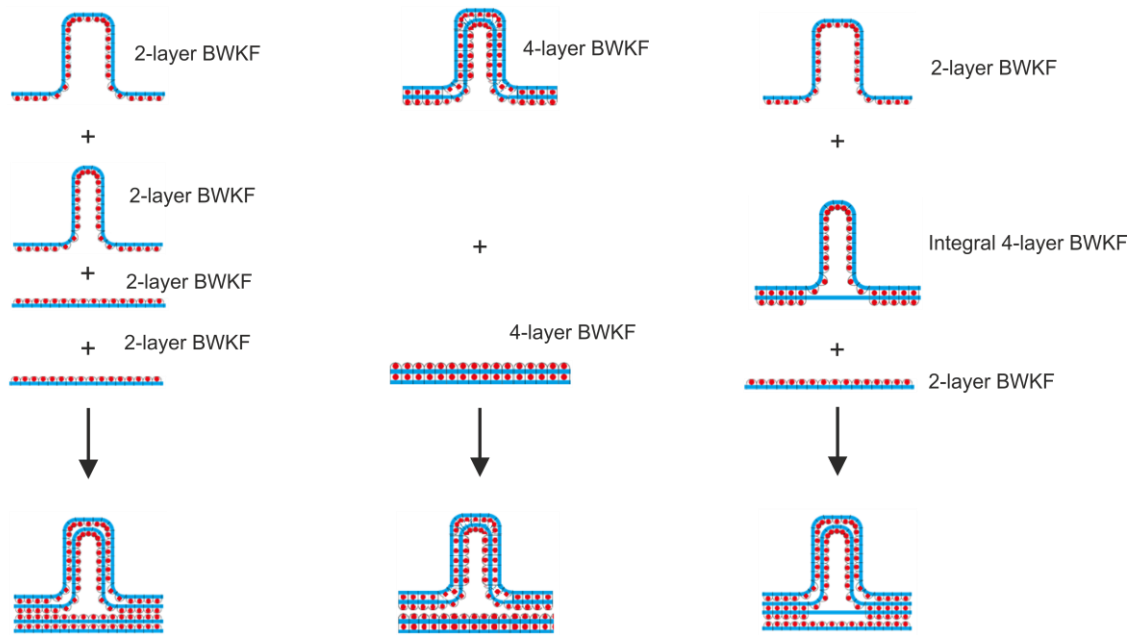
Density (g/cm ³)	Young's modulus (GPa)	Tensile strength (MPa)	Compressive strength (MPa)	Break elongation (%)
1.18 - 1.20	2.7-3.2	60-75	80-90	5.0-10.0

The VARTM process is one of the modifications of the resin transfer molding (RTM) process. In the original RTM process, the textile semi-finished products are impregnated by injecting the reactive resin under pressure. In the VARTM process, air is additionally evacuated at the risers before the reaction resin is injected. This can facilitate the injection of the reactive resin from the gate through the textile preform to the risers. Before positioning the textile reinforcement, the plate mold is cleaned with acetone and applied with release agent (Loctite 700NC) to facilitate demolding. The textile reinforcements are then carefully inserted into the plate mold and the two mold halves are closed. The reaction resin is then injected under pressure (maximum 6 bar) while the mold is heated. After the composites have cured under a pressure of 6 bar, the produced composites are finally demolded. Before testing, the produced composites are post-cured at 80°C for 15 hours. This allows the reaction resin to be fully crosslinked to achieve its maximum strength.

Table 5-13: Configuration of FRP samples for composite characterisation on coupon level made from BWKF GF

Variant	Configuration	Cross-section along warp direction
FRP-C1	4 x 2-layer with the symmetric lay-up of $[(0^\circ/90^\circ)_2]_s$	
FRP-C2	2 x 4-layer with the symmetric lay-up of $[(0^\circ/90^\circ/0^\circ/90^\circ)]_s$	
FRP-C3	2-layer/4-layer/2-layer with the lay-up of $[(0^\circ/90^\circ)(90^\circ/0^\circ/90^\circ/0^\circ)(90^\circ/0^\circ)]$	

The T-shaped rib-stiffened FRP are produced with vacuum assisted resin infusion (VARI) process based on the BWKF preforms with three different preform constructions as shown in Figure 5-23. In contrast to VARTM, VARI uses one mould half and vacuum bag instead of two mould halves. For the consolidation of T-shaped FRP, additional aluminium profiles are necessary. The infusion setup with the aluminium profiles and vacuum bag is shown in Figure 5-24. Table 5-14 gives the dimensions of the T-shaped FRP specimens for bending tests. The variants of rib-stiffened FRP are named after their length L and rib height H, e.g., T300-33 has a length of 300 mm and a rib height of 33 mm. Any variant in Table 5-14 can be produced from BWKF with one of the three constructions presented in Figure 5-23. Three different constructions are established for the T-shaped samples: 4 by BWKF GF 2-layer (named FRP-T1), 2 by BWKF GF 4-layer (FRP-T2), and an BWKF GF integral 4-layer with a BWKF GF 2-layer on each side (FRP-T3). To reduce the quantity of specimens, a systematic testing plan for T-shaped FRP is used as shown in Table 5-15. While other dimensions meet the nominate design requirements, the rib height H varies across different specimens. Especially the rib height of variant T120-33 with a 4 x 2-layer BWKF setup is 38.4 mm in average.

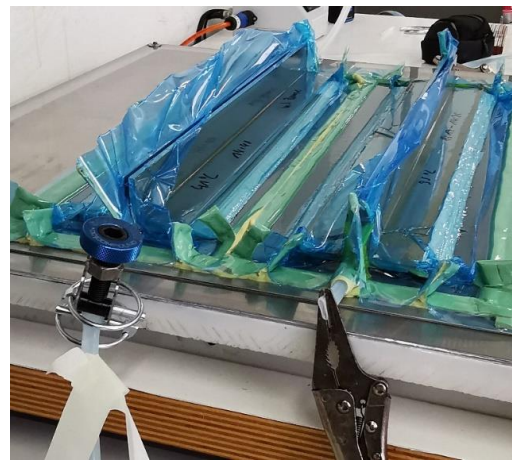


(a) Hand lay-up with 4x of 2-layer BWKF (b) Hand lay-up with 2x of 4-layer BWKF (c) Hand lay-up with integral BWKF

Figure 5-23: Construction of 8-layer BWKF preforms for T-shaped FRP: (a) with 4 x 2-layer BWKF (FRP-T1), (b) with 2 x 4-layer BWKF (FRP-T2) and (c) with integral layer (FRP-T3)

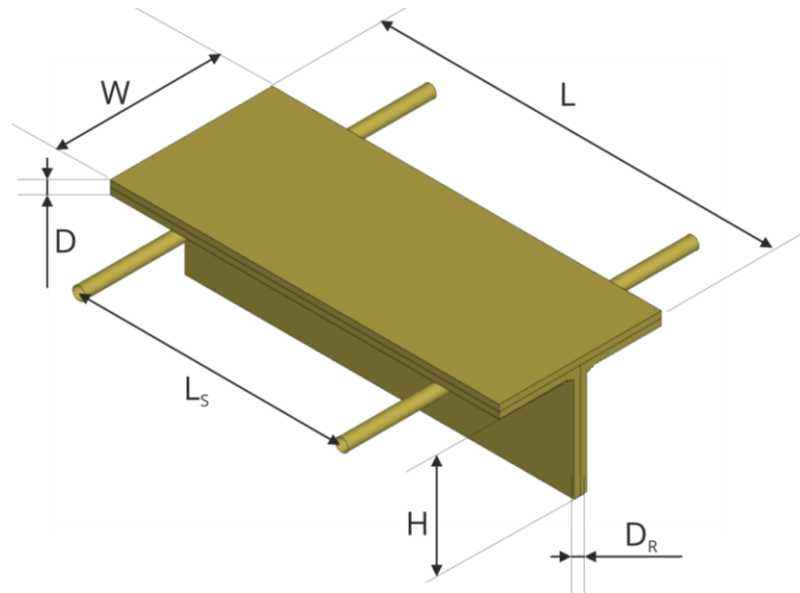


Aluminium profiles



Vacuum bag setup

Figure 5-24: Production of T-shaped FRP samples with VARI process

Table 5-14: Nominal dimensions of T-shaped FRP samples for structural bending tests

Variant	Length L (mm)	Support length L _s (mm)	Width W (mm)	Flange thickness D (mm)	Rib height H (mm)	Rib thickness D _R (mm)
T120-0	120	90	50	4	0	0
T120-33	120	90	50	4	33	4
T300-33	300	225	50	4	33	4
T400-33	400	300	50	4	33	4

Table 5-15: Quantity of produced T-shaped FRP samples per variant and per construction, in parentheses: average of actual rib height H in mm

Variant/Construction	FRP-T1	FRP-T2	FRP-T3
T120-0	3 (0)	0	3 (0)
T120-33	6 (38.4)	6 (31.6)	6 (32.9)
T300-33	2 (32.1)	0	0
T400-33	3 (32.1)	0	0

5.4.2 Fiber volume content

Test methods

The fiber volume content of FRP of selected textile material are determined according the method A of the standard DIN EN ISO 3451-1. The test specimen is burned inside a muffle

furnace Controller B170 (Nabertherm GmbH, Germany) at a temperature of max. 450° for 1 hour. The fiber volume content is calculated with described procedure (in section 2.7.4), and shown in Table 5-16. For the calculation of fiber volume content for BWKF CF/PA, the GF portion in stitching yarn is neglected.

Table 5-16: Fiber volume content of FRP of selected textile material

Specimen	Fiber volume content (%)
FRP-UD3.5	58.7
FRP-C0 (BWKF CF/PA 2-layer V1)	56.0
FRP-C1 (BWKF GF 2-layer)	47.0
FRP-C2 (BWKF GF 4-layer)	42.6
FRP-C3 (BWKF GF 2-layer/4-layer/2-layer)	43.4
FRP-T1	55.4
FRP-T2	55.9
FRP-T3	56.3

5.4.3 Tensile test of FRP

Test method

Tensile test of coupon level FRP specimens are carried according to the standard DIN EN ISO 527-4, as shown in Figure 5-25. The clamp length is 150 mm and the test is carried out at the velocity of 2 mm/min. The max pressure of clamp is 45 bar. Strain of FRP specimens in tensile tests is measured by an optical extensometer. Specimen dimensions (average value in format width x length x thickness) are 14.5 x 250 x 1.16 mm³ for FRP-UD, 25 x 250 x 2.5 mm³ for the thermoplastic FRP-C0 and 25 x 250 x 3.2 mm³ for the thermoset from FRP-C1 to C3. Before tested, the specimens are stored under normalized climate condition at 23°C room temperature and relative humidity of 50% for at least 24 hours according to DIN EN ISO 291.

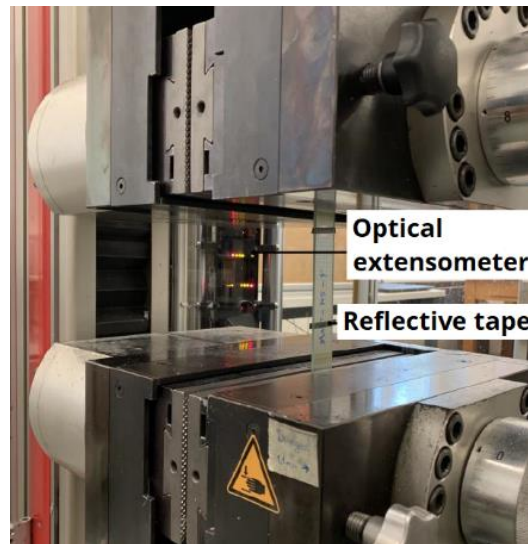


Figure 5-25: Tensile test of FRP coupon specimens on Zwick Z100 tensile machine

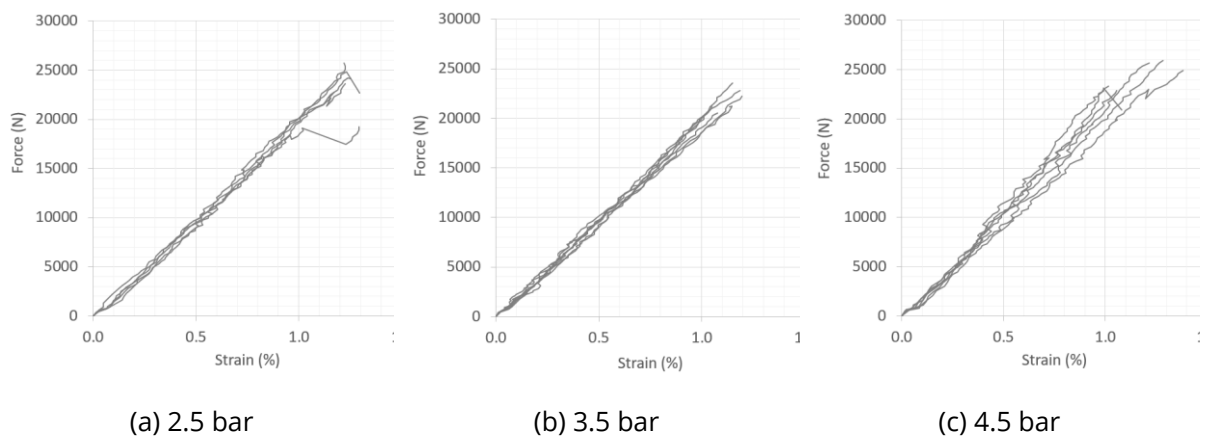
Test results

A summary of the test results of tensile test is shown in Table 5-17. The Young's modulus of FRP-UD is measured between the strain of 0.05-0.15%, and of FRP-C0, -C1, -C2, and -C3 0.05-0.25 %. The force-strain curves are shown in Figure 5-26 (FRP-UD), Figure 5-27 (thermoplastic FRP-C0) and Figure 5-28 (thermoset FRP-C1, -C2, -C3). While the force-strain curve of FRP-UD3.5 and thermoset FRP-C1, -C2, -C3 show linear tensile behavior, the thermoplastic FRP-C0 curves show strong non-linear behavior, especially from the area after 0.5 % strain.

The tensile strength and Young's modulus of FRP-UD3.5 made from hybrid yarn produced at 3.5 bar air pressure is not the highest in three variants but it shows smallest deviation, which indicates that the process at this parameter is stable and the produced hybrid commingling yarn is expected to be uniformly under such condition. On this reason, the air pressure of 3.5 bar is chosen for the production of hybrid commingling CF/PA 6.6 yarn in the project AMARETO.

Table 5-17: FRP characterization results as mean value (standard deviation)

Variant	Young's modulus (GPa)		Tensile strength (MPa)		Elongation at break (%)	
	Warp	Weft	Warp	Weft	Warp	Weft
FRP-UD	in 0° direction					
FRP-UD2.5	118 (26)		1384 (141)		1.2 (0.04)	
FRP-UD3.5	113 (15)		1308 (62)		1.1 (0.07)	
FRP-UD4.5	113 (21)		1334 (69)		1.2 (0.16)	
BWKF FRP	Warp	Weft	Warp	Weft	Warp	Weft
FRP-C0	29.8 (2.4)	26.1 (2.7)	221 (12)	212 (14)	1.4 (0.1)	1.5 (0.2)
FRP-C1	17.2 (2.3)	19.8 (2.4)	297 (17)	352 (11)	2.3 (0.1)	2.2 (0.1)
FRP-C2	17.8 (1.8)	17.9 (1.4)	322 (13)	324 (17)	2.3 (0.2)	2.2 (0.1)
FRP-C3	17.6 (1.2)	16.9 (1.4)	347 (14)	340 (13)	2.3 (0.4)	2.5 (0.3)

**Figure 5-26: Force-strain curves of tensile test for UD FRP made from hybrid commingling yarn CF/PA 6.6 under different air pressure**

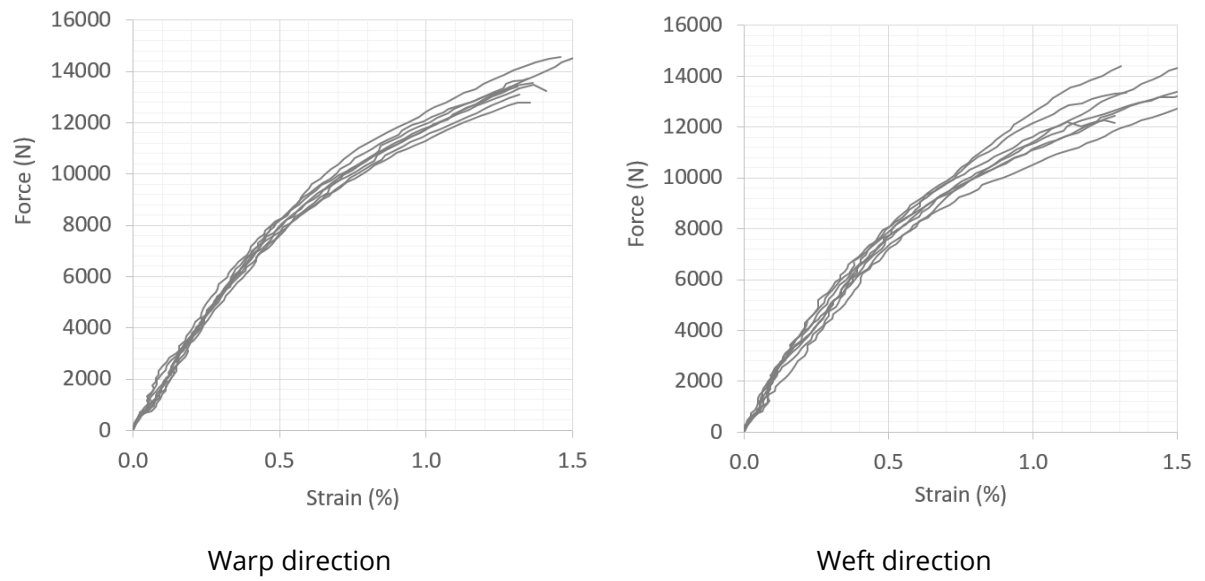
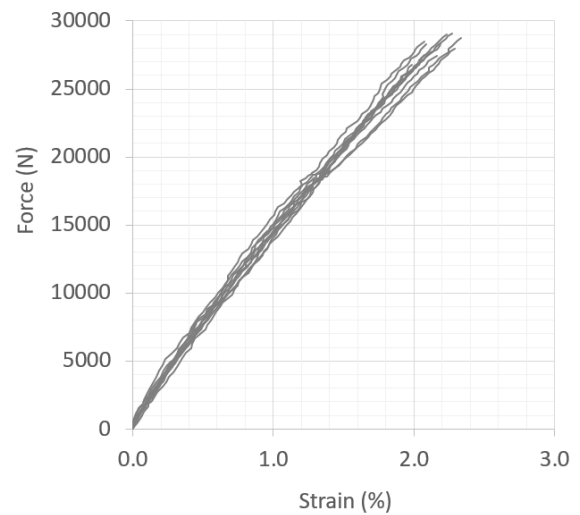
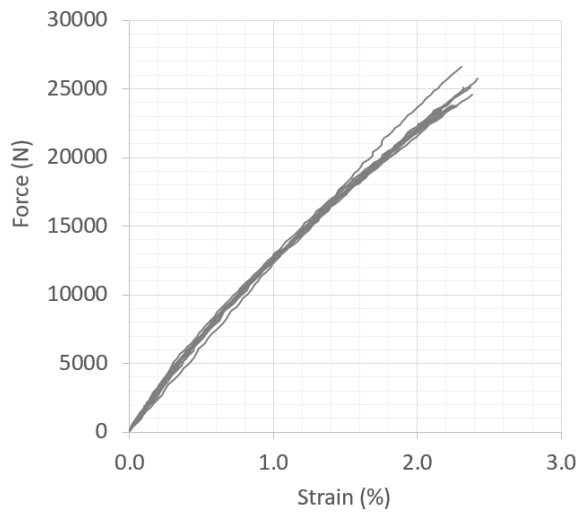
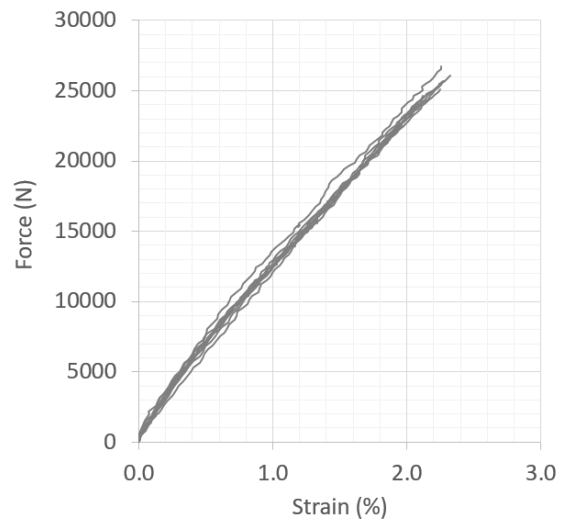
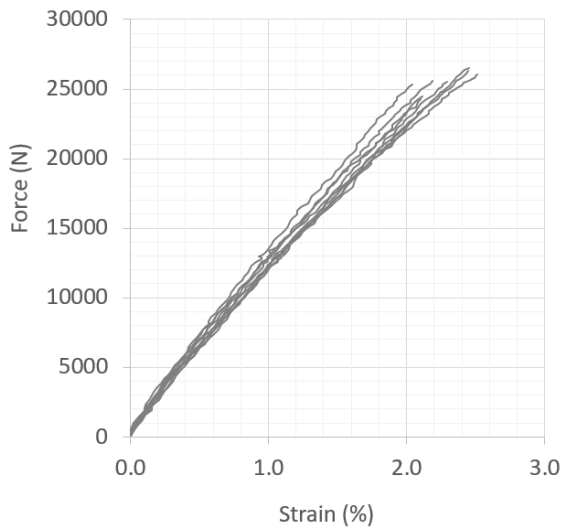


Figure 5-27: Force-strain curves of tensile test for FRP-C0



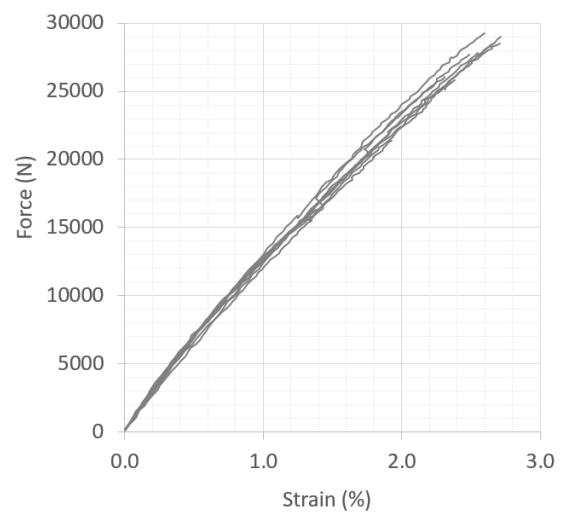
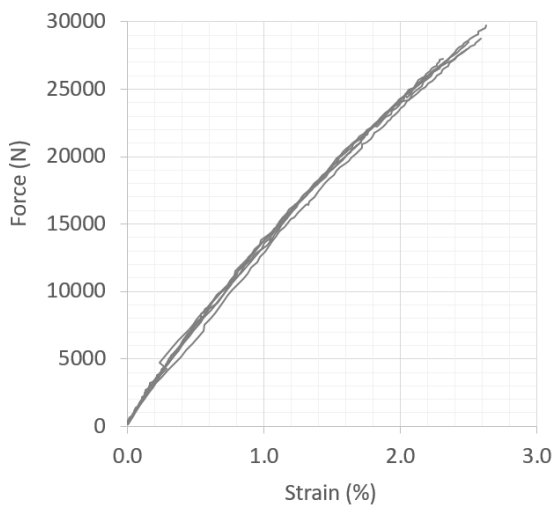
BWKF GF 2-layer (FRP-C1) warp direction

BWKF GF 2-layer (FRP-C1) weft direction



BWKF GF 4-layer (FRP-C2) warp direction

BWKF GF 4-layer (FRP-C2) weft direction



BWKF GF 2/4/2-layer (FRP-C3) warp direction

BWKF GF 2/4/2-layer (FRP-C3) weft direction

Figure 5-28: Force-strain curves of tensile test for FRP made of BWKF GF

5.4.4 Four-point bending test of FRP

Test method

The four-point bending test of FRP is carried out according to DIN EN ISO 14125 – Method B (Figure 5-29). The support width is 66 mm for FRP-C0 and 45 mm for FRP-C1,-C2 and – C3. The distance between two pressing point of stamp is 22 mm. The test velocity is 2 mm/min. The dimension of test specimens are 10 mm x 60 mm x 2.5 mm (FRP-C0) and 15 mm x 60 mm x 3.2 mm (FRP-C1,-C2 and –C3). The bending Young’s modulus is calculated between 0.34-1.5 mm deformation.



Figure 5-29: Four-point bending test of FRP coupon specimens on Zwick Z100 tensile machine

Test results

A summary of four-point bending test results of FRP is shown in Table 5-18. The force-deformation curves are shown in Figure 5-30 (FRP-C0) and Figure 5-31 (FRP-C1,-C2 and – C3).

Table 5-18: Four-point bending test results of FRP

BWKF FRP	Bending Young’s modulus (GPa)		Bending strength (MPa)	
	Warp	Weft	Warp	Weft
FRP-C0	31.0 (4.1)	15.9 (0.8)	259 (26)	200 (10)
FRP-C1	14.2 (0.5)	11.1 (0.5)	278 (16)	173 (20)
FRP-C2	17.5 (0.6)	13.0 (0.5)	385 (26)	390 (15)
FRP-C3	18.2 (0.5)	12.9 (0.3)	356 (28)	277 (21)

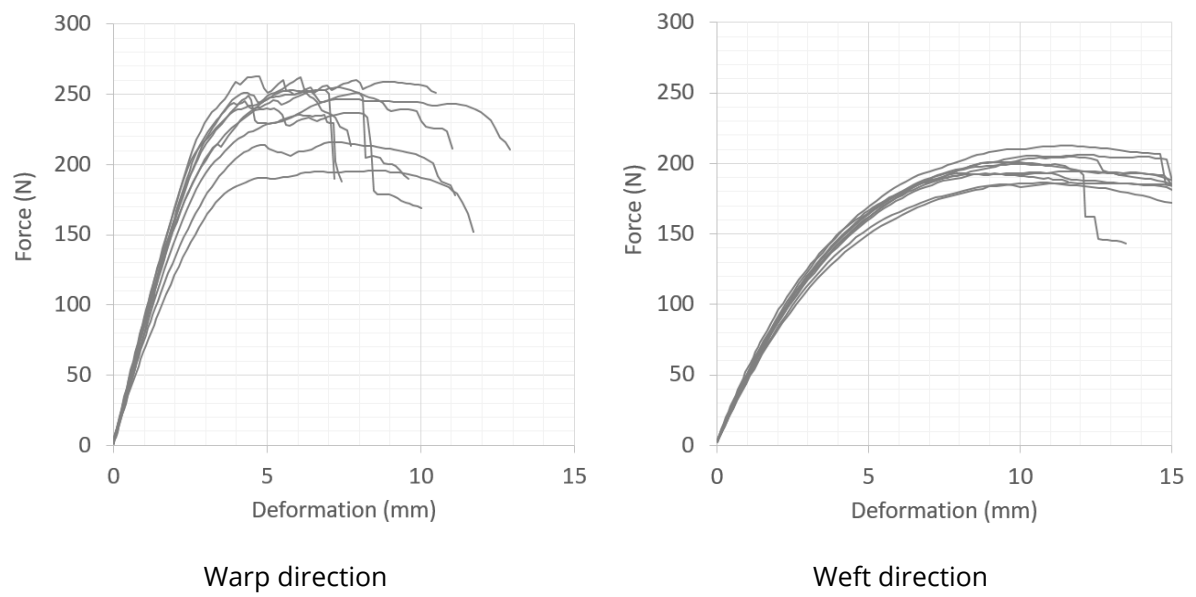


Figure 5-30: Force-deformation curves of four-point bending test for FRP-C0

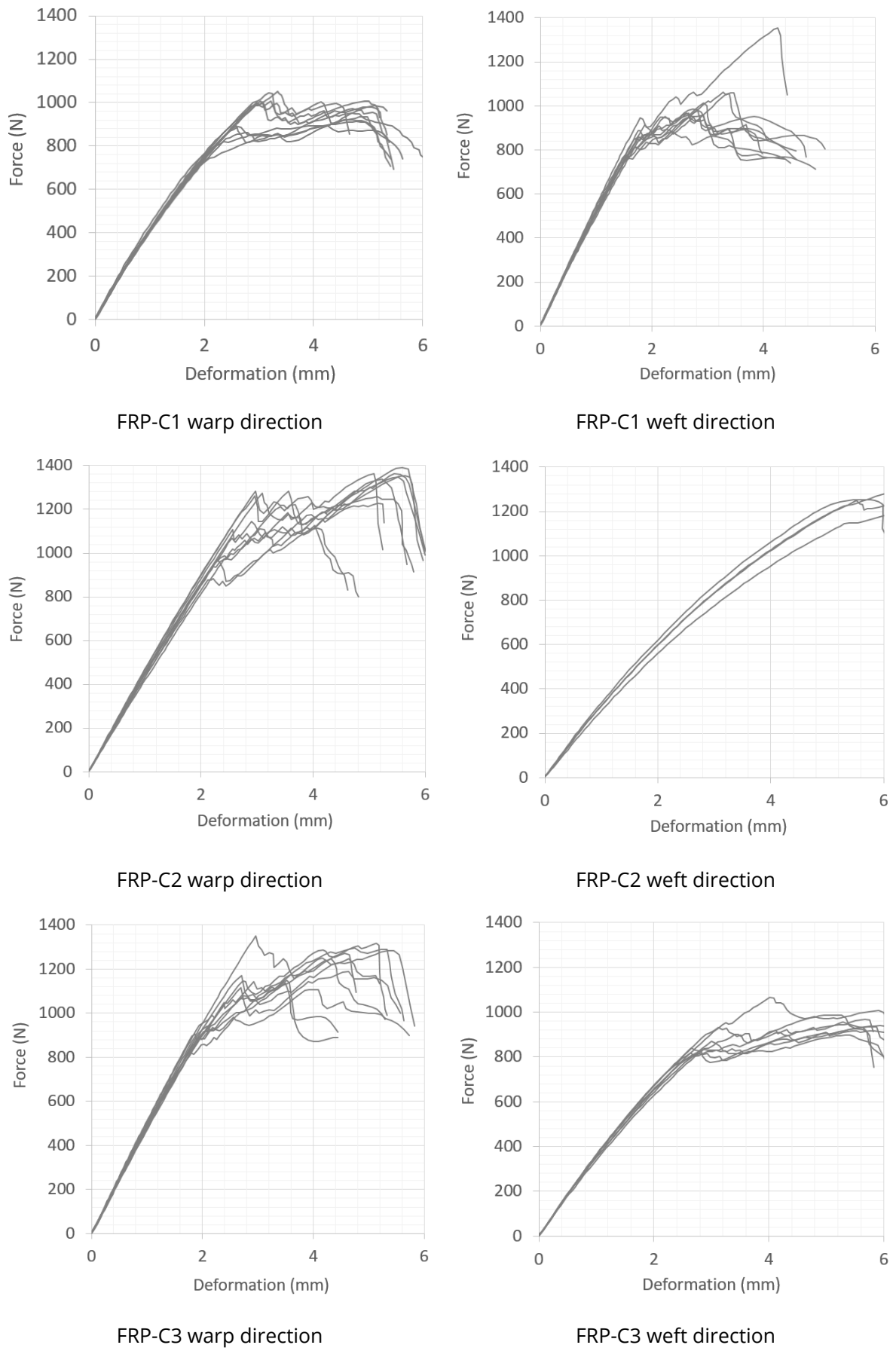


Figure 5-31: Force-deformation curves of four-point bending test for FRP-C1, -C2 and -C3

5.4.5 Interlaminar shear strength (ILSS)

Test method

The interlaminar shear strength test ILSS is carried out according to the standard EN ISO 14130. The test data of ILSS is necessary for the modelling of T-shaped FRP, so that only BWKF FRP GF (including three variants FRP-C1, -C2 and C3) are tested. The dimension of the test specimen is 15 x 30 x 3.2 mm³. Specimens cut in both warp and weft direction are tested. As the support length in ILSS test (15 mm) is significantly shorter than in four-point bending test (45 mm), failure of FRP specimen due to shear stress is expected (Figure 5-32). The radius of the stamp is 5 mm and of the bearing is 2 mm. The test is carried out at the velocity of 1 mm/min. The ILSS is calculated from force-deformation curve according to the formula given by the standard EN ISO 14130:

$$\tau = \frac{3}{4} \times \frac{F}{b \cdot h} \quad (5-7)$$

with τ (MPa) is the ILSS, F (N) is the max. force, b (mm) and h (mm) are width and thickness of the specimen, respectively.

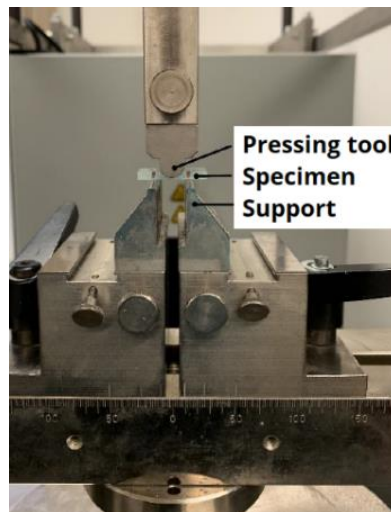


Figure 5-32: ILSS test of FRP coupon specimens on a Zwick Zmart.Pro tensile machine

Test results

A summary of the ILSS test results for FRP-C1, -C2 and -C3 is shown in Table 5-19. The force-deformation curves are shown in Figure 5-33.

Table 5-19: ILSS test results for FRP-C1, -C2 and -C3

	ILSS (MPa)	
	Warp	Weft
FRP-C1	31.5 (1.3)	31.5 (1.6)
FRP-C2	32.5 (3.5)	30.9 (1.3)
FRP-C3	48.1 (11.9)	31.8 (0.7)

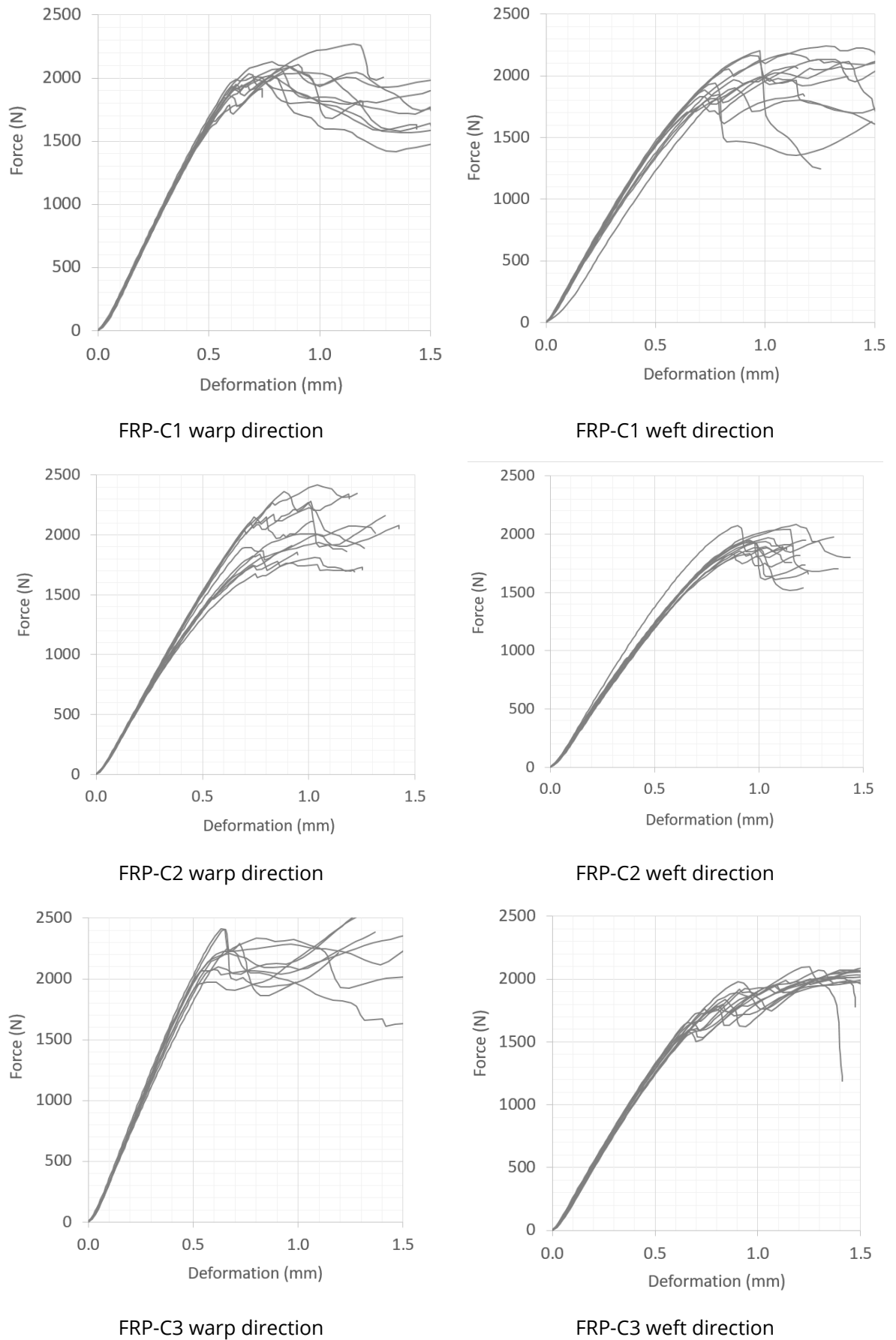


Figure 5-33: Force-deformation curves of ILSS test for FRP-C1, -C2 and -C3

5.4.6 Three-point bending test of T-shaped FRP

Test method

To evaluate the structural stiffness and strength of T-shaped FRP specimens under bending load, 3-point bending tests according to DIN 14125 (method A) are conducted while special support and pressing tool are used (Figure 5-34). Different support lengths are applied for the specimens with different lengths according to Table 5-14. The fiber volume content of the T-shaped FRP samples is also tested according to DIN 1172 and presented in Table 5-16.



Figure 5-34: Three-point bending tests according to DIN 14125 (method A) of T shaped rib-stiffened FRP

Test results

The results of 3-point bending tests of T-shaped FRP samples are summarized in Table 5-20. The specimens with different rib-lengths undergo different failure modes under bending loading (Figure 5-35). Failure mode depends on the sample length. Short specimens ($L=120$ mm) with rib height of 33 mm fail due to delamination, which is initiated by break of matrix or debonding between matrix and fiber. At longer specimens ($L=300$ mm and 400 mm) with the same rib height of 33 mm, breakage of fibers in the center of the rib is dominant. The short specimens ($L=120$ mm) show no rib fail due to break of fibers on the tension side and matrix break on the tension and compression sides at the middle position. The force-strain curves are shown in Figure 5-36 (T120-0 no rib), Figure 5-37 (T120-33), Figure 5-38 (T300-33 and T400-33).

To compare the strength of FRP with different rib height (due to production), the max. F is standardised to a rib height of 33 mm. The standardised results in Table 7 reveal highest strength in FRP-T3 specimens for variant T120-33, which has an integral fabric in the center. In FRP-T1 configuration with different length (120 mm, 300 mm and 400 mm), the

standardised results show a clear decline of max. F with an increased support length in the bending test.

The crack opening in T120-33 specimen can be seen in Figure 14b. The crack is propagated in both flange and rib areas from the gusset, where the fiber volume is low.

Table 5-20: Test results of 3-point bending of T-shaped FRP samples as mean value (standard deviation), max. F is standardised to rib height of 33 mm

Variant	Construction	Max. F (N)	Standardised Max. F (N)	Deformation at max. F (mm)
T120-0	FRP-T1	976 (53)	-	10.0 (1.6)
	FRP-T3	835 (49)	-	11.0 (4.2)
T120-33	FRP-T1	11540 (575)	9917 (494)	2.9 (0.2)
	FRP-T2	9301 (431)	9713 (450)	3.3 (0.7)
	FRP-T3	10689 (1217)	10721 (1221)	3.9 (0.3)
T300-33	FRP-T1	9504 (881)	9770 (906)	6.1 (0.7)
T400-33	FRP-T1	7649 (940)	7863 (966)	8.4 (0.7)

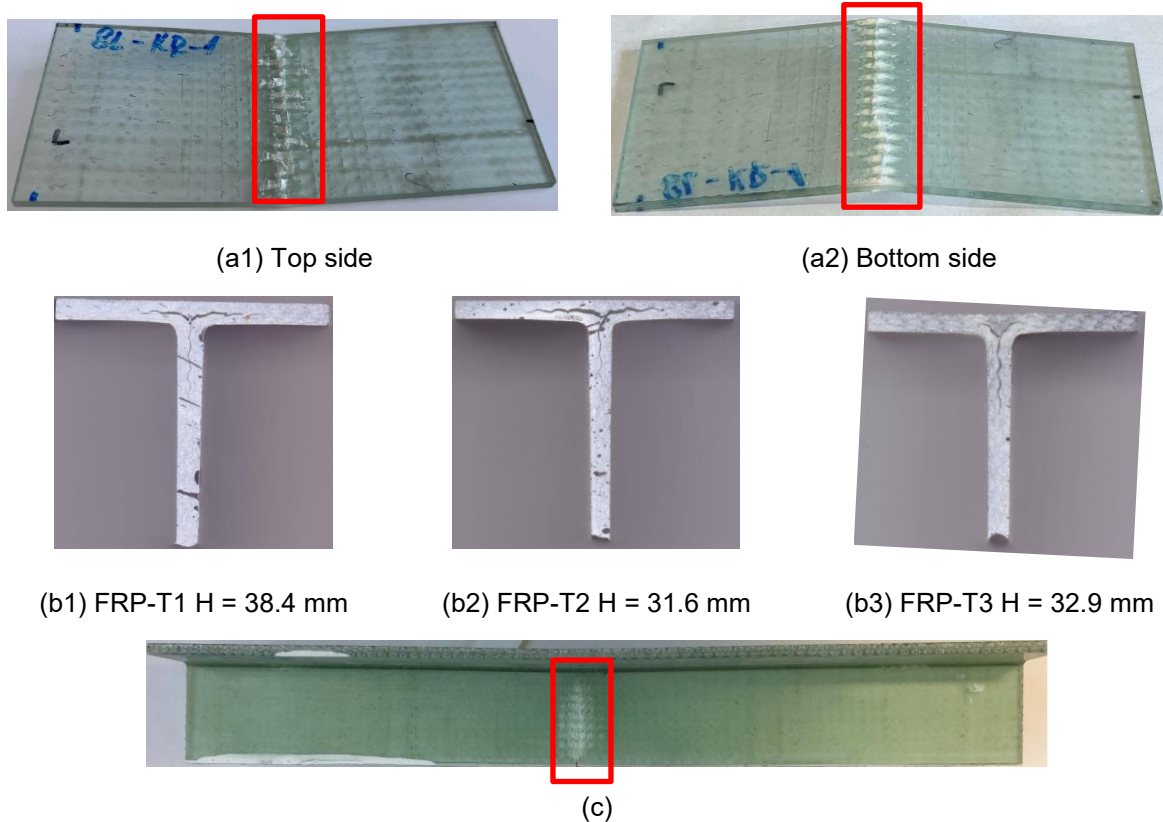
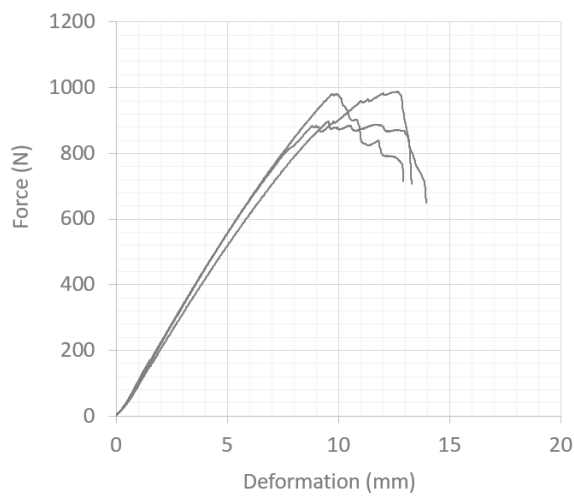
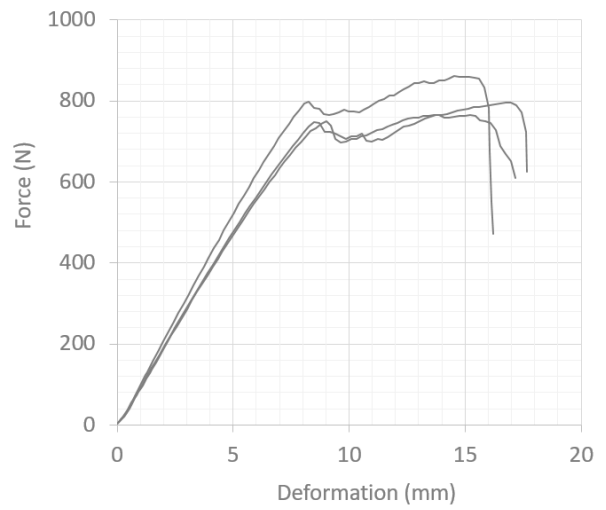


Figure 5-35: Failure modes of T-shaped FRP samples with different rib heights: a) variant T120-0, construction FRP-T1, b) T120-33 (3 variants), and c) T300-33, FRP-T1, H = 32.1 mm

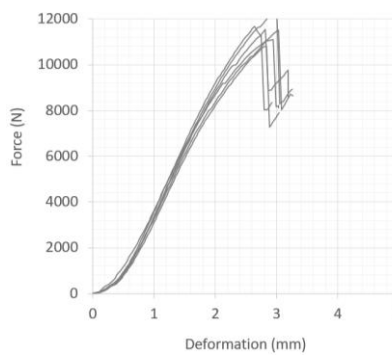


FRP-T1 (break of matrix and fiber)

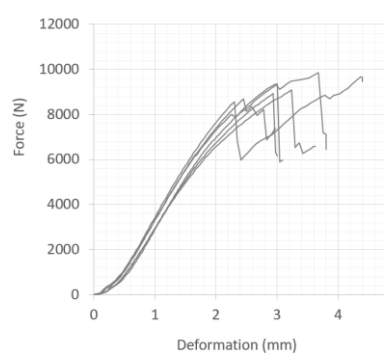


FRP-T3 (break of matrix and fiber)

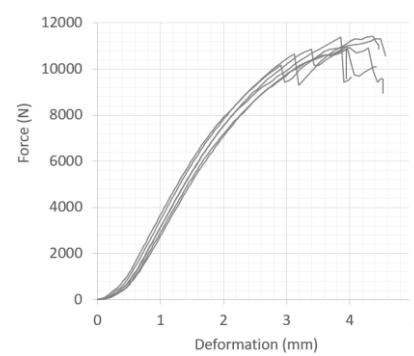
Figure 5-36: Force-deformation-curves from 3-point bending test of FRP T120-0 (no rib) with different construction of BWKF preforms



FRP-T1
(rib height $H = 38$ mm,
delamination failure)



FRP-T2
(rib height $H = 32$ mm,
delamination failure)



FRP-T3
(rib height $H = 33$ mm,
delamination failure)

Figure 5-37: Force-deformation curves from 3-point bending tests of FRP T120-33 with different constructions of the preforms

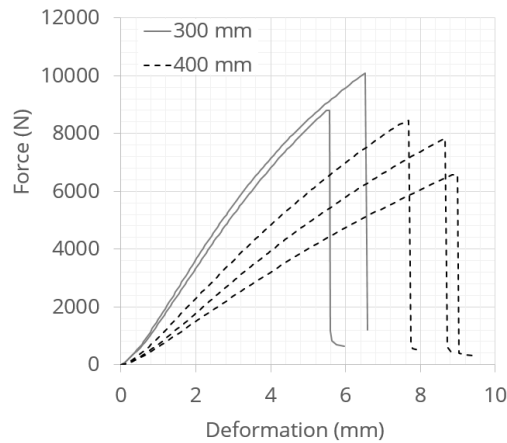


Figure 5-38: Force-deformation curves from three-point bending tests of long T-shaped FRP samples with 300 mm and 400 mm length, configuration FRP-T1 (rib height $H = 32$ mm, failure of yarn in rib)

5.5 Summary

The textile material as well as their FRP have been tested systematically from the fiber level to fabric. Based on the test results of commingling yarn as well as the FRP made of them under different air jet pressure, a reasonable value of air jet pressure has been selected for the production of all hybrid commingling yarn.

The textile material test results serve as input data for the development of textile numerical models as well as the validation in Chapter 5. Additionally, the test data also provide an insight on the different of textile behavior (tensile, bending, shear and friction) by different configuration (type of fabrics, yarn, quantity of layer), which can influence the forming behavior. The test data of FRP serve as input data for the development of FRP models and the validation in Chapter 7

6 Development and validation of BWKF models

As introduced in Chapter 4, the application of the models in this thesis focusses on forming simulations of flat textiles to 3D preforms. In this niche, analytical and kinematic models are not suitable because they lack the ability to describe the influence of external forces on the textile model. Kinematic models calculate the pure geometrical transformation between the 2D textiles and 3D preforms, where only the shear angle of the fabrics is predicted. The influence of force on the forming process is not considered and a constitutive behavior of textile material is not necessary. Kinematic models cannot ensure that a theoretically calculated solution is feasible in the practical forming process, where interaction with external forces plays an important role [104,158,511,512]. The FEM approach can overcome this problem. Three types of FEM models are introduced: macro-scale model, and two type of meso-scale models: model with beam elements and model with shell elements. The macro-scale model is based on the well established model of Döbrich et al. [166,285]. The model with beam element is based on the assumption that the cross-section of the yarn can be simplified as a circle, which is convenient for modelling purposes but can cause great deviation as the interaction between yarns cannot be described correctly. To overcome this problem, a further meso-scale model with shell elements is suggested, which provides an enhanced description for the cross-section of the yarns. The main challenge is to accurately model the geometry of the structure as well as assure the mechanical performance of the models. The modelling process, calibration and validation of each model are presented and compared accordingly. The explicit solver of LS-DYNA is used to carry out the simulations as the non-linear geometries and large deformation of the fabrics prevent the use of an implicit solver.

6.1 Macro-scale model

The macro model for textile in this thesis is based on continuum mechanics with the implementation of the model of Döbrich et al. [166,285] for the software LS-DYNA by the mean of MAT_USER_DEFINED_MATERIAL_MODELS via Fortran subroutine.

Material model development

Details of the material model development is based the on works of Döbrich et al. [166,285] as well as another implementation by Hübner [165]. Forming of fabrics often involves great (in case of single curved surface) to extreme (in case of doubly curved or free form surface) strain and rotation deformation of continuum elements. According to test results in Section 5.3, tensile and shear behavior of textiles are non-linear. Thus, an

accurate calculation of deformation requires an appropriate stress-strain description. The incremental form of the Equation (3-9) of motion then allows the stepwise consideration of material nonlinearities. The fabric is modelled in LS-DYNA using 4-node shell elements. For every step of calculation, with the help of Cauchy stress σ , not only the deformation of the 4-node shell element but also the translation of these four nodes are captured as shown in Figure 6-1. An arbitrary node "a" in the Figure 6-1 has the original coordinates $a = (x, y, z)$ at the time point $t = 0$ by initial position $a = a(\vec{X}, t = 0)$, and is transformed to the deformed position $a = a(\vec{x}, t)$ by the vector $\vec{u} = (u, v, w)$. Hence, the use of Green-Lagrangian strain tensor \mathbf{E} is advised, whereas the 2nd Piola-Kirchhoff stress tensor \mathbf{S} is energy conjugate to the Green-Lagrangian strain tensor \mathbf{E} [513]. The 2nd Piola-Kirchhoff stress tensor \mathbf{S} describes the relationship between forces in the reference configuration to areas in the reference configuration.

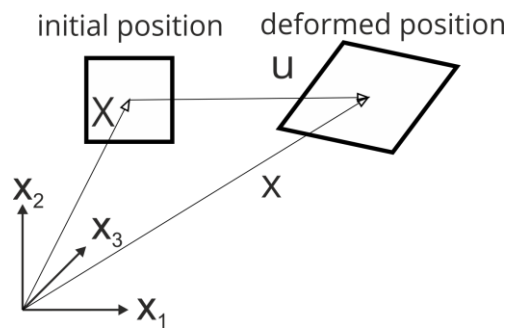


Figure 6-1: State of strain and translation of a 4-node shell element (adapted from [166])

The deformation gradient \mathbf{F} is then calculated by Equation (6-1). This equation allows describing the deformation independently from movement. It can also be used to determine the change of length (strain) any section of the line in the deformed position in comparison to the initial position, as well as the change of angle (rotation) of the lines to each other.

$$F_{ij} = \frac{\partial x_i}{\partial X_j} = \begin{bmatrix} \frac{\partial u}{\partial X} & \frac{\partial u}{\partial Y} & \frac{\partial u}{\partial Z} \\ \frac{\partial v}{\partial X} & \frac{\partial v}{\partial Y} & \frac{\partial v}{\partial Z} \\ \frac{\partial w}{\partial X} & \frac{\partial w}{\partial Y} & \frac{\partial w}{\partial Z} \end{bmatrix}; i, j = 1, 2, 3; F_{ij} = F_{ji} \quad (6-1)$$

The Green-Lagrangian strain tensor \mathbf{E} can describe the deformation with the help of the coordinates of the initial position. A variation is taken from [513], with the general form as shown in Equation (6-2).

$$E_{ij} = \frac{1}{2} \left(\frac{\partial u_i}{\partial x_j} + \frac{\partial u_j}{\partial x_i} + \sum_{k=1}^3 \frac{\partial u_k}{\partial x_i} \frac{\partial u_k}{\partial x_j} \right) \quad (6-2)$$

The Green-Lagrangian strain tensor \mathbf{E} can also be described by the deformation gradient \mathbf{F} as the Equation (6-3).

$$E_{ij} = \frac{1}{2} \cdot (F^T F - I) \quad (6-3)$$

with \mathbf{I} as the identity matrix. The 2nd Piola-Kirchhoff stress tensor \mathbf{S} is calculated through the Green-Lagrangian strain tensor \mathbf{E} and the material stiffness tensor \mathbf{C} according to [513] as Equation (6-4). The 2nd Piola-Kirchhoff stress tensor \mathbf{S} is symmetric and suitable for incremental consideration, which is necessary for the description of material nonlinearities.

$$S_{kl} = C_{klij} : E_{ij} \quad (6-4)$$

The Cauchy stress σ , which in practical use is more important than the 2nd Piola-Kirchhoff stress tensor \mathbf{S} , is calculated via deformation gradient \mathbf{F} and the 2nd Piola-Kirchhoff stress tensor \mathbf{S} as in Equation (6-5).

$$\sigma = \frac{1}{J} F \cdot S \cdot F^T \quad (6-5)$$

with $\mathbf{J} = \det \mathbf{F}$ (determinant of the deformation gradient \mathbf{F}). For textile structure with reinforcement in warp and weft direction such as plain-woven or BWKF, their mechanical behavior can be considered as orthotropic. In that case, the components of the material stiffness tensor \mathbf{C} can be calculated from the group of Equations (6-6), where the stiffness E_{ii} in the main spatial direction i , the shear stiffness G_{ij} , and the Poisson's ratio ν_{ij} are necessary and should be derived from test results in Section 5.3. For some textile structure such as NCF with reinforcement in $\pm 45^\circ$ direction, where the shear behavior is asymmetric [373], the value of G_{12} can be divided into two separated direction dependent shear modulus (positive and negative shear). This has been already implemented in the subroutine Fortran code.

$$\begin{aligned}
C_{1111} &= (1 - \nu_{23}\nu_{32}) \cdot E_{11} \cdot D^{-1} \\
C_{2222} &= (1 - \nu_{31}\nu_{13}) \cdot E_{22} \cdot D^{-1} \\
C_{3333} &= (1 - \nu_{21}\nu_{12}) \cdot E_{33} \cdot D^{-1} \\
C_{1122} &= (\nu_{12} + \nu_{32}\nu_{13}) \cdot E_{22} \cdot D^{-1} \\
C_{2233} &= (\nu_{23} + \nu_{21}\nu_{13}) \cdot E_{33} \cdot D^{-1} \\
C_{1133} &= C_{3311} = (\nu_{13} + \nu_{12}\nu_{23}) \cdot E_{22} \cdot D^{-1} \\
C_{1212} &= G_{12} \\
C_{2323} &= G_{23} \\
C_{3131} &= G_{31}
\end{aligned} \tag{6-6}$$

$$D = 1 - \nu_{12}\nu_{21} - \nu_{23}\nu_{32} - \nu_{31}\nu_{13} - 2\nu_{21}\nu_{13}\nu_{32}$$

$$\nu_{21} = \frac{E_{22}}{E_{11}} \cdot \nu_{12}$$

$$\nu_{32} = \frac{E_{33}}{E_{22}} \cdot \nu_{23}$$

$$\nu_{13} = \frac{E_{11}}{E_{33}} \cdot \nu_{31}$$

On basis of the test results in Section 5.3 , the following macroscopic characteristics of textiles can be determined:

- tensile behavior: direction dependent tensile force – strain curves $F_x(\epsilon_x)$ and $F_y(\epsilon_y)$, which can be converted to elasticity modulus – strain curves $E_x(\epsilon_x)$ and $E_y(\epsilon_y)$
- in-plane shear behavior: shear force – shear angle curves $F_{Sxy}(\varphi_{xy})$, which can be converted to shear modulus – shear strain curves $G_{xy}(\tan(\varphi_{xy}))$ for symmetric shear behavior, or positive- and negative shear curves for asymmetric shear behavior
- bending behavior: B_{x-top} , $B_{x-bottom}$, B_{y-top} , $B_{y-bottom}$ in case of fabrics with side dependent bending stiffness, otherwise just B_x and B_y for side independent bending stiffness

With the described material model, most of the important mechanical behaviors of textile can be correctly simulated, including the non-linearity of tensile and shear behavior. However, the bending behavior needs one extra procedure, so that the bending stiffness can be correctly described.

Laminate formulation for correct bending behavior

The bending stiffness of textile is generally low in comparison to the value calculated through tensile elasticity modulus and moment of inertia as shown in Equation (3-12). For application such as airbag simulation, the bending stiffness can just be ignored by using membrane element (see Table 3-2). But it has been proven, that the bending stiffness should be taken into account for forming simulation, as neglecting it would limit the ability of numerical model by predicting wrinkle formation significantly [509].

Different approaches have been suggested as reviewed in Section 3.3. In this thesis, the decoupling bending and tensile behavior by laminate formulation [165,166,285] is applied. The advantage of this method is that the bending behavior can be correctly described, without changing any parameters of tensile and shear behavior in model. In the laminate formulation approach, textile is modelled with multiple integration layers of different thickness as shown in Figure 6-2 (demonstration for the case of three layers).

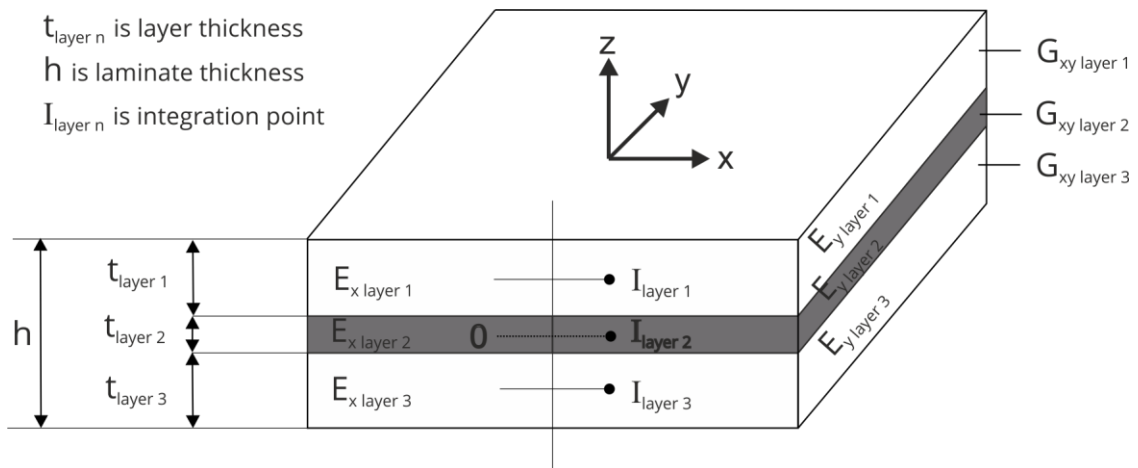


Figure 6-2: Example of a laminate design with three integration layers (adapted from [285])

Every integration layer in Figure 6-2 has its own independent set of parameters for tensile behavior in warp and weft direction ($E_{x \text{ layer } n}$) as well as in-plane shear behavior ($G_{xy \text{ layer } n}$). Each integration layer has a thickness $t_{\text{layer } n}$, where the total thickness of all integration layers is equal to laminate thickness. $\lambda_{\text{layer } n}$ is the fraction of the thickness of layer n in the whole laminate.

$$h = \sum t_{\text{layer } n} \quad (6-7)$$

$$\lambda_{\text{layer } n} = \frac{t_{\text{layer } n}}{h} \quad (6-8)$$

The integration point $l_{layer\ n}$ is positioned at the middle of the layer. $z_{layer\ n}$ is the distance from the exterior of the integration layer to the laminate neutral plane. The bending stiffness of an integration layer can be calculated according to Kirchhoff theory [382] and the difference energy method [514]. The bending stiffness of the whole laminate is calculated by Equation (6-9) [166], which can be applied separately for x- and y-direction in combination with the orthotropic material law.

$$B_{laminat e} = \int_{-\frac{h}{2}}^{\frac{h}{2}} E \cdot z^2 dz = \frac{1}{3} \sum E_{layer\ n} \cdot (z_{layer\ n}^3 - z_{layer\ n-1}^3) \quad (6-9)$$

The tensile stiffness (of each x- or y-direction) and the in-plane shear stiffness of the laminate are calculated according to rule of mixtures [379,380] as shown in Equation (6-10) and (6-11), respectively.

$$E_{laminat e} = \sum E_{layer\ n} \cdot \lambda_{layer\ n} \quad (6-10)$$

$$G_{xy\ laminat e} = \sum G_{xy\ layer\ n} \cdot \lambda_{layer\ n} \quad (6-11)$$

For a correct description of the bending behavior of the textile, it is necessary to determine suitable parameter of several integration layers of the laminate. Namely, the group of Equation (6-9), (6-10) and (6-11) is needed to be solved for each integration layer so that the laminate characteristics can meet all the requirements of the measured elasticity modulus – strain curves $E_x(\epsilon_x)$ and $E_y(\epsilon_y)$, shear modulus – shear strain curves $G_{xy}(\tan(\varphi_{xy}))$, as well as the bending stiffness $B_{x\ top}$, $B_{x\ bottom}$, $B_{y\ top}$, $B_{y\ bottom}$ at the same time.

For simple side independent bending stiffness, where only the bending stiffness of each direction B_x and B_y need to be met, the elasticity modulus $E_{layer\ n}$ and thickness $t_{layer\ n}$ should be found. For the complicated side dependent bending stiffness, a correct description of all four engineering constant bending stiffness $B_{x\ top}$, $B_{x\ bottom}$, $B_{y\ top}$, $B_{y\ bottom}$, the elasticity modulus $E_{layer\ n}$ of outer layer (such as layer 1 and layer 3 in case of three layer) must be divided into tension elasticity modulus and compression elasticity modulus [285].

However, the group of Equation (6-9), (6-10) and (6-11) still needs some assumptions to become solvable, as the quantity of unknown variable is greater than the quantity of equation. Döbrich recommended to use same value of tension elasticity modulus for symmetrical outer integral layers ($E_{layer\ 1} = E_{layer\ 3}$ in case of three layers) to avoid areal distortion under tension loading, as bi-moments occur. He also recommended to use the

same thickness for the symmetrical outer layers ($t_{layer\ 1} = t_{layer\ 3}$ in case of three integration layers). An important assumption is that, the thickness of the middle layer ($t_{layer\ 2}$ in case of three layers) is far smaller in comparison to the outer layers. Consequently, the elasticity modulus of the middle layer ($E_{layer\ 2}$ in case of three layer) must be significantly greater than in other layers, so that the laminate stiffness according to Equation (6-10) is mostly dependent on this elasticity of the middle layer. Thus, the elasticity modulus of other layers can now be chosen freely to meet the requirement of laminate bending stiffness in Equation (6-9), without changing the tensile stiffness of the laminate. This closed-form solution is accompanied by the listed assumptions.

Once all parameters are found, the calculating procedure of the Fortran subroutine for MAT_USER_DEFINED_MATERIAL_MODELS is carried out. LS-DYNA is a commercial FEM software that offers the possibility to handle layered material [285]. In case a solid material law is used, shell elements are numerically pre-integrated in the thickness direction at the integration point $l_{layer\ n}$ as shown in Figure 6-2. The volume integral of the material stiffness tensor \mathbf{C} can be transformed into an area integral as Equation (6-12) [515].

$$\int_V C_{ijkl} dV = \int_A C_{ijkl} \cdot z \cdot \frac{h}{2} dz dA \quad (6-12)$$

The membrane tensile force, traverse force and moments are calculated with the area integral in Equation (6-12). The moments are calculated via the 2nd Piola-Kirchhoff stress tensor \mathbf{S} with the help of the area integral as Equation (6-13).

$$m_{ij} = \int_{-1}^1 z \cdot S_{ij} \cdot \frac{h^2}{4} dz \quad (6-13)$$

In case of three integration layers, where $z_{layer\ 1} = h/2$, $z_{layer\ 2} = \pm(t_{layer\ 2}/2)$, $z_{layer\ 3} = -h/2$, Equation (6-9) for x direction becomes Equation (6-14).

$$B_{laminate} = \frac{1}{3} \left[E_{x\ layer\ 1} \cdot \left(\frac{h^3}{8} - \frac{t_{layer\ 2}^3}{8} \right) + E_{x\ layer\ 2} \cdot \left(\frac{t_{layer\ 2}^3}{4} \right) + E_{x\ layer\ 3} \cdot \left(\frac{-t_{layer\ 2}^3}{8} - \frac{h^3}{8} \right) \right] \quad (6-14)$$

An additional failure criterion can be defined through the limitation of the shell element strain. Ultimate strain at the point of failure can be taken from experimental data of the textile stripe test (Table 5-6). Any elements that exceed this strain limitation in any direction are automatically deleted. Shell elements of quadratic size (aspect ratio 1:1) were used in the models for all fabric variants despite the different construction and

density of reinforcing yarn. The element size used for the simulations was determined in a sensitivity analysis.

Despite its simplicity, the macro-scale model can describe most of the important forming mechanisms. However, for the forming of composite components with complex geometries, a higher degree of objectivity is required. The approach with continuum mechanics encounters difficulties to describe some important phenomena, such as the slippage between the fibers, fiber damage and gap formation. In fact, textile structures are discrete in general and build up from smaller elements, namely the yarns, which are fixed together in the textile structure by their structural configuration. This architecture allows a relative movement between yarns, which can only be described by discrete FEM approaches.

6.2 Meso-scale model

6.2.1 Beam element model

Multifilament yarns in textile fabrics are a fibrous material, i.e. a yarn consists of many filaments that can move relatively to each other. Thus, bending stiffness of yarn is very small in comparison with the value calculated from tensile elasticity modulus and moment of inertia (Equation (3-12)). An independent description of the tensile and the bending behavior of the yarns in the beam element is required. The bending stiffness of the beam element can just ignored by applying the Digital-Element chains [352,516,517], where the stiffness matrix of the element is reduced to a minimum as in Equation (6-15). This Digital-Element approach is suitable for modelling filament within yarn on the micro-scale (Figure 3-7).

$$K = \frac{EA}{\Delta L} \begin{bmatrix} G & 0 & 0 & -G & 0 & 0 \\ 0 & 0 & 0 & 0 & 0 & 0 \\ 0 & 0 & 0 & 0 & 0 & 0 \\ -G & 0 & 0 & G & 0 & 0 \\ 0 & 0 & 0 & 0 & 0 & 0 \\ 0 & 0 & 0 & 0 & 0 & 0 \end{bmatrix} \quad (6-15)$$

On the meso-scale, modelling of yarn with beam element requires a correct description of the tensile and the bending behavior. One possibility is the use of Belytschko-Schwer resultant beam formulation [518,519], where the area moment of inertia I about local axes can be arbitrary defined, i.e., the bending stiffness B . However, the Belytschko-Schwer formulation is not stable for beam elements under compression load, namely the blank-holder force in forming simulation. Therefore, the beam element formulation of

Hughes-Liu with cross-section integration is preferred [21,520]. The Hughes-Liu beam element formulation is based on the Hughes-Liu shell element formulation [521–523] and a degeneration of the isoparametric 8-node solid element, which is an approach originated by Ahmad et al. [524] (Figure 6-3). Hughes-Liu beam was the first beam element implemented in LS-DYNA [525]. This formulation is simple, which helps to improve the computational efficiency and robustness.

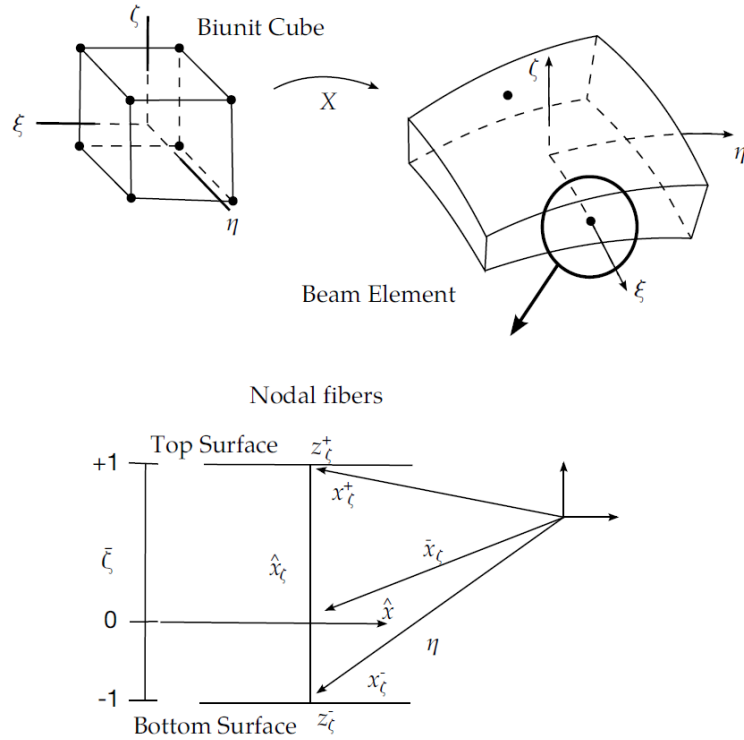


Figure 6-3: Hughes-Liu beam [525]

The detail description of Hughes-Liu beam formulation is taken from the “LS-DYNA Theory Manual” of Dr. Hallquist [525]. The solid element isoparametric mapping of biunit cube is given by Ahmad et al in Equation (6-16) and (6-17).

$$\mathbf{x}(\xi, \eta, \zeta) = \sum_{a=1}^8 N_a(\xi, \eta, \zeta) \mathbf{x}_a \quad (6-16)$$

$$N_a(\xi, \eta, \zeta) = \frac{(1 + \xi_a \xi)(1 + \eta_a \eta)(1 + \zeta_a \zeta)}{8} \quad (6-17)$$

where \mathbf{x} is an arbitrary point in the element. ξ, η, ζ are the parametric coordinates, with ξ determines the axis direction and the pair η, ζ determining the cross-section. \mathbf{x}_a are the

global nodal coordinates of node a , and N_a are the element shape functions evaluated at node a . For example, (ξ_a, η_a, ζ_a) are (ξ, η, ζ) evaluated at node a .

The degeneration of the 8-node brick geometry into the 2-node beam geometry is carried out by combination of the four nodes at $\xi = -1$ and $\xi = +1$ to one single point with three translational and three rotational degrees of freedom. The mapping of the biunit cube into beam element is given as in Equation (6-18) and the group of Equation (6-19), where the three variable function \mathbf{x} is broken into three functions with less variable.

$$\mathbf{x}(\xi, \eta, \zeta) = \bar{\mathbf{x}}(\xi) + \mathbf{X}(\xi, \eta, \zeta) = \bar{\mathbf{x}}(\xi) + \mathbf{X}_\eta(\xi, \eta) + \mathbf{X}_\zeta(\xi, \eta) \quad (6-18)$$

$$\bar{\mathbf{x}}(\xi) = \sum_{a=1}^2 N_a(\xi) \bar{\mathbf{x}}_a$$

$$\mathbf{X}_\eta(\xi, \eta) = \sum_{a=1}^2 N_a(\xi) \mathbf{X}_{\eta a}(\eta) \quad (6-19)$$

$$\mathbf{X}_\zeta(\xi, \zeta) = \sum_{a=1}^2 N_a(\xi) \mathbf{X}_{\zeta a}(\zeta)$$

Arbitrary points on the reference line $\bar{\mathbf{x}}$ are interpolated by the one-dimensional shape function $N(\xi)$ operating on the global position of the two beam nodes that define the reference axis $\bar{\mathbf{x}}_a$. For the points off the reference axis, further interpolation is carried out by a one-dimensional shape function along the directions of the cross-section $\mathbf{X}_{\eta a}(\eta)$ and $\mathbf{X}_{\zeta a}(\zeta)$ as shown in the group of Equation (6-20) and (6-21).

$$\mathbf{X}_{\eta a}(\eta) = z_{\eta a}(\eta) \hat{\mathbf{X}}_{\eta a}$$

$$z_{\eta a}(\eta) = N_+(\eta) z_{\eta a}^+ + N_-(\eta) z_{\eta a}^-$$

$$N_+(\eta) = \frac{(1 + \eta)}{2} \quad (6-20)$$

$$N_-(\eta) = \frac{(1 - \eta)}{2}$$

$$\mathbf{X}_{\zeta a}(\zeta) = z_{\zeta a}(\zeta) \hat{\mathbf{X}}_{\zeta a}$$

$$z_{\zeta a}(\zeta) = N_+(\zeta) z_{\zeta a}^+ + N_-(\zeta) z_{\zeta a}^-$$

$$N_+(\zeta) = \frac{(1 + \zeta)}{2} \quad (6-21)$$

$$N_-(\zeta) = \frac{(1 - \zeta)}{2}$$

where $z_\eta(\eta)$ and $z_\zeta(\zeta)$ and are thickness functions. The bending stiffness matrix \mathbf{B} is calculated on the cross-section located at the mid-point of the beam axis (Figure 6-4). The bending stiffness matrix \mathbf{B} is a 6 x 18 matrix as shown in Equation (6-22) and Equation (6-23), where the thickness function is a variable.

$$\mathbf{B}_a = \begin{bmatrix} B_1 & 0 & 0 & B_4 & 0 & 0 & B_7 & 0 & 0 \\ 0 & B_2 & 0 & 0 & B_5 & 0 & 0 & B_8 & 0 \\ 0 & 0 & B_3 & 0 & 0 & B_6 & 0 & 0 & B_9 \\ B_2 & B_1 & 0 & B_5 & B_4 & 0 & B_8 & B_7 & 0 \\ 0 & B_3 & B_2 & 0 & B_6 & B_5 & 0 & B_9 & B_8 \\ B_3 & 0 & B_1 & B_6 & 0 & B_4 & B_9 & 0 & B_7 \end{bmatrix} \quad (6-22)$$

$$B_i = \begin{cases} N_{a,i} = \frac{\partial N_a}{\partial y_i}; i = 1,2,3 \\ (N_a z_{\eta a})_{,i-3}; i = 4,5,6 \\ (N_a z_{\zeta a})_{,i-6}; i = 7,8,9 \end{cases} \quad (6-23)$$

Thus, the tensile and bending properties of Hughes-Liu beam element can be independently described by choosing a suitable value for the thickness functions. In LS-DYNA, the value of these thickness functions are defined through the keyword INTEGRATION_BEAM. The bending stiffness of the beam element is configured by shifting the position integration points across the beam cross-section with the help of the thickness function [518]. The bending stiffness is considered as a constant value and independent from the curvature of the yarn. Figure 6-4 shows an example of 8 integration points on a beam cross-section.

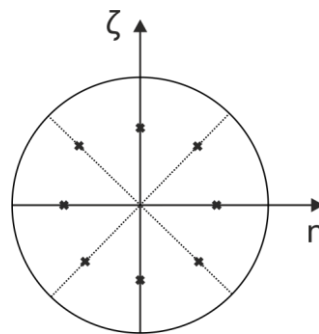


Figure 6-4: Round cross-section of a beam element with 8 arbitrary integration point position

Geometrical modelling of BWKF with beam element

As the first step, diameter d_R and d_S are chosen for the beam elements, which represent reinforcing yarn and stitching yarn in the FEM model, respectively. Suitable values should

be used to assure that the thickness of the model (where the beam elements stack on each other) is close to the thickness of the real fabric.

Modelling of the stitching yarn system

The stitching yarn system in the biaxial reinforced weft-knitted fabric is a single jersey structure. As the configuration of the fabrics is known, the mathematical description of the stitching yarn system by Choi and Lo [526] is used for modelling the geometry of the FEM fabric model with beam elements. The coordinators of one stitching yarn is governed by Equations (6-24), (6-25), and (6-26).

$$x(t) = at^3 - 1.5at^2 + 0.5(a + w)t \quad (6-24)$$

$$y(t) = 0.5(c + 2e)(1 - \cos(\pi t)) \quad (6-25)$$

$$z(t) = 0.5(t_h - d_s)(1 - \cos(2\pi t)) \quad (6-26)$$

In these equations, x, y, z (mm) are coordinates of every single point on the knitting loop. w (mm) is the loop width. $c+2e$ (mm) is the loop height. e (mm) is the adjacent loop overlapping distance. t_h (mm) is the fabric thickness. d_s (mm) is the chosen yarn diameter. a (-) is a free parameter. t (-) ($t \sim [0,1]$) is a parameter of the space curve. An example of a simple single jersey structure modelled by these equations is shown in Figure 6-5. Beam elements for stitching yarn use the approach of Digital-Element approach, as the bending stiffness is not significant.

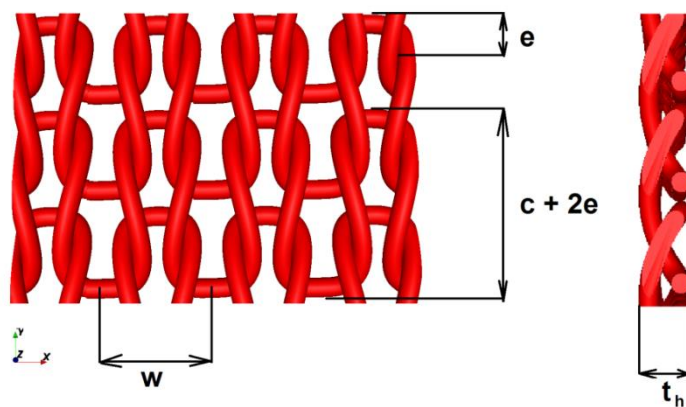


Figure 6-5: Single jersey weft-knitting structure according to Choi and Lo [526] (created with TexGen)

Modelling of reinforcing yarn system

The reinforcing yarn systems come with a prescribed waviness, which is based on the harmonic function as in Equation (6-27). It is assumed that the yarn waviness behaves in

a harmonic manner along the yarn axis in the out-of-plane direction (thickness direction). The prescribed waviness helps to describe the non-linear tensile behavior of the fabrics. An example of yarn modelled by beam element with different length is shown in Figure 6-6.

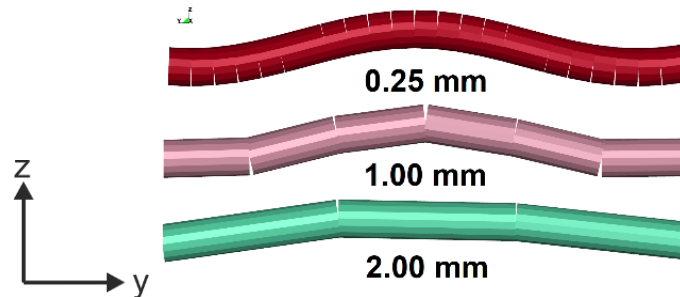


Figure 6-6: Decrease of the curvature of the beam element chain by increasing the length of beam elements

The z-coordinate of an arbitrary node along the yarn axis is described by the Equation (6-27) as follows:

$$z(y) = A \sin\left(\frac{\pi y}{D}\right) \quad (6-27)$$

In this equation, z (mm) is the z-coordinate of the node (thickness direction of fabrics); A (mm) is the amplitude of the wave arc; y (mm) is y-coordinate of the node and D (mm) is the distance between two reinforcing yarns in the perpendicular direction, which can be calculated from the reinforcing yarn density from Table 5-1. The value of parameter A is calibrated with the help of a tensile test simulation to meet the non-linearity of the tensile force – tensile strain curve.

A suitable beam length should be chosen. If the beam element is too short, the computing demand increases and exceeds the limited available computing resources. In contrast, if the beam element is too long, the curvature shape of the yarn is not assured anymore. Figure 6-6 illustrates the decrease of beam chain curvature by increasing the length of beam elements. As the curvature of the beam chain decreases, the tensile behavior of the textile model can no longer be guaranteed. That can also lead to bad contact formulation and impede the mechanical performance of the model. In a convergence study, the length of beam elements for reinforcing yarn is determined to 0.25 mm. The length of beam element for stitching yarn must be shorter, namely 0.15 mm, because of the high curvature of stitching yarn. Figure 6-7 shows the meso-scale model of BWKF CF/PA V1 with beam elements, which is generated by a Python subroutine. Modelling of plain woven

fabrics also uses the Equation (6-27) for the waviness, where parameter A has a practical value around 50% thickness of the textile. Figure 6-8 shows the meso-scale model of plain woven W GF with beam elements.

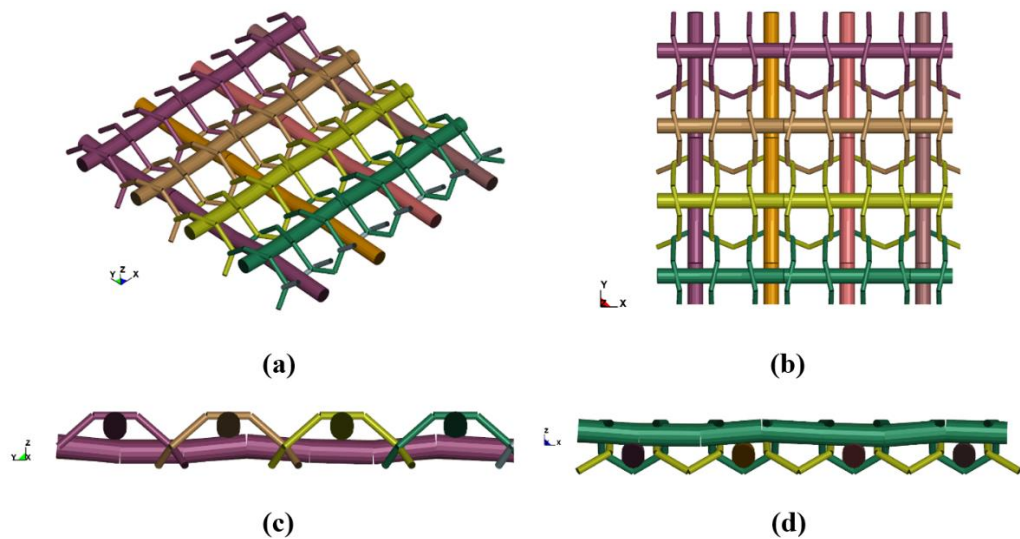


Figure 6-7: Model of a unit cell 4 x 4 of BWKF CF/PA V1 with beam elements: (a) isometric view, (b) top view and (c) side view along warp direction and (d) side view along weft direction

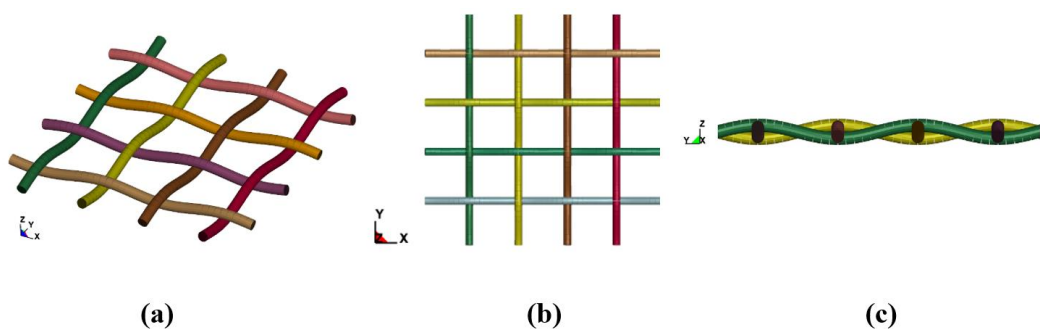


Figure 6-8: Model of a unit cell 4 x 4 of plain woven with beam elements: (a) isometric view, (b) top view and (c) side view

6.2.2 Shell element model

Beam element has round cross-section, so that it cannot represent the cross-section of yarn in textile correctly, which normally is an ellipse or oval (see Figure 2-9 and Figure 5-1). There is great empty space between beam elements (Figure 6-7cd), which would eventually lead to inaccurate prediction of gap formation in forming simulations, where sliding and contact of yarn with their neighbors in the transverse direction play an important role. A shell element model is developed with the purpose to fix this

disadvantage while still maintaining the performance in other aspects. Shell elements have been used in fabric modelling on the meso-scale as reinforcing yarn for various purposes [132,306]. The model of Boisse [132] has a minimum degree of freedom but still provides a good performance under shear load in bias extension testing. This model can eventually predict the loss of cohesion in textile fabric during the forming process. Hübner et al. [306] used shell elements with a higher degree of freedom and an edited cross-section to predict the performance of a composite structure, where woven fabric is used as reinforcing structure. The meso-scale FEM model for fabrics with shell element as reinforcing yarn in this thesis follows the approach of Hübner et al. [306].

Firstly, a single yarn is modelled and a simulation of the yarn tensile test helps to validate the tensile behavior of the yarn model. Each yarn is represented by a stripe of shell elements and the thickness of the shell elements is edited to approximate the oval shape of the yarn cross-section (Figure 6-9). The more shell elements are used along the width direction, the better the approximation of the cross-section. However, to keep the computing cost at a reasonable level, only four shell elements along the width of the yarn are used (Figure 6-9b). By further reducing the amount of shell elements along the width, the thickness of the shell element cannot approximate the yarn cross-section correctly. The thickness of these shells is based on the measurement of microscopic images of the real fabric cross-section (Figure 2-9 and Figure 5-1).

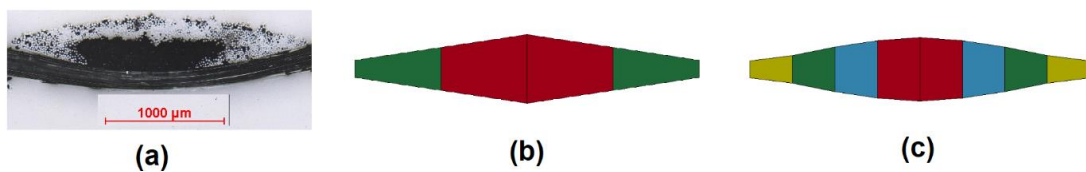


Figure 6-9: Comparison of (a) real cross-section of woven fabrics with (b) meso-model with 4 shell segments and (c) 8 shell segments

The same laminate formulation according to Döbrich et al. [285], which has been presented in section 6.1 for macro-scale model, is used for shell elements in combination with a linear elastic material model. This allows describing the tensile and bending behavior of reinforcing yarn independently. Shell elements are comprised of three integration layers, in which the middle layer has a significant smaller thickness and higher tensile elasticity modulus in comparison with the top and bottom layers. The overall tensile stiffness of the shell element is governed by the tensile elasticity modulus of the middle layer, while the small tensile elasticity modulus of the other layers controls the bending stiffness of the shell. This method of modelling reinforcing yarn with shell element and laminate formulation can be used for modelling any type of textile.

Shell model of BWKF

Cross-section of stitching yarn is small in comparison to reinforcing yarn and can be considered as round. The bending stiffness of stitching yarn can be neglected. Thus, stitching yarns are still modelled by beam elements. With good topological model such as the one by Kyosev [371] (Figure 3-8), an accurate FEM model with beam element as stitching yarn and shell element as reinforcing yarn can be created. However, such model requires a special material model to describe the non-linearity of reinforcing yarn under tensile load, as reinforcing yarn is considered perfectly non-crimp. Due to stability, only linear elastic material model is used for shell element as reinforcing yarn in this thesis. That leads to the requirement of modelling the interaction between the stitching yarn system and the reinforcing yarn system, which helps to create waviness of shell element stripe. A process-like simulation is employed, where reinforcing and stitching yarns are initially set up in a loose state in the model of a unit cell with no contact between them (Figure 6-10a). The setup of this model is based on the configuration of the real fabric (Table 5-1) and initially, reinforcing yarns lay straight (Figure 6-10a). With a simulation of artificially thermal shrinkage of the beam elements that represent stitching yarns, the interaction between the yarn systems is realized. This interaction between stitching yarns and reinforcing yarns causes a moderate degree of waviness of the reinforcing yarns (Figure 6-10b). With such waviness, the non-linear tensile behavior of the fabrics can be correctly described, even though only linear elastic material model is used for the shell elements. The described modelling principle can also be applied to further BWKF with higher quantity of layer and different construction as shown in Figure 6-11.

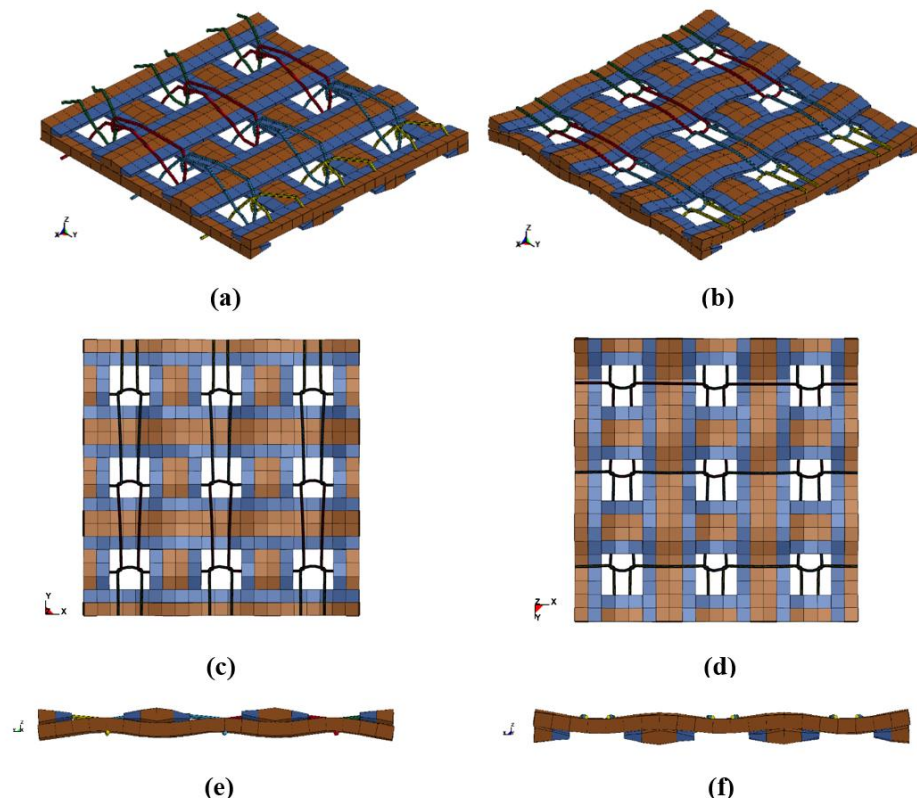


Figure 6-10: Model of a unit cell 3 x 3 of BWKF 2-layer asymmetric with shell and beam elements generated by process-like simulation: (a) initial state, (b) generated structure, (c) right side, (d) left side, (e) side view along warp direction

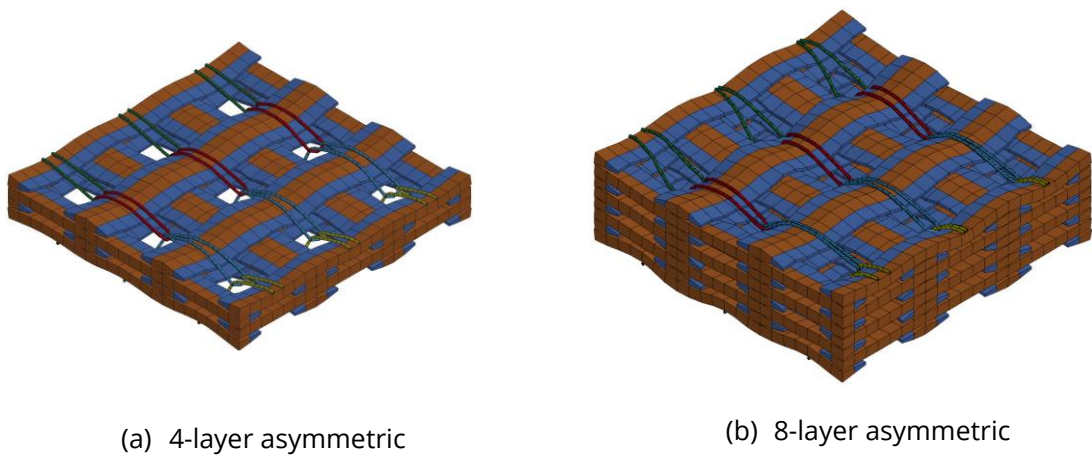


Figure 6-11: Further models of a unit cell 3 x 3 of BWKF with shell and beam elements generated by process-like simulation

Shell model of plain-woven fabric

The geometry of the plain-woven fabric with shell elements is generated with the help of a process-like simulation of the weaving process. A unit cell with a limited quantity of warp

and weft yarns is sufficient in this context. A unit cell of four warp and four weft yarns is generated (Figure 6-12). The setup of this simulation is based on the fabric configuration as shown in Figure 2-9. As boundary condition, the ends at one side of the warp yarn are fixed in all translational motion while the ends at the other side are prescribed with translational motion in vertical direction to mimic the shed opening/closing process. In-plane translational motion of the second ends are also fixed. In contrast, just one in-plane translational motion and the vertical translational motion of both ends of the weft yarns are fixed. Furthermore, the remaining translational motion is also prescribed to mimic the weft insertion process. The simulation ends when all wefts are inserted and the warps ends return to their original positions. The outcome is a unit-cell of shell elements with the desired weave pattern (Figure 6-12). This approach can be applied to any kind of woven fabrics if the configuration of the weave pattern is known.

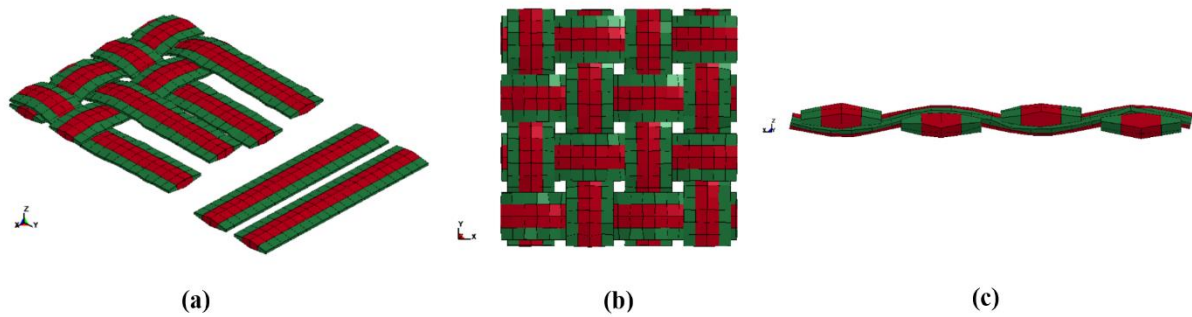


Figure 6-12: (a) Process-like weaving simulation of a unit cell of 4 warp x 4 weft yarns, (b) top view of the generated structure and (c) side view of the generated structure

6.3 Validation of FEM models

The mechanical performance of the created model is calibrated and validated based on the experimental data of Section 5.3. A series of five simulations is created for this purpose: tensile test of yarn, tensile test of fabric, cantilever test of fabric, picture frame test of fabric and friction test of fabric. The validation process of FEM models for BWKF CF/PA 2-layer V1 and W GF is used to demonstrate the validation method. Details of validation of BWKF CF/PA 2-layer V2 and can be found in [21] and BWKF CF/PA 4-layer in [527].

6.3.1 Tensile behavior

Validation of yarn tensile behavior

In the simulation with beam elements of the tensile test of yarn, a straight yarn with a length of 500 mm is modelled. One end of the yarn/ chain of beam elements is fixed in all

translational movements and the other end is pulled with a constant velocity in the direction along the length, as in the standard ISO 3341 or DIN EN ISO 2062. As shell element is also used to model reinforcing yarn, simulation of tensile test with shell elements is also carried out for GF 1200 tex and hybrid yarn CF/PA 6.6 300 tex. The boundary conditions are similar to the one for the beam element model. The cross-section of the shell elements is edited to approximate the actual textile cross-section. Suitable thickness and width of the shell elements are chosen, so that the model of textile later has the same thickness as the real fabrics (Figure 6-9).

A linear elastic material model is used for modelling GF 68 tex x 2, GF 1200 tex and hybrid commingling yarn CF/PA 6.6, the Young's modulus of the beam element is configured such that the force-strain curve in the model agrees with the test results (Figure 6-13). This isotropic, hypoelastic material is selected for the stability of the computation. For a more realistic mechanical behavior of the yarn, an anisotropic material model can be implemented, e.g., a non-linear elastic-orthotropic material model. However, an anisotropic material model cannot be implemented for beam elements, as they are 1-D continua. Anisotropic material model describes the different behavior of material between at least 2 different directions, thus, at least 2-D continua (shell elements) is required. For shell elements, the available anisotropic models cause an instability during the computation, if combined with the laminate formulation. To overcome this problem, a subroutine for a user material should be implemented for shell elements in further research. For PA 6.6 94 tex, an elastic-plastic material model is used.

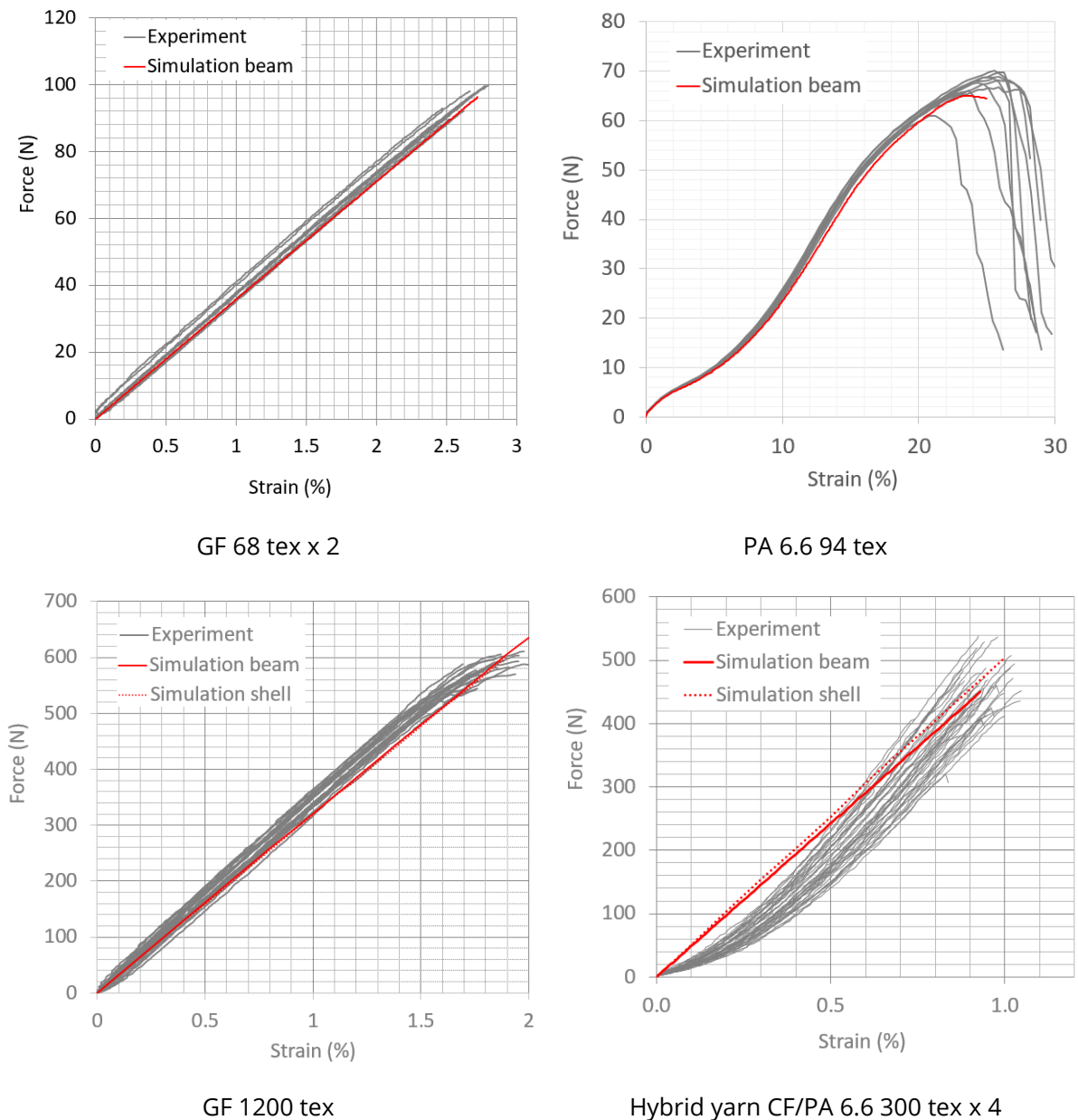


Figure 6-13: Comparison of tensile force - strain curve between simulation and experiment

Validation of fabric tensile behavior

In the simulation of the tensile test of fabrics, a model of a textile stripe with the dimension of $200 \times 50 \text{ mm}^2$ is used. The translational motion of one end of the textile stripe model is completely fixed in all directions, while the other end is pulled with a constant velocity in the direction along the length. These boundary conditions are based on the standard DIN EN ISO 13934-1. An overview of textile stripe models (of all three type of model: macro, meso beam, meso shell) for BWKF CF/PA 2-layer V1 and W GF is shown in Figure 6-14. Figure 6-15 shows the comparison of tensile force-strain curves between experiment and simulation.

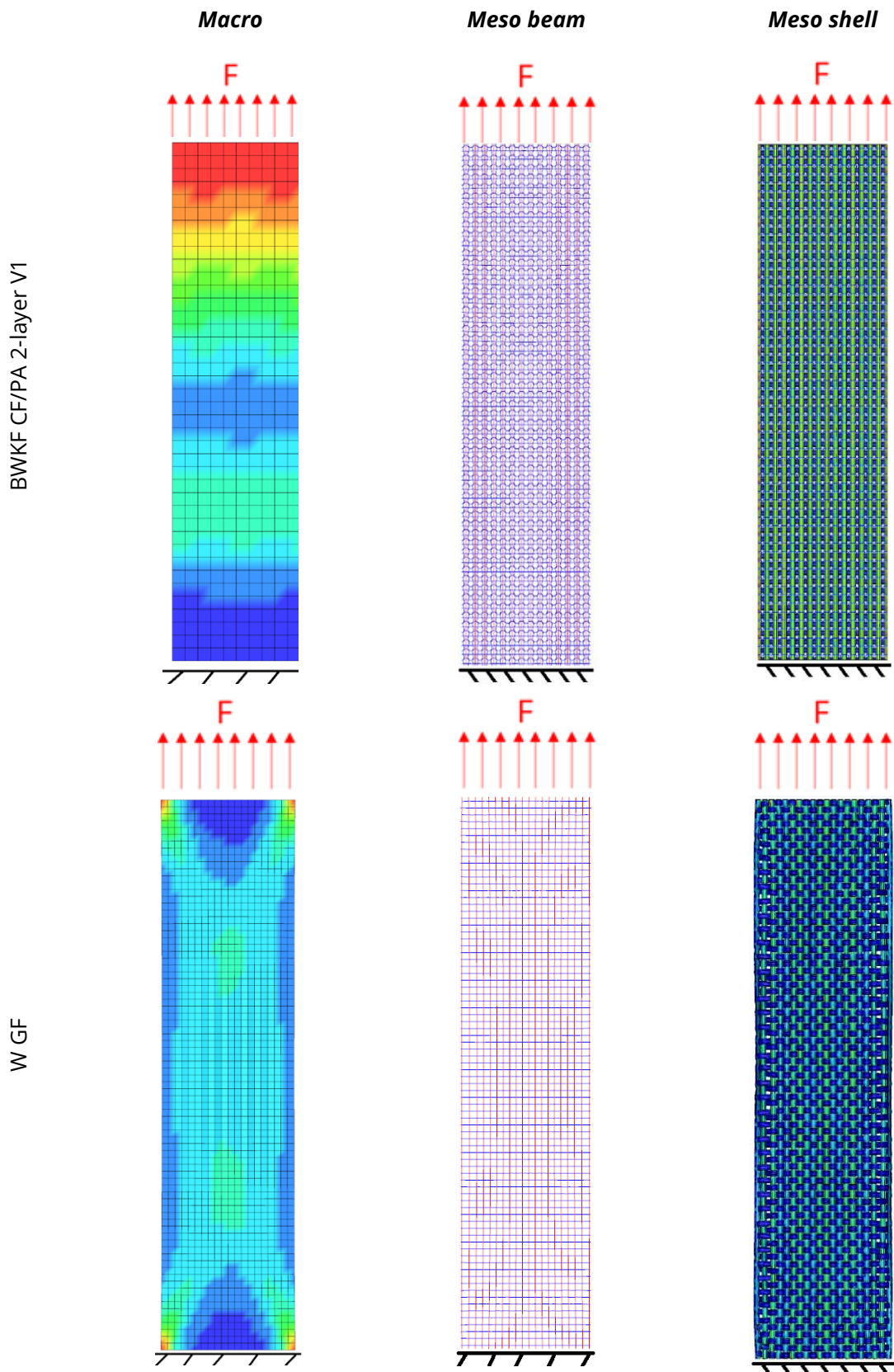


Figure 6-14: Tensile test simulation of BWKF CF/PA 2-layer V1 and W GF (warp direction)

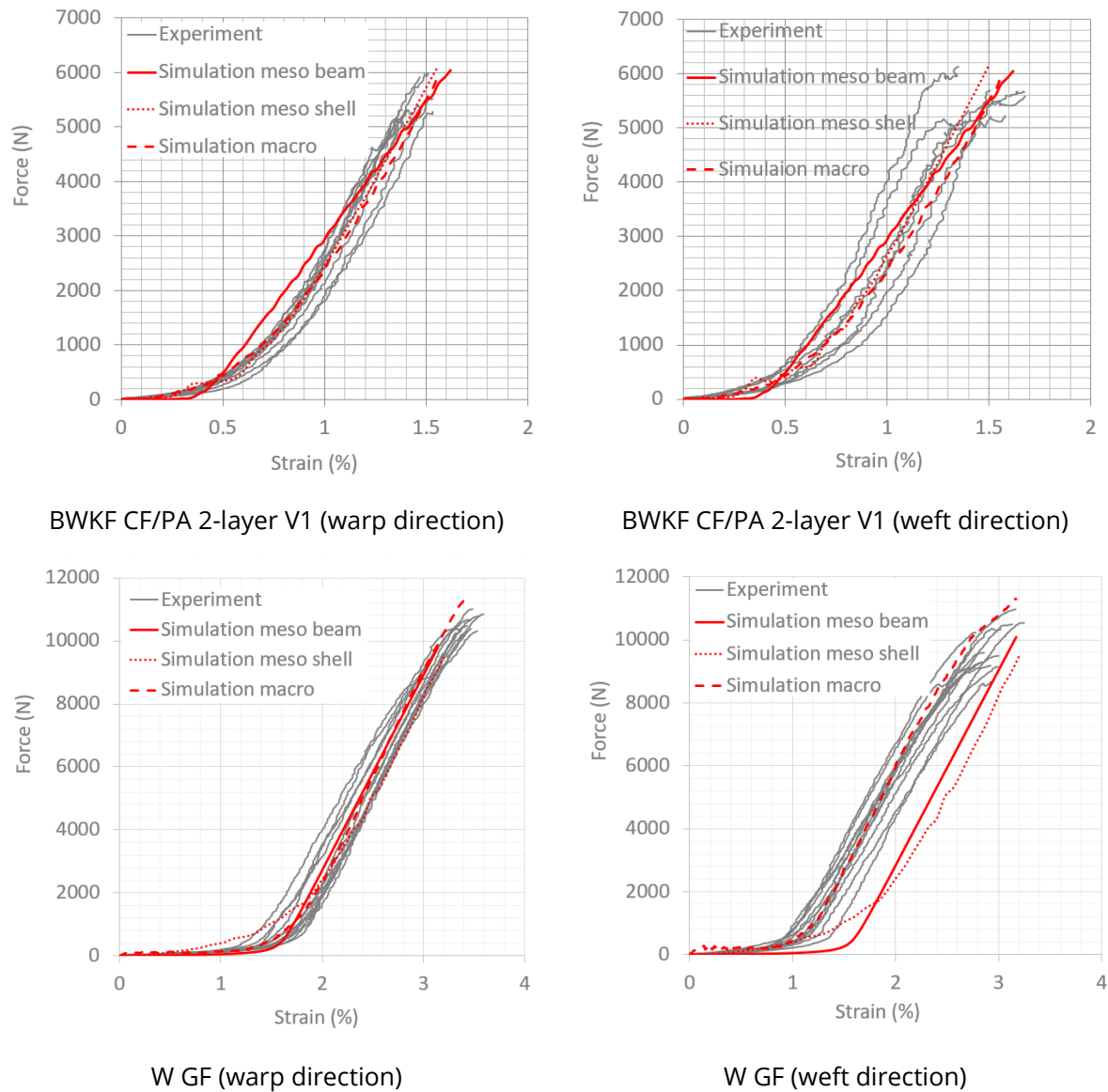


Figure 6-15: Comparison of tensile force - strain curves between experiment and simulation

Macro models describe the tensile behavior of the textile most accurately, as the elasticity modulus – strain curves $E_x (\epsilon_x)$ and $E_y (\epsilon_y)$ are used as input parameter. The meso models on the other hand, describe the non-linear tensile behavior purely by the prescribed structural waviness of the beam element chains and shell element stripe. The tensile behavior of the meso model is almost identical in both warp and weft direction of the fabric. This leads to a moderate deviation from the experimental data and simulation. As the yarn is modelled discretely in the meso model, it can be clearly observed in the tensile test simulation that only one yarn system carries most of the load while the other remains almost intact (Figure 6-14).

6.3.2 Bending behavior

The simulation of the cantilever test is used to calibrate the bending stiffness of the fabric model. As introduced in Section 6.1 and 6.2, the bending stiffness of all type of model can be adjusted arbitrarily. As reinforcing yarn in meso model is modelled separately, the bending stiffness in the warp and weft direction is calibrated independently. In the simulation of the cantilever test, a stripe of fabric in the warp or weft direction with a width of 50 mm is used. The stripe of fabric has a length equal to the overhang length in that direction (see Table 5-7). Only the nodes at one side of the fabrics are totally fixed in all translational and rotational motions. The gravity is gradually applied in form of body load in the negative direction of the z-axis. To minimize the inertial effect, the body load is increased slowly within 10 seconds. A rigid shell element, which lays diagonally with an angle of 41.5° is used as the reference plane. The rigid shell is fixed in all degrees of freedom and has no contact to the fabric model. The bending stiffness is configured to ensure that the free end of the fabric model touches the reference plane when the gravity is fully applied, as shown in Figure 6-16. The results of cantilever test simulation of three types of model are compared in Figure 6-17. The curvature of the bended textile model for BWKF CF/PA 2-layer V1 are not identical between types of model as W GF.

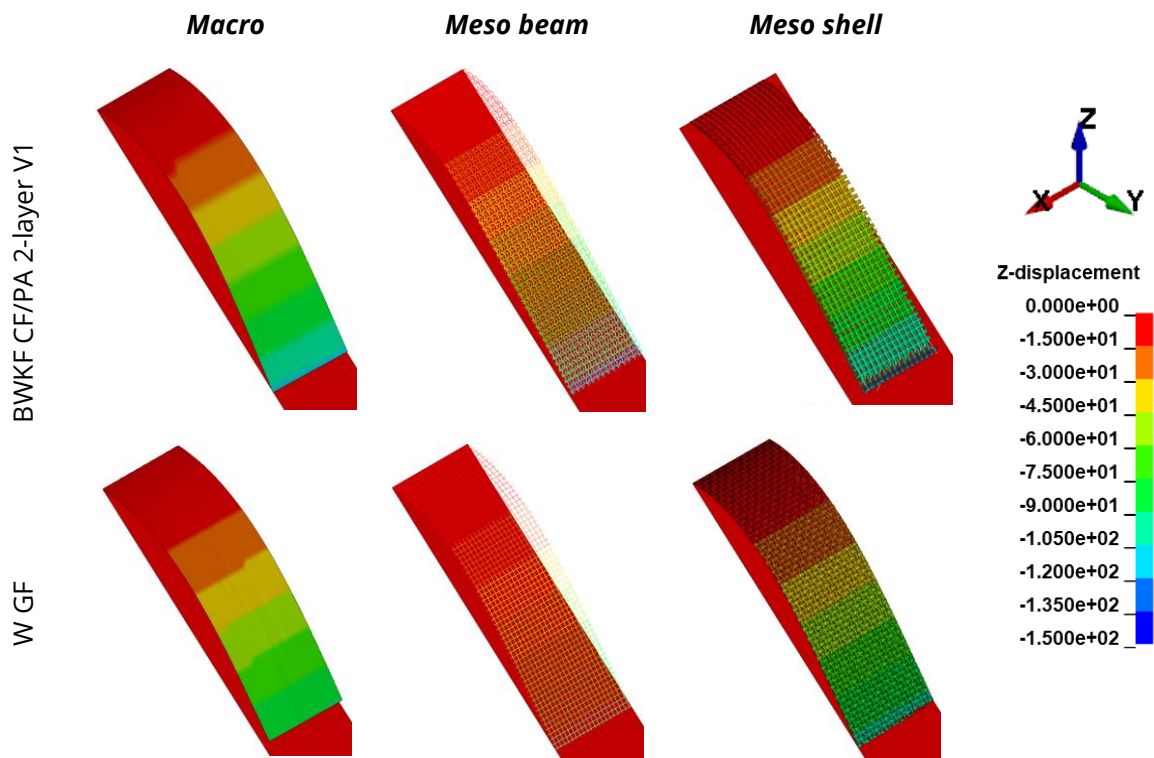


Figure 6-16: Cantilever test simulation of BWKF CF/PA 2-layer V1 and W GF (warp direction)

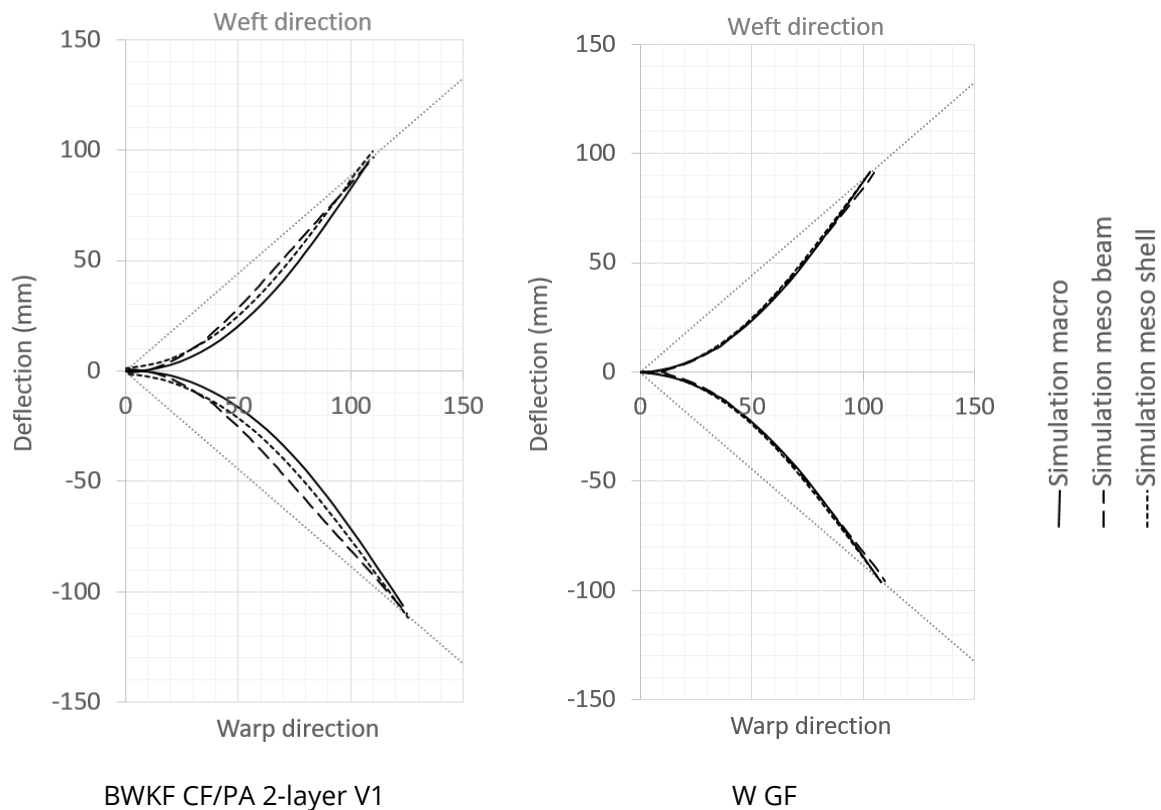


Figure 6-17: Comparison of cantilever test simulation of three types of model

6.3.3 Shear behavior

The shear behavior of the textile FEM models is validated with a picture frame test simulation. For macro model, a fabric model with 4-node shell elements with the size of $200 \times 200 \text{ mm}^2$ is created. The picture frame itself is modelled with four stripes of shell elements, which use a linear elastic material model with the parameters of standard structural steel (Table 2-1). The lower end of the picture frame is fixed in all translational motions, while the upper end is pulled up with a constant velocity (Figure 6-18). The nodes at the edge of the textile model and the edge of the picture frame, where they contact each other, are coupled by the keyword `CONSTRAINED_NODE_SET` in LS-DYNA. This keyword allows constraining the translational movement of nodes within a defined group, while leaving them free to rotate around themselves (Figure 6-19). This agrees with realistic test conditions in Section 5.3.3, where the fabric with a size of $300 \times 300 \text{ mm}^2$ is attached to the frame by rows of needles, which allow the fabric to rotate freely while being sheared. This prevents the occurrence of yarn tensile loads.

The same approach with the use of `CONSTRAINED_NODE_SET` is applied for the meso scale model with beam elements (Figure 6-20). Each end of the beam chains in the fabric model, which represent the reinforcing yarns, is coupled to the picture frame. Thus, the

end of the beam chain is free to rotate. End of the beam chains, which represent the stitching yarn nearby, is also included in the node set of that constrained.

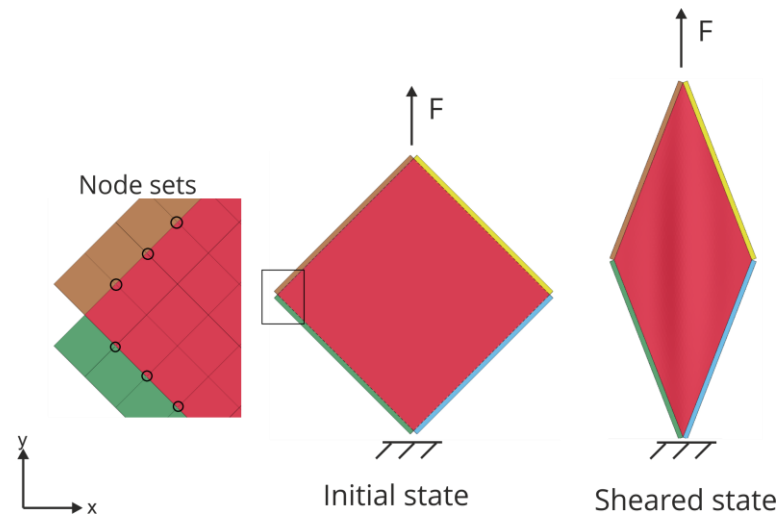


Figure 6-18: Picture frame test simulation with macro model

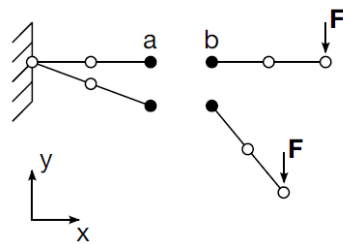


Figure 6-19: Explanation of the keyword CONSTRAINED_NODE_SET [518]

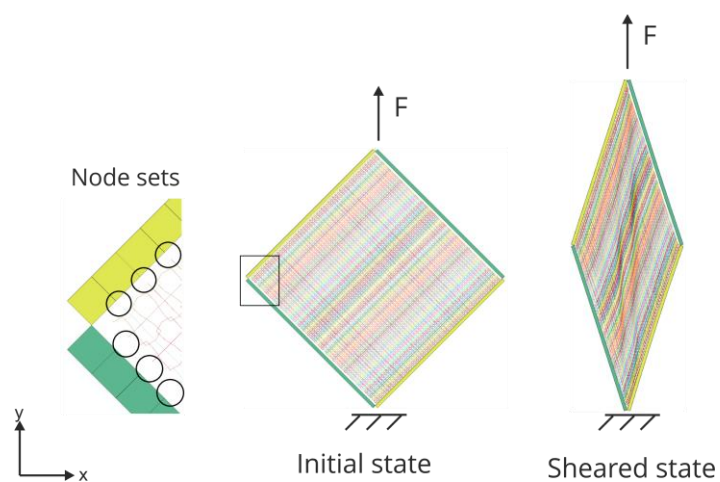


Figure 6-20: Picture frame test simulation with meso beam model

However, the approach with `CONSTRAINED_NODE_SET` cannot be applied for the meso shell model to simulate the shear process. Contact error occurs between continuum element of the textile FEM model and the frame, which causes instability and prevent the simulation from being computed. To overcome this challenge, a periodic boundary condition is applied. The method has been suggested by Sun [528] and successfully applied by Döbrich [166] to create shear simulation of textile unit cell. All pairs of opposite nodes on the shell and beam elements of the textile model (for example in Figure 6-21: A and B, C and D) are constrained to the movement of the node I and II, in x and y direction, with the group of Equation (6-28).

$$\begin{aligned}
 u_B - u_A - u_I &= 0 \\
 v_B - v_A - v_I &= 0 \\
 u_D - u_C - u_{II} &= 0 \\
 v_D - v_C - v_{II} &= 0
 \end{aligned}
 \tag{6-28}$$

In Equation (6-28), $u(x)$ and $v(y)$ are the displacement of the nodes in x and y direction, respectively. In LS-DYNA, the periodic boundary condition is implemented by the keyword `CONSTRAINED_MULTIPLE_GLOBAL`. Node I and node II are two help nodes, whose movement is prescribed with a constant velocity in y and x direction, respectively. Movement of all nodes on the four edges of the textile is fixed in z direction. With the described simulation method, the shear behavior of the models are tested. The results are shown in Figure 6-22.

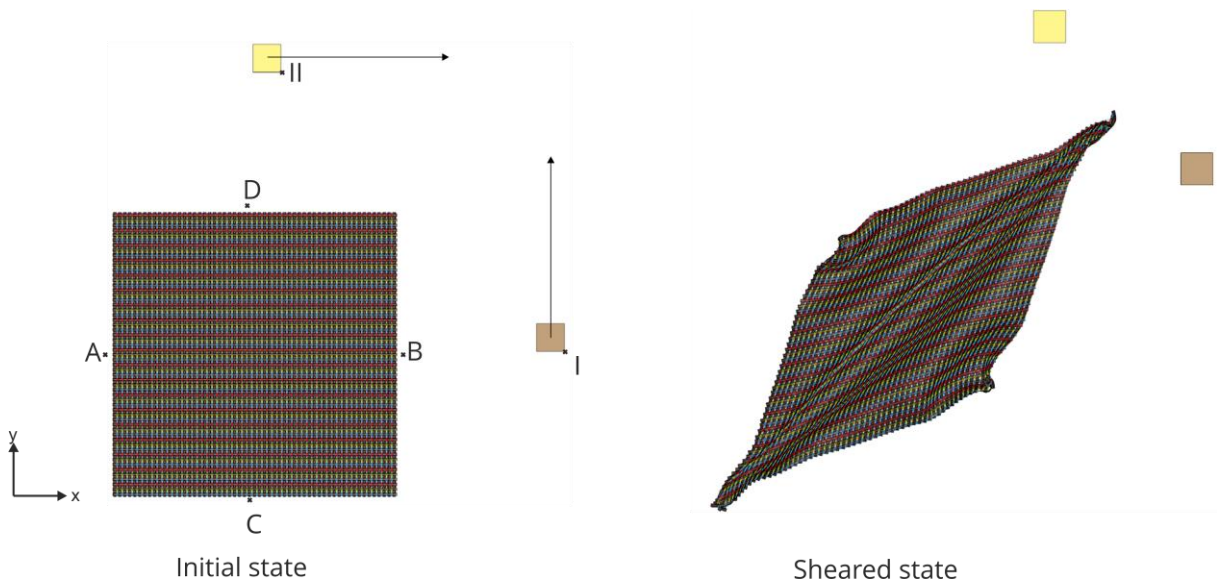


Figure 6-21: Shear test simulation with meso beam model by periodic boundary conditions

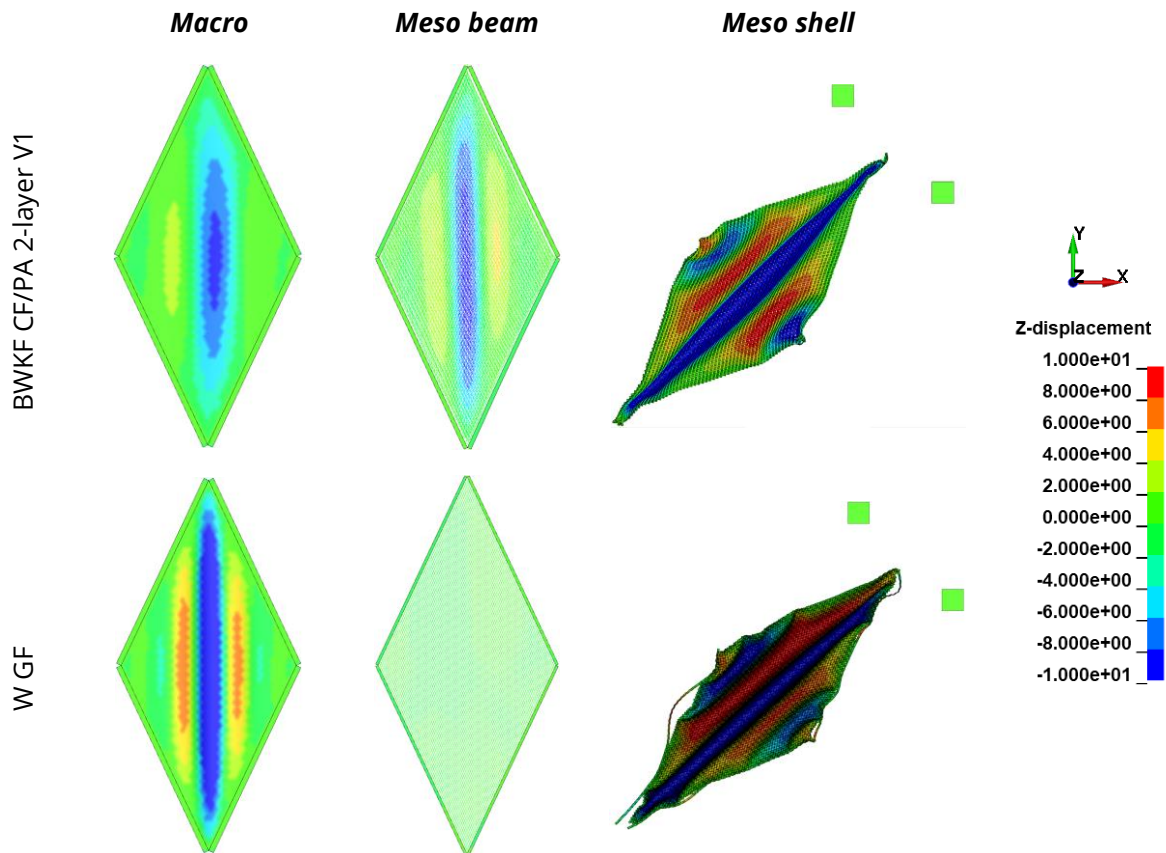


Figure 6-22: Displacement in thickness direction (z direction) of textile FEM models at 40° shear angle

The shear force of the fabric is recorded and compared with the simulation results, which is only possible for macro and meso beam models. The shear force – shear angle curves of macro model agree pretty well with the experimental data (Figure 6-23), as the shear modulus – shear strain curves $G_{xy}(\tan\varphi_{xy})$, which are calculated from the experimental data, are used directly as input for the macro scale model.

In meso beam model, the contact between yarns (beam/beam contact) was also taken into account in the models. A contact formulation based on penalty penetration between segments was used. The shear force – shear angle curves of BWKF meso beam model can be calibrated by varying the friction between beam/beam elements. Thus, the shear force – shear angle curves of BWKF CF/PA 2-layer V1 meso beam model can be reasonably fitted to the experimental data (Figure 6-23). In contrary, the friction coefficient in this contact between yarns in the beam model for W GF does not have any influence on the shear behavior of the model. This phenomenon can be explained by the cross-section of the

models. The beam model of plain woven fabric oversimplifies the cross-section and leaves significant free spaces between yarns (Figure 6-8). Thus, no contact between neighboring yarns occurs at larger shear angles. Thus, there is no pressing force of yarns acting on one another, generating no friction force between yarns. The friction force between neighboring yarns determines the shear resistance. However, for beam model of W GF, it does not occur at all. In contrast, the meso beam model of BWKF has less free space due to the presence of the weft-stitching yarn system.

Therefore, the shear behavior of meso beam model for W GF deviates from the real fabric behavior in both ways: no wrinkle formation can be observed in the picture frame test simulation (Figure 6-22), and no shear force occurs (Figure 6-23). Further improvement or calibration for the meso beam model of W GF is not possible.

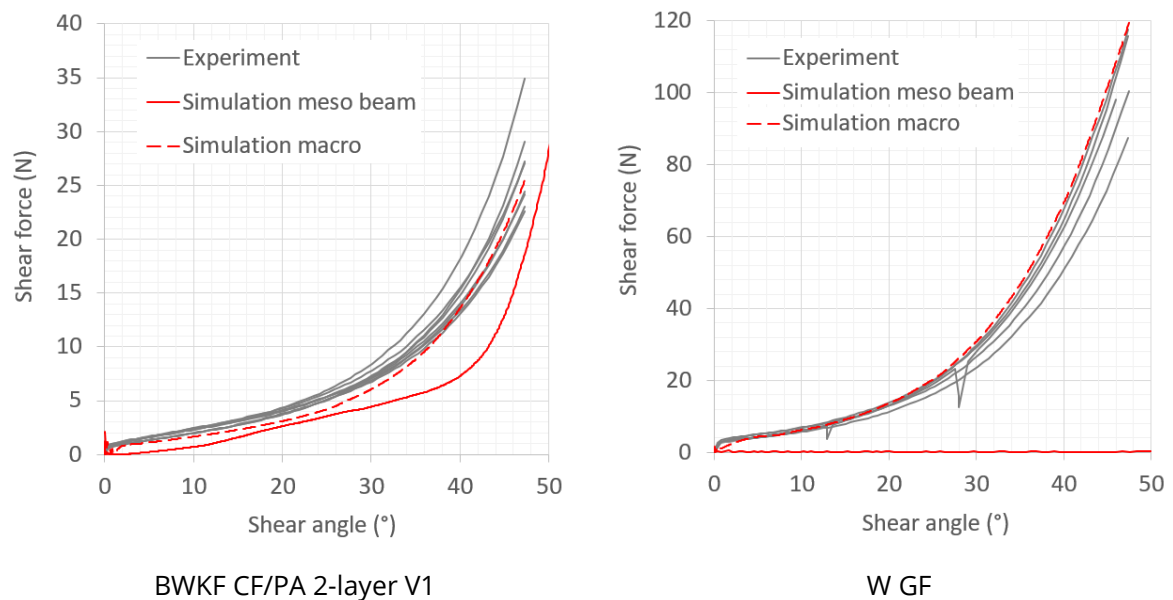


Figure 6-23: Comparison of shear force - shear angle curves between experiment and simulation

In the meso shell models, contact problems occurs, namely penetration between shell/shell as well as shell/beam elements (Figure 6-24), which causes exceptional high force in the data. Thus, a validation by comparison of the shear force - shear angle curves between simulation and experiment is not possible. Alternatively, the max. displacement in the thickness direction (z direction) during the shear test, which can be measured from the 3D scan data (Figure 5-15), as well as in the simulation (Figure 6-22), is used for the validation. As the 3D scan data is only available at three different shear angles, a trend line is added to the diagram for better comparison. The trend line is a polynomial second grade line, and is interpolated from the available measure points. The results show

reasonable agreement between the measured data from 3D scan and simulation for both type of fabrics (Figure 6-25). Thus, the shear behavior of meso shell model is validated.

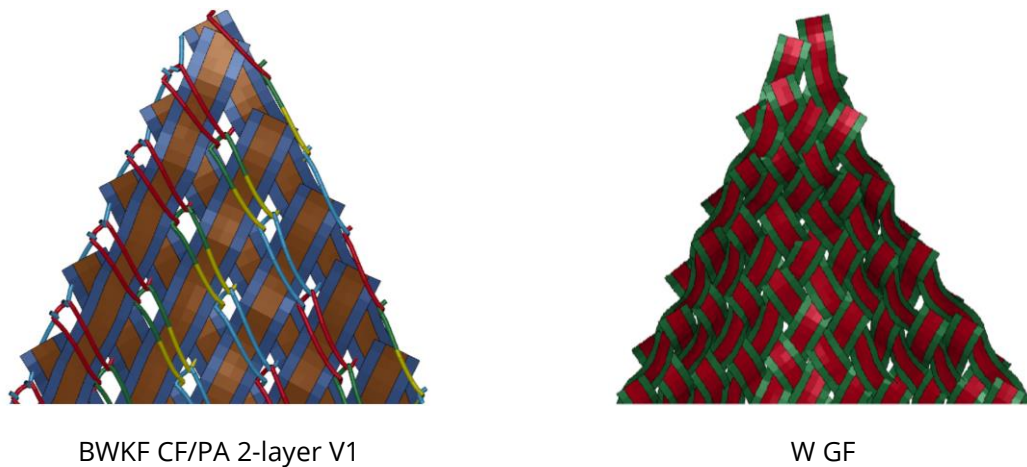


Figure 6-24: Penetration between shell/shell and shell/beam elements during shear test simulation

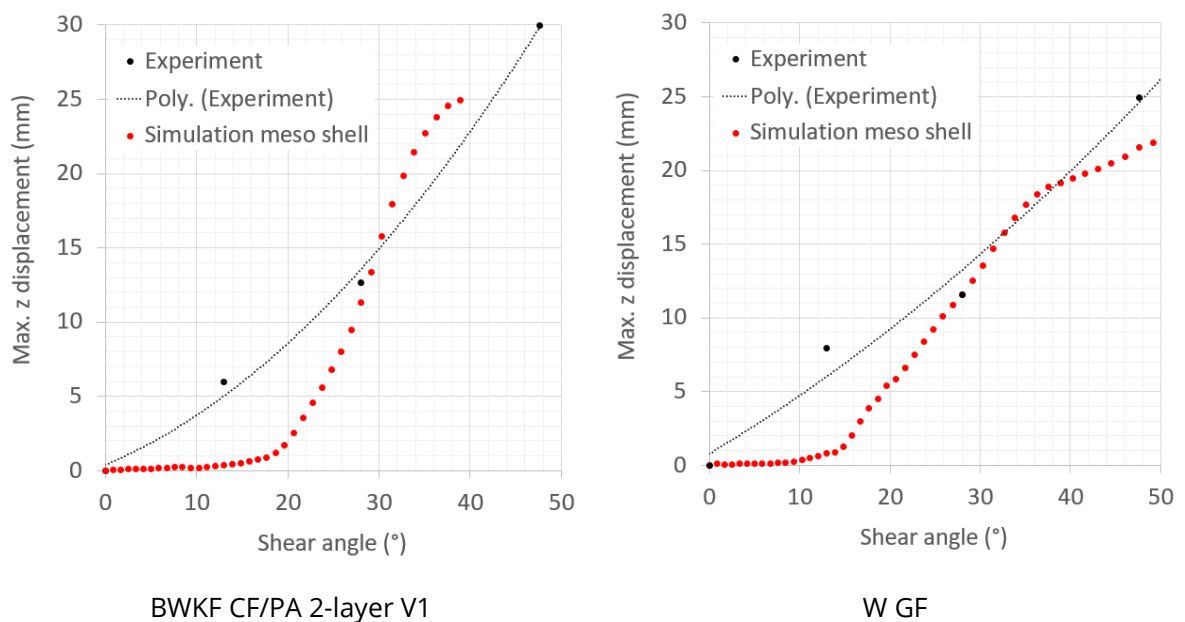


Figure 6-25: Comparison of max. z displacement - shear angle curves between experiment and simulation

6.3.4 Friction

The simulation of the friction test is used to assure the correctness of the contact formulation between the fabric model and the forming tools. During the forming process, the fabric is under compression stress of the blank holder, which induces in-plane tensile stress into the fabric via friction interaction. The deformation of the fabric during the

forming process depends significantly on the in-plane tensile stress. The model of the friction test attempts to replicate the test condition in Section 5.3.4, where a fabric model with the size of 150 x 50 mm² is used. This fabric model is put in between two rigid shells, in which one is completely fixed in all degrees of freedom and the other can only move vertically (Figure 6-26). At the start of the simulation, a pressing load is applied on the shell, which can move vertically. When the load is fully applied, one end of the fabric is pulled out at a constant velocity and the pulling force is recorded and compared with the experimental data. The results prove a good performance of the penalty contact formulation (Figure 6-27).

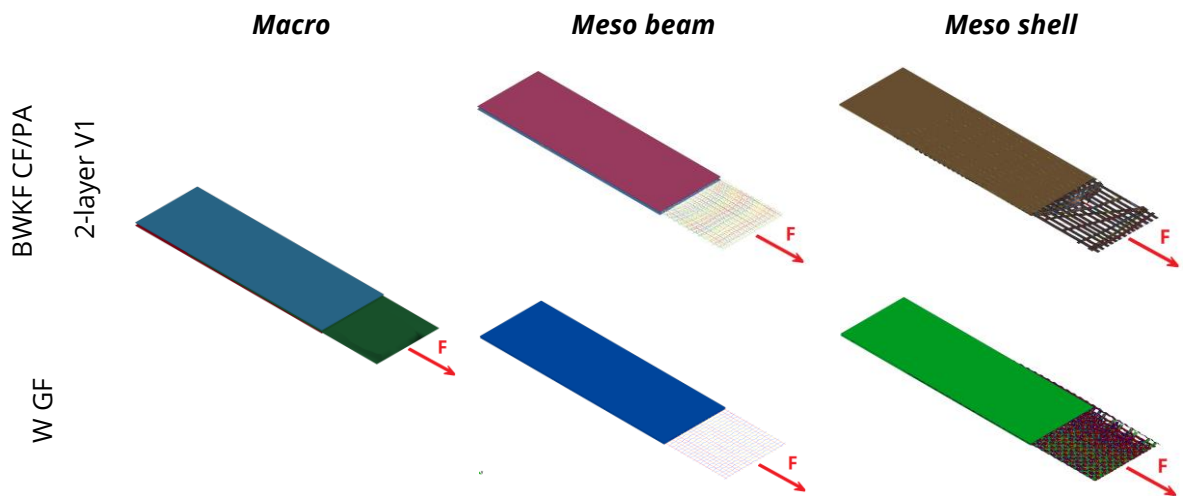


Figure 6-26: Friction test simulation

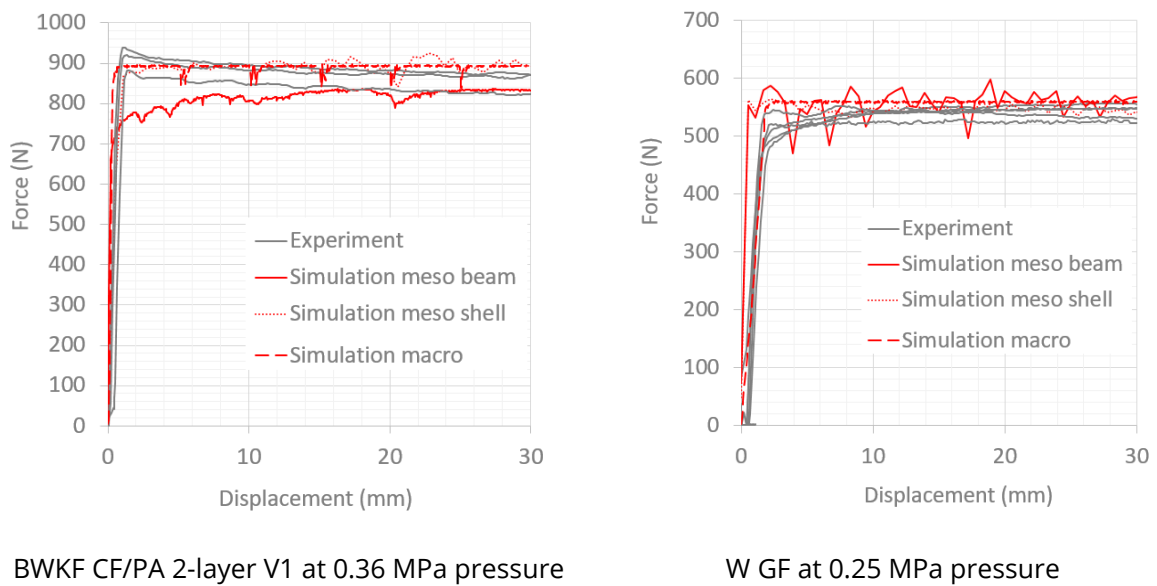


Figure 6-27: Comparison of force - displacement curves of friction test between experiment and simulation

Macro models provide the most stable force–displacement curves, as the contact between shell of textile model and shell of pressing tools is well regulated. The contact force simulated with the meso beam model of woven fabric indicates fluctuation in the first phase of the test but is more stable as the test proceeds. In the case of weft-knitted fabrics, the fluctuation of the force is less critical, but the deviation between experiment and simulation is significant in the initial phase. This issue is probably caused by the segment based penalty contact formulation, where beam elements are not compressible and the penetration depth fluctuates continuously in the initial phase. In the further course of the simulated force-displacement behavior, however, the force is stable. An explanation for this phenomenon is that the unstable penetration between segments decreases as the tensile force straightens the warp yarn system.

6.4 Summary

In this chapter, the development and validation of various textile models for BWKF and W GF have been presented. In general, the mechanical behaviors of textiles can be well described by the developed FEM models, except the shear behavior of meso beam model for W GF. The developed FEM textile models can now be used for investigation of the forming process in next chapter.

7 Simulation of forming process

7.1 Fabric forming with hemisphere tools

7.1.1 Experiment

The forming of 2D fabrics to 3D preform is tested on two different draping machines. Both of the machines were built by Nezami to serve his doctorate study [170]. The first draping machine has a stamp with hemisphere geometry (Figure 7-1). This draping machine was originally equipped with 8 segments of blank holder, where pressure on each segment of blank holder can be set independently. The hemisphere draping machine was later improved with a force sensor, which is attached directly above the stamp, and that allows to record the reaction force – displacement curve of the stamp during the forming process. The forming experiments were carried out with BWKF GF 2-layer and W GF. To investigate the role of blank holder force on defects in 3D preforms, the experiments were performed with and without blank holder. The blank holder force is applied by setting the pneumatic pressure at 2 bar, which causes a pressing force of circa 115 N on each blank holder segment. The experiments without blank holder force are hereafter denoted as “0 bar”, where the pneumatic system for the blank holder is practically not activated during the forming process. The experimental results (Figure 7-2) show clearly that without the presence of blank holder force, wrinkle formation by forming with doubly-curved surfaces such as hemisphere is not avoidable. The force – displacement curves of the stamp are recorded during the forming process by the force sensor and shown in Figure 7-3. The information from the force – displacement curves provides further insight on the forming mechanism of the textiles and their FEM models.

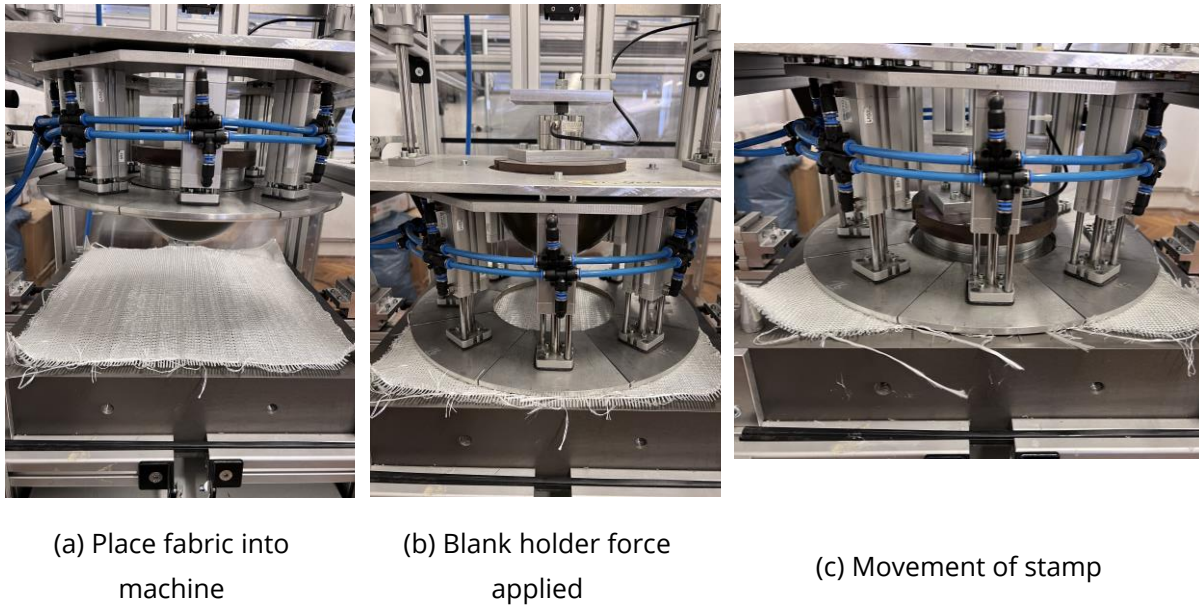


Figure 7-1: Forming of BWKF GF 2-layer with hemisphere draping machine with blank holder

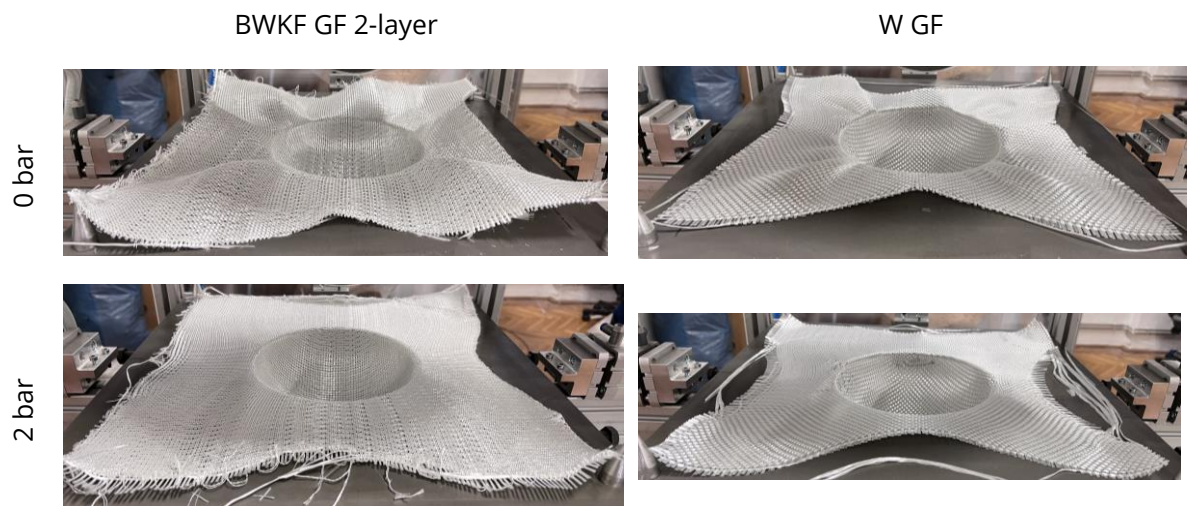


Figure 7-2: 3D preforms at different setting of blank holder pressure (right after forming)

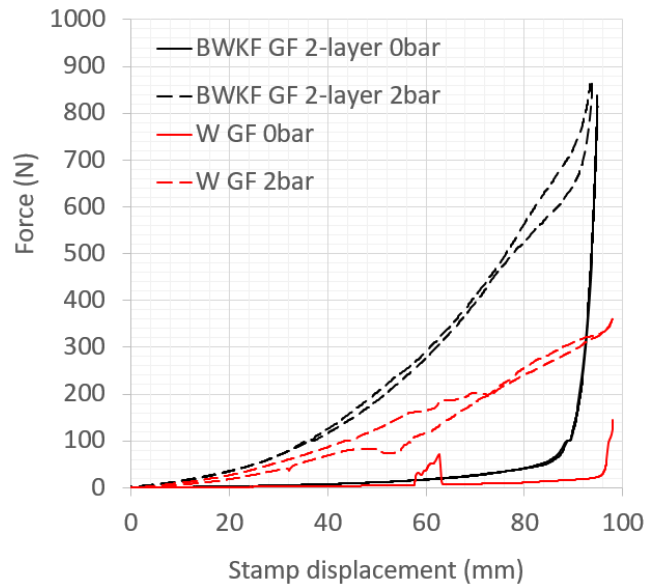


Figure 7-3: Force - displacement curves of stamp during forming process at different air pressure settings

7.1.2 Simulation

To evaluate the performance of each type of model that were introduced in Section 6.1 and 6.2, simulation with hemisphere draping tool is used. Only the most important parts of the machine, which have direct contact with the fabric, are modeled with rigid shell elements (Figure 7-4). The female tool is opened, not closed as on the draping machine. The simulation results are shown in Figure 7-5 (macro model), Figure 7-6 (meso beam model) and Figure 7-7 (meso shell model) for both type of fabrics.

The macro models provide good predictions of the risk of wrinkle formation for both type of fabrics and different forming conditions. At the pressure setting of 2 bar on blank holder segment, only few little wrinkles can be observed on 3D preform of plain woven fabric W GF. On the 3D preform of BWKF GF 2-layer, wrinkle formation is almost completely suppressed.

The meso-scale models with beam element for W GF, which failed to describe the shear behavior of the fabrics, deliver almost identical results for both cases with and without blank holder pressure. Such results again confirm the importance of including shear behavior in modelling technical textiles forming. The meso beam models for BWKF GF 2-layer give good results, as the shear behavior of the fabrics is taken into account.

The meso shell model of W GF provides very detailed results, where not only wrinkle formation is predicted but also other defect such as yarn sliding and yarn fall out. The

meso shell model of BWKF GF 2-layer also provides near reality results. As long as the shear behavior is taken into account, the model can predict wrinkle formation well.

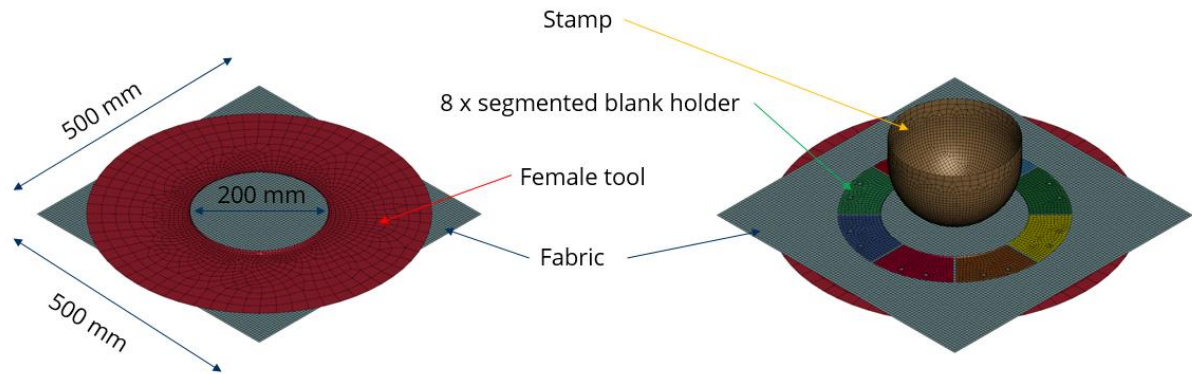


Figure 7-4: FEM model of hemisphere draping machine with macro model of fabric

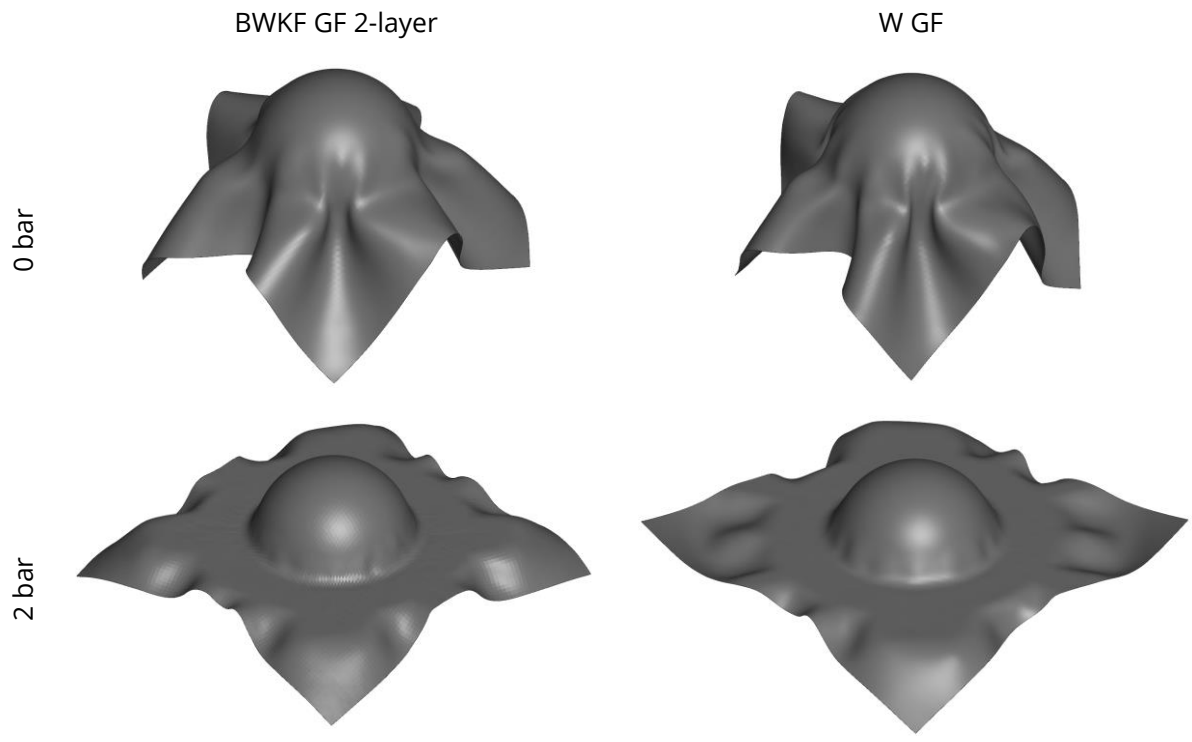


Figure 7-5: FEM forming simulation results with hemisphere tools with macro model of fabric

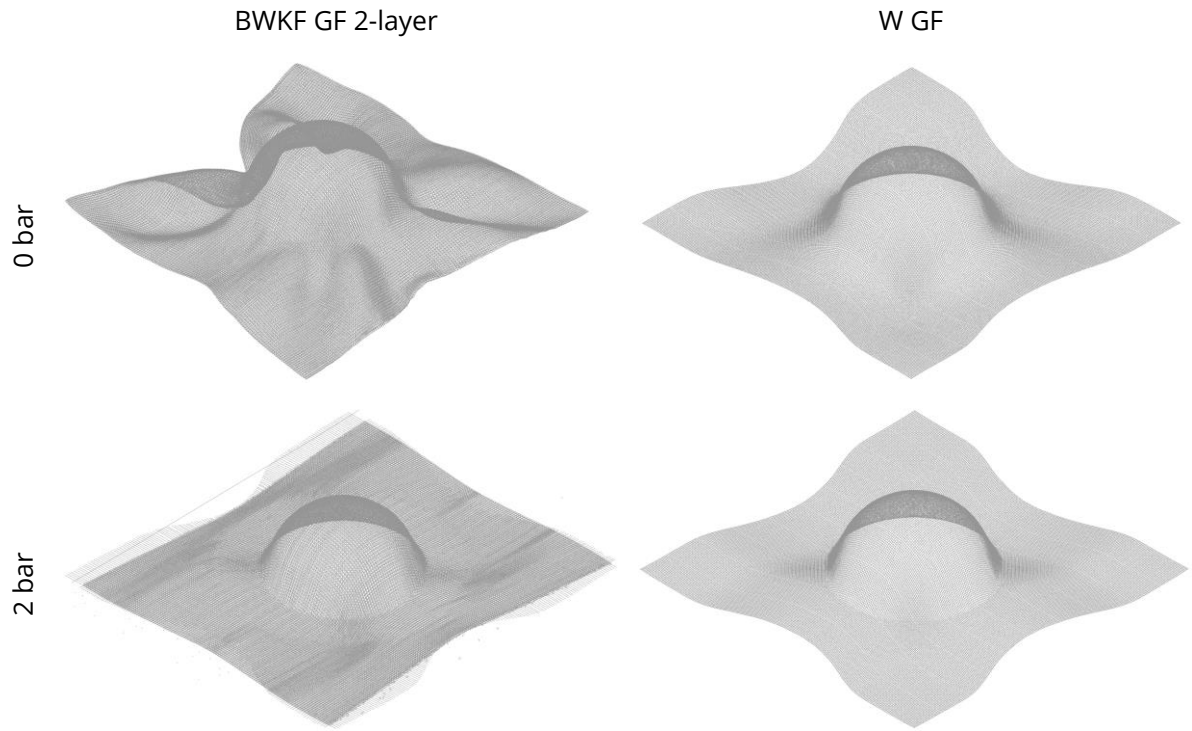


Figure 7-6: FEM forming simulation results with hemisphere tools with meso beam model of fabric

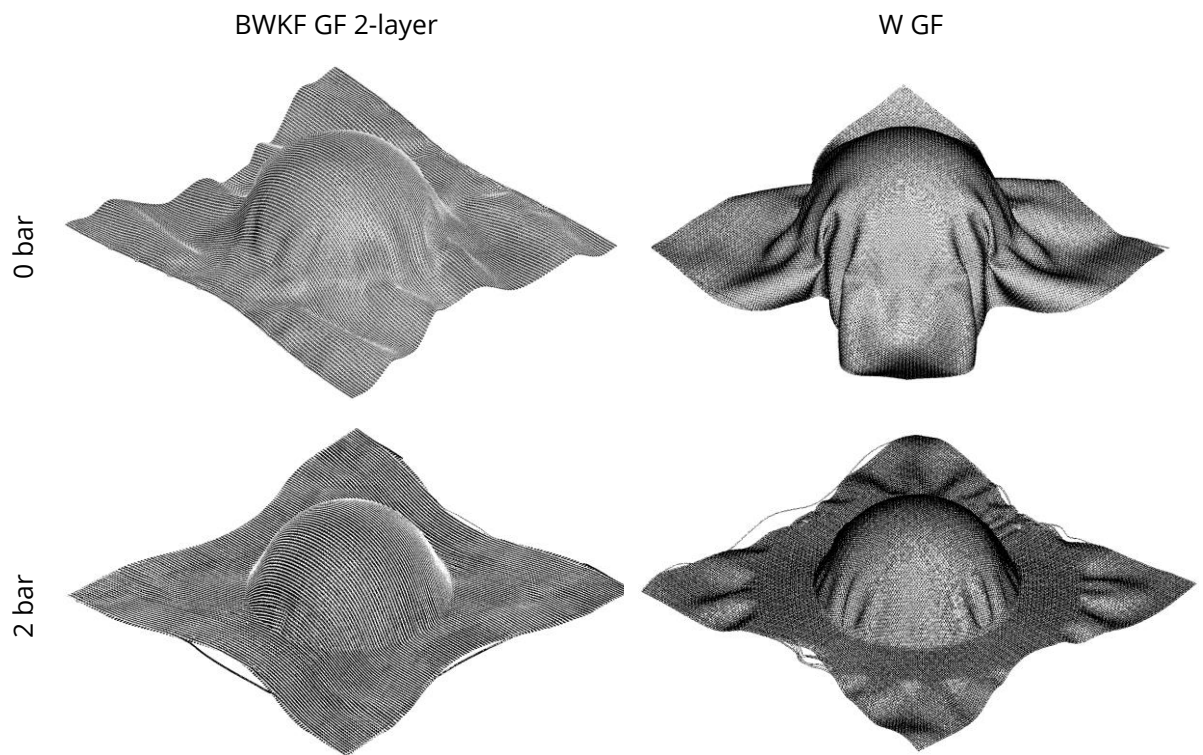


Figure 7-7: FEM forming simulation results with hemisphere tools with meso shell model of fabric

The contact force between textile model and forming tool is recorded and compared to the force that recorded by the force sensor on the hemisphere stamp during forming process (Figure 7-8). Meso beam model provides curves that deviate far from experiment in all cases. The contact force between beam (textile model) and shell element (tool model) was not properly recorded.

In the case of draping without blank holder force, the force – stamp displacement curves tend to rise rapidly from 80 mm displacement, which is probably the results of contact between stamp – wrinkle – female tool. As the female tool is modelled as opened in FEM model, such rise of force can barely be observed. Nevertheless, the simulation force – stamp displacement curves show agreement with the experiment curves in the initial area.

In the case of draping with 2 bar blank holder pressure, macro model provides good prediction for both type of fabrics with moderate deviation from 60 mm displacement. The meso shell model provides the most accurate prediction for force – stamp displacement curves, with lower deviation and better stability of curve. Based on the quantitative comparison of the force – stamp displacement curves between simulation and experiment, the meso shell model is the most reliable.

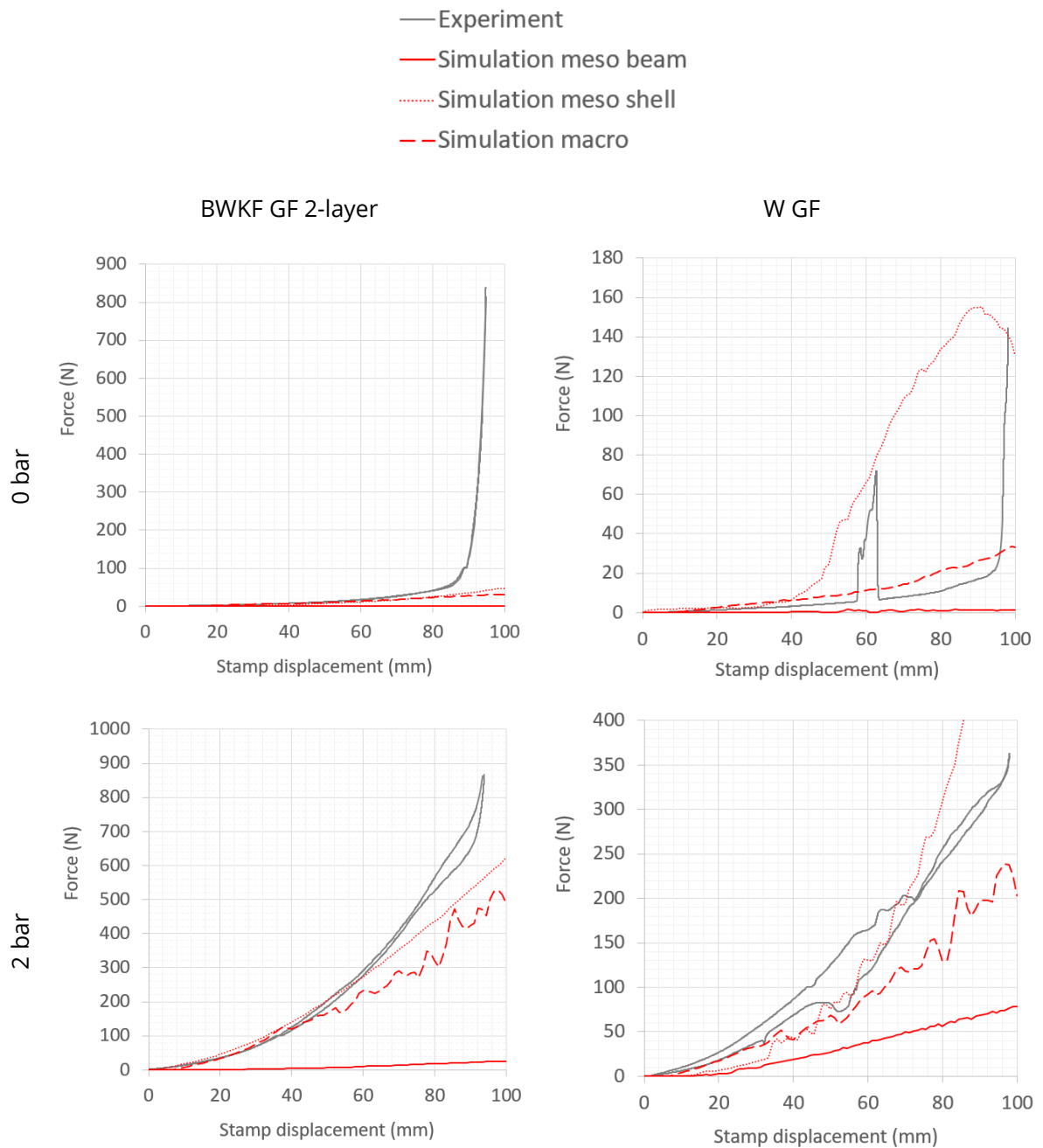


Figure 7-8: Comparison of the force - displacement curves of stamp during forming process between experiment and simulation

7.1.3 Influence of fabric configuration on forming behavior of BWKF

Influence of stitch length on in-plane shear behavior

In the work of Orawattanasrikul [225], BWKF were produced from GF 1200 tex for weft and GF 2400 tex for warp as reinforcement and GF 68 tex x 2 as stitching yarn with different setting of stitch cam depth (SCD at 14, 15, 16, 17 and 18 mm), which results in different stitch length SL (11.3, 12.4, 13.4, 14.4 and 15.4 mm). All variants of the BWKF were

tested with the picture frame. The test results show that the setting of SCD has significant influence on the in-plane shear behavior of BWKF. In principle, with shorter SCD (which also means shorter SL) the in-plane shear resistance is increased, while the critical shear angle is decreased (Figure 2-25). The BWKF GF 2-layer used in this thesis was produced with a SCD of 16 mm, where the actual SL of fabrics is about 13.6 mm. For the convenience, the SCD is here after used to denote the difference between variants of BWKF with different SL. Another difference between the BWKF in this work and the tested BWKF of Orawattanasrikul is the reinforcing yarn density in both weft and warp direction, namely 28 x 28 versus 39 x 20 (yarn/100mm). Supposed that the influence of SCD on in-plane shear behavior is reproducible (despite of the difference reinforcing yarn density) and shear force – shear angle curve of BWKF with certain SCD can be predicted by scaling the known curve of BWKF with other SCD. Another assumption is that, the scale factor between variants of BWKF with different SCD in this thesis is similar to BWKF in the work of Orawattanasrikul, the shear force – shear angle curves of BWKF GF 2-layer with different SCD can be predicted as shown in Figure 7-9. Here the shear force – shear angle curve of the tested BWKF GF 2-layer (16 mm SCD) is used as the start point. The other curves are produced by manipulating the shear force – shear angle curve of BWKF GF 2-layer (16 mm SCD) with 2 scale factors: scale factor for abscissa (sfa) and scale factor for ordinate (sfo), which can be set directly by the definition of the curve [518]. The calculation of sfa and sfo is according to the Equation (7-1) and (7-2). The max. shear force of BWKF x mm SCD and the corresponding shear angle are taken from the tested results of Orawattanasrikul.

$$sfo (x \text{ mm SL}) = \frac{\text{max. shear force of BWKF } x \text{ mm SCD}}{\text{max. shear force of BWKF } 16 \text{ mm SCD}} \quad (7-1)$$

$$sfa (x \text{ mm SL}) = \frac{\text{shear angle at max. shear force of BWKF } x \text{ mm SCD}}{\text{shear angle at max. shear force of BWKF } 16 \text{ mm SCD}} \quad (7-2)$$

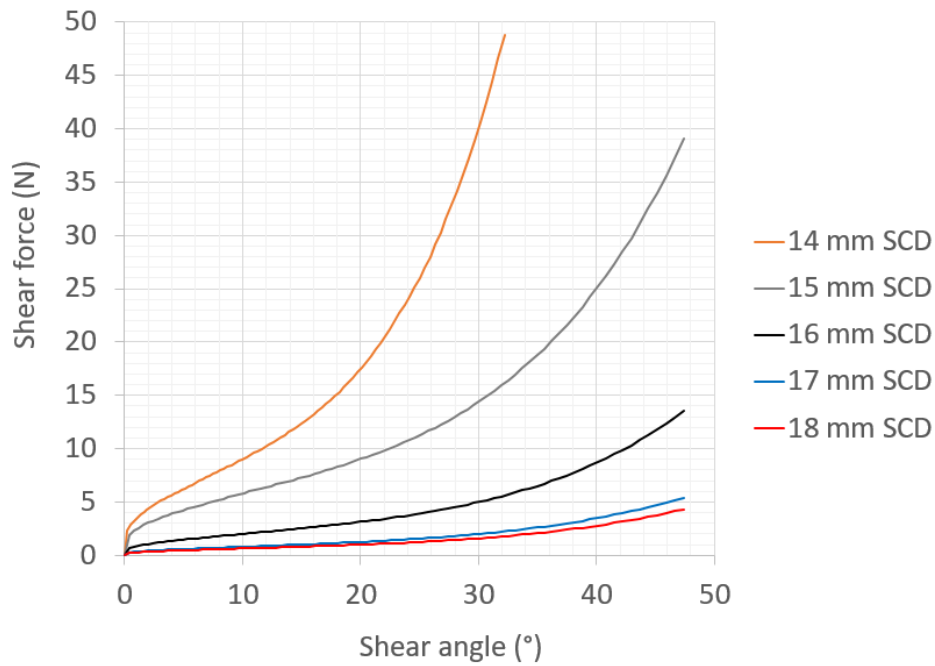


Figure 7-9: Shear force - shear angle curves of BWKF GF 2-layer with different SCD

To answer the question, how the SCD of BWKF can influence the quality of 3D preforms, macro model can be used, where the shear modulus – shear strain curves $G_{xy}(\tan(\varphi_{xy}))$ is used directly as an input of the model. The draping simulation with hemisphere tools is carried out with the shear modulus – shear strain curves of 14 mm and 18 mm SCD setting, while other parameter stay the same as the tested BWKF GF 2-layer 16 mm SCD. Bending stiffness of BWKF also increases by the decrease of SCD, but as no quantitative experimental data is available, this phenomenon is neglected here. The blank holder pressure is set at 2 bar. The simulation results suggest that, when the shear resistance of textile increased by changing SCD, there is risk of wrinkle formation by the model with 14mm SCD. The shear ability of BWKF with 14 mm SCD is limited, and can hardly reach further shear angle without wrinkle formation. In contrary, when the shear resistance is decreased with the setting of 18 mm SCD, the difference is not significant in comparison to the 16 mm SCD.

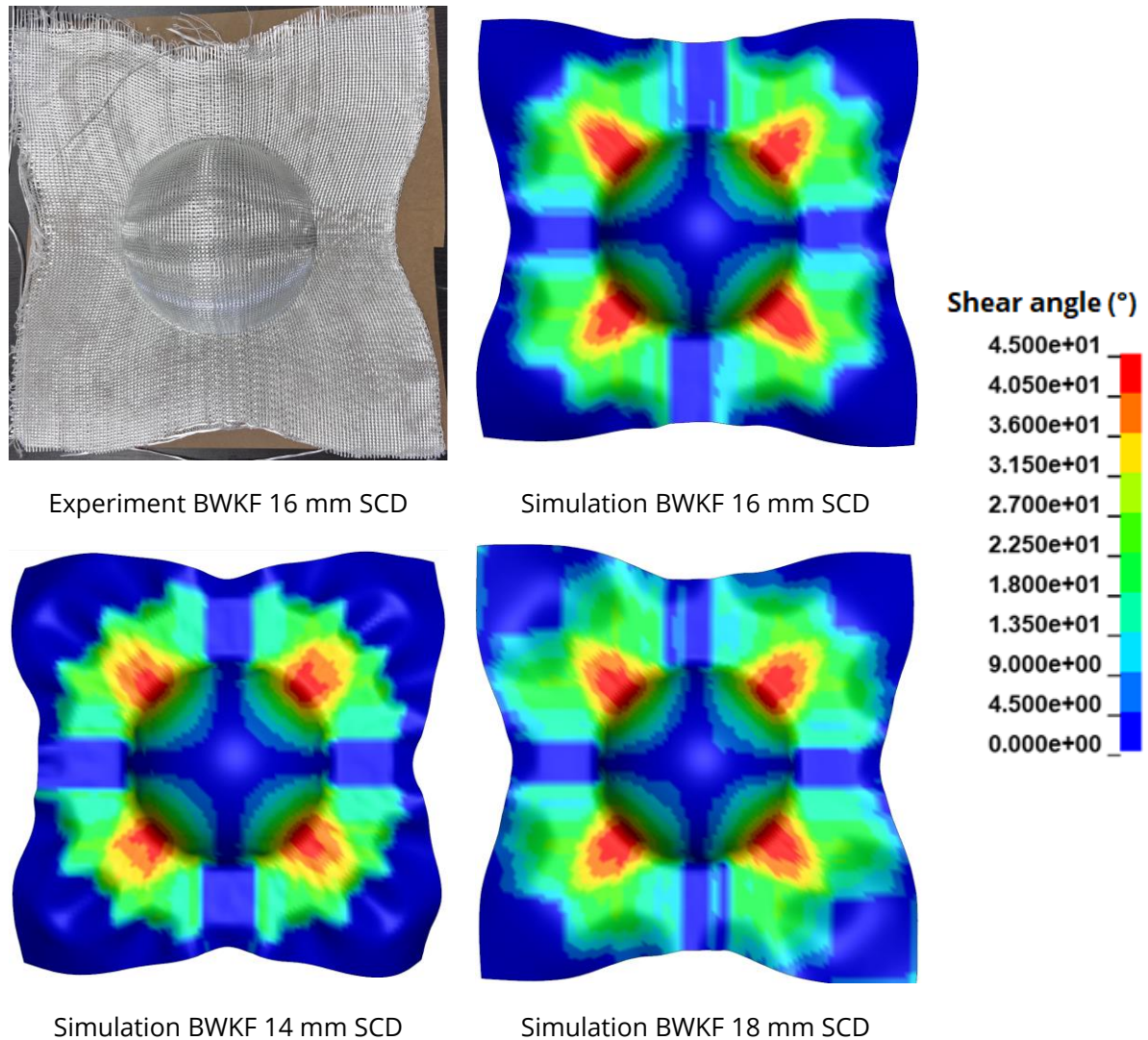


Figure 7-10: Simulative analysis of the influence of SCD on 3D preform quality (BWKF GF 2-layer)

Influence of yarn sliding resistance on shear behavior

Another influence of SCD on forming behavior is indirectly via the interaction between the stitching yarn and the reinforcing yarns. The shorter the stitching yarn is, the stronger interact the stitching yarn and reinforcing yarns with each other, and that prevents the reinforcing yarns from sliding. A quantitative assessment of the yarns sliding resistance in textile can be carried out by yarn pull-out test, which has been done by Orawattanasrikul in his doctorate study, as well as in Section 5.3.5 for BWKF CF/PA 2-layer V1. According to the finding of Orawattanasrikul, the pull-out force in both warp and weft direction is increased significantly when the SCD is decreased in the range of 15-18 mm, e.g., about double from SCD 16 to 15 mm. Another important finding of Orawattanasrikul is, that the pull-out force of plain woven fabrics is absolutely higher than BWKF, as the

yarns in woven structure are firmly fixed through the interwoven of yarns. That fact would partly explain the high shear resistance of plain woven during picture frame test (Figure 5-13).

The experimental data in Section 5.3.3 suggested that BWKF with high yarn sliding resistance reaches the incompressible state faster under shear loading, i.e., decrease of the critical shear angle. It would be useful, if the relation between yarn sliding resistance and in-plane shear can be numerically investigated. Here, a meso-scale model is necessary, where stitching yarn and reinforcing yarn are modelled separately.

With the help of the meso shell model for BWKF (Section 6.2.2), the influence of SCD on yarn sliding, eventually on in-plane shear behavior can be investigated. Firstly, the pull-out force of meso shell model for BWKF CF/PA 2-layer V1 is tested with the help of a simple yarn pull-out simulation (Figure 7-11). Here, the boundary conditions are taken exactly from the experiment in Section 5.3.5. As the friction coefficient CoF between yarns was not available, the friction between textile and metal from Table 5-9 is used instead. The simulation results show good correlation between experiment and simulation (Figure 7-12). Due to instability of the contact formulation, great vibrations occur in the pull-out force – displacement curves.

Supposed that the yarn sliding resistance is doubled by changing SCD of BWKF CF/PA 2-layer V1 from 16 to 15 mm. The friction coefficient between beam and shell element in the meso shell model for BWKF can be artificially set to double to increase the yarn sliding resistance in model. The simulation of picture frame test with periodic boundary condition (Figure 6-21) is used. The simulation result suggests that, by such increase of yarn sliding resistance, the max. z-displacement of BWKF under shear loading is also increased faster, i.e., the shear locking angle is reached sooner.

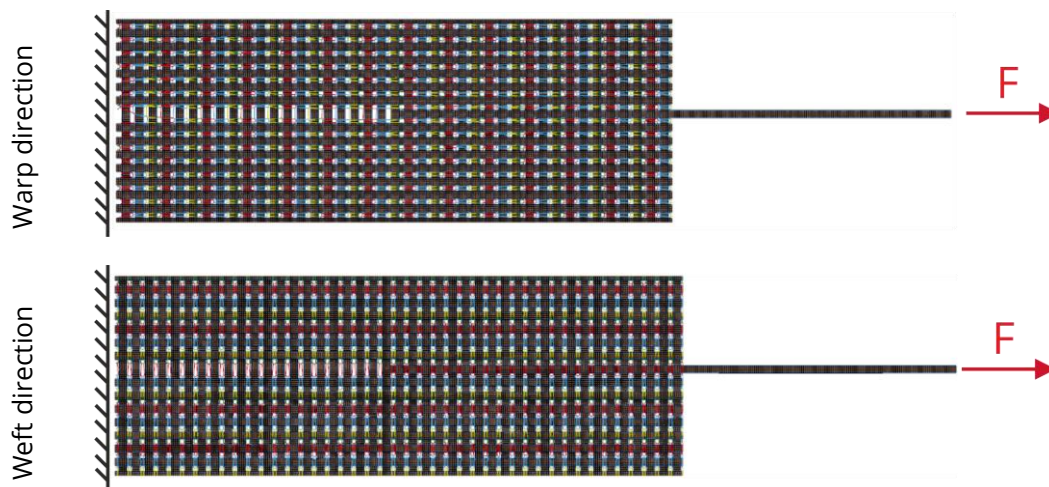


Figure 7-11: Yarn pull-out simulation for BWKF CF/PA 2-layer V1 with meso shell model

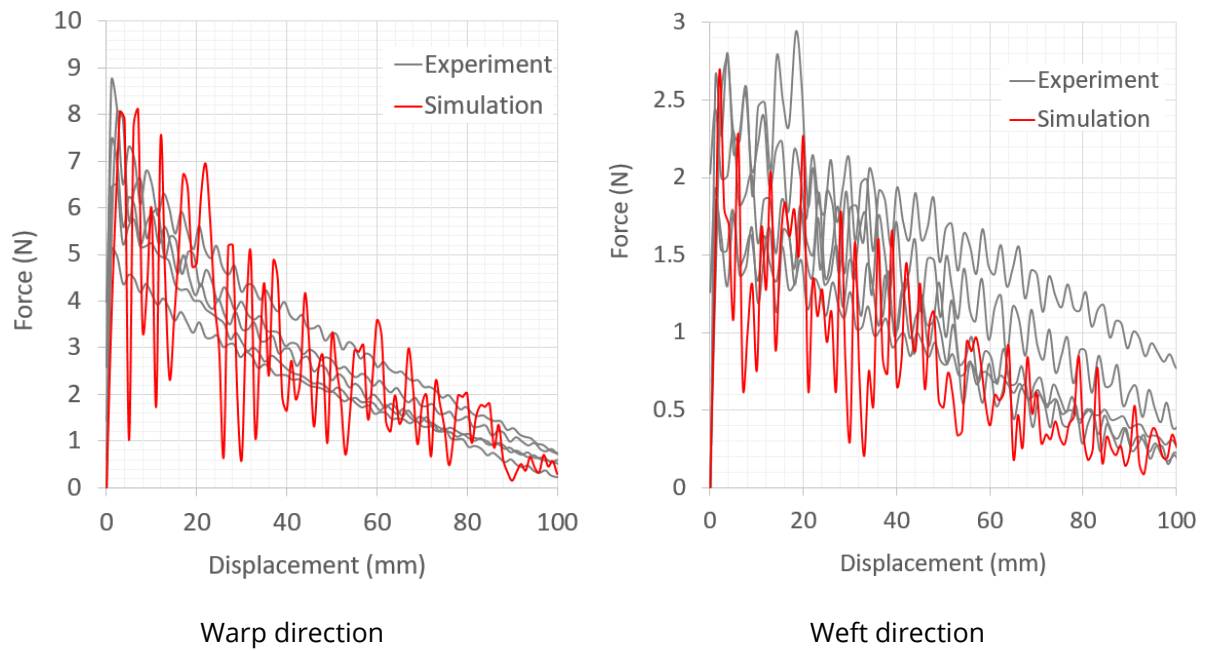


Figure 7-12: Comparison of yarn pull-out force between experiment and simulation of BWKF CF/PA 2-layer V1 (Friction coefficient CoF = 0.15)

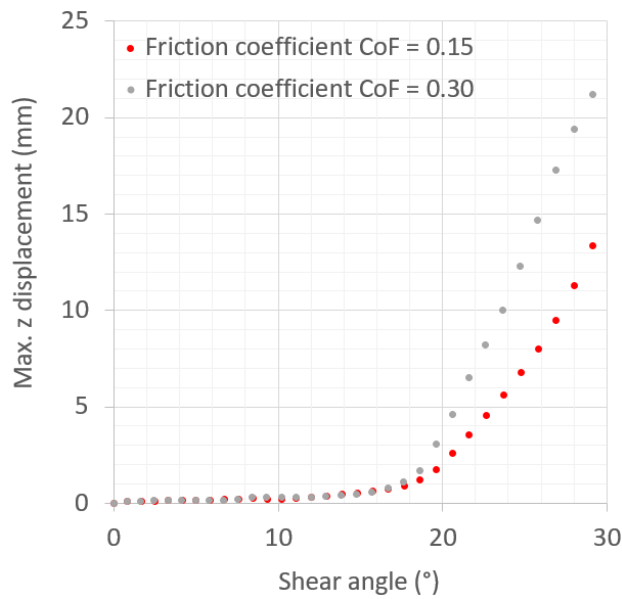


Figure 7-13: Influence of yarn sliding resistance on shear behavior

Influence of stitch yarn material on in-plane shear

The GF 68 tex x 2 is the standard stitching yarn for BWKF and was used earlier [225]. It was used as sole stitching yarn for BWKF GF 2-layer and in combination with PA 6.6 94 tex as fold yarn for BWKF CF/PA 6.6. In contrary to GF, which is a high performance fiber with

great stiffness and low break elongation, PA 6.6 is an elastic plastic material with lower stiffness and great break elongation (see Figure 5-3). To investigate the role of the knitting yarn on in-plane shear behavior of BWKF, the meso shell model is used again. This time, the material parameter of stitching yarn in model for BWKF CF/PA 2-layer V1 is set to PA 6.6. The simulation results show no significant different of the max. z displacement - shear angle curves between the two variants (Figure 7-14) but noticeable different of the wrinkle shape at 40° shear angle (Figure 7-15). This result suggests that the material properties of stitch yarn has limited influence on the in-plane shear behavior. However, under actual forming process, where blank holder force is strong, greater gap formation due to reinforcing yarn sliding can be expected, as elastic-plastic material such as PA 6.6 has low stiffness and great elongation.

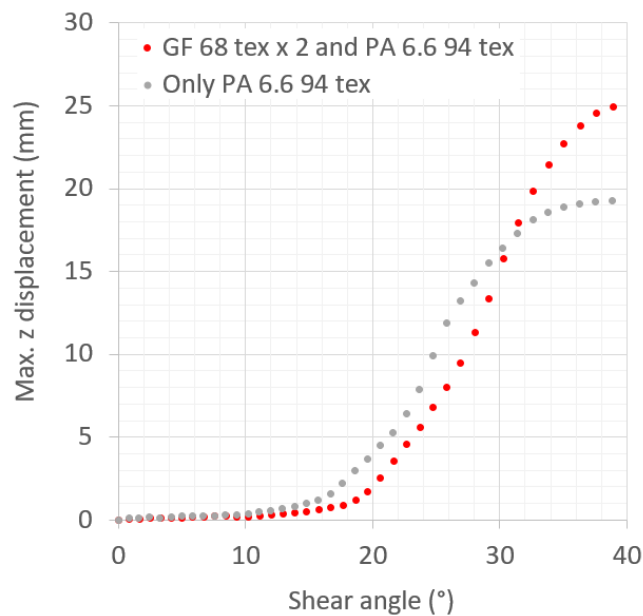


Figure 7-14: Comparison of max. z displacement - shear angle curves between simulation with different stitch yarn material

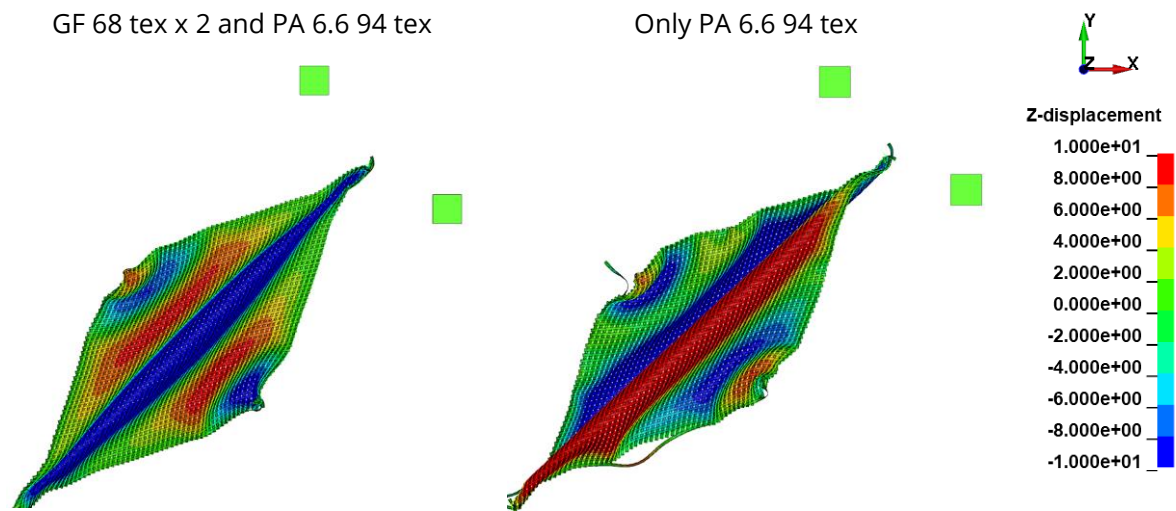


Figure 7-15: Displacement in thickness direction (z direction) of textile FEM models with different stitch yarn material at 40° shear angle

Influence of weft yarn density on forming behavior

In contrary to the warp yarn density, which is dependent on the machine gauge (or machine fineness, defined as needle per inch) of the knitting machine, the weft yarn density can be adjusted in-flight by configuration of SCD and velocity of take-out roller. For example, the BWKF CF/PA 2-layer has a setting of SCD 17 mm (SL 14.4 mm) for V1 and SCD 16 mm (SL 13.4 mm) for V2, where the weft yarn density is increased from 28 to 41 yarn/dm. Eventually, the difference of the shear force – shear angle curves between V1 and V2 is clearly recognizable (Figure 5-14). Under shear loading, BWKF with higher weft reinforcing yarn density tends to reach the shear locking state faster. Same conclusion was also drawn in the work of Orawattanasrikul.

Again, with the help of the forming simulation with hemisphere tools and macro-scale model of textile, the influence of weft yarn density on 3D preform is numerically investigated. All of the forming behavior of the macro-scale model such as tensile, bending and in-plane shear of BWKF CF/PA 2-layer V1 are validated in Section 6.3. The macro-scale model of V2 is also validated with the same method as presented in the paper [520]. The influence of weft yarn density on the bending stiffness is also taken into account (see Table 5-7). Bending stiffness of textile in both warp and weft direction is increased, when the weft yarn density is increased. Based on the simulation results as shown in Figure 7-16, the forming ability of BWKF CF/PA 2-layer has no major change and is still good, despite of the increase of weft reinforcing yarn density up to factor 1.5.

layer on the hemisphere forming machine (Figure 7-18). The force – displacement curves also show good agreement between simulation and experiment with deviation from 80 mm displacement (Figure 7-19).

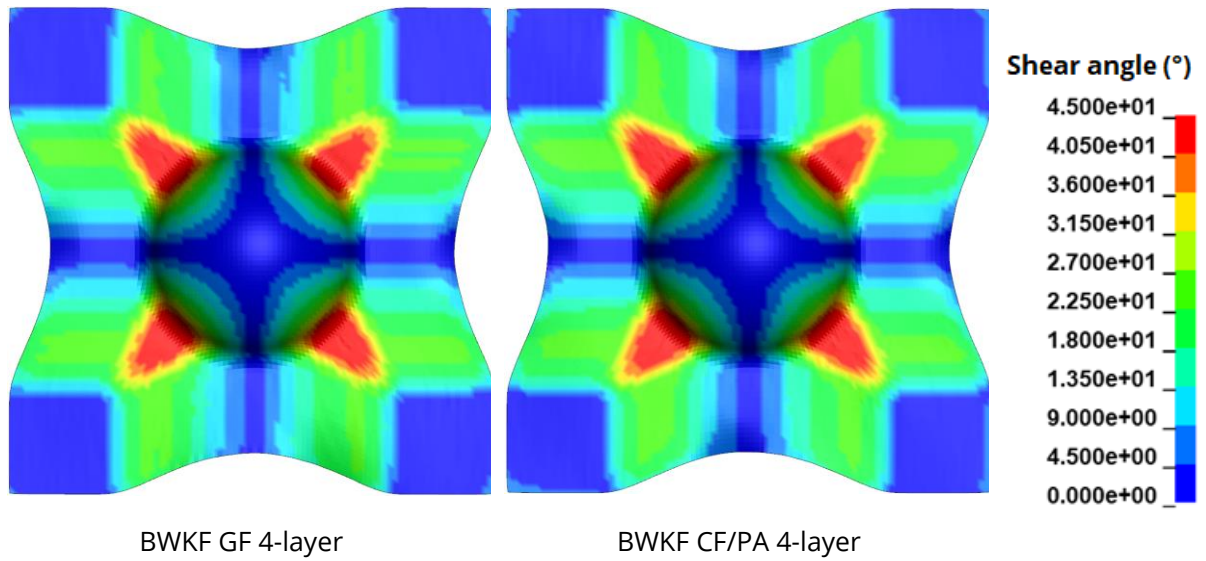


Figure 7-17: Simulative analysis of the influence 3D preform quality by forming BWKF 4-layer



Figure 7-18: 3D preform of BWKF CF/PA 4-layer at 2 bar setting of blank holder pressure (right after forming)

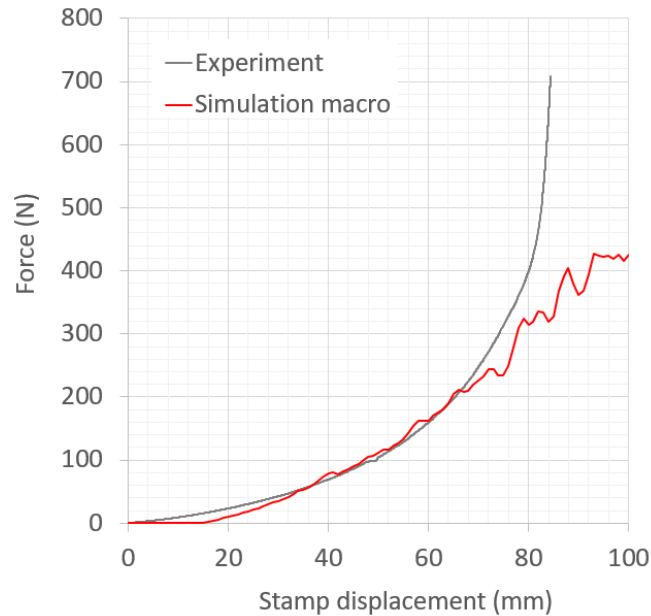


Figure 7-19: Comparison of the force - displacement curves of stamp during forming process between experiment and simulation for BWKF CF/PA 4-layer

7.2 Fabric forming with L-profile shape tools

7.2.1 Experiment

The second forming machine has L-profile tools (Figure 7-20). The geometry of the stamp is a free form surface and a simplification of the geometry of the lamp pot on an automobile (Figure 7-21). This forming machine was built by Nezami [170] to demonstrate the idea that the quality of the 3D preform can be improved by active manipulation of the blank holder forces. The forming simulation with the L-profile forming tool is used for benchmarking the performance of the models by predicting the fiber orientation under certain forming condition. The forming experiments are carried out with two types of fabrics BWKF CF/PA 2-layer V1 (Figure 7-22) and W GF. Two arrangements of the fabrics are used: $0^{\circ}/90^{\circ}$ and $+45^{\circ}/-45^{\circ}$ (Figure 7-23). An identical load of 44 N is set for each of the 8 blank holder segments. In general, the 3D preforms of BWKF CF/PA 2-layer V1 have almost no wrinkle formation but only some gap formation due to yarn sliding (Figure 7-30). The 3D preforms of W GF have minor wrinkle formation and gap formation (Figure 7-31).

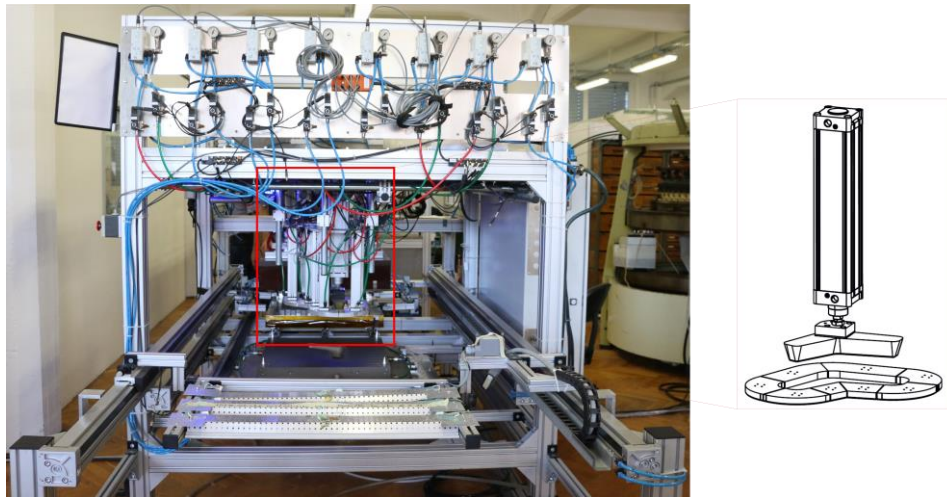


Figure 7-20: Overview of the L-profile draping machine

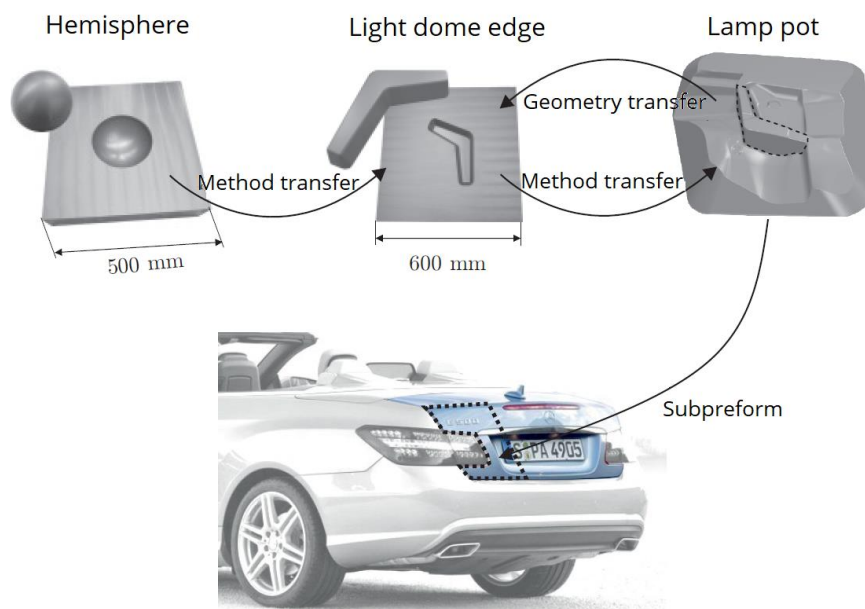


Figure 7-21: Origin of the L-profile geometry © Nezami [170]

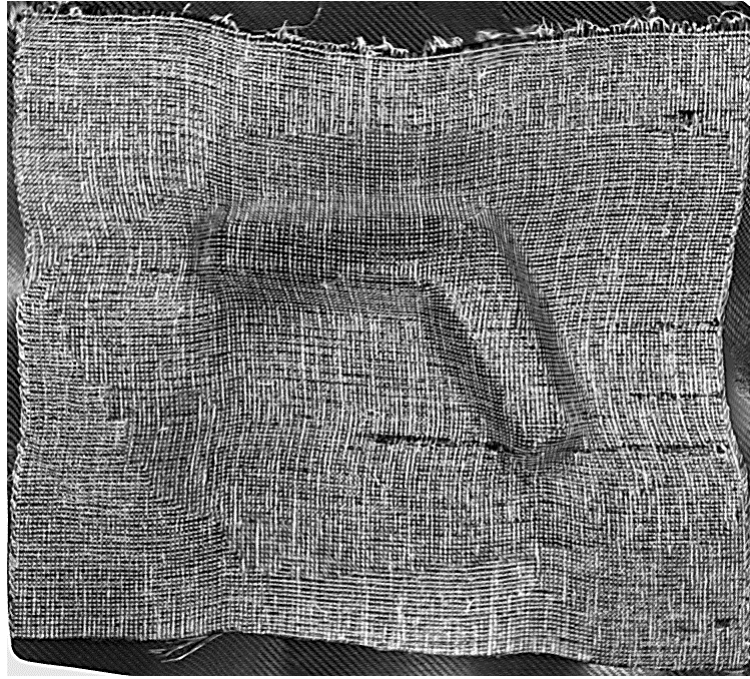


Figure 7-22: 3D preforms of BWKF CF/PA 2-layer V1 with homogenous blank holder pressure on the L-profile draping machine at 0°/90° orientation (overview)

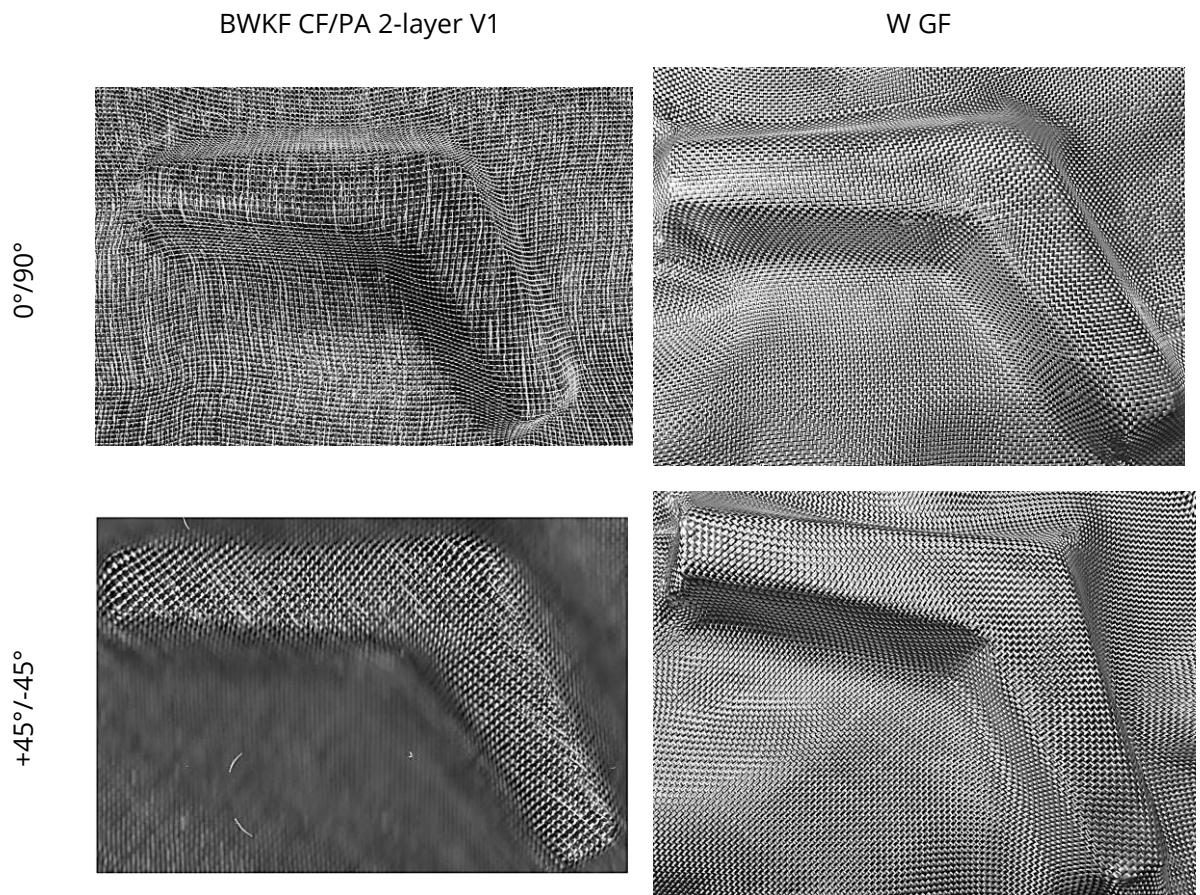


Figure 7-23: 3D preforms with homogenous blank holder pressure on the L-profile draping machine at different textile orientation (detail view)

7.2.2 Simulation

Forming tools are modelled with rigid shell elements (Figure 7-24). The female tool (yellow) has a dimension of $600 \times 600 \text{ mm}^2$ and is fixed in all translational and rotational motions. The stamp (green) and the blank holder segments (in various colors) can only move in the vertical direction. The motion of the stamp is prescribed with a constant velocity, while each blank holder segment is under a load of 44 N, exactly as the setting on the forming machine for the experiments. The models of the fabric are placed in between the female tool and the segmented blank holders. Two lay-ups with different orientation of the fabrics are used for the forming simulation: $0^\circ/90^\circ$ and $+45^\circ/-45^\circ$ (Figure 7-25 and Figure 7-26). The results of the simulations are shown in Figure 7-27 (macro model), Figure 7-28 (meso beam model) and Figure 7-29 (meso shell model). The macro model of both type of textile predict some wrinkle formation at the middle of the top of the L-profile, which did not really occur in the experiments. The forming simulation results with meso model show no such wrinkle at the middle of the top 3D preform. This can be explained by the ability to slide independently of warp and weft reinforcing yarn in experiment as well as meso models, which macro model cannot correctly describe because it simplifies whole textile structure as continuum matter.

Models of BWKF CF/PA 2-layer V1 predict no further major wrinkle formation in the useful area of the preforms, which agrees good with the experiment. Meso beam model for W GF is not able to predict any wrinkle formation, due to its lacking of shear resistance properties, while macro and meso shell model of W GF show clear wrinkle formation.

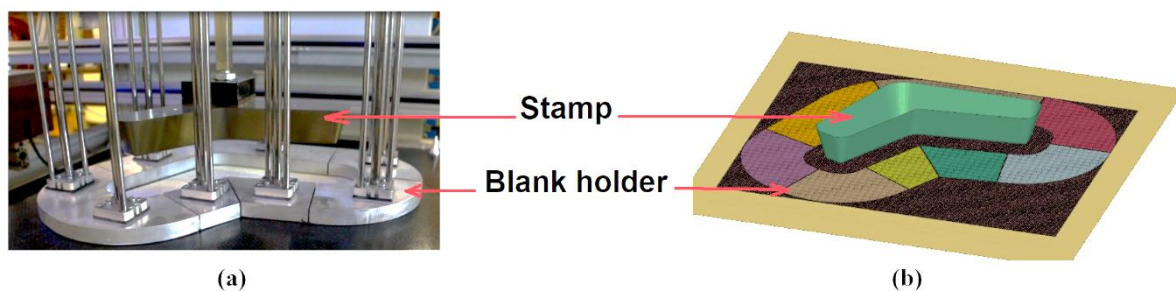


Figure 7-24: (a) Forming tool with L-profile and (b) FEM model

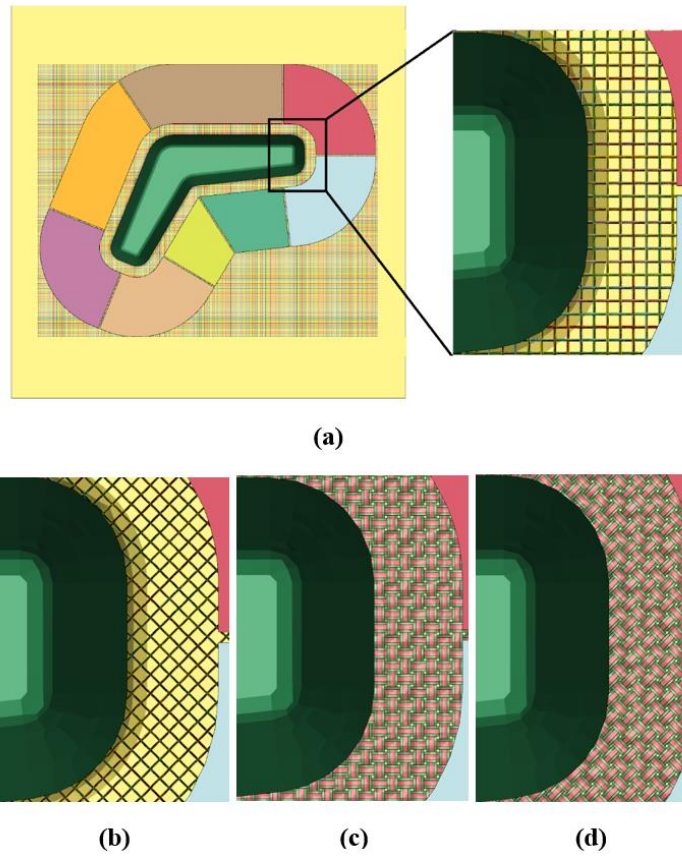


Figure 7-25: Lay-up of the W GF models in the forming simulation model: (a) meso beam model $0^{\circ}/90^{\circ}$, (b) meso beam model $+45^{\circ}/-45^{\circ}$, (c) meso shell model $0^{\circ}/90^{\circ}$ and (d) meso shell model $+45^{\circ}/-45^{\circ}$

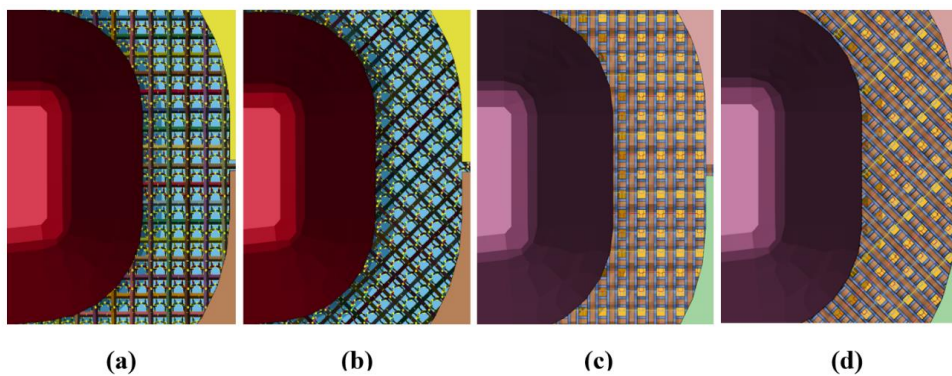


Figure 7-26: Lay-up of the BWKF CF/PA 2-layer V1 model in the forming simulation: (a) beam model $0^{\circ}/90^{\circ}$, (b) beam model $+45^{\circ}/-45^{\circ}$, (c) shell model $0^{\circ}/90^{\circ}$ and (d) shell model $+45^{\circ}/-45^{\circ}$

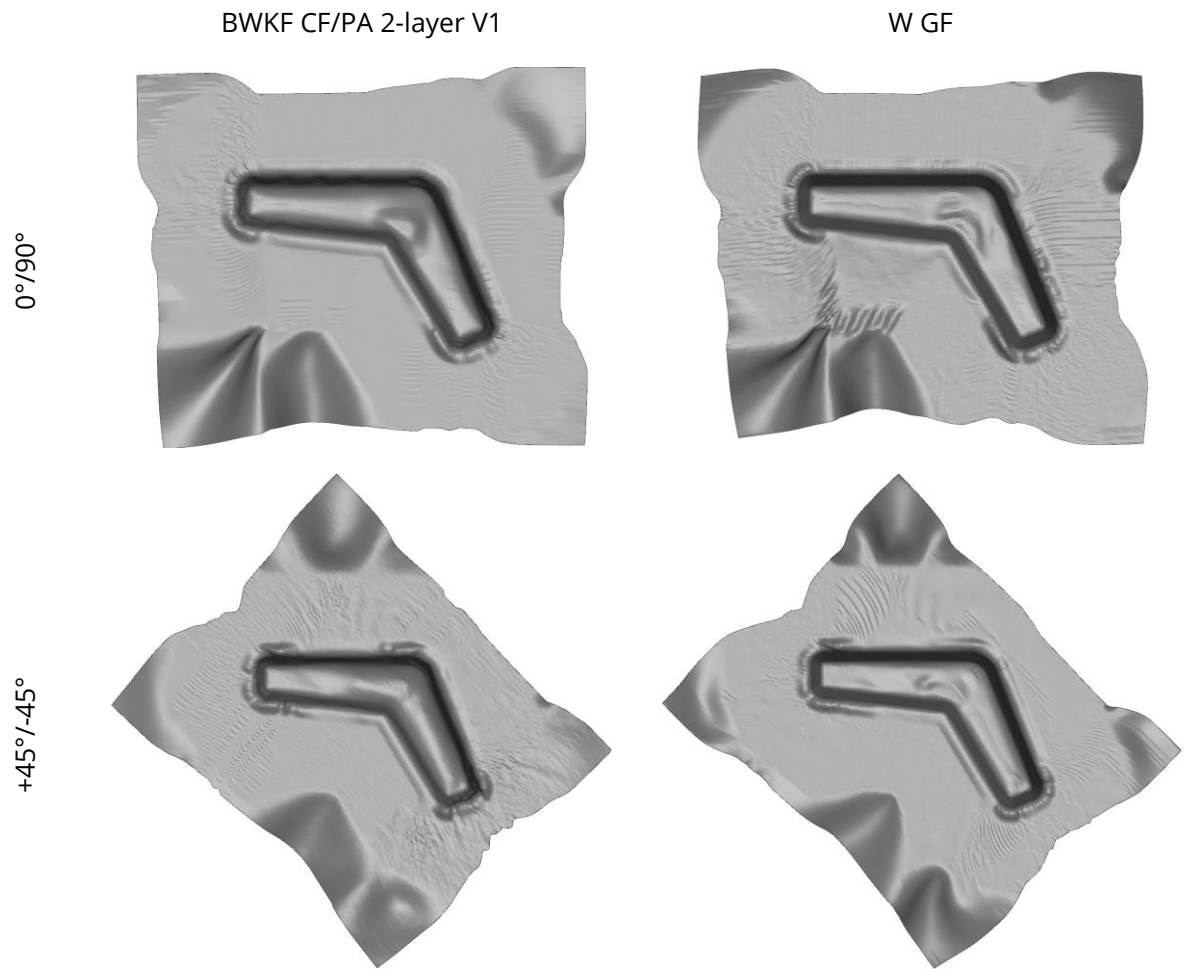


Figure 7-27: 3D preforms results from simulation with macro models

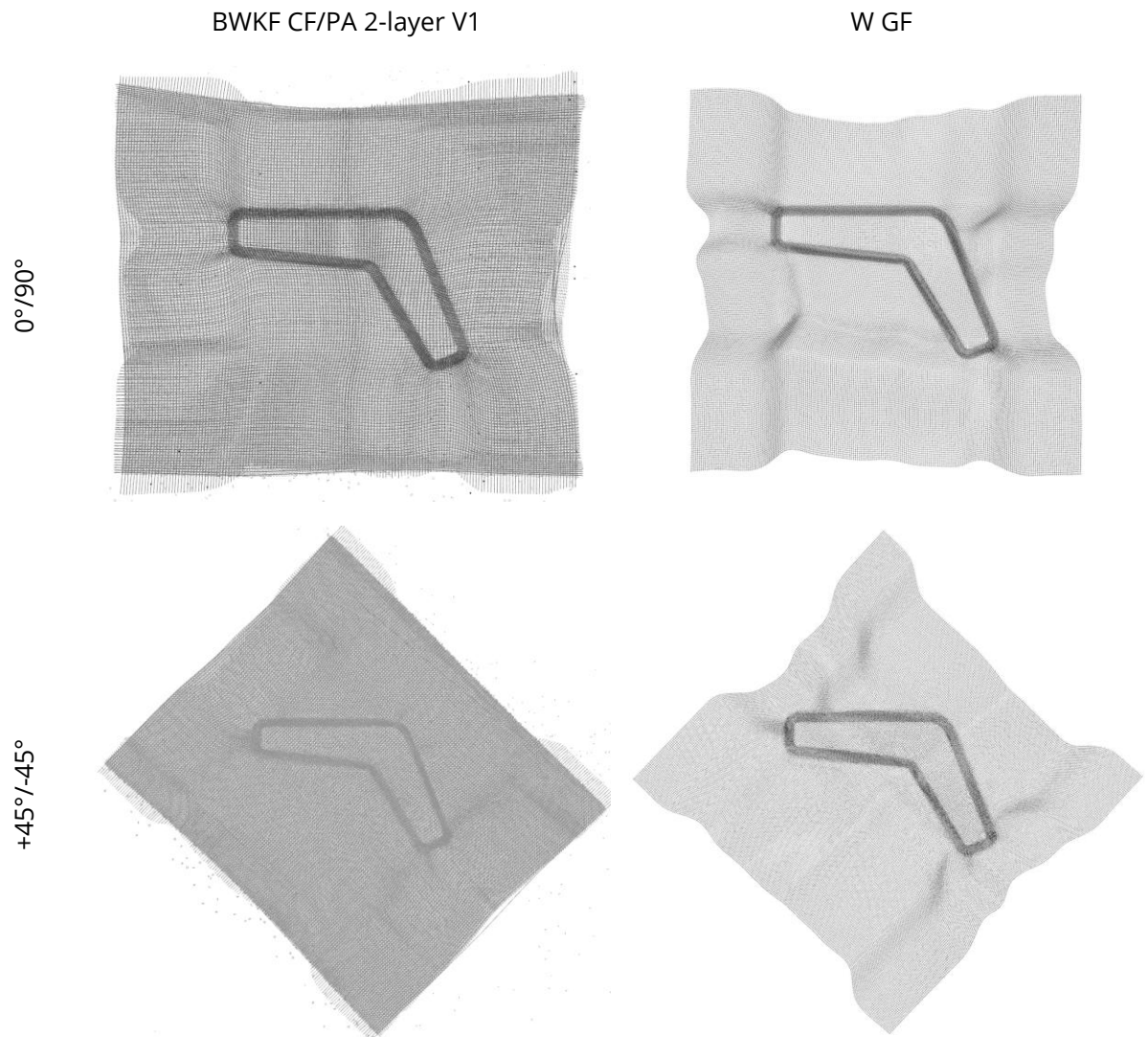


Figure 7-28: 3D preforms results from simulation with meso beam models

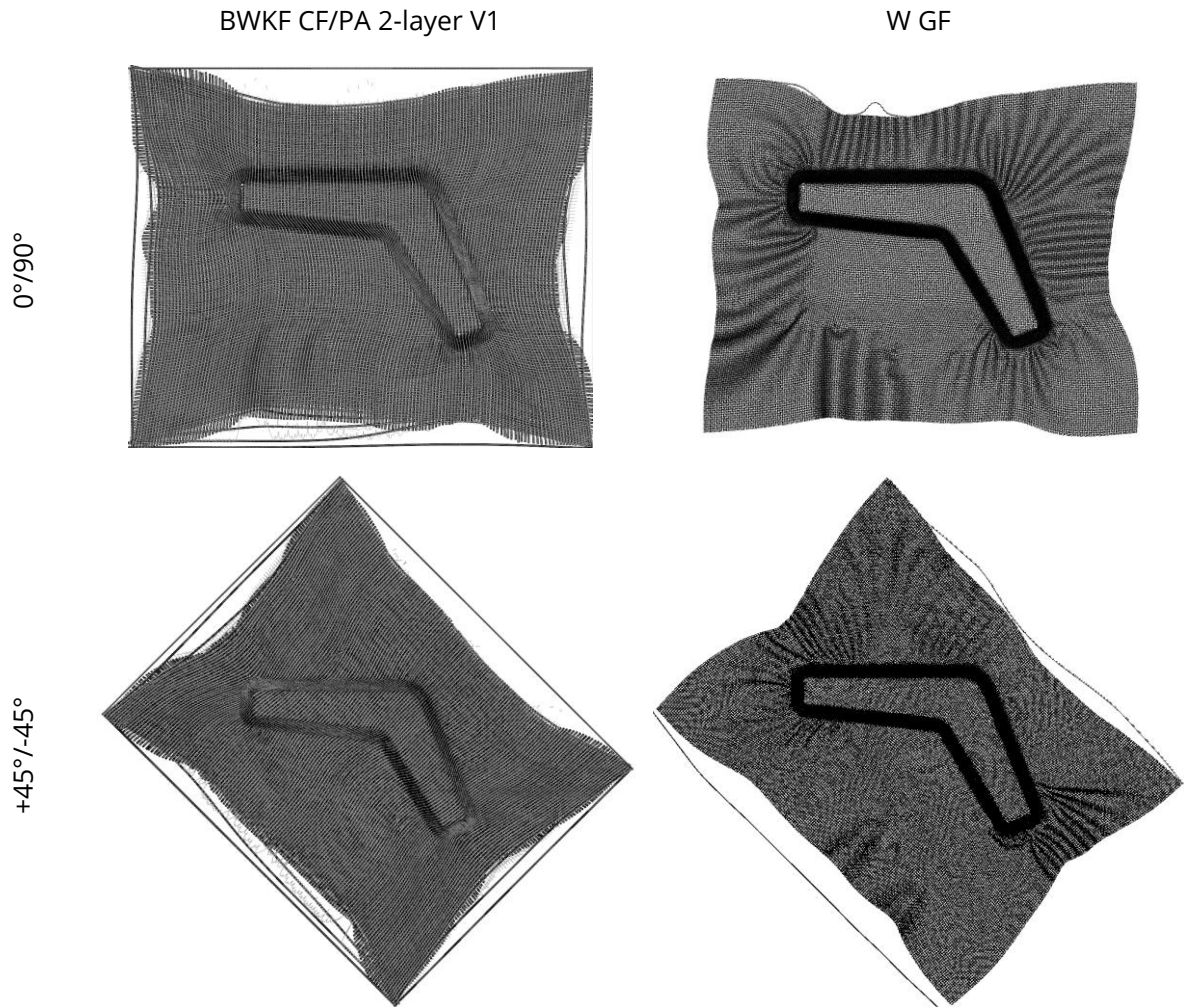
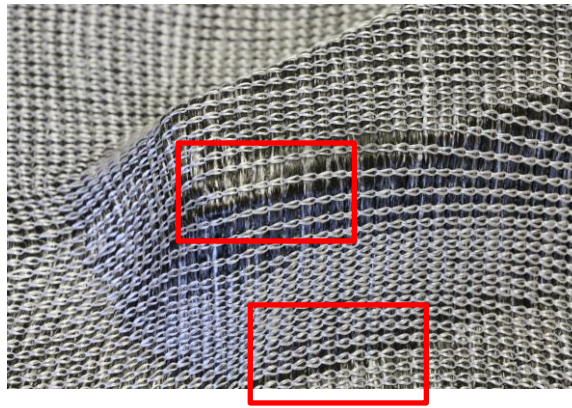
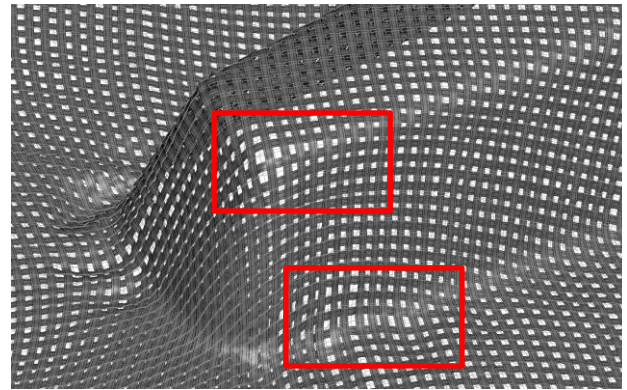


Figure 7-29: 3D preforms results from simulation with meso shell models

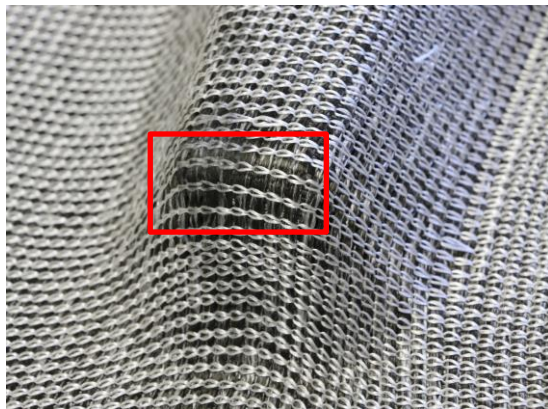
The gap formation can be observed at the lower right corner and upper left corner of the 3D preform. The cause of such gap formation is sliding of yarn far away from their neighbours. The gap formation on 3D preform of BWKF CF/PA 2-layer V1 (Figure 7-30) and W GF (Figure 7-31) can be predicted well by the meso models. Such prediction cannot be given by macro model, where the whole textile is considered as a continuum. Without a clear description of constitutional yarn systems and the relative movement between them, prediction of gap formation is simply impossible.



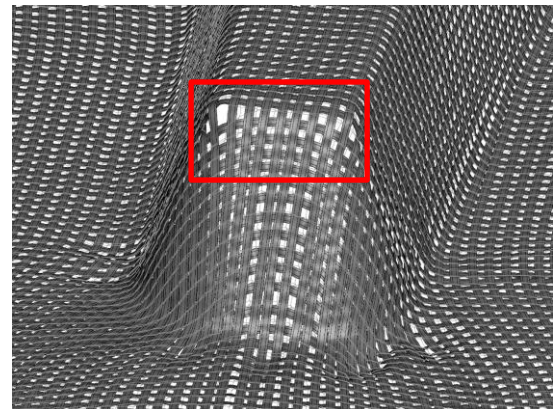
Experiment (lower right corner)



Simulation meso shell (lower right corner)

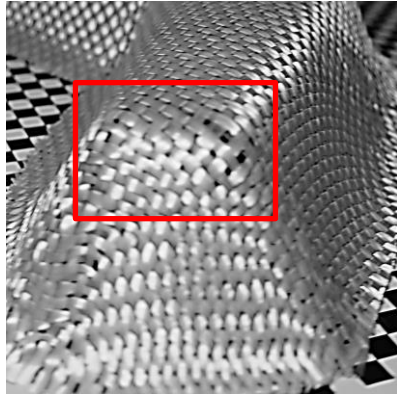


Experiment (upper left corner)

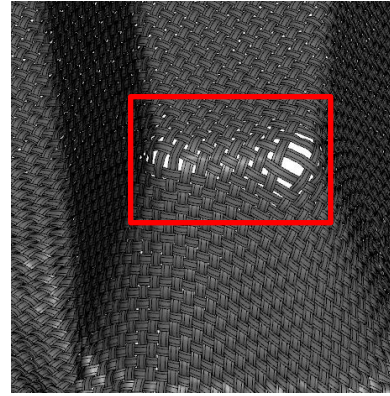


Simulation meso shell (upper left corner)

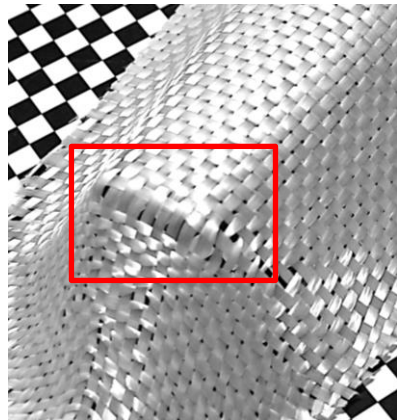
Figure 7-30: Gap formation of the 3D preform due to yarn sliding by forming BWKF CF/PA 2-layer V1 with orientation 0°/90° of textile



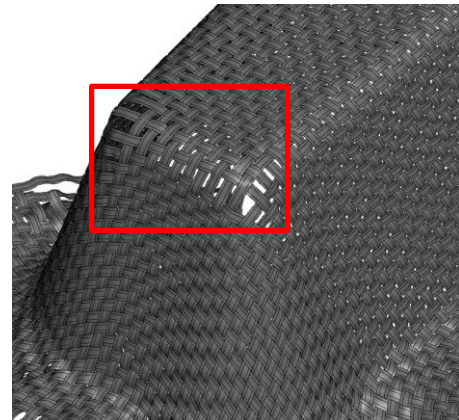
Experiment (lower right corner)



Simulation meso shell (lower right corner)



Experiment (upper left corner)



Simulation meso shell (upper left corner)

Figure 7-31: Gap formation of the 3D preform due to yarn sliding by forming W GF with orientation 0°/90° of textile

The orientation of the reinforcing yarns in the warp direction on top of the L-profile 3D preforms is used as a quantitative evaluation criterion for the performance of the models. Fiber orientation is the angle of the fiber measured from the horizontal line as shown in Figure 7-32. Both results from forming experiments (Figure 7-23) and simulation with different types of FEM model (Figure 7-27, Figure 7-28 and Figure 7-29) are employed for the measurement. The measuring results are presented in Figure 7-33 and Figure 7-34.

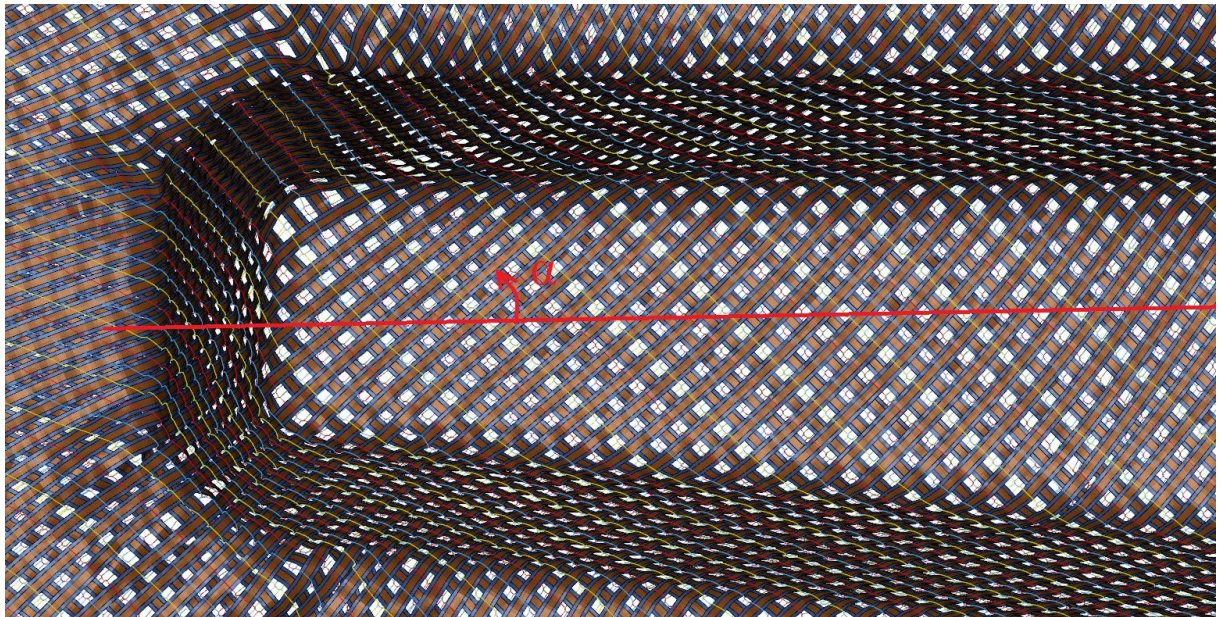


Figure 7-32: Measurement of the fiber orientation for meso shell model of BWKF CF/PA 2-layer V1 with orientation +45°/-45° at the upper left corner

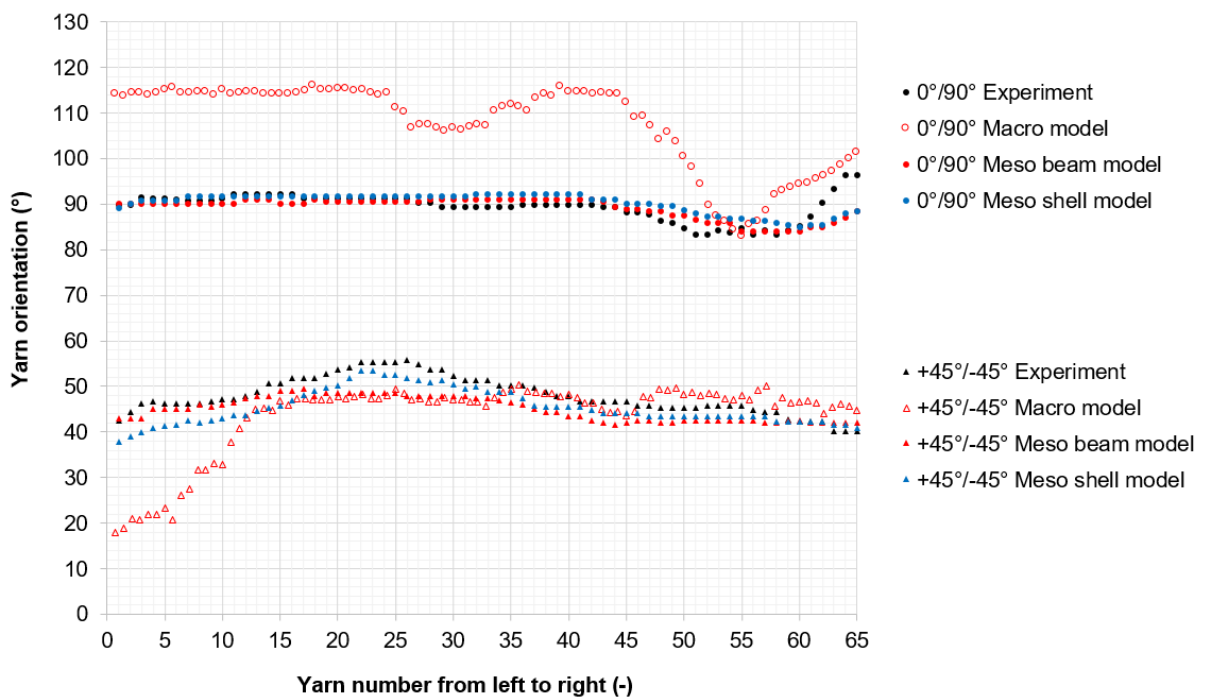


Figure 7-33: Orientation of yarns on the top side of L-profile 3D preforms from BWKF CF/PA 2-layer V1 in the experiment and prediction with the meso-scale models

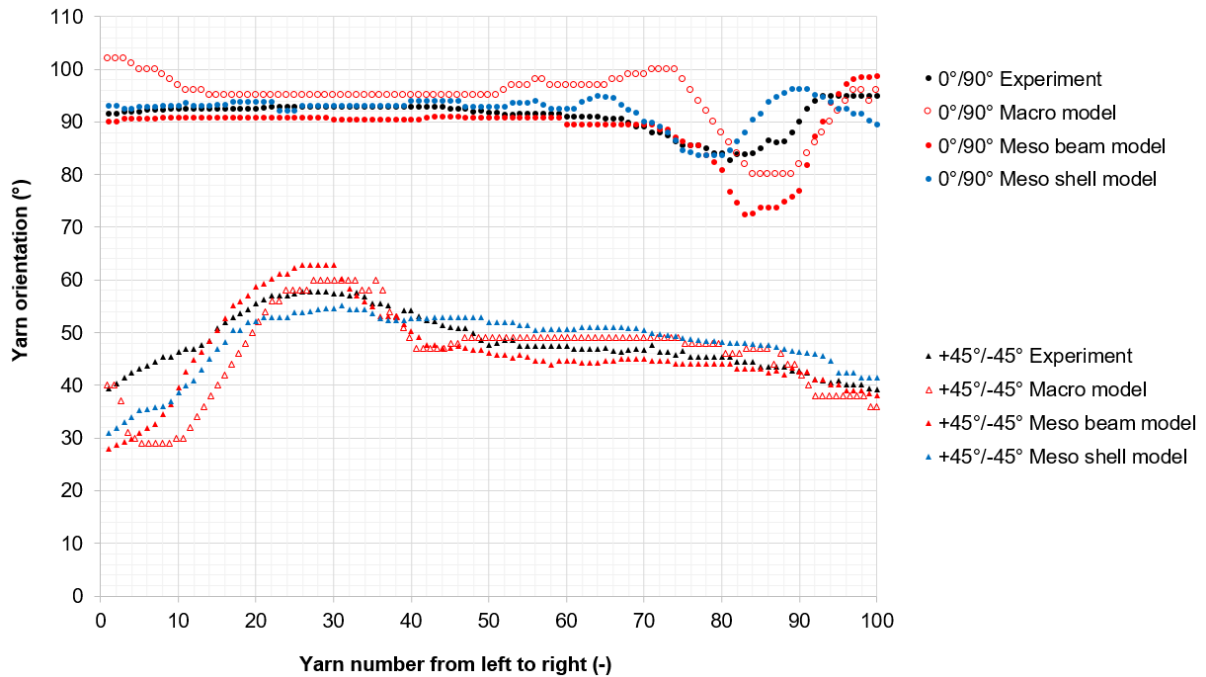


Figure 7-34: Orientation of yarns on the top side of L-profile 3D preforms from W GF in the experiment and prediction with the meso-scale models

In general, the prediction of all models (except the macro scale) approach is quite near to the real yarn orientation. According to the measuring results of the 3D preforms from experiments with $0^\circ/90^\circ$ lay-up, the orientation of the reinforcing warp yarn remains relatively stable at the beginning, and the orientation starts decreasing around the 70th yarn (for plain woven fabrics) and the 45th yarn (for the biaxial reinforced weft-knitted fabrics). The orientation reaches a minimum value before it increases again. In the case of the $+45^\circ/-45^\circ$ lay-up, the orientation starts increasing from the beginning, reaches a maximum value around the 25th yarn (for both fabrics), and decreases towards the end. The predictions of the FEM models are generally good as they can capture the tendency of the yarn orientation in both lay-ups. In the case of W GF, the model with shell elements shows a recognizable improvement by the prediction of the fluctuation of the yarn orientation. In the case of BWKF CF/PA 2-layer V1, the prediction with the models with shell elements also lead to less deviation. In the area of lower right corner (the last 20 yarns) and upper left corner (the first 20 yarns) as shown in Figure 7-30 and Figure 7-31, where the yarn tends to slide away from its neighboring yarns to form a gap between them, the model with beam element has a significantly higher deviation of yarn orientation compared with the shell element model. This is due to the simplification of the beam cross-section, thus, the beam element having more space for sliding than in the case of a shell element. Hence, in this context, models with shell elements offer considerable advantages.

The axial force of beam elements as well as effective stress of shell elements can be observed by means of forming simulation results (Figure 7-35). This information can be used to evaluate the risk of fabric damage during the forming process. However, due to the lack of means for evaluating the damage to 3D preforms, a direct comparison between beam and shell models is not possible in this aspect. Nevertheless, the lower right corner and the upper left corner appear to be with high risk of yarn damage due to high tensile stress.

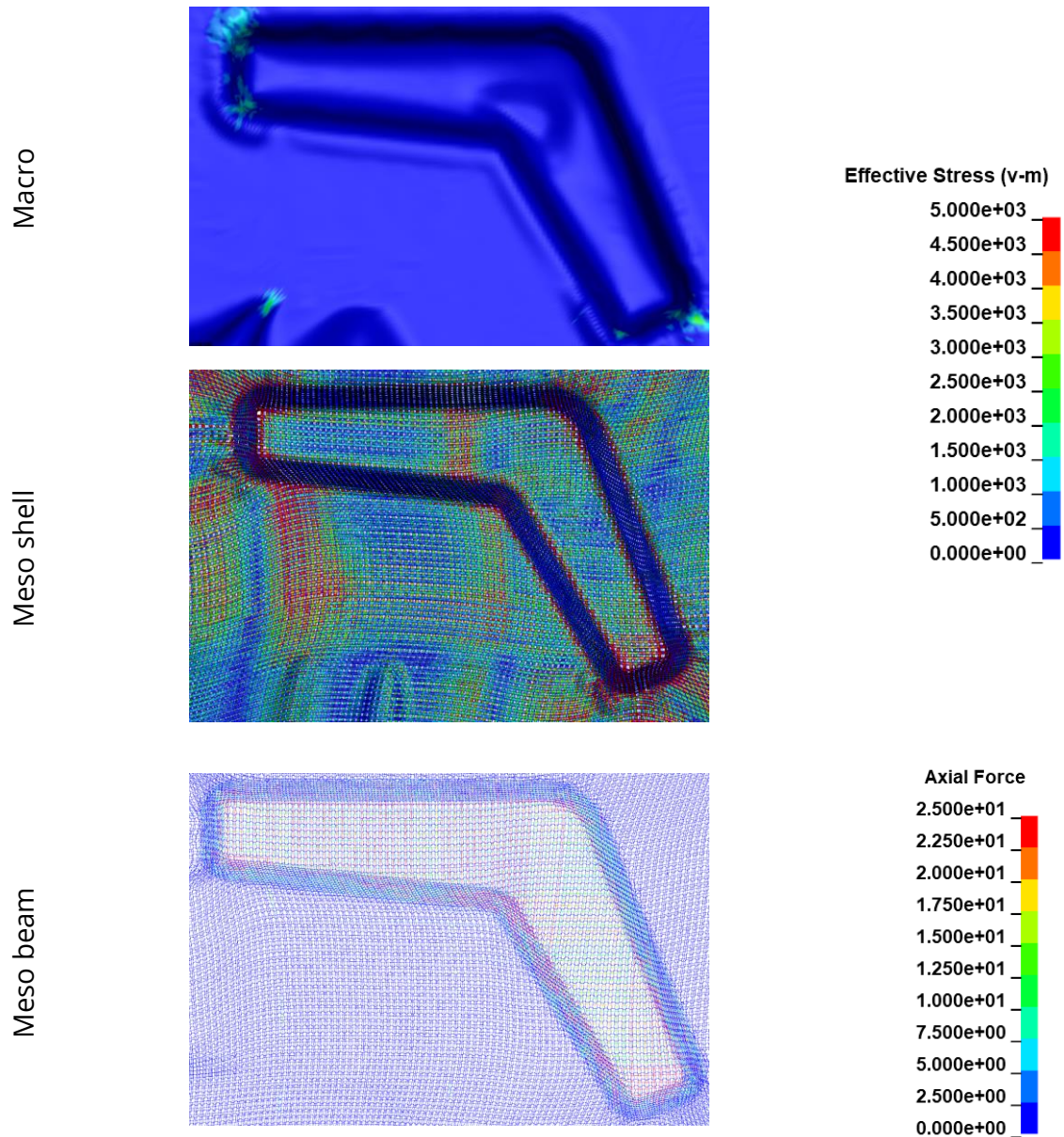


Figure 7-35: Effective stress (in MPa) of macro and meso shell model; axial force (in N) of meso beam model of BWKF CF/PA 2-layer V1 with 0°/90° lay-up

7.3 Simulative development of T-cup forming tools

A conceptual forming tools has been initially suggested to investigate the influence of dimension of the T-cup geometry on the 3D preform (Figure 7-36). The stamp has a height of 100 mm and the female tool is open. A blank holder is available to test the influence of blank holder force on 3D preforms.

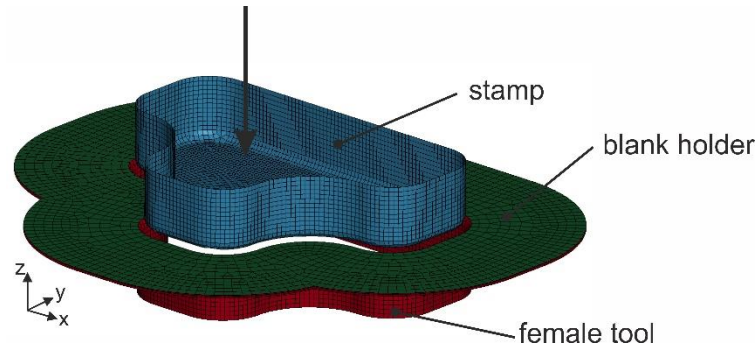


Figure 7-36: Model of the forming tool with T-shape geometry (arrow showing movement of the stamp)

The forming simulations are carried out with macro and meso beam model. The textile model is placed between the blank holder and the female tool. The stamp forms the textile into the female tool while the blank holder restrains the textile. Two different blank holder forces are initially tested: 0 N (no blank holder force at all) and 100 N. The results of forming simulation with both macro and meso beam models for the BWKF CF/PA 2-layer V1 are shown in Figure 7-37. In general, the results from both models show similar results with some difference on the wrinkle formation. Larger wrinkles are predicted with macro- and meso-scale simulations when no blank holder force is applied. With macro-scale model, the shear angle of the whole textile can be observed, while the meso-scale model can give more details about axial force of every single yarn. Small wrinkles occurred at the edges of the geometry when a blank holder force of 100 N is applied during fabric forming. Further simulations with increased blank holder force are carried out, but the results suggest that the two great wrinkles at the top of the T-cup cannot be eliminated. As a resolution for that problem, suggestion has been made to reduce the height of the final forming tool to 50 mm, so that these two great wrinkles is not a problem anymore. Simulation with the final geometry of T-cup forming tools with the help of meso shell model for BWKF CF/PA 2-layer V1 confirms that, the two great wrinkles on top of the T-cup is not significant anymore with $0^\circ/90^\circ$ orientation of the textile, even without blank holder force. This final geometry of forming tool is used to manufacture the consolidation tools, where no blank holder is necessary (Figure 5-20 and Figure 7-38).

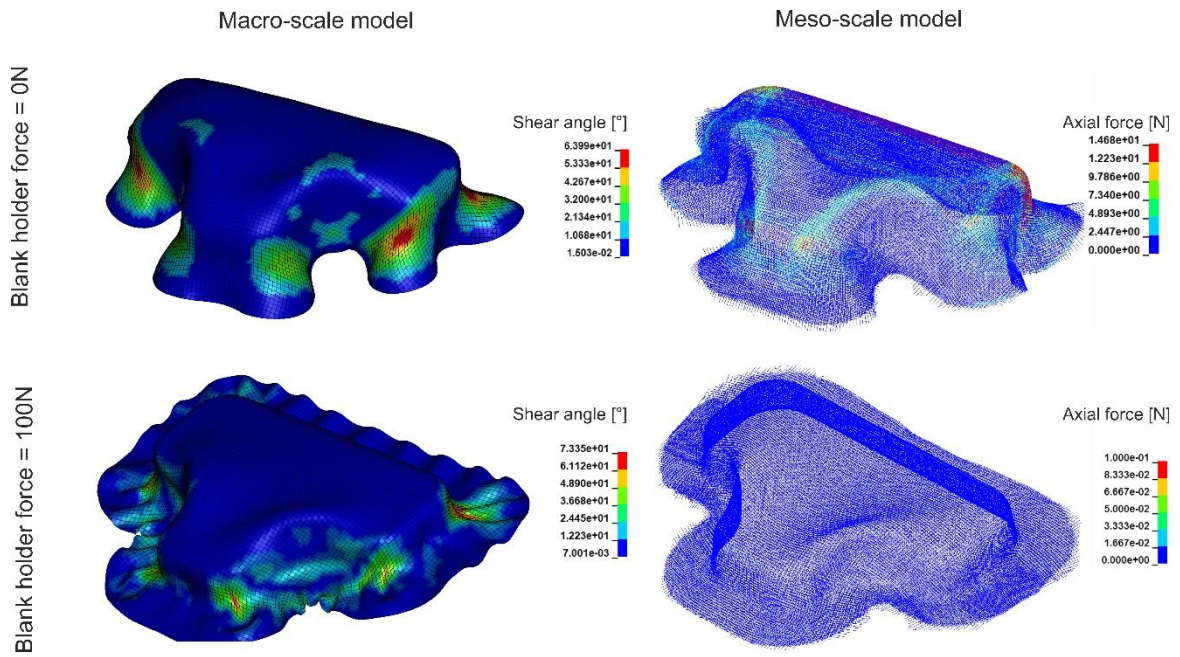


Figure 7-37: Results of forming simulation of BWKF CF/PA 2-layer V1 with conceptual T-cup tools with macro and meso beam models at different blank holder forces

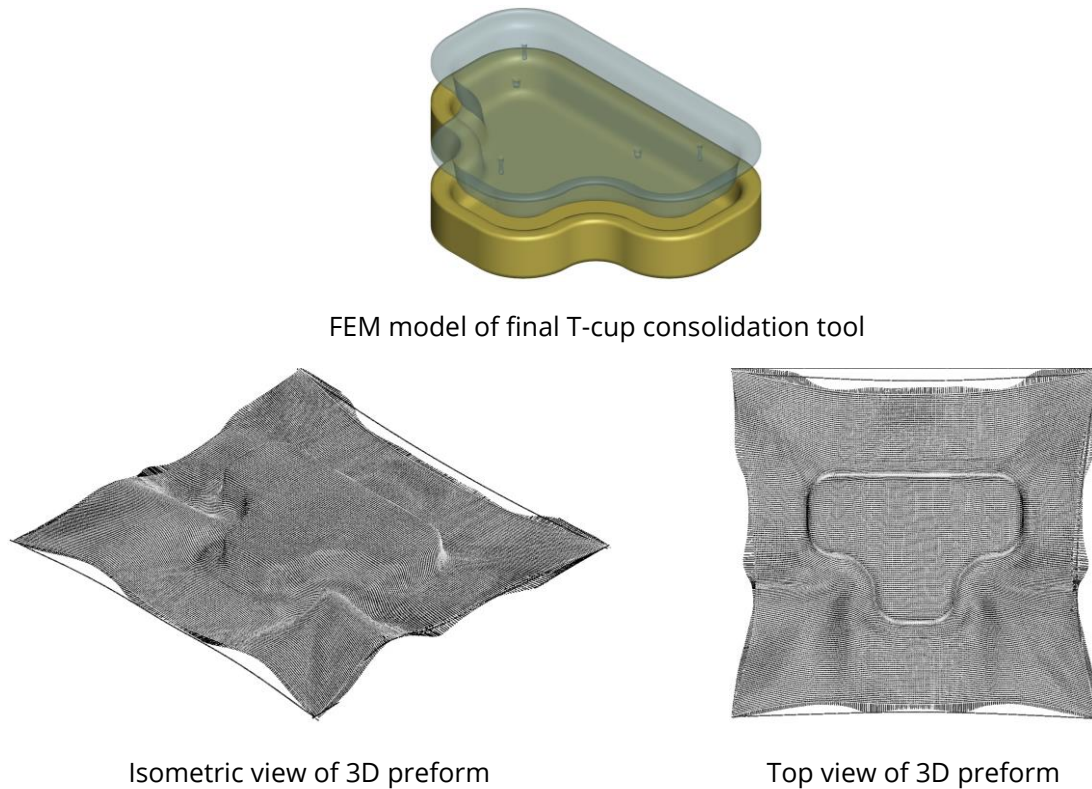


Figure 7-38: FEM model of final forming tools for T-cup and the 3D preform BWKF CF/PA 2-layer V1 predicted with meso shell model

7.4 Computational cost

It was presented in [21,520], that the computing cost of a meso-scale model is significantly higher than that of a macro-scale model for the biaxial reinforced weft-knitted fabrics. The use of shell elements to describe the reinforcing yarn, instead of beam elements in meso model has improved the performance of the models but also increased the computing cost even further. The explosion of computing cost is not only caused by higher quantity of elements, but also by the handling of the contact between them. Figure 7-39 shows exemplary the increasing of computational cost of forming process simulation with L-profile tool for BWKF CF/PA 2-layer V1. The computation of macro model is carried out on a workstation with Intel(R) Core(R) CPU i9-9900X @ 3.50 GHz. Simulation with meso models is computed on TU Dresden ZiH HPC system with Intel(R) Xeon(R) CPU E5-2630 @ 2.30 GHz. Dependent on the requirement of the description details and the available computing resource, a suitable model for a certain case can be properly chosen.

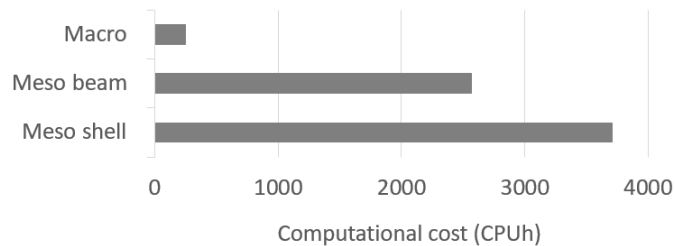


Figure 7-39: Computational cost of forming process simulation with L-profile tool for BWKF CF/PA 2-layer V1 with different models

7.5 Summary

This chapter presented the experiments and equivalent simulations of forming process with forming tools with different geometries. All three types of model that were introduced and validated in Chapter 6 are used for the forming simulations. The experimental and simulation results of forming process with hemispheres confirm the performance of the FEM models by predicting of the wrinkle formation. A further benchmarking by prediction of yarn orientation on the L-profile preforms are carried out. The results show clearly that macro model has no capacity to predict yarn orientation under complex forming scenario. Between the two types of meso-scale models the model used shell element for the description of reinforcing yarn provides better prediction of the orientation than the one with beam element. Additionally, the meso-scale model has the capacity to predict the gap formation, which macro model cannot. However, the increase of computational cost is significant. Care should be taken by the choice of a suitable model for certain application, where computational resource is limited.

8 Modelling of FRP made from BWKF

8.1 Macroscale FRP model

8.1.1 Mapping method

The conclusion of Chapter 7 confirms the advantage of using meso-scale models for predicting the yarn orientation of complex 3D preform. There are many ways to use the information gained from forming simulation with the meso-scale model. The FEM model of 3D preform can be exported and combined with a model of the matrix to form a meso-scale model of FRP. Alternatively, the yarn orientation predicted by the FEM meso-scale model can be exported and mapped to a new shell element mesh, which will be used for structural analysis of the FRP component. The influence of the yarn orientation on tensile strength of FRP has been addressed in Figure 2-3. An FRP model with correct orientation of the reinforcing fibers would provide a better prediction of the mechanical properties of the FRP under certain loading scenarios. Another advantage of transferring the yarn orientation with mapping method is the ability to change the computing environment. The software that is used for structural analysis of FRP can be different from the one used for forming simulation. The mapping process can be carried out automatically by software such as ENVYO [529,530]. ENVYO has great capability of mapping, where the orientation of different element types of the source mesh can be mapped directly to the target mesh. In the framework of research project AMARETO, the mapping process has been successfully carried out by D. Weck [527] (Figure 8-1), where the source mesh is the result of forming process simulation with L-profile by meso beam model for BWKF CF/PA V1 (Figure 7-28), and the target mesh is meshed from CAD data of the L-profile stamp (Figure 7-24). The structural analysis for L-profile component under bending load has been carried out by D. Weck, which shows very good correlation to the test data [527].

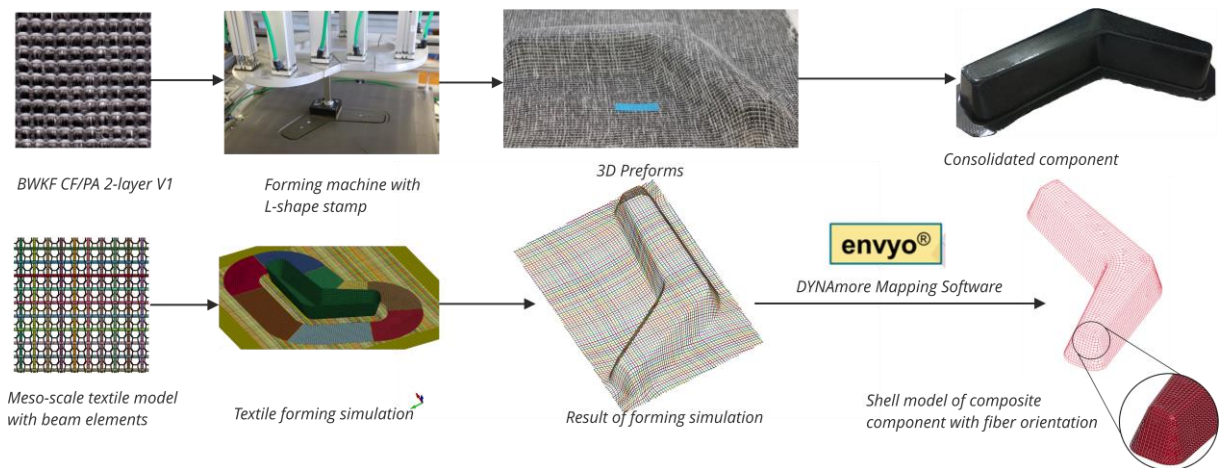
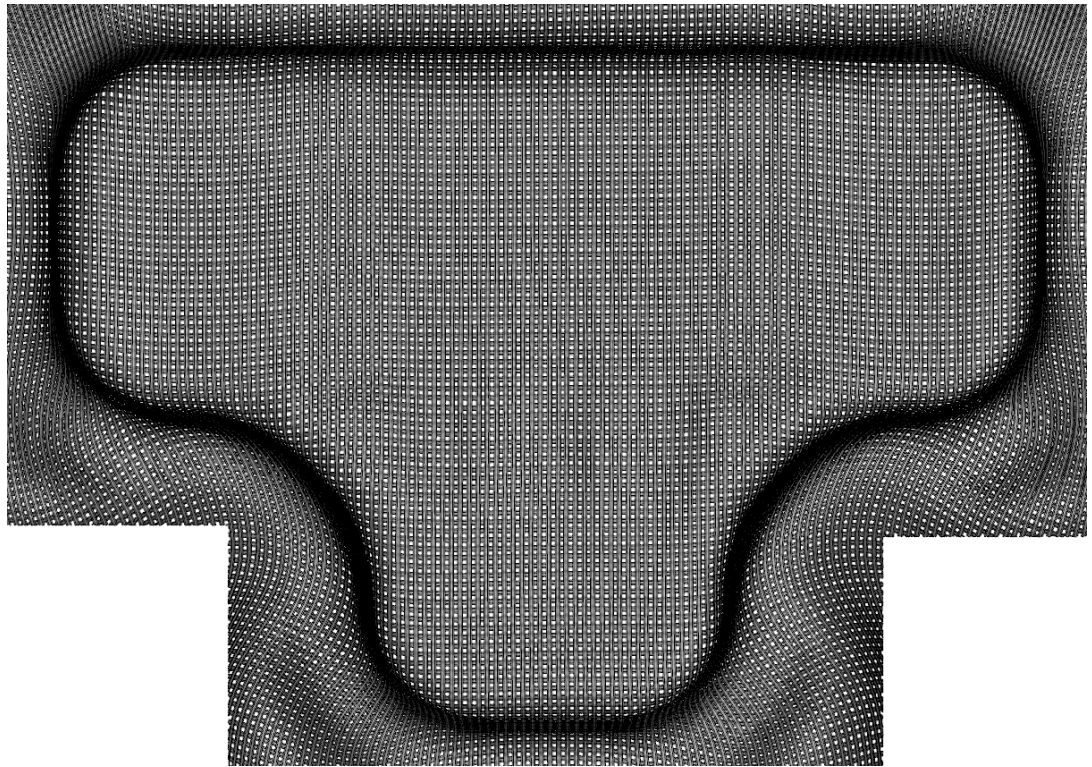


Figure 8-1: Twin digital FRP production chain process including forming simulation and structural analysis with the help of ENVYO

To demonstrate the importance of yarn orientation on the mechanical performance of a composite part, the mapping process is carried out manually for a T-cup part. This T-cup composite part was produced by thermopressing (Figure 5-22) based on BWKF CF/PA 2-layer V1. The forming simulation is carried out with the help of a meso shell model to virtually generate 3D preforms for the textile orientation of $0^\circ/90^\circ$ and $+45^\circ/-45^\circ$, and they are used as source mesh for the mapping process. The beam elements as knitting yarns in the model are blended out and not used for mapping. The inner surface of the FEM model of the T-cup stamp (Figure 7-38) is used as target mesh, which contains 4-node shell elements. The mapping results are shown in Figure 8-2 ($0^\circ/90^\circ$ textile orientation) and Figure 8-3 ($+45^\circ/-45^\circ$ textile orientation). Here, the orientation of the 4-node shell element on the target mesh is mapped on the basis of the orientation of the reinforcing yarn from the source mesh. With such accurate orientation, the mechanical performance of FRP at every position in the model is ensured to correlate with the experiment.

Source mesh



Target mesh

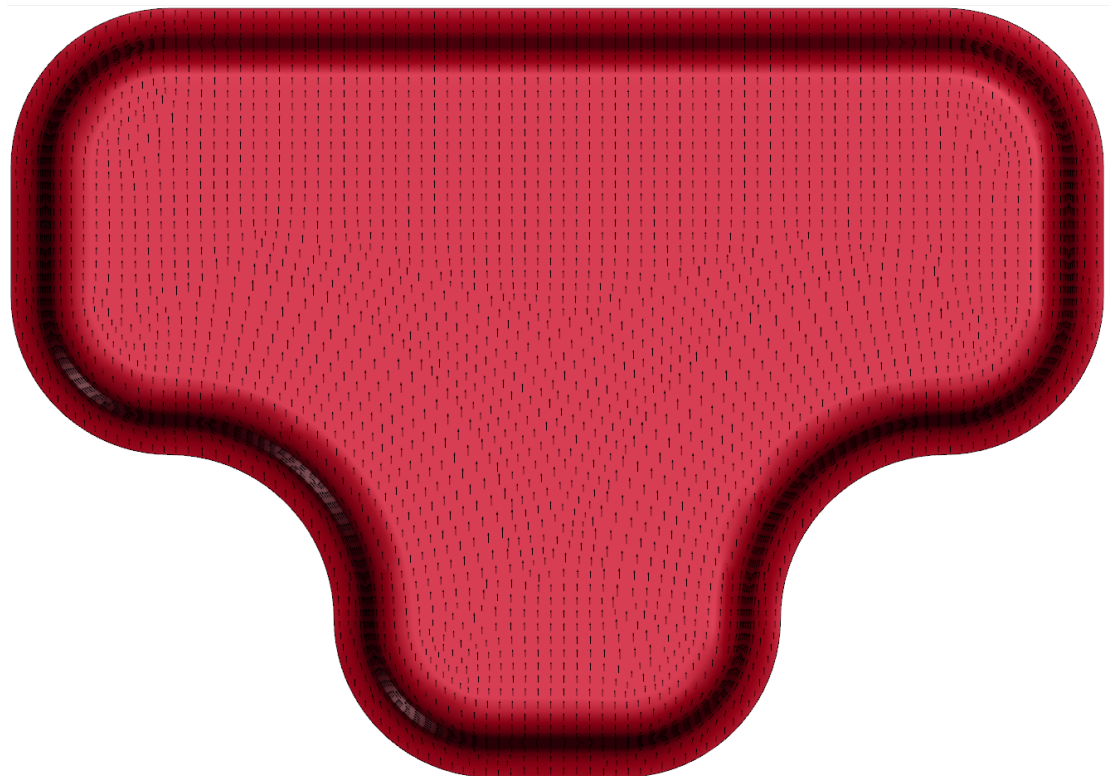


Figure 8-2: Mapping result with orientation of source mesh in 0°/90° orientation

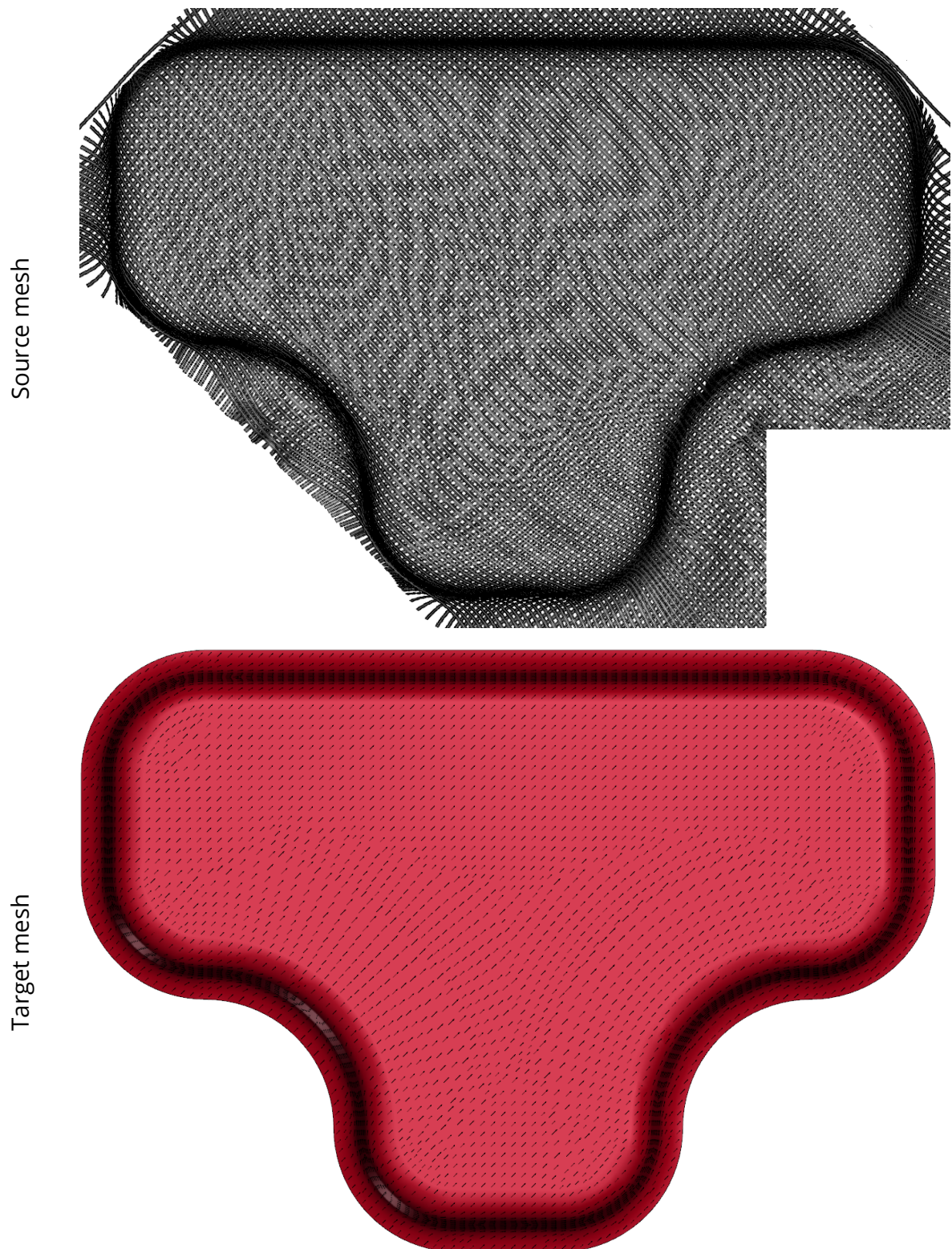


Figure 8-3: Mapping result with orientation of source mesh in +45°/-45° orientation

8.1.2 Validation of composite model

The FRP produced from BWKF CF/PA 2-layer V1 with thermopressing method is called FRP-C0, and tested in Section 5.4. The test results are shown in Table 5-17. The tensile behavior in both warp and weft direction of FRP-C0 is non-linear. In LS-DYNA, MAT_LAMINATED_COMPOSITE_FABRIC (MAT_058) [531] is a suitable material model, which can describe the non-linear tensile behavior of FRP on the macro scale correctly. With the help of tensile test and 4-point bending test simulation (Figure 8-4), the tensile and bending properties of FRP material model can be validated. The boundary condition of these models are based on the test standard DIN EN ISO 527-4 and DIN EN ISO 14125 as presented in Section 5.4.3 and Section 5.4.4 for tensile and 4-point bending test, respectively. A smooth surface failure criterion (FS=1.0 in keyword of MAT_58 [531]) is used (Figure 8-5), where XT, XC, YT, YC are the tensile and compression strength of composite in warp and weft direction, respectively. XT and YT are calculated from the tensile test data (Table 5-17 and Figure 5-27). XC and YC are ignored due to the lack of experimental data. SC is the shear strength, and calibrated on basis of 4-point bending test experimental data (Figure 5-30). The comparison between experimental data and simulation results show good agreement (Figure 8-6 and Figure 8-7).

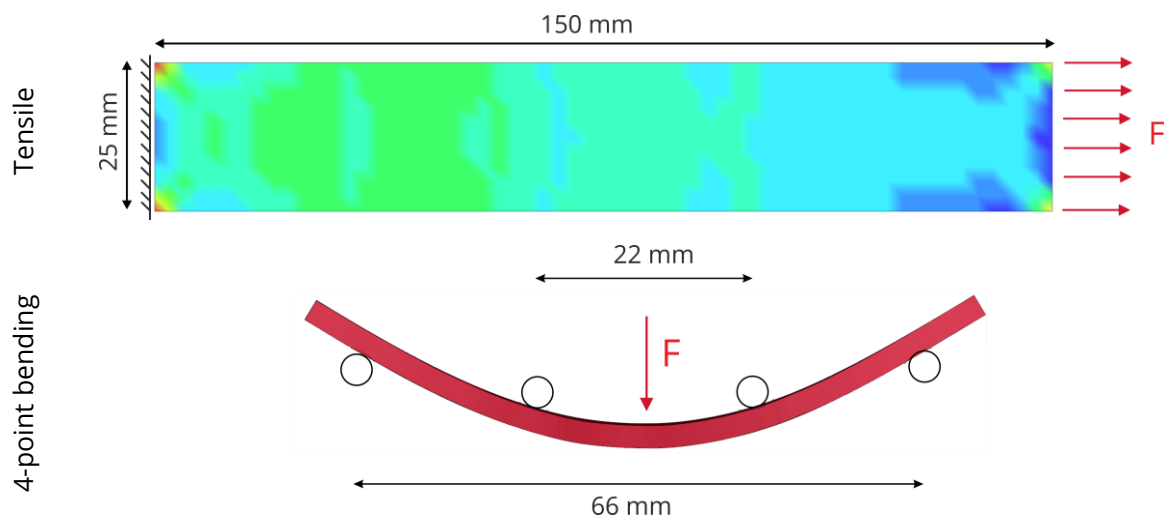


Figure 8-4: Test simulation of thermoplastic FRP on the macro scale

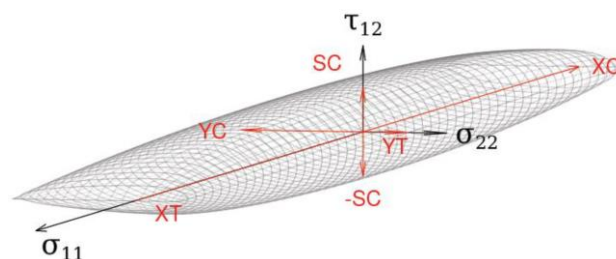


Figure 8-5: Smooth surface failure criterion (FS=1.0) [531]

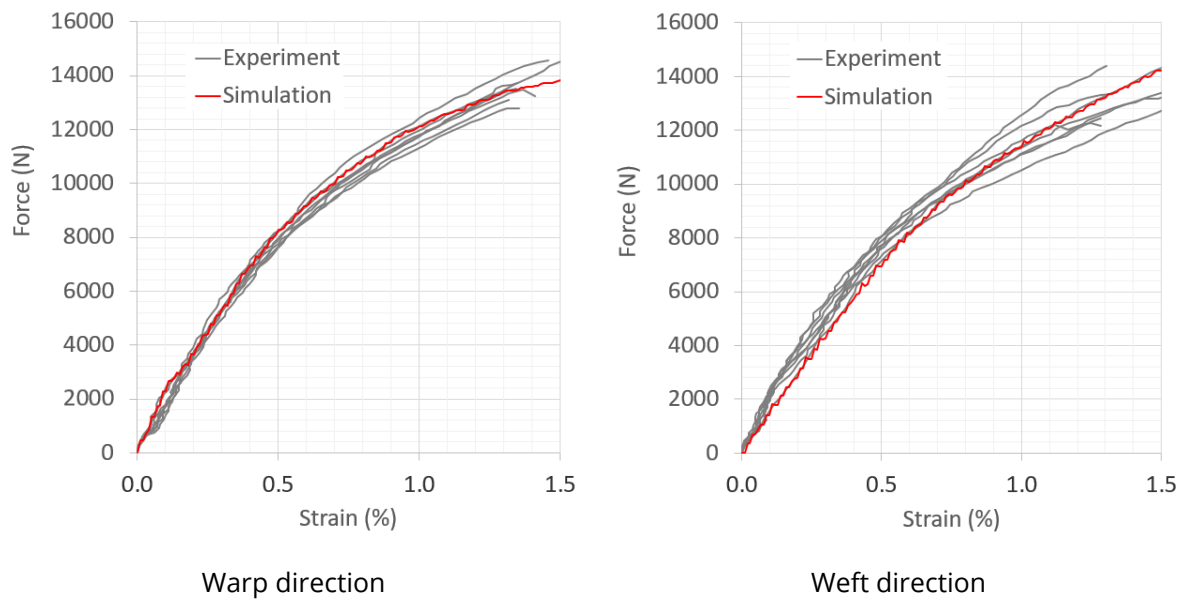


Figure 8-6: Comparison of force-strain curves of tensile test for FRP-C0 between experiment and simulation

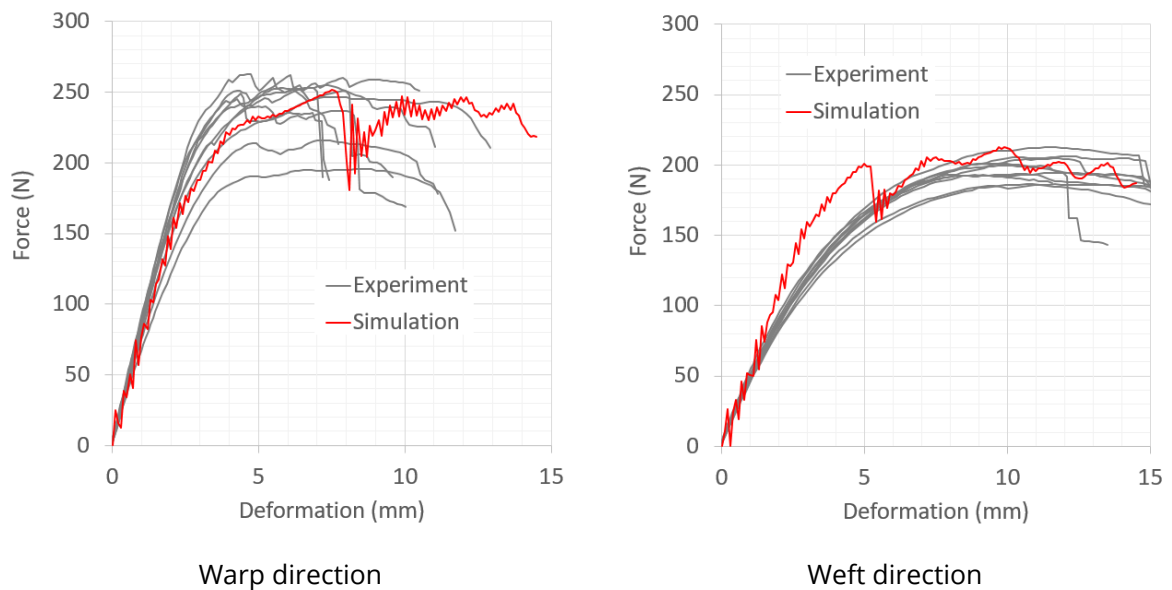


Figure 8-7: Comparison of force-strain curves of 4-point bending test for FRP-C0 between experiment and simulation

8.1.3 Investigation of the influence of yarn orientation on FRP properties

The mechanical performance of the T-cup component is tested virtually by two loading scenarios: tensile load and compression load (Figure 8-8). In the tensile loading scenario, one edge of the T-cup component is firmly constrained in all degrees of freedom by

boundary condition, while the other end is pulled with constant velocity. In the compression loading scenario, all the nodes at the edge of the lower side are constrained in all degrees of freedom by boundary condition. A rigid circle plate with a diameter of 130 mm is used as pressing tool at the top of the T-cup component, which also moved down with a constant velocity.

The force - deformation curves (Figure 8-9) show large difference of tensile strength between the two fiber orientations under tensile loading scenarios, while the difference of compression strength is not significant. This can be explained by the geometry of the T-cup. In the tensile loading scenario, the component is firstly deformed due to bending; the force deformation curves in this area are non-linear. From 50 mm deformation, tensile stress starts to build up at the front side of the T-cup (Figure 8-10), where the force - deformation curves behave linearly until failure. Due to the different of fiber orientation in the front side area, the variant with $0^{\circ}/90^{\circ}$ orientation of reinforcement has significant higher strength than the $+45^{\circ}/-45^{\circ}$ variant.

In the compression loading scenario, the T-cup component is mainly deformed due to bending at the top (Figure 8-11) until failure. Thus, the force - deformation curves behave non-linearly from the start to failure. Due to the plasticity of the thermoplastic matrix, the stress level is not abruptly reduced but maintained at a stable level after failure due to bending. Such phenomenon can be also observed by the force-strain curves of 4-point bending test (Figure 8-7).

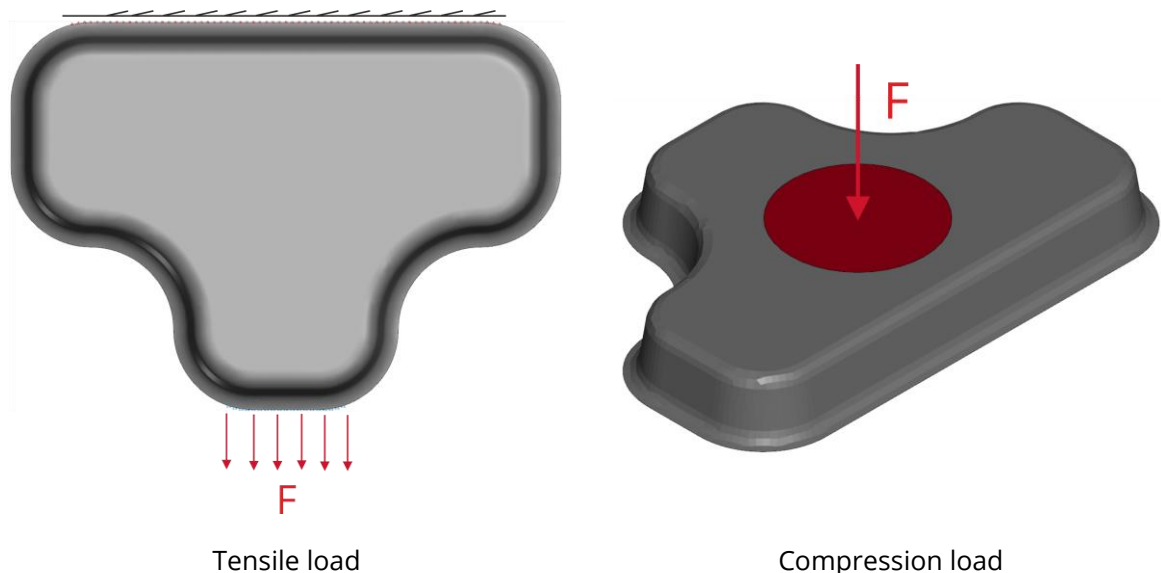


Figure 8-8: Loading scenarios on T-cup component

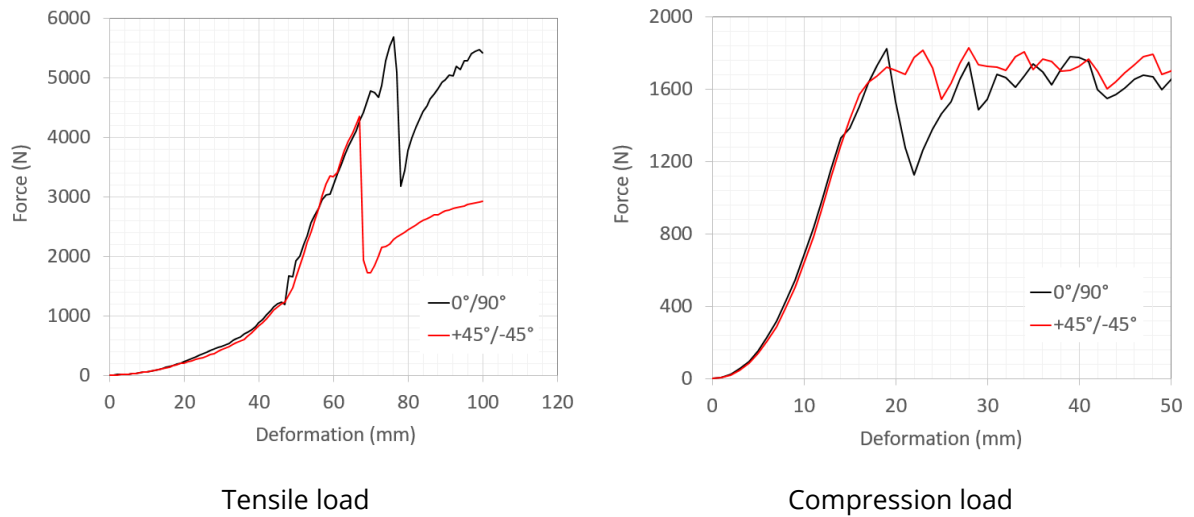


Figure 8-9: Force - deformation curves by different loading scenarios

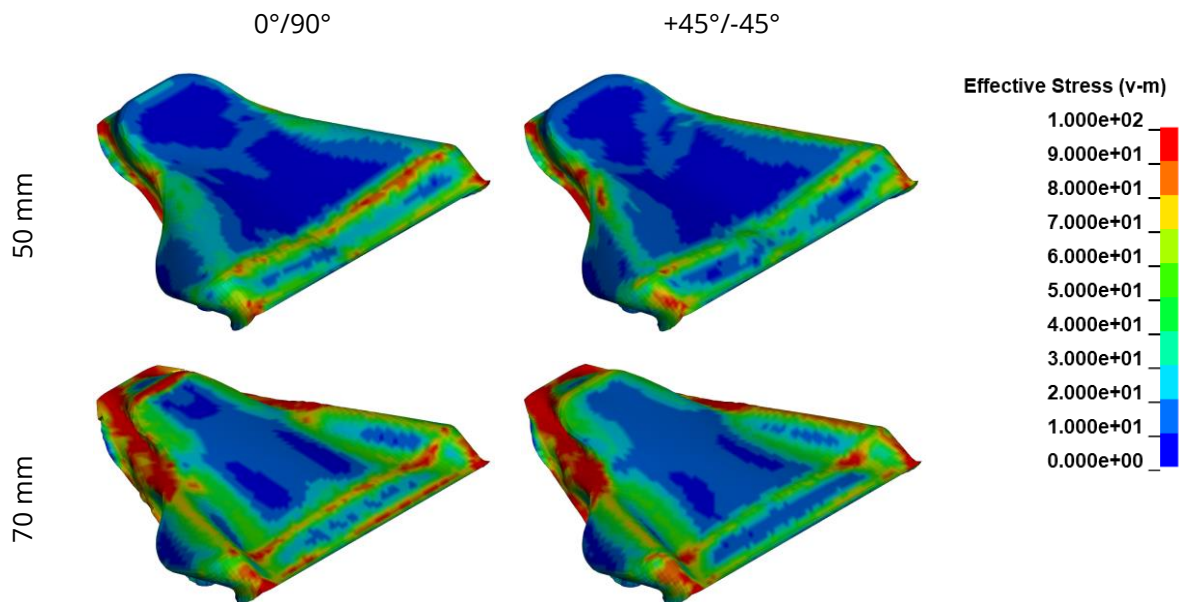


Figure 8-10: Effective stress (MPa) in T-cup component by tensile loading at different deformation

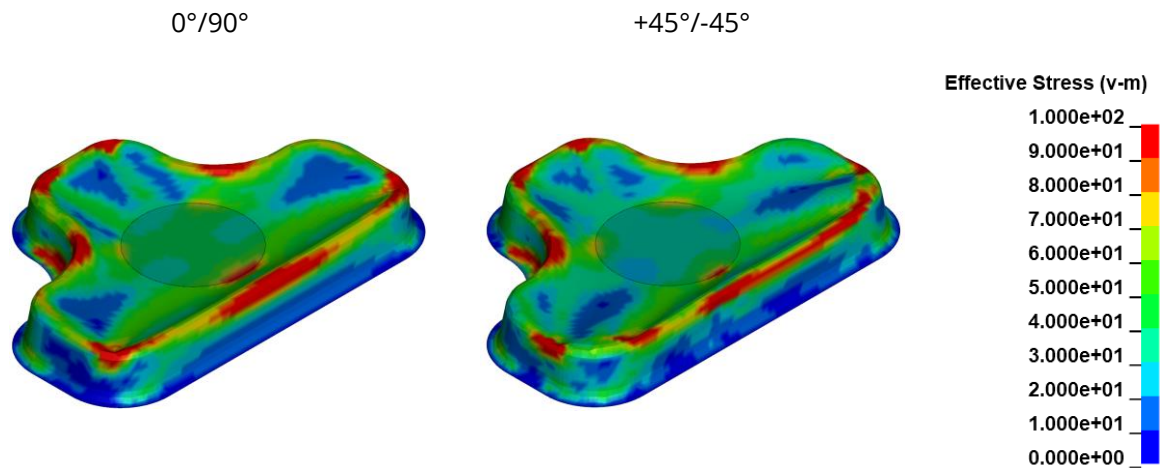


Figure 8-11: Effective stress (MPa) in T-cup component by compression loading at 20 mm deformation

8.2 Mesoscale FRP model

The macro-scale modelling approach for FRP, which is presented in Section 8.1, is suitable for thin-walled FRP component. As the failure mechanism of FRP is complicated (Figure 3-10), when the thickness of the FRP increases, further failure modes such as delamination become significant and cannot be neglected. Model of thick FRP can be built up with laminate construction, where multiple layer of shell elements are coupled, but such model cannot separated the failure between yarn and matrix, and the influence of yarn path in structures cannot be taken into account. Thus, a FEM model for FRP with higher degree of representation is required.

Potential industrial applications of rib-stiffened shell structures include highly load-bearing rib-stiffened FRP components in rail vehicle construction, automotive and mechanical engineering, hull structures in ship construction as well as load-bearing structures in aerospace (e.g., aircraft fuselage as in Figure 1-2 or isogrid structures). An excellent textile technology for manufacturing net shape shell-rib structures is the weft-knitting technology. The possibilities of the knitting technique for production of shell-rib structures are investigated with the help of a meso-scale FEM model for FRP.

8.2.1 Shell-rib structures as stiffened element

According to the state of the art, these components are usually manufactured in differential construction at preform level by assembling the preform from different textile structures (e. g. by stitching or sewing) or at component level by subsequent joining of the separately manufactured shell and the stiffening structure (e. g. by adhesive bonding).

Therefore, production of such FRP components is currently very cost-intensive and, outside the aircraft industry, only suitable for small series or niche applications. The use of fiber placement technique FPT for complex 3D rib-stiffened FRP is limited [110]. A continuous fiber reinforcement between shell and stiffeners is due to process restrictions almost impossible. The lightweight construction potential of high-performance fibers is therefore not fully exploited. Depending on load cases and requirements for stiffness and strength, the dimension and shape of the 3D rib-stiffened FRP can be adapted accordingly. Among many factors, the orientation and height of the ribs play an important role. Figure 8-12 shows some typical variations of 3D rib-stiffened FRP with different orientation of rib.

The possibility to manufacture integral multilayer BWKF [37] has high potential for reinforcement of shell-rib components as shown in Figure 8-12. Yarns can be guided in a way that strongly connects shell and rib. This section investigates the possibilities of the knitting technique and enables comparing of different variants through development and validation of a finite element model. This integral BWKF is produced as flat fabric on a knitting machine with a reserve layer of warp yarns (Figure 5-2). This warp yarn reserve is pulled out and thus transforms the 2D fabric into the 3D integral preform. The possible orientation of the ribs is 0° or 90° (variant 1 and 2 in Figure 8-12). This manufacturing technique has been further developed for more complex rib orientations such as variant 3 to variant 7 (Figure 8-12). Details of this advanced technique are part of future research papers of weft-knitting experts. The production and testing of T-shaped FRP made from BWKF have been presented in Section 5.4.

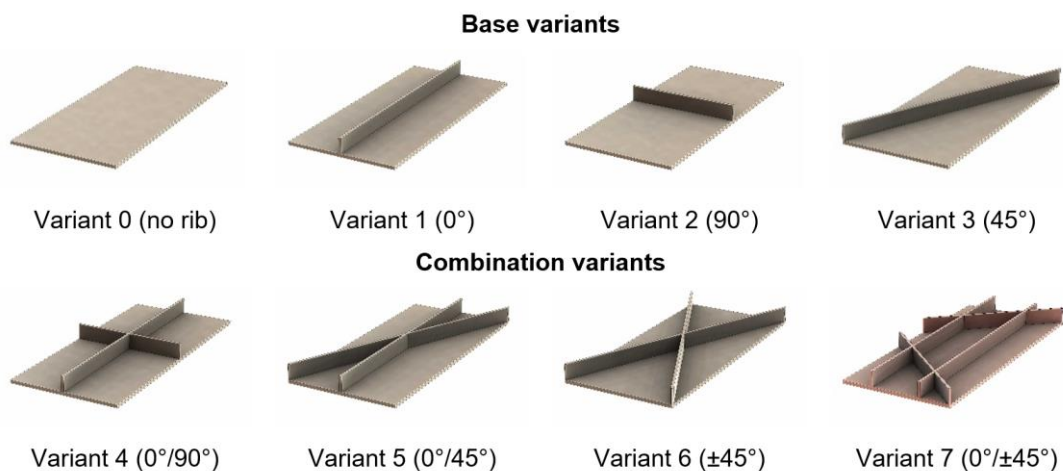


Figure 8-12: Some typical designs of shell-rib structures

8.2.2 Modelling of FRP

A meso-scale model for 3D rib-stiffened FRP made of BWKF reinforcement is introduced to predict structural mechanical behavior and failure modes. This model is based on the meso shell model for BWKF, which has been presented in Section 6.2.2, where the textile reinforcement was described on meso-scale with shell elements for the reinforcing yarns and beam elements for the stitch yarns (Figure 6-10 and Figure 6-11). In composite model, the shell elements for the reinforcing rovings are adopted unchanged from the textile model. This allows the lay-up of BWKF to be modelled accurately for each variant (Figure 8-13). However, the beam elements are removed from the fabric model because the influence of stitch yarn on delamination resistance is later implemented with a contact element. The epoxy matrix is modelled with solid elements and linear elastic material based on the material parameters provided by the manufacturer (Table 5-12). To model the FRP in this section, a penalty-based coupling is established between coupled nodes of shell and solid elements as an implementation of the Domain Superposition Technique (DST) [306,532] as shown in Figure 8-14. In a penalty-based coupling, such as on that implemented in LS-DYNA code, *“a penalty string is attached between coupling points on shell and in the solid element. The stiffness of this penalty string is calculated based on the geometric mean of shell and solid’s bulk modulus. The magnitude of this coupling force can be controlled using a penalty string stiffness scale factor”* [518]. Thus, strength of the interface between fiber and matrix can be calibrated through this penalty string stiffness scale factor. However, debonding still cannot be described. By calibrating the break elongation of shell elements, the tensile strength of FRP specimen can be described. However, the non-linearity of force-strain-curve (by area near the end of test) due to the progressive damage cannot be simulated accurately as no treatment for this phenomenon is implemented (Figure 8-17).

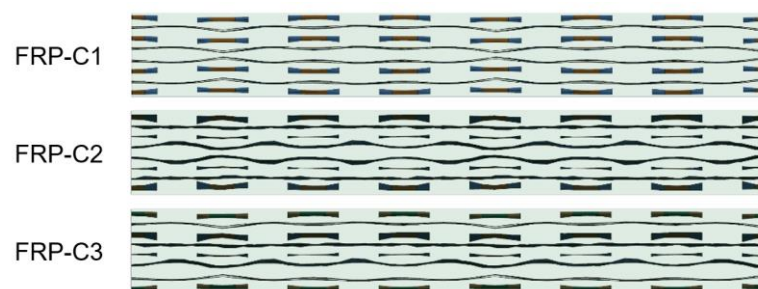


Figure 8-13: View of the cross-sections along the weft direction of FRP models

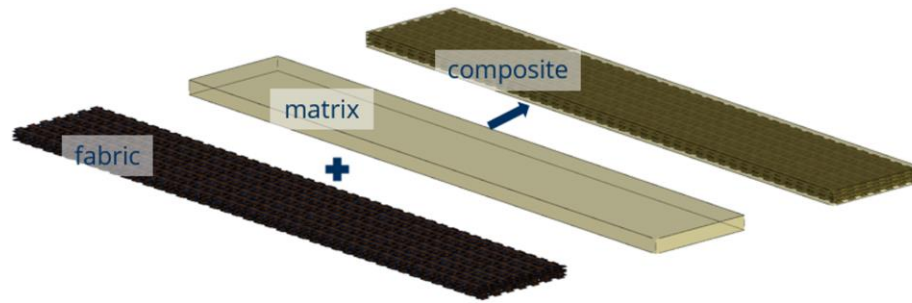


Figure 8-14: Modelling FRP with a meso-scale fabric model and Domain Superposition Technique

Certain load conditions and specimen dimensions of the T-shaped FRP cause a failure due to matrix cracking. Thus, including failure criteria for matrix cracking is necessary for a reasonable prediction of stiffness and strength of the T-shaped FRP. Failures can be initiated by failure of fiber, matrix or interface between them (debonding). Matrix cracking can be initiated by matrix break under normal loading (tensile or compression), and shear loading. With the help of a tiebreak contact in LS-DYNA between solid element surface, crack initiation due to normal and shear components is modelled [518]. The failure criterion is described by Equation (8-1):

$$\left(\frac{|\sigma_{\perp}|}{\text{NFLS}}\right)^2 + \left(\frac{|\tau_{\perp}|}{\text{SFLS}}\right)^2 \geq 1 \quad (8-1)$$

where σ_{\perp} is tensile normal stress (only tensile stress counts, compression stress is treated as zero). Only failure mode I crack opening is taken into account, as failure due to compression is excluded from this contact failure formulation. The shear stress $|\tau_{\perp}|$ represents for $\max(|\tau_{\perp\parallel}|, |\tau_{\perp\perp}|)$. Thus, there is no distinction between delamination mode II and mode III failure. NFLS and SFLS are normal failure stress and shear failure stress, respectively. Any tie contact meeting the requirement of failure criterion (8-1) will be excluded in the next computation step. Thus, cracking at that contact position is modelled.

The parameter NFLS is also known as mode I fracture toughness. The setting of the NFLS parameter in the FEM model is calibrated based on experimental and simulation results of 3-point bending tests of T-shaped specimens. In this 3-point bending test of the T-shaped FRP, the test specimens are cracked open (as shown in Figure 5-34), which helps to calibrate the NFLS parameter accordingly. FEM model of 3-point bending test of T-shaped FRP specimen is thus built to serve this purpose. The construction of the FEM

model for T-shaped FRP with an interface between the solid elements for the surface-to-surface tiebreak contact formulation is shown in Figure 8-15.

The parameter SFLS is taken directly from the test results of the ILSS tests (Table 5-19). Thus, the shear strength τ_{II} (or mode II in-plane fracture toughness) and shear strength τ_{III} (or mode III out-of-plane fracture toughness) share the same value in the model. To avoid an overestimation, only the minimum value of both directions is used.

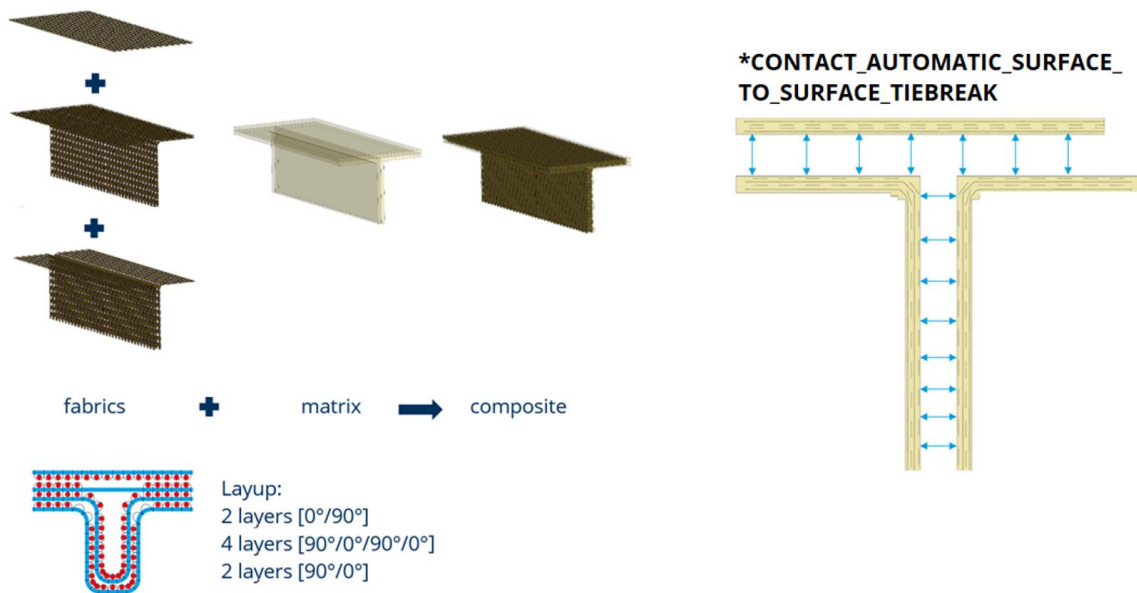


Figure 8-15: FEM model of T-shaped FRP from 2-layer/4-layer/2-layer BWKF preform

8.2.3 Validation of the FRP model

In order to validate the meso-scale model, tests simulations of BWKF and FRP are carried out. Validation of textile model has been presented in Section 6.3. Hereafter, only the validation of FRP is presented. Configuration of FRP samples for composite coupon level test (FRP-C1, -C2 and C3) can be found in Table 5-13. The boundary conditions of FRP test simulation are based on the following test standards: FRP tensile test DIN EN ISO 527-4 and 3-point bending test DIN 14125 – Method A. In the FRP tensile test simulation, the nodes on one side of the shell and solid elements are fixed in all translational movements, while the nodes on the other side are only fixed in translational movements in x- and z-direction. These nodes are then pulled with a constant velocity along the y-direction, which is the main direction of the specimen (Figure 8-16). The simulation results show good agreement with the experimental data (Figure 8-17).

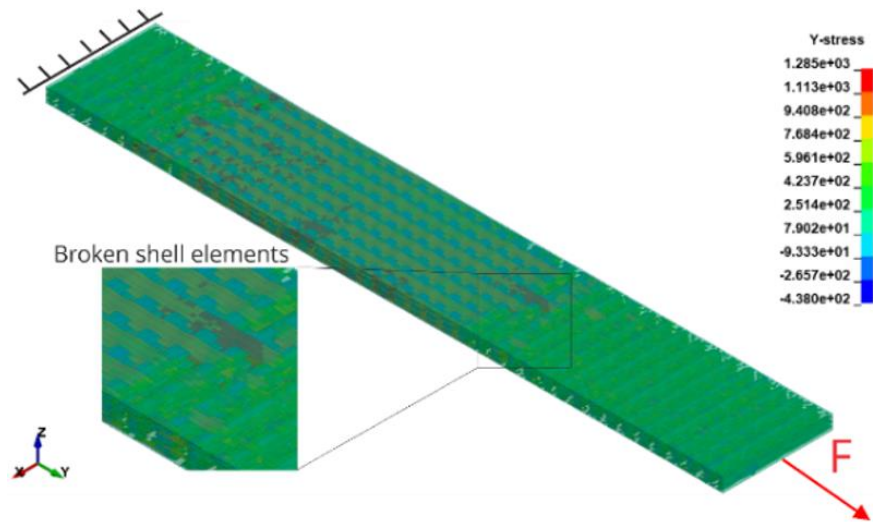


Figure 8-16: Tensile test simulations with meso-scale model of FRP-C1 made from 4 x BWKF GF 2-layer

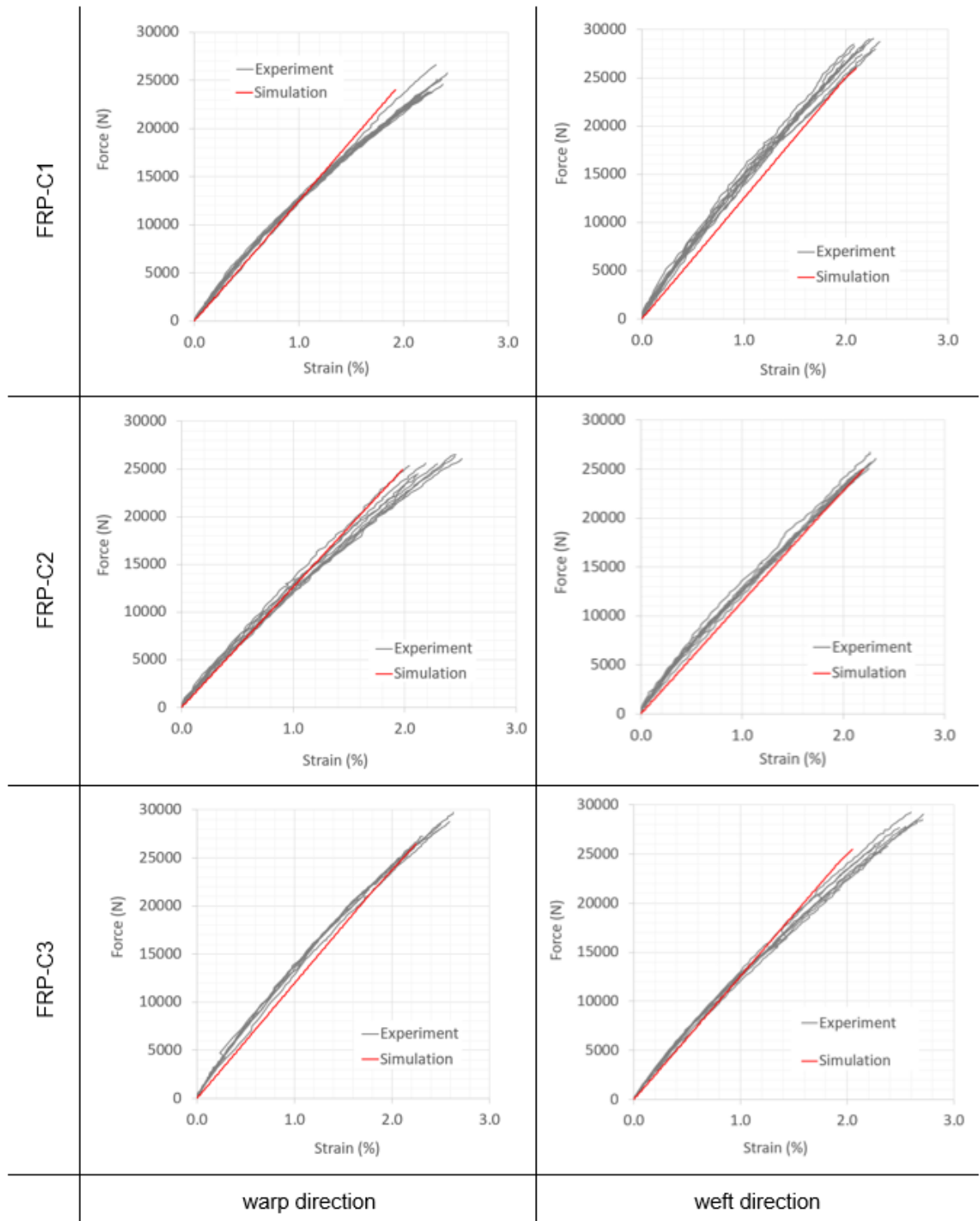


Figure 8-17: Tensile test simulation results and experimental results of FRP samples

T-shaped FRP are produced with 3 different constructions of BWKF (FRP-T1, -T2 and T3) as shown in Figure 5-23. The 3-point bending simulation is carried out for T-shaped FRP with and without rib. The specimens have the dimensions as shown in Table 5-14. Figure 8-18 provides results of FRP T120-0 samples in configurations FRP-T1 and -T3, i.e. FRP

samples with length of 120 mm and no rib. Model predictions are identical for both configurations with observed matrix and fiber breakage. Compared to the samples with a rib, the maximum force is low and deformation is high (above 10 mm), which is due to the flat shape of the samples. The experimental bending tests reveal differences of bending strength between the two configurations, but the simulation model cannot describe these differences. This is due to simplifications of the meso-scale FEM model. Although it correctly replicates the structure of the reinforcing layers with shell elements, it is still far from the reality in which the fiber are distributed across the thickness direction. Only a micro-scale model can meet this requirement.

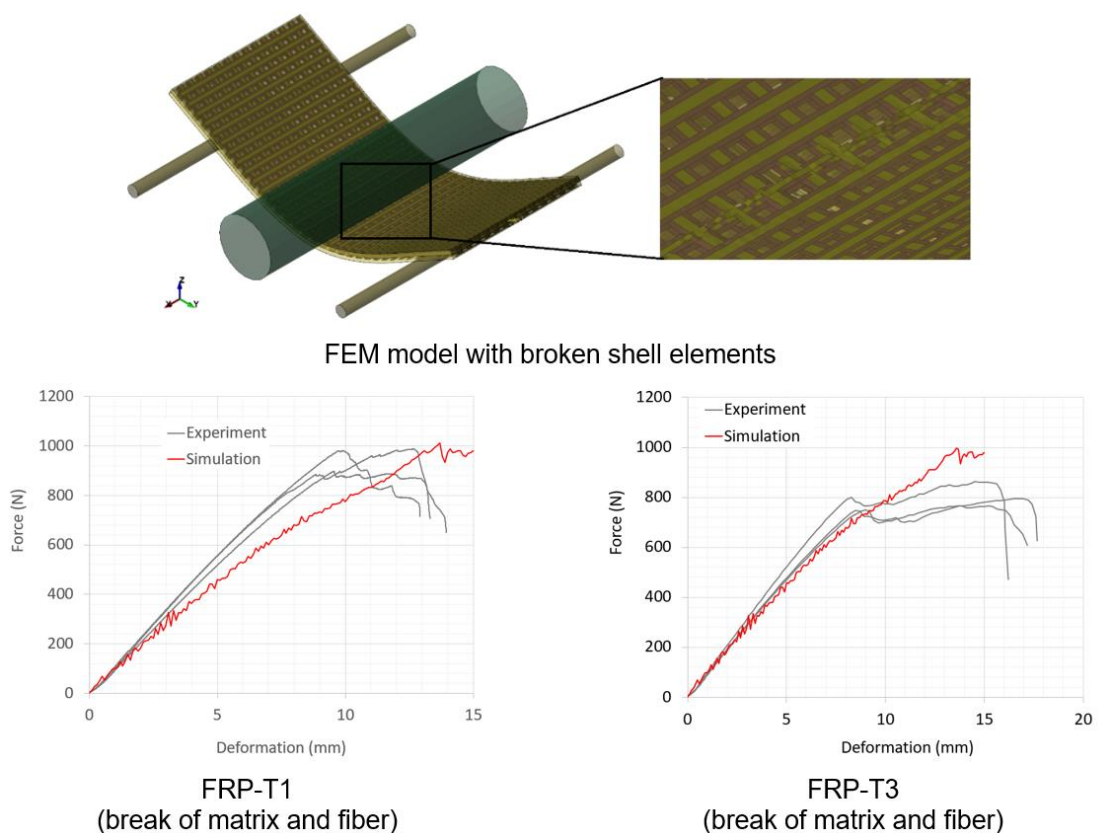


Figure 8-18: Comparison of force-deformation-curves from 3-point bending test of FRP T120-0 (no rib) with different construction of BWKF preforms

Figure 8-19 shows the simulated bending test of the T-shaped FRP variant T120-33 with fabric construction FRP-T1, FRP-T2 and FRP-T3 at 3 mm deformation (tools are blended out by the comparison of three variant). Since the actual rib height H is different for each variant, each FEM model is adapted to the actual sample size. In FEM models, all variants show crack opening in both flange and rib area at 3 mm deformation (Figure 8-19). In the rib, the size of crack is large and varies between variants. The crack length in the flange

area is smaller in comparison with rib area for all variants. At 4 mm deformation (for example FRP-T1 as shown in Figure 8-19), the crack in the flange area is widely opened, which is in agreement with the experimental observation (Figure 5-34).

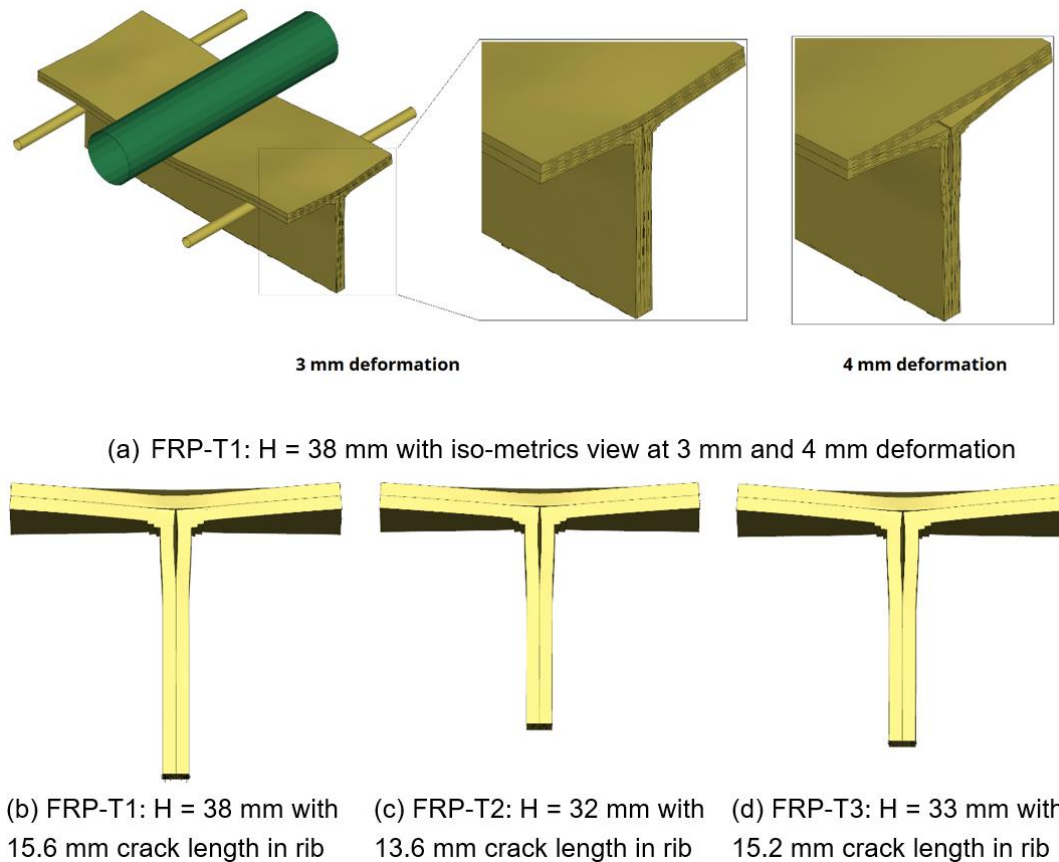


Figure 8-19: 3-point bending test of T-shaped FRP variant T120-33 simulation with support length of 90 mm for FRP specimen with length of 120 mm (failure due to delamination) at deformation of 3 mm

Figure 8-20 compares the force-deformation behavior of FRP T120-33 in real and simulated 3-point bending tests. The three different preform constructions are presented in the figure. The simulation model shows good correlation to experiments for stiffness and strength. However, the non-linear behavior of the force-deformation curves at the start of the test with short length support is not described correctly and deviations are unavoidable. The non-linearity may be caused by the progressive Mode I crack opening and Mode II in-plane fracture failure due to shear stress by the short support length. In the tests with long support length, the non-linearity of force-strain curves are not significant as shown in Figure 8-21.

It is no surprise that NFLS is the largest with 4 x 2-layer BWKF construction (FRP-T1). In this construction, the proportion of stitch yarn in the thickness direction is the largest (4x) compared to the other two. 2 x 4-layer BWKF (FRP-T2) has the least stitch yarn in the

thickness direction (only 2x), resulting in the smallest NFLS. In the middle is the integral 4-layer BWKF version with 3x stitch yarn system in the flange and 4x stitch yarn system in the rib.

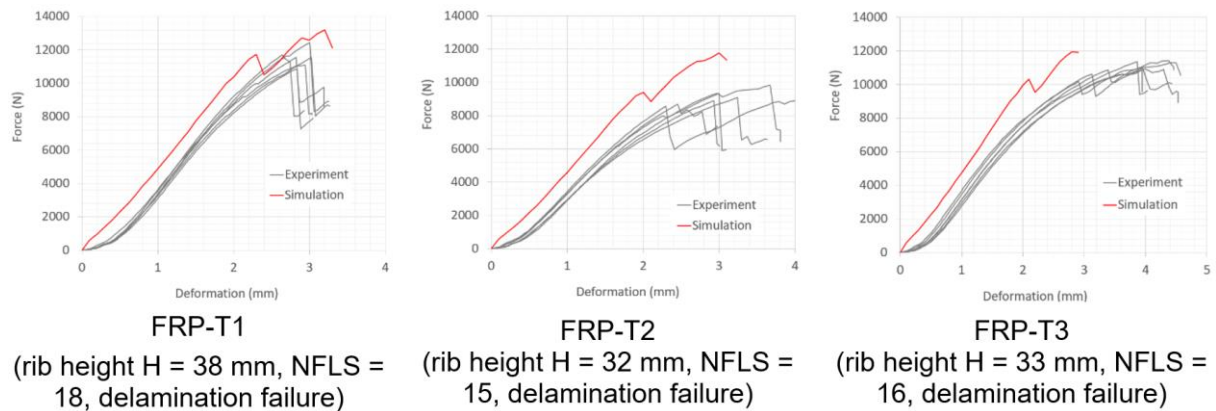


Figure 8-20: Comparison of force-deformation curves from 3-point bending tests of FRP T120-33 with different constructions of the preforms

To investigate the leverage effect, both experiments and simulations were carried out using longer T-shaped FRP components (300 mm and 400 mm) with a 4 x 2-layer BWKF construction (FRP-T1). The dominant failure is the fracture of the rib due to tensile stresses (Figure 8-21). Although the failure mechanism and strength can be predicted correctly, the model underestimates the stiffness of the long FRP specimens. Since the FEM model can describe the mechanical behavior of T-shaped FRP components with BWKF reinforcement in both failure scenarios (delamination as shown in Figure 8-19 and break of yarn in rib as shown in Figure 8-21), it can be further used to predict the behavior of other rib stiffened components with different dimensions and configurations.

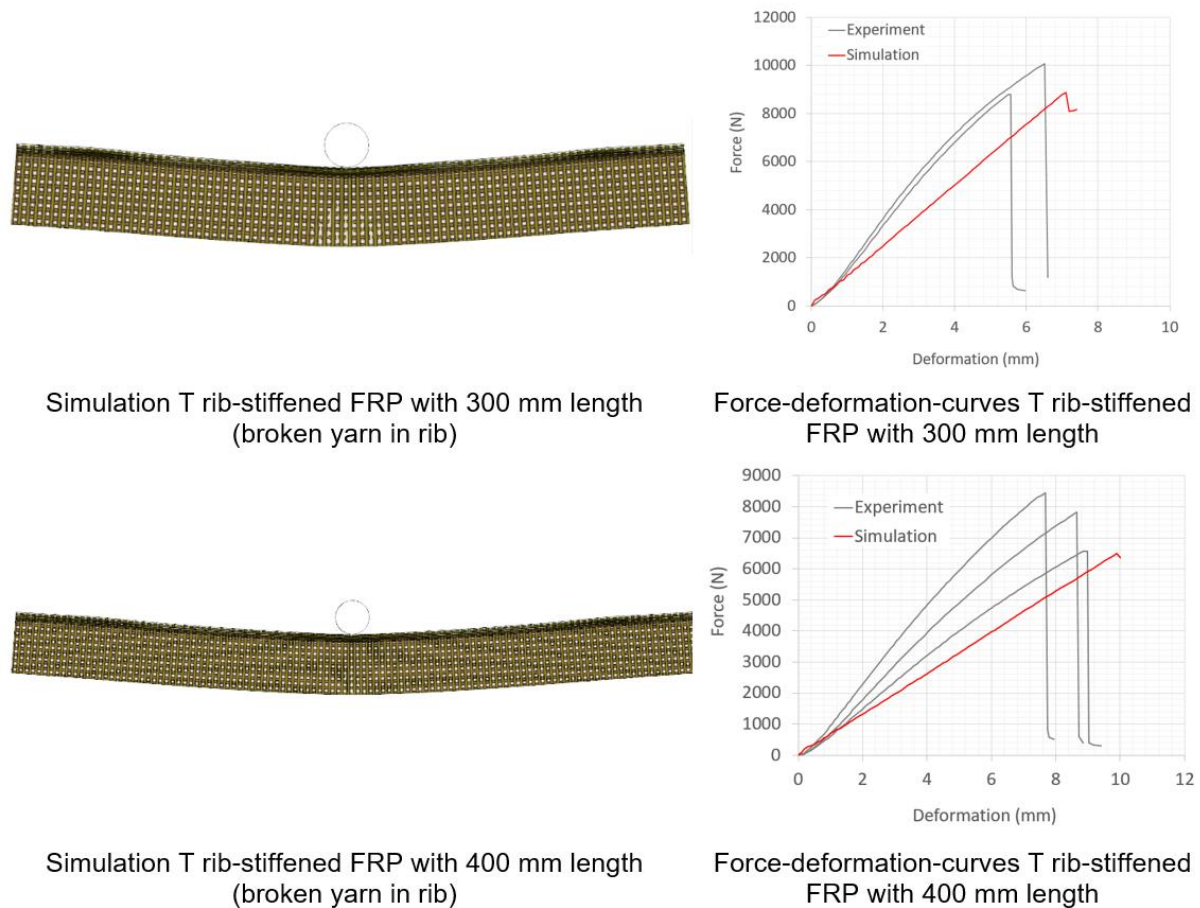


Figure 8-21: Comparison between experiment and simulation of three-point bending tests of long T-shaped FRP samples with 300 mm and 400 mm length, configuration FRP-T1 (rib height $H = 32$ mm, NFLS = 18, failure of yarn in rib)

8.3 Numerical structural analysis of further shell-rib FRP variants

After validation, the models are used to predict the behavior of rib-stiffened FRP with further constructions and dimensions. FEM models of combined variants of rib-stiffened FRP are created to support the research and development process of direct manufacturing of 3D preforms for rib-stiffened FRP with more complex rib designs (as shown in Figure 8-12). Result of the direct manufacturing is an integral 4-layer BWKF. Suppose that this 4-layer BWKF is further used for the construction of FRP with the lay-up of 2-layer/integral 4-layer/2-layer BWKF. These FEM models are manually built up, as the yarn path is known (e.g., variant 3 as shown in Figure 8-22). The advantage of this manufacturing technique is that the thread can run continuously in the rib in many directions, which increases the stiffness in different directions at the same time (e.g., variant 4 with continuous reinforcing yarn inside rib in both 0° and 90° directions as shown in Figure 8-23).

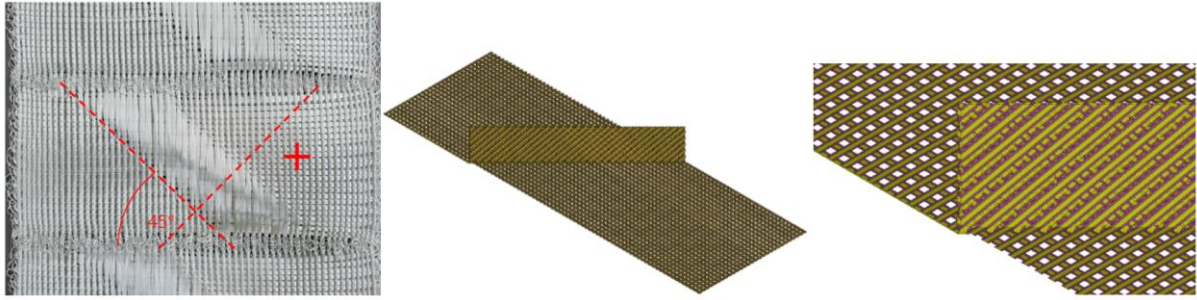


Figure 8-22: Detail yarn path in a real preform and in the FEM model of variant 3 (45°)

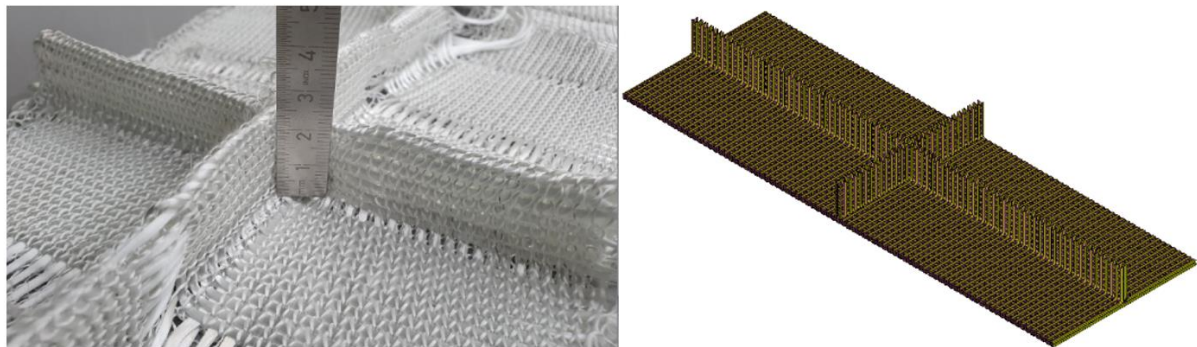


Figure 8-23: Detail yarn path on actual 3D preform and in FEM model of variant 4 (0°/90°)

A simulative investigation is carried out for other variants of shell-rib structure with more complex geometries of the ribs. Variants 0-7 as displayed in Figure 8-12 are analysed in three-point bending simulations. The dimensions of the rib-stiffened FRP in FEM models are: 100 mm in width, 300 mm in length, and 20 mm rib height. Support length for the bending tests is 225 mm. Flange and rib thickness are 4 mm. Figure 8-24 shows the predicted force-deformation-curves of 3-point bending tests with a maximum deformation of 10 mm. Variants without rib in 0° direction, i.e. variants 0, 2, 3, and 6 exhibit a very small stiffness for bending in 0° direction. The influence of ribs in perpendicular and diagonal direction on the stiffness of FRP in the tested direction is not significant. Variants 1 and 4 have similar force-deformation curves, as both of them have rib in 0° direction, which yarn failure predominating in the rib.

In variant 5, crack opening of matrix in the middle of the diagonal rib occurs (Figure 8-25). This leads to a disturbance of the force-deformation curve and thus to a noticeable reduction in bending strength. Such a large crack only occurs when both of the following conditions are fulfilled: thread breakage in the rib in the 0° direction and delamination of the rib in the diagonal direction. With double ribs in the 0° direction, variant 7 has a significantly higher stiffness than other variants. The failure mode is delamination of the

diagonal rib as in variant 5. However, the cracks are not as wide open as in variant 5 (see Figure 8-26). In general, the FEM model provides logical predictions for the base and combination variants. Further experimental results of 3-point bending tests of the complex rib-stiffened FRP would help to confirm the prognosis capability of the model and suggest further improvements to the FEM model.

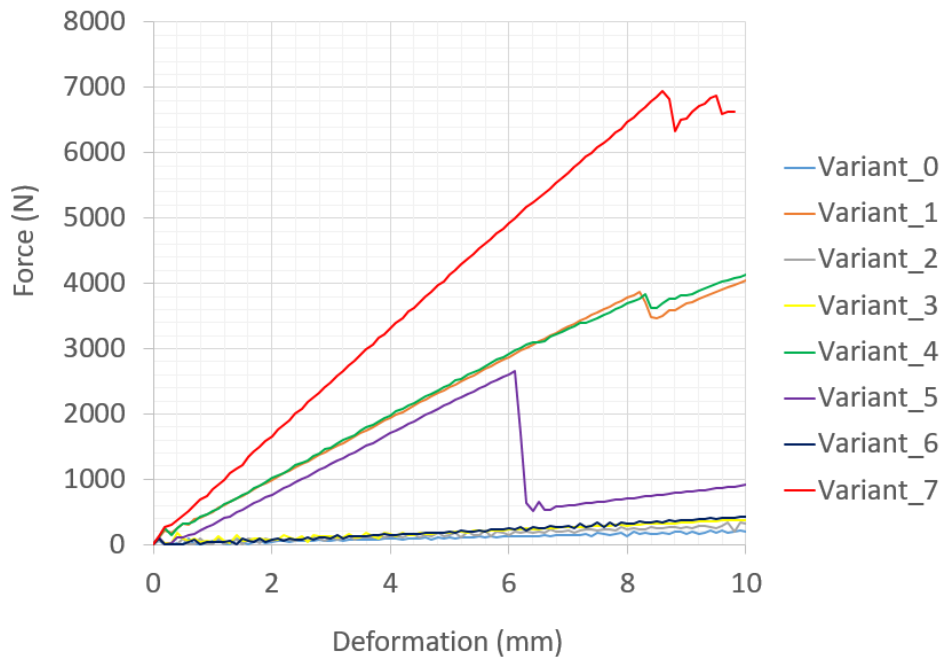


Figure 8-24: Predicted force-deformation-curves of FRP during 3-point bending test for all typical designs of rib with chosen dimension by max deformation of 10 mm

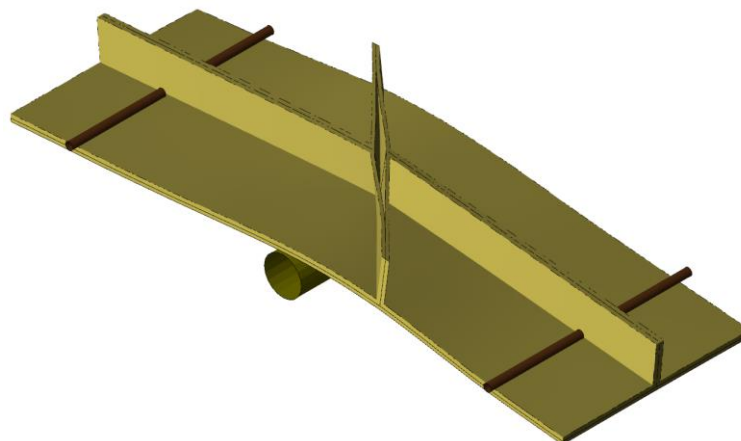


Figure 8-25: Crack opening of matrix in the diagonal rib in variant 5

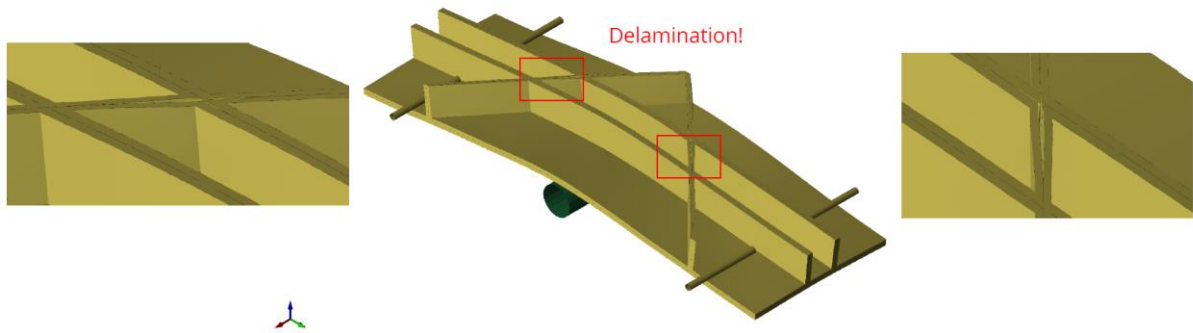


Figure 8-26: Crack opening of matrix in variant 7

8.4 Summary

This chapter provides exemplary applications of modelling FRP on macro- and meso-scale. Information of the fiber orientation, which is gained from textile forming process simulation, can be further used in the macro-scale FRP model with the help of mapping method. Numerical structural analysis of T-cup component proved the important of fiber orientation on mechanical performance of the FRP, especially under tensile loading condition.

While the macro-scale approach is suitable for thin-walled FRP component, a model with higher representation degree is necessary for complex FRP with large thickness, as the failure mechanism such as delamination is dominant and cannot be neglected. An approach with macro-scale model in combination with laminate construction of multiple layer of thin shell elements, which are coupled to each other, can be used to model thick FRP with delamination failure, but the failure between yarn and matrix cannot be clearly separated. Thus, the influence of continuous running yarn in rib cannot be investigated with such model. For that reason, the meso-scale model of FRP comes into use. The simulation results with meso-scale model of T-shaped stiffened component show good correlation with experimental data by description of bending strength and stiffness of different FRP configuration variations. The model is used in further investigation of FRP made from BWKF. However, there is still room for improvement, namely, additional failure modes such as debonding and mode III out-of-plane fracture toughness should be implemented into the FEM model in future research.

9 Conclusion and outlook

The production technique of Biaxial Weft-Knitted Fabrics (BWKF) was invented more than 20 years ago. Great effort has been put into research to extend the capability of BWKF production technique for complex reinforcement structures as well as to assess the forming behavior of BWKF quantitatively. The first commercial weft-knitting machine for BWKF was just introduced to the market in 2022 by Shima Seiki. There is good basis to spread the use of BWKF in the industry. The weft-knitting experts work tirelessly to push the boundary of the BWKF production technique to a new horizon. At the same time, numerical approach tries to assist and accelerate the development process in different ways.

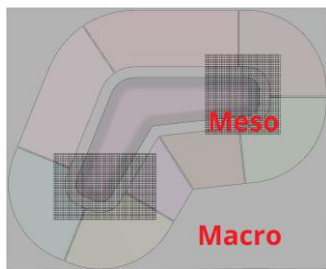
In this thesis, the application of FEM for modelling of BWKF and their FRP on different scales was introduced. The macro-scale model is based on a continuum mechanics approach for general textile forming. Meso-scale modelling approaches with beam and shell elements for the reinforcing yarn were suggested and validated. The performance of these models was tested to predict forming defects and yarn orientation. The meso-scale models proved their advantage in comparison with macro model, but it comes at the cost of higher requirement for computation resources. Nevertheless, further improvement can be made.

On further development of textile FEM model

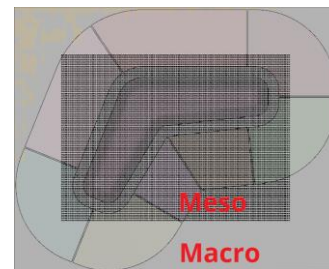
If the Moore's law is kept up, the spread of model with higher representation for large scale forming simulation in the near future is possible. Otherwise, a hybrid approach should be considered, where models of different scales are combined in a single simulation. The higher representation model can locally replace the lower representation model or can be coupled to it. Position and size of the models with high representation can be chosen to meet the requirement such as prediction of defects or yarn orientation at certain areas (Figure 9-1). This hybrid approach would help to reduce the computational costs without compromising the predictive capability of the model.

The meso shell model can be further improved by using an orthotropic material model for the shell elements representing the reinforcing yarns instead of the current linear elastic model. The use of a higher representation model to predict the forming behavior of BWKF with the help of virtual test of small unit cell should also be considered. Modelling the reinforcing yarns with solid elements is also worth trying, where the deformability in the transverse direction would be improved significantly, which can lead to a better prediction of forming mechanisms such as in-plane shear and compression. A unit cell of

near micro scale model, where filaments in yarn are modelled with beam elements, would provide more accurate predictions. The gained information from virtual tests could be transferred to a lower representation model. However, generating a unit cell model with high representation is also challenging. A process simulation of weft-knitting process could provide information of the influence of machine parameters on the BWKF structure. However, the computing effort is extremely high. A process-like simulation, as the method to generate the unit cell for the meso shell model in Section 6.2.2 is a good compromise, whereby most geometric fabric configurations can be taken into account and the influence of machine parameters can be quasi-substituted with suitable boundary conditions.



For prediction of gap formation



For prediction of yarn orientation

Figure 9-1: Possibilities of a hybrid textile FEM model for BWKF forming simulation with L-profile tools

On the use of artificial neural network (ANN)

The production of BWKF is a challenge where many machine parameters and fabric configurations play a decisive role for the forming behavior of the BWKF reinforcement. The work of Orawattanasrikul [225] was dedicated to the investigation the role of stitch cam depth SCD / stitch length SL, weft yarn density on in-plane shear behavior as well as yarn resistance (via pull-out tests). The role of further input factors such as yarn material, yarn fineness, stitch yarn structure (single jersey, double jersey), layer quantity of reinforcing yarn, machine gauge / warp yarn density, and the interdependence of output factors such as bending stiffness, yarn crimp, or even air permeability have not yet been investigated. Air permeability plays an important role in the impregnation process of fiber reinforcement with thermoset matrix by liquid composite molding (LCM). Micro-scale model is one way to investigate such interdependence. There is other approach to answer such question.

Malik [533] has successfully trained an artificial neural network (ANN) to predict the yarn crimp and air permeability of PES multifilament woven fabrics. Training an ANN to investigate the interdependence between all of the named input and output factors above

is challenging but also very helpful. Manufacturer of BWKF would save tremendous amount of time and effort compared to trial-and-error methods to come up with optimal machine parameters and finally a fabric configuration that meets a specific requirement. The size of the data set for the ANN training depends on the quantity of input and output factors. In principle, a very large data set is required for a reliable prediction of the ANN, so that a great deal of effort must be expended in producing and testing all variants. Therefore, decision on input and output factors for the data set should be discussed with weft-knitting experts.

On further development of FRP FEM model

An FEM model is very useful for the development of FRP components, as the mechanical behavior of FRP with predetermined dimensions and configurations can be predicted without the need to produce a prototype. The assistance of the FEM model saves time, material and costs during the development process. The macro-scale approach is well-established and development of new generation of model is on the way. The meso-scale approach for FRP as shown in Section 8.2, where yarn and matrix are modelled separately, enables simulation-based prediction of the change of mechanical behavior of FRP depending on the reinforcing fiber and the matrix. Although the current FEM model can describe the most important FRP failure mechanisms and provides good predictions of the bending behavior, there is still room for further improvement. Further failure mechanisms such as debonding should be taken into account. The contact interface should also be improved, where mode II in-plane fracture toughness in warp and weft direction can be set separately. Further improvement of the contact interface can be done afterwards, e.g., measuring and modelling the mode III out-of-plane fracture toughness. The ILSS test results show multiple shear failure along the thickness direction. Thus, increasing the number of contact interfaces along the thickness direction can improve the accuracy of the model, but also involves additional computational costs.

To save computational costs, a hybrid approach would also be advised here. The mechanics of FRP are tested on different levels: coupon, component and structural level as mentioned in Section 2.7.4. The unit cell of BWKF with high representation can be used in combination with a suitable matrix model and a coupling method such as Domain Superposition Technique DTS to create a composite unit cell model. The coupling method should assure the accuracy of force transfer between fiber and matrix in the model. Such unit cell model of FRP can be used to virtually characterize the FRP as well as to investigate the influence of fiber structure on FRP properties, e.g., influence of stitching yarn fineness on ILSS properties. The gained information is then transferred to a model with lower representation for component and structural analyses. A combination of models with

lower and higher representation in one simulation is also worth a try. For example, if the location with high risk of failure in FRP is known, the FRP model at that position can be substituted with a meso-scale model, while the macro model is still used for the large structure.

On extension of the virtual FRP production process chain

Figure 8-1 shows exemplary a virtual FRP production chain, where it starts with BWKF production and ends with the FRP at component level. This chain can be further extended in both directions. The supply chain of FRP is long and involves many suppliers, contractors, and end users in many different industries. In the top-down point of view, it starts with the demand of producing certain FRP to meet a specific working condition and ends up with a decision of how that FRP component should be produced with the current state of technology. If the necessary database is available and a virtual analysis across the chain is reliable, the whole process would be accelerated significantly.

In bottom-up point of view, when any supplier or research institute comes up with a solution for a commonly known unsolved problem, it will come to the question, how would the end users benefit? For example, suppose that weft-knitting technique can produce multiaxial reinforcements with integral stiffened elements for cylinder shaped FRP, would it eventually lead to a lighter and more durable space rocket?

The classical way is prototyping and testing. The virtual FRP production process chain is not an alternative to the classical way, but at least it can give an orientation on go / no go decision with certain grade of confidence. For the examples above, a textile unit cell of weft-knitted structure is generated and the equivalent FRP is tested virtually on coupon and component level. The simulation results are then compared with the database of a currently used material. This would indicate that there has been a significant improvement. The next question is whether defects would occur during the forming of the textile and consolidation of the composite. Finally, the virtual test can be carried out for FRP on large-scale level to check the flightworthiness. Thus, an extension of the current virtual FRP production chain to include large-scale structural analysis would be of great benefit.

Epilogue

The weft-knitting technique for the production of fiber reinforcements has its advantages and disadvantages. One day, BWKF should take its rightful place in the industry. Until then, the research continues. Even though said is always easier than done, let this thesis end with the quote of Alan Turing:

"We can only see a short distance ahead, but we can see plenty there that needs to be done."

10References

- [1] Ehlers, Ernest G. and Potter, Simeon. *Encyclopedia Britannica: "phase"*, 2019. <https://www.britannica.com/science/phase-state-of-matter> (accessed March 25, 2022).
- [2] Soboyejo, W. *Mechanical properties of engineered materials*; Dekker: New York, Basel, 2003.
- [3] Jambur, V.; Tangpatjaroen, C.; Xi, J.; Tarnsangpradit, J.; Gao, M.; Sheng, H.; Perepezko, J. H.; Szlufarska, I. Effects of minor alloying on the mechanical properties of Al based metallic glasses. *Journal of Alloys and Compounds* **2021**, *854*, 157266. DOI: 10.1016/j.jallcom.2020.157266.
- [4] Zia, A. W.; Zhou, Z.; Shum, P. W.; Li, L. K. Y. The effect of two-step heat treatment on hardness, fracture toughness, and wear of different biased diamond-like carbon coatings. *Surface and Coatings Technology* **2017**, *320*, 118–125. DOI: 10.1016/j.surfcoat.2017.01.089.
- [5] Antistatic agent incorporation method and its performance. In *Handbook of Antistatics*; George, W., Jurgen, P., Eds.; Elsevier, 2016; pp 129–139.
- [6] Dobrzański, L. A.; Tański, T.; Dobrzańska-Danikiewicz, A. D.; Jonda, E.; Bonek, M.; Drygała, A. Structures, properties and development trends of laser-surface-treated hot-work steels, light metal alloys and polycrystalline silicon. *Laser Surface Engineering*; Elsevier, 2015; pp 3–32.
- [7] Pilvin, P.; Feaugas, X.; Clavel, M. A Micro—Macro Structural Approach of the Cyclic Behavior of a Two—Phase Alloy. In *IUTAM Symposium on Micromechanics of Plasticity and Damage of Multiphase Materials*; Gladwell, G. M. L., Pineau, A., Zaoui, A., Eds.; Springer Netherlands: Dordrecht, 1996; pp 141–148.
- [8] Klein, B. *Leichtbau-Konstruktion*; Springer Fachmedien Wiesbaden: Wiesbaden, 2013.
- [9] Steinegger, R. *Fuel economy for aircraft operation as a function of weight and distance*, 2017.
- [10] van der Woude, J.; Lawton, E. L. Composite Design and Engineering. In *Fiberglass and Glass Technology: Energy-Friendly Compositions and Applications*; Wallenberger, F. T., Bingham, P. A., Eds.; Springer: New York, N.Y., 2010; pp 125–173.
- [11] Tenney, D. R.; Davis, John G., Jr.; Pipes, R. B.; Johnson, N. NASA Composite Materials Development: Lessons Learned and Future Challenges.
- [12] Tenney, D. R.; Davis John G., JR.; Johnston, N. J.; Pipes, R. B.; McGuire, J. F. *Structural Framework for Flight I: NASA's Role in Development of Advanced Composite Materials for Aircraft and Space Structures*, 2019.

- [13] Raj, K.; Vasudevan, A.; Pugazhendhi, L. A review on different hybrid composites for aircraft structures. *Materials Today: Proceedings* **2021**. DOI: 10.1016/j.matpr.2020.10.774.
- [14] Das, M.; Sahu, S.; Parhi, D. R. A Review of Application of Composite Materials for Aerospace Structures and its Damage Detection Using Artificial Intelligence Techniques. *SSRN Journal* **2020**. DOI: 10.2139/ssrn.3714181.
- [15] Setlak, L.; Kowalik, R.; Lusiak, T. Practical Use of Composite Materials Used in Military Aircraft. *Materials* **2021**, *14*. DOI: 10.3390/ma14174812.
- [16] O'Connor, J. S.; Frankhauser, W. Advances in Fiber-Reinforced Polymer Composites in Transportation Infrastructure. *Transportation Research Record* **2016**, *2592*, 56–64. DOI: 10.3141/2592-07.
- [17] Kim, Y. J. State of the practice of FRP composites in highway bridges. *Engineering Structures* **2019**, *179*, 1–8. DOI: 10.1016/j.engstruct.2018.10.067.
- [18] Möhring, H.-C. Composites in Production Machines. *Procedia CIRP* **2017**, *66*, 2–9. DOI: 10.1016/j.procir.2017.04.013.
- [19] Kusmaul, R.; Zogg, M.; Weiss, L.; Relea, E.; Jacomet, R.; Ermanni, P. Carbon Fiber Reinforced Polymers for High-dynamic Testing Machines. *Procedia CIRP* **2017**, *66*, 10–15. DOI: 10.1016/j.procir.2017.03.300.
- [20] Olabi, A. G.; Wilberforce, T.; Elsaid, K.; Sayed, E. T.; Salameh, T.; Abdelkareem, M. A.; Baroutaji, A. A Review on Failure Modes of Wind Turbine Components. *Energies* **2021**, *14*, 5241. DOI: 10.3390/en14175241.
- [21] Pham, M. Q.; Wendt, E.; Häntzsche, E.; Gereke, T.; Cherif, C. Numerical modeling of the mechanical behavior of textile structures on the meso-scale for forming process simulations of composite 3D preforms. *Engineering Reports* **2020**. DOI: 10.1002/eng2.12348.
- [22] Xiao Chen; Martin A. Eder. A Critical Review of Damage and Failure of Composite Wind Turbine Blade Structures. *IOP Conf. Ser.: Mater. Sci. Eng.* **2020**, *942*, 12001. DOI: 10.1088/1757-899x/942/1/012001.
- [23] Katnam, K. B.; Comer, A. J.; Roy, D.; Da Silva, L. F. M.; Young, T. M. Composite Repair in Wind Turbine Blades: An Overview. *The Journal of Adhesion* **2015**, *91*, 113–139. DOI: 10.1080/00218464.2014.900449.
- [24] Thomas, L.; Ramachandra, M. Advanced materials for wind turbine blade- A Review. *Materials Today: Proceedings* **2018**, *5*, 2635–2640. DOI: 10.1016/j.matpr.2018.01.043.
- [25] H Ahmad; A A Markina; M V Porotnikov; F Ahmad. A review of carbon fiber materials in automotive industry. *IOP Conf. Ser.: Mater. Sci. Eng.* **2020**, *971*, 32011. DOI: 10.1088/1757-899x/971/3/032011.

- [26] Ravishankar, B.; Nayak, S. K.; Kader, M. A. Hybrid composites for automotive applications – A review. *Journal of Reinforced Plastics and Composites* **2019**, *38*, 835–845. DOI: 10.1177/0731684419849708.
- [27] Sivanur, K.; Umananda, K. V.; Pai, D. Advanced materials used in automotive industry-a review. In *PROCEEDINGS OF THE 14TH ASIA-PACIFIC PHYSICS CONFERENCE*; AIP Publishing, 2021; p 20032.
- [28] Caramatescu, A.; Mocanu, C.-I. Review of composite materials applications in marine industry. *AnnUGalShipBuilding* **2019**, *42*, 169–174. DOI: 10.35219/AnnUGalShipBuilding.2019.42.23.
- [29] Barsotti, B.; Gaiotti, M.; Rizzo, C. M. Recent Industrial Developments of Marine Composites Limit States and Design Approaches on Strength. *J. Marine. Sci. Appl.* **2020**, *19*, 553–566. DOI: 10.1007/s11804-020-00171-1.
- [30] Mistry, P. J.; Johnson, M. S.; Galappaththi, U. I. Selection and ranking of rail vehicle components for optimal lightweighting using composite materials. *Proceedings of the Institution of Mechanical Engineers, Part F: Journal of Rail and Rapid Transit* **2021**, *235*, 390–402. DOI: 10.1177/0954409720925685.
- [31] Mathes, V. *17. Composites-Markterhebung*; Composites Germany.
- [32] Michael Sauer. *Composites Market Report 2020: The global CF-Production capacity. Market Development, Trends, Outlook and Challenges*; Composites United, 2021.
- [33] Advani, S. G.; Hsiao, K.-T. Introduction to composites and manufacturing processes. *Manufacturing Techniques for Polymer Matrix Composites (PMCs)*; Elsevier, 2012; pp 1–12.
- [34] Palmer, R., Ed. *Techno-economic requirements for composite aircraft components: Innovative Composite Aircraft Primary Structure*; NASA. Langley Research Center, 1994.
- [35] Trümper, W.; Lin, H.; Callin, T.; Bollengier, Q.; Cherif, C.; Krzywinski, S. Recent developments in multi-layer flat knitting technology for waste free production of complex shaped 3D-reinforcing structures for composites. *IOP Conf. Ser.: Mater. Sci. Eng.*, *141*, 12015. DOI: 10.1088/1757-899X/141/1/012015.
- [36] Lin, H. *Entwicklung einer Prozesskette zur Umsetzung komplexer Geometrien in formgerechte 2D/3D Hybridgarn-Mehrlagengestricke für Faserkunststoffverbundanwendungen*. Zugl.: Dresden, Techn. Univ., Fak. Maschinenwesen, Diss., 2015; TUDpress Verl. der Wiss: Dresden, 2015.
- [37] Bollengier, Q.; Wieczorek, F.; Hellmann, S.; Trümper, W.; Cherif, C. One-step manufacturing of innovative flat-knitted 3D net-shape preforms for composite applications. *IOP Conf Ser-Mat Sci* **2017**, *254*, 42007. DOI: 10.1088/1757-899X/254/4/042007.

- [38] *Manufacturing Techniques for Polymer Matrix Composites (PMCs)*; Elsevier, 2012.
- [39] Anthony R. Bunsell. 1 - Fibers for composite reinforcements: Properties and microstructures. In *Composite Reinforcements for Optimum Performance (Second Edition)*, Second Edition; Philippe Boisse, Ed.; Woodhead Publishing, 2021; pp 3–34.
- [40] Mazumdar, S. *Composites Manufacturing: Materials, Product, and Process Engineering*; CRC Press, 2001.
- [41] Cherif, C. *Textile Materials for Lightweight Constructions*; Springer-Verlag Berlin Heidelberg, 2016.
- [42] Freudenberg, C. Textile Fiber Materials. In *Textile Materials for Lightweight Constructions*; Cherif, C., Ed.; Springer Berlin Heidelberg: Berlin, Heidelberg, 2016; pp 37–101.
- [43] Paul, C. *Funktionalisierung von duroplastischen Faserverbundwerkstoffen durch Hybridgarne: Adaptive Strukturen durch die Integration von Formgedächtnislegierungen*; Vieweg+Teubner Verlag: Wiesbaden, 2012.
- [44] Ashir, M. M. *Development of innovative textile-based adaptive fiber-reinforced plastics with shape memory alloys*, 1. Auflage; Verlag Dr. Hut: München, 2021.
- [45] Lohse, F.; Kopelmann, K.; Grellmann, H.; Ashir, M.; Gereke, T.; Häntzsche, E.; Sennewald, C.; Cherif, C. Experimental and Numerical Analysis of the Deformation Behavior of Adaptive Fiber-Rubber Composites with Integrated Shape Memory Alloys. *Materials* **2022**, *15*. DOI: 10.3390/ma15020582.
- [46] Mahendrarajah, G.; Kandare, E.; Khatibi, A. A. Enhancing the Fracture Toughness Properties by Introducing Anchored Nano-Architectures at the Metal-FRP Composite Interface. *J. Compos. Sci.* **2019**, *3*, 17. DOI: 10.3390/jcs3010017.
- [47] Wallenberger, F. T.; Bingham, P. A., Eds. *Fiberglass and Glass Technology: Energy-Friendly Compositions and Applications*; Springer: New York, N.Y., 2010.
- [48] Hausrath, R. L.; Longobardo, A. V. High-Strength Glass Fibers and Markets. In *Fiberglass and Glass Technology: Energy-Friendly Compositions and Applications*; Wallenberger, F. T., Bingham, P. A., Eds.; Springer: New York, N.Y., 2010; pp 197–225.
- [49] Longobardo, A. V. Glass Fibers for Printed Circuit Boards. In *Fiberglass and Glass Technology: Energy-Friendly Compositions and Applications*; Wallenberger, F. T., Bingham, P. A., Eds.; Springer: New York, N.Y., 2010; pp 175–196.
- [50] *JEC observer: Current trends in the global composites industry 2020-2025*; JEC Group: Paris, DL 2021.
- [51] Döbrich, O.; Gereke, T.; Hengstermann, M.; Cherif, C. Microscale finite element model of brittle multifilament yarn failure behavior. *Journal of Industrial Textiles* **2018**, *47*, 870–882. DOI: 10.1177/1528083716674908.

- [52] Younes, A.; Seidel, A.; Engler, T.; Cherif, C.; Ehlig, D. Mechanical behavior of carbon and glass filament yarns under high temperatures for composite applications. *Journal of the Textile Institute* **2013**, *104*, 251–259. DOI: 10.1080/00405000.2012.717752.
- [53] Flemming, M.; Roth, S. *Faserverbundbauweisen Eigenschaften*; Springer Berlin Heidelberg: Berlin, Heidelberg, 2003.
- [54] Pierson, H. O. *Handbook of carbon, graphite, diamond and fullerenes: Properties, processing and applications / by Hugh O. Pierson*; Noyes Publications: Park Ridge, N.J., 1993.
- [55] Gorbatikh, L.; Lomov, S. V. Nano-engineered Carbon Fibre-Reinforced Composites: Challenges and Opportunities. In *The Structural Integrity of Carbon Fiber Composites*; Beaumont, P. W. R., Soutis, C., Hodzic, A., Eds.; Springer International Publishing: Cham, 2017; pp 117–135.
- [56] Romanov, V. S.; Lomov, S. V.; Verpoest, I.; Gorbatikh, L. Stress magnification due to carbon nanotube agglomeration in composites. *Composite Structures* **2015**, *133*, 246–256. DOI: 10.1016/j.compstruct.2015.07.069.
- [57] Song, Y. S.; Youn, J. R. Influence of dispersion states of carbon nanotubes on physical properties of epoxy nanocomposites. *Carbon* **2005**, *43*, 1378–1385. DOI: 10.1016/j.carbon.2005.01.007.
- [58] Qian, H.; Greenhalgh, E. S.; Shaffer, M. S. P.; Bismarck, A. Carbon nanotube-based hierarchical composites: a review. *J. Mater. Chem.* **2010**, *20*, 4751. DOI: 10.1039/C000041H.
- [59] Morgan, P. *Carbon Fibers and Their Composites*; CRC Press, 2005.
- [60] Martino, M.; Meloni, E.; Festa, G.; Palma, V. Propylene Synthesis: Recent Advances in the Use of Pt-Based Catalysts for Propane Dehydrogenation Reaction. *Catalysts* **2021**, *11*, 1070. DOI: 10.3390/catal11091070.
- [61] Brazdil, J. F. A critical perspective on the design and development of metal oxide catalysts for selective propylene ammoxidation and oxidation. *Applied Catalysis A: General* **2017**, *543*, 225–233. DOI: 10.1016/j.apcata.2017.06.022.
- [62] Kopeć, M.; Krys, P.; Yuan, R.; Matyjaszewski, K. Aqueous RAFT Polymerization of Acrylonitrile. *Macromolecules* **2016**, *49*, 5877–5883. DOI: 10.1021/acs.macromol.6b01336.
- [63] Phung, T. K.; Le Pham, T. M.; Vu, K. B.; Busca, G. (Bio)Propylene production processes: A critical review. *Journal of Environmental Chemical Engineering* **2021**, *9*, 105673. DOI: 10.1016/j.jece.2021.105673.

- [64] Grasselli, R. K.; Trifirò, F. Acrylonitrile from Biomass: Still Far from Being a Sustainable Process. *Top Catal* **2016**, *59*, 1651–1658. DOI: 10.1007/s11244-016-0679-7.
- [65] Matsumoto, T. Mesophase pitch and its carbon fibers. *Pure and Applied Chemistry* **1985**, *57*, 1553–1562. DOI: 10.1351/pac198557111553.
- [66] Mochida, I.; Yoon, S.-H.; Korai, Y. Mesoscopic structure and properties of liquid crystalline mesophase pitch and its transformation into carbon fiber. *Chemical record (New York, N.Y.)* **2002**, *2*, 81–101. DOI: 10.1002/tcr.10016.
- [67] Chudoba, R.; Vořechovský, M.; Eckers, V.; Gries, T. Effect of Twist, Fineness, Loading Rate and Length on Tensile Behavior of Multifilament Yarns (A Multivariate Study). *Textile Research Journal* **2007**, *77*, 880–891. DOI: 10.1177/0040517507081280.
- [68] Golzar, M.; Brünig, H.; Mäder, E. Commingled hybrid yarn diameter ratio in continuous fiber-reinforced thermoplastic composites. *Journal of Thermoplastic Composite Materials* **2007**, *20*, 17–26. DOI: 10.1177/0892705707068069.
- [69] Park, S.-W.; Yoo, S.-H.; An, S.-T.; Chang, S.-H. Material characterization of glass/polypropylene composite bone plates according to the forming condition and performance evaluation under a simulated human body environment. *Composites Part B* **2012**, *43*, 1101–1108. DOI: 10.1016/j.compositesb.2011.09.008.
- [70] Hasan, M. M. B.; Staiger, E.; Ashir, M.; Cherif, C. Development of carbon fibre/polyamide 6,6 commingled hybrid yarn for textile-reinforced thermoplastic composites. *Journal of Thermoplastic Composite Materials* **2015**, *28*, 1708–1724. DOI: 10.1177/0892705715604677.
- [71] Rajesh, P.; Delarosa, C.; Gagné, M.; Klemberg-Sapieha, J. E.; Sirois, F.; Therriault, D. Continuous and selective-area coating of silver on fiber-reinforced polymer composites for aerospace applications. *Materials Today Communications* **2019**, *18*, 206–212. DOI: 10.1016/j.mtcomm.2018.11.002.
- [72] Onggar, T.; Häntzsche, E.; Hund, R.-D.; Cherif, C. Multilayered Glass Filament Yarn Surfaces as Sensor Yarn for In-situ Monitoring of Textile-reinforced Thermoplastic Composites. *Fibers Polym* **2019**, *20*, 1945–1957. DOI: 10.1007/s12221-019-1237-2.
- [73] Hund, H.; Hund, R.-D. Textile Finishing and Finishing Technologies. In *Textile Materials for Lightweight Constructions*; Cherif, C., Ed.; Springer Berlin Heidelberg: Berlin, Heidelberg, 2016; pp 427–477.
- [74] Tiwari, S.; Bijwe, J. Surface Treatment of Carbon Fibers - A Review. *Procedia Technology* **2014**, *14*, 505–512. DOI: 10.1016/j.protcy.2014.08.064.
- [75] Kruppke, I.; Scheffler, C.; Simon, F.; Hund, R.-D.; Cherif, C. Surface Treatment of Carbon Fibers by Oxy-Fluorination. *Materials* **2019**, *12*. DOI: 10.3390/ma12040565.

- [76] Jones, F. R. Serendipity in Carbon Fibres: Interfaces and Interphases in Composites. In *The Structural Integrity of Carbon Fiber Composites*; Beaumont, P. W. R., Soutis, C., Hodzic, A., Eds.; Springer International Publishing: Cham, 2017; pp 71–97.
- [77] Pukánszky, B. Interfaces and interphases in multicomponent materials: past, present, future. *European Polymer Journal* **2005**, *41*, 645–662. DOI: 10.1016/j.eurpolymj.2004.10.035.
- [78] Ehrenstein, G. W. *Faserverbund-Kunststoffe: Werkstoffe - Verarbeitung - Eigenschaften*, 2., völlig überarb. Aufl.; Hanser: München, Wien, 2006.
- [79] Kutzt, M.; Hornig, A.; Richter, J.; Gude, M. Increasing the structural energy dissipation of laminated fibre composite materials by delamination control. *Materials & Design* **2018**, *156*, 93–102. DOI: 10.1016/j.matdes.2018.06.039.
- [80] Kelly, A.; Tyson, W. R. Tensile properties of fibre-reinforced metals: Copper/tungsten and copper/molybdenum. *Journal of the Mechanics and Physics of Solids* **1965**, *13*, 329–350. DOI: 10.1016/0022-5096(65)90035-9.
- [81] DiFrancia, C.; Ward, T. C.; Claus, R. O. The single-fibre pull-out test. 1: Review and interpretation. *Composites Part A: Applied Science and Manufacturing* **1996**, *27*, 597–612. DOI: 10.1016/1359-835X(95)00069-E.
- [82] Dollar, A.; Steif, P. S.; Wang, Y. C.; Hui, C. Y. Analyses of the fiber push-out test. *International Journal of Solids and Structures* **1993**, *30*, 1313–1329. DOI: 10.1016/0020-7683(93)90214-R.
- [83] Molina-Aldareguía, J. M.; Rodríguez, M.; González, C.; LLorca, J. An experimental and numerical study of the influence of local effects on the application of the fibre push-in test. *Philosophical Magazine* **2011**, *91*, 1293–1307. DOI: 10.1080/14786435.2010.480947.
- [84] Khalid, M. Y.; Arif, Z. U.; Al Rashid, A.; Shahid, M. I.; Ahmed, W.; Tariq, A. F.; Abbas, Z. Interlaminar shear strength (ILSS) characterization of fiber metal laminates (FMLs) manufactured through VARTM process. *Forces in Mechanics* **2021**, *4*, 100038. DOI: 10.1016/j.finmec.2021.100038.
- [85] Chua, P. S.; Piggott, M. R. The glass fibre-polymer interface: II—Work of fracture and shear stresses. *Composites Science and Technology* **1985**, *22*, 107–119. DOI: 10.1016/0266-3538(85)90079-X.
- [86] Ogihara, S.; Koyanagi, J. Investigation of combined stress state failure criterion for glass fiber/epoxy interface by the cruciform specimen method. *Composites Science and Technology* **2010**, *70*, 143–150. DOI: 10.1016/j.compscitech.2009.10.002.
- [87] Scholtens, B.; Brackman, J. Influence of the Film Former on Fibre-Matrix Adhesion and Mechanical Properties of Glass-Fibre Reinforced Thermoplastics. *The J. of Adhesion* **1995**, *52*, 115–129. DOI: 10.1080/00218469508015189.

- [88] Tjong, S. Short glass fiber-reinforced polyamide 6,6 composites toughened with maleated SEBS. *Composites Science and Technology* **2002**, *62*, 2017–2027. DOI: 10.1016/S0266-3538(02)00140-9.
- [89] Hengstermann, M.; Hasan, M. M. B.; Scheffler, C.; Abdkader, A.; Cherif, C. Development of a new hybrid yarn construction from recycled carbon fibres for high-performance composites. Part III: Influence of sizing on textile processing and composite properties. *Journal of Thermoplastic Composite Materials* **2021**, *34*, 409–430. DOI: 10.1177/0892705719847240.
- [90] Dányádi, L.; Gulyás, J.; Pukánszky, B. Coupling of carbon fibers to polycarbonate: surface chemistry and adhesion. *Composite Interfaces* **2003**, *10*, 61–76. DOI: 10.1163/156855403763586792.
- [91] Day, R.; Hewson, K.; Lovell, P. Surface modification and its effect on the interfacial properties of model aramid-fibre/epoxy composites. *Composites Science and Technology* **2002**, *62*, 153–166. DOI: 10.1016/S0266-3538(01)00135-X.
- [92] Bahl, S. Fiber reinforced metal matrix composites - a review. *Materials Today: Proceedings* **2021**, *39*, 317–323. DOI: 10.1016/j.matpr.2020.07.423.
- [93] Lamon, J. Reinforcement of ceramic matrix composites by ceramic continuous fibers. *Composite Reinforcements for Optimum Performance*; Elsevier, 2021; pp 55–93.
- [94] Fathima, S.; Deeraj, B.; Appukuttan, S.; Joseph, K. Carbon fiber and glass fiber reinforced elastomeric composites. *Fiber Reinforced Composites*; Elsevier, 2021; pp 307–340.
- [95] Kuch, H.; Palzer, U.; Schwabe, J.-H. *Herstellung von Betonwaren und betonfertigteilen: Verfahren und ausrüstungen*; Verlag Bau+Technik: Düsseldorf [Germany], 2009.
- [96] Diestel, O.; Hausding, J. Pre-impregnated Textile Semi-finished Products (Prepregs). In *Textile Materials for Lightweight Constructions*; Cherif, C., Ed.; Springer Berlin Heidelberg: Berlin, Heidelberg, 2016; pp 361–379.
- [97] Vaidya, U. K.; Chawla, K. K. Processing of fibre reinforced thermoplastic composites. *International Materials Reviews* **2008**, *53*, 185–218. DOI: 10.1179/174328008X325223.
- [98] Cherif, C. Introduction. *Textile Materials for Lightweight Constructions: Technologies - Methods - Materials - Properties*, 2016; pp 1–7.
- [99] Murphy, J. *The Reinforced Plastics Handbook*; Elsevier, 1998.
- [100] Liu, S.-J. Injection molding in polymer matrix composites. *Manufacturing Techniques for Polymer Matrix Composites (PMCs)*; Elsevier, 2012; pp 15–46.
- [101] Mitschang, P.; Christmann, M. Continuous fiber reinforced profiles in polymer matrix composites. In *Manufacturing Techniques for Polymer Matrix Composites*

- (PMCs); Suresh G. Advani, Kuang-Ting Hsiao, Eds.; Woodhead Publishing, 2012; pp 209–242.
- [102] Neitzel, M.; Mitschang, P.; Breuer, U., Eds. *Handbuch Verbundwerkstoffe: Werkstoffe, Verarbeitung, Anwendung, 2.*, aktualisierte und erweiterte Auflage; Hanser: München, 2014.
- [103] Minsch, N. P. Verfahrens- und Methodenentwicklung für die generative Fertigung von komplexen Leichtbaustrukturen in Hybridbauweise. Dissertation, Technische Universität Dresden.
- [104] Mack, C.; Taylor, H. M. 39—The Fitting of Woven Cloth to Surfaces. *Journal of the Textile Institute Transactions* **1956**, *47*, T477-T488. DOI: 10.1080/19447027.1956.10750433.
- [105] M. Bulat; H. Ahlborn; F. Gnädinger; D. Michaelis. 15 - Braided carbon fiber composites. In *Advances in Braiding Technology*; Yordan Kyosev, Ed.; Woodhead Publishing, 2016; pp 383–394.
- [106] J. Schäfer; T. Gries. 17 - Braiding pultrusion of thermoplastic composites. In *Advances in Braiding Technology*; Yordan Kyosev, Ed.; Woodhead Publishing, 2016; pp 405–428.
- [107] B. Arold; A. Gessler; C. Metzner; K. Birkefeld. 1 - Braiding processes for composites manufacture. In *Advances in Composites Manufacturing and Process Design*; Philippe Boisse, Ed.; Woodhead Publishing, 2015; pp 3–26.
- [108] Jason P. Carey. *Handbook of Advances in Braided Composite Materials*; Elsevier, 2017.
- [109] Wendland, B.; Ramaswamy, S.; Schäfer, J.; Gries, T. Three-dimensional composite manufacturing processes. In *Advances in composites manufacturing and process design*; Boisse, P., Ed.; Woodhead Publishing: Cambridge, UK, 2015; pp 131–146.
- [110] Crosky, A.; Grant, C.; Kelly, D.; Legrand, X.; Pearce, G. 4 - Fibre placement processes for composites manufacture. In *Advances in Composites Manufacturing and Process Design*; Philippe Boisse, Ed.; Woodhead Publishing, 2015; pp 79–92.
- [111] Grundmann, T. C. *Automatisiertes Preforming für schalenförmige komplexe Faserverbundbauteile*. Zugl.: Aachen, Techn. Hochsch., Diss., 2009; Shaker: Aachen, 2009.
- [112] Sloan, J. AFP/ATL design-to-manufacture: Bridging the gap. *High-Performance Composites* **2009**.
- [113] Grant, C. Automated processes for composite aircraft structure. *Industrial Robot: An International Journal* **2006**, *33*, 117–121. DOI: 10.1108/01439910610651428.
- [114] Gliesche, K. Application of the tailored fibre placement (TFP) process for a local reinforcement on an “open-hole” tension plate from carbon/epoxy laminates.

- Composites Science and Technology* **2003**, 63, 81–88. DOI: 10.1016/S0266-3538(02)00178-1.
- [115] Koricho, E. G.; Khomenko, A.; Fristedt, T.; Haq, M. Innovative tailored fiber placement technique for enhanced damage resistance in notched composite laminate. *Composite Structures* **2015**, 120, 378–385. DOI: 10.1016/j.compstruct.2014.10.016.
- [116] Schade, M. Embroidered Semi-finished Products and Embroidery Techniques. In *Textile Materials for Lightweight Constructions*; Cherif, C., Ed.; Springer Berlin Heidelberg: Berlin, Heidelberg, 2016; pp 347–360.
- [117] Meyer, O. *Kurzfaser-Preform-Technologie zur kraftflussgerechten Herstellung von Faserverbundbauteilen*, 2008.
- [118] Isobe, T.; Tanaka, T.; Nomura, T.; Yuasa, R. Comparison of strength of 3D printing objects using short fiber and continuous long fiber. *IOP Conf. Ser.: Mater. Sci. Eng.* **2018**, 406, 12042. DOI: 10.1088/1757-899X/406/1/012042.
- [119] Ning, F.; Cong, W.; Qiu, J.; Wei, J.; Wang, S. Additive manufacturing of carbon fiber reinforced thermoplastic composites using fused deposition modeling. *Composites Part B: Engineering* **2015**, 80, 369–378. DOI: 10.1016/j.compositesb.2015.06.013.
- [120] J. Mack; R. Schledjewski. 7 - Filament winding process in thermoplastics. In *Manufacturing Techniques for Polymer Matrix Composites (PMCs)*; Suresh G. Advani, Kuang-Ting Hsiao, Eds.; Woodhead Publishing, 2012; pp 182–208.
- [121] F. Boussu; C. Dufour; F. Veyet; M. Lefebvre. 3 - Weaving processes for composites manufacture. In *Advances in Composites Manufacturing and Process Design*; Philippe Boisse, Ed.; Woodhead Publishing, 2015; pp 55–78.
- [122] Sennewald, C.; Hoffmann, G.; Kleicke, R. Woven Semi-finished Products and Weaving Techniques. In *Textile Materials for Lightweight Constructions*; Cherif, C., Ed.; Springer Berlin Heidelberg: Berlin, Heidelberg, 2016; pp 159–211.
- [123] El-Dessouky, H. M.; Saleh, M. N. 3D Woven Composites: From Weaving to Manufacturing. In *Recent Developments in the Field of Carbon Fibers*; Khanna, R., Cayumil, R., Eds.; InTech, 2018.
- [124] Abounaim, M.; Diestel, O.; Hoffmann, G.; Cherif, C. High performance thermoplastic composite from flat knitted multi-layer textile preform using hybrid yarn. *Composites Science and Technology* **2011**, 71, 511–519. DOI: 10.1016/j.compscitech.2010.12.029.
- [125] Trümper, W. Semi-finished weft knitted fabrics and weft knitting techniques. *Textile Materials for Lightweight Constructions*; Springer Berlin Heidelberg, 2016; pp 213–250.

- [126] G. Dusserre; G. Bernhart. 2 - Knitting processes for composites manufacture. In *Advances in Composites Manufacturing and Process Design*; Philippe Boisse, Ed.; Woodhead Publishing, 2015; pp 27–53.
- [127] Hausding, J.; Märtin, J. Warp-Knitted Semi-finished Products and Warp-Knitting Technologies. In *Textile Materials for Lightweight Constructions*; Cherif, C., Ed.; Springer Berlin Heidelberg: Berlin, Heidelberg, 2016; pp 251–287.
- [128] Pietsch, K.; Fuchs, H. Nonwoven Semi-finished Products and Nonwoven Production Technology. In *Textile Materials for Lightweight Constructions*; Cherif, C., Ed.; Springer Berlin Heidelberg: Berlin, Heidelberg, 2016; pp 307–345.
- [129] Hofmann, M.; Wenzel, D.; Gulich, B.; Illing-Günther, H.; Nestler, D. Development of Nonwoven Preforms Made of Pure Recycled Carbon Fibres (rCF) for Applications of Composite Materials. *Key Engineering Materials* **2017**, *742*, 555–561. DOI: 10.4028/www.scientific.net/KEM.742.555.
- [130] K. Potter; C. Ward. 5 - Draping processes for composites manufacture. In *Advances in Composites Manufacturing and Process Design*; Philippe Boisse, Ed.; Woodhead Publishing, 2015; pp 93–109.
- [131] Nosrat Nezami, F.; Gereke, T.; Cherif, C. Active forming manipulation of composite reinforcements for the suppression of forming defects. *Composites Part A: Applied Science and Manufacturing* **2017**, *99*, 94–101. DOI: 10.1016/j.compositesa.2017.04.011.
- [132] Boisse, P. Textile composite forming simulations. *Woven Composites*; IMPERIAL COLLEGE PRESS, 2014; pp 215–237.
- [133] Rödel, H. Ready-Made Technologies for Fiber-Reinforced Plastic Composites. In *Textile Materials for Lightweight Constructions*; Cherif, C., Ed.; Springer Berlin Heidelberg: Berlin, Heidelberg, 2016; pp 381–426.
- [134] Nuss, D.; Pham, Q.; Hoffmann, G.; Cherif, C. Neue Technologie zur direkten Fertigung sphärisch gekrümmter Gewebe. *Technische Textilien* **2021**, *64*, 14–17. DOI: 10.51202/0323-3243-2021-1-014.
- [135] Schegner, P.; Fazeli, M.; Sennewald, C.; Hoffmann, G.; Cherif, C. Technology Development for Direct Weaving of Complex 3D Nodal Structures. *Appl Compos Mater* **2019**, *26*, 423–432. DOI: 10.1007/s10443-018-9734-9.
- [136] Vorhof, M.; Sennewald, C.; Schegner, P.; Meyer, P.; Hühne, C.; Cherif, C.; Sinapius, M. Thermoplastic Composites for Integrally Woven Pressure Actuated Cellular Structures: Design Approach and Material Investigation. *Polymers* **2021**, *13*. DOI: 10.3390/polym13183128.

- [137] Sankaran, V.; Rittner, S.; Hahn, L.; Cherif, C. Development of multiaxial warp knitting technology for production of three-dimensional near net shape shell preforms. *Textile Research Journal* **2017**, *87*, 1226–1241. DOI: 10.1177/0040517516651102.
- [138] Hull, J. L. Injection Molding of Thermosets. In *Spi plastics engineering handbook of the society of the plastics industry*; Berins, M. L., Ed.; Springer: [Place of publication not identified], 1991; pp 239–250.
- [139] Park, C. H.; Lee, W. I. Compression molding in polymer matrix composites. *Manufacturing Techniques for Polymer Matrix Composites (PMCs)*; Elsevier, 2012; pp 47–94.
- [140] Creasy, T. Sheet forming in polymer matrix composites. *Manufacturing Techniques for Polymer Matrix Composites (PMCs)*; Elsevier, 2012; pp 123–138.
- [141] Sherwood, J. A.; Fetfatsidis, K. A.; Gorczyca, J. L.; Berger, L. Fabric thermostamping in polymer matrix composites. *Manufacturing Techniques for Polymer Matrix Composites (PMCs)*; Elsevier, 2012; pp 139–181.
- [142] Haorong, L. I.; Gutowski, T. Chapter 11 The forming of thermoset composites. *Composite Sheet Forming*; Elsevier, 1997; pp 441–472.
- [143] Hubert, P.; Fernlund, G.; Poursartip, A. Autoclave processing for composites. *Manufacturing Techniques for Polymer Matrix Composites (PMCs)*; Elsevier, 2012; pp 414–434.
- [144] Sozer, E. M.; Simacek, P.; Advani, S. G. Resin transfer molding (RTM) in polymer matrix composites. In *Manufacturing Techniques for Polymer Matrix Composites (PMCs)*; Suresh G. Advani, Kuang-Ting Hsiao, Eds.; Woodhead Publishing, 2012; pp 245–309.
- [145] Hsiao, K.-T.; Heider, D. Vacuum assisted resin transfer molding (VARTM) in polymer matrix composites. In *Manufacturing Techniques for Polymer Matrix Composites (PMCs)*; Suresh G. Advani, Kuang-Ting Hsiao, Eds.; Woodhead Publishing, 2012; pp 310–347.
- [146] Malheiro, J. M.; Nunes, J. P. Simulation of Vacuum Assisted Resin Infusion (VARI) Process for the Production of Composite Material Parts. In *Advances in Evolutionary and Deterministic Methods for Design, Optimization and Control in Engineering and Sciences*; Gaspar-Cunha, A., Periaux, J., Giannakoglou, K. C., Gauger, N. R., Quagliarella, D., Greiner, D., Eds.; Springer International Publishing: Cham, 2021; pp 319–340.
- [147] Bickerton, S.; Kelly, P. A. Compression resin transfer moulding (CRTM) in polymer matrix composites. In *Manufacturing Techniques for Polymer Matrix Composites (PMCs)*; Suresh G. Advani, Kuang-Ting Hsiao, Eds.; Woodhead Publishing, 2012; pp 348–380.

- [148] Rout, D.; Nayak, R. K.; Praharaj, S. Aerospace and vehicle industry. *Handbook of Polymer Nanocomposites for Industrial Applications*; Elsevier, 2021; pp 399–417.
- [149] Reese, J.; Vorhof, M.; Hoffmann, G.; Böhme, K.; Cherif, C. Joule heating of dry textiles made of recycled carbon fibers and PA6 for the series production of thermoplastic composites. *Journal of Engineered Fibers and Fabrics* **2020**, *15*, 155892502090582. DOI: 10.1177/1558925020905828.
- [150] Reese, J.; Hoffmann, G.; Fieres, J.; Cherif, C. Characterization of the electrical behavior of a discontinuous hybrid yarn textile made of recycled carbon and PA6 fibers during Joule heating. *Journal of Thermoplastic Composite Materials* **2020**, *33*, 1317–1335. DOI: 10.1177/0892705720930794.
- [151] Miracle, D. B.; Donaldson, S. L. *Composites*; ASM International, 2001.
- [152] Schwartz, M. M. *Post processing treatment of composites*; Society for the Advancement of Material and Process Engineering: Covina, Calif., 1996.
- [153] Ashir, M.; Nocke, A.; Bulavinov, A.; Pinchuk, R.; Cherif, C. Influence of defined amount of voids on the mechanical properties of carbon fiber-reinforced plastics. *Polym. Compos.* **2019**, *40*, E1049-E1056. DOI: 10.1002/pc.24820.
- [154] Rawlings, R. D. *MATERIALS SCIENCE AND ENGINEERING -Volume III*; EOLSS Publications, 2009.
- [155] Heslehurst, R. B. *Defects and Damage in Composite Materials and Structures*; CRC Press, 2014.
- [156] Mesogitis, T. S.; Skordos, A. A.; Long, A. C. Uncertainty in the manufacturing of fibrous thermosetting composites: A review. *Composites Part A: Applied Science and Manufacturing* **2014**, *57*, 67–75. DOI: 10.1016/j.compositesa.2013.11.004.
- [157] Thor, M.; Sause, M. G. R.; Hinterhölzl, R. M. Mechanisms of Origin and Classification of Out-of-Plane Fiber Waviness in Composite Materials—A Review. *J. Compos. Sci.* **2020**, *4*, 130. DOI: 10.3390/jcs4030130.
- [158] Gereke, T.; Döbrich, O.; Hübner, M.; Cherif, C. Experimental and computational composite textile reinforcement forming: A review. *Composites Part A: Applied Science and Manufacturing* **2013**, *46*, 1–10. DOI: 10.1016/j.compositesa.2012.10.004.
- [159] Vallons, K.; Duque, I.; Lomov, S.; I; A. V and Verpoest direction dependence of the tensile stiffness, strength and fatigue life of biaxial carbon/epoxy NCF composites *Compos. Part Sci Manuf* **2011**, 16–21.
- [160] Bagherpour, S. Fibre Reinforced Polyester Composites. In *Polyester*; Saleh, H. E.-D., Ed.; InTech, 2012.
- [161] Hörsting, K. *Rationalisierung der Fertigung langfaserverstärkter Verbundwerkstoffe durch den Einsatz multiaxialer Gelege*, Als Ms. gedr; Shaker: Aachen, 1994.

- [162] Rudd, C. D.; Kendall, K. N.; Long, A. C. *Liquid moulding technology: A guide to RTM, SRIM and related composites processing techniques*; Woodhead: Cambridge, 1996.
- [163] Creech, G.; Pickett, A. K. Meso-modelling of Non-Crimp Fabric composites for coupled drape and failure analysis. *Journal of Materials Science* **2006**, *41*, 6725–6736. DOI: 10.1007/s10853-006-0213-6.
- [164] Cao, J.; Akkerman, R.; Boisse, P.; Chen, J.; Cheng, H. S.; Graaf, E. F. de; Gorczyca, J. L.; Harrison, P.; Hivet, G.; Launay, J.; *et al.* Characterization of mechanical behavior of woven fabrics: Experimental methods and benchmark results. *Composites Part A: Applied Science and Manufacturing* **2008**, *39*, 1037–1053. DOI: 10.1016/j.compositesa.2008.02.016.
- [165] Hübner, M. *Entwicklung einer skalenübergreifenden Simulationsmethodik für das Strukturverhalten von Mehrlagengeweben*, [1. Auflage]; Matthias Hübner: Dresden, 2018.
- [166] Döbrich, O. *Mehrskalensimulation von textilverstärkten Strukturen für Faserverbundanwendungen zum Einsatz in der Industrie 4.0*; Dissertation Technische Universität Dresden, epubli, 2018.
- [167] Cherouat, A.; Borouchaki, H. Present State of the Art of Composite Fabric Forming: Geometrical and Mechanical Approaches. *Materials* **2009**, *2*, 1835–1857. DOI: 10.3390/ma2041835.
- [168] Khan, M. A.; Mabrouki, T.; Vidal-Sallé, E.; Boisse, P. Numerical and experimental analyses of woven composite reinforcement forming using a hypoelastic behavior. Application to the double dome benchmark. *Journal of Materials Processing Technology* **2010**, *210*, 378–388. DOI: 10.1016/j.jmatprotec.2009.09.027.
- [169] Allaoui, S.; Boisse, P.; Chatel, S.; Hamila, N.; Hivet, G.; Soulat, D.; Vidal-Salle, E. Experimental and numerical analyses of textile reinforcement forming of a tetrahedral shape. *Composites Part A: Applied Science and Manufacturing* **2011**, *42*, 612–622. DOI: 10.1016/j.compositesa.2011.02.001.
- [170] Nezami, F. N. *Automated Preforming of Carbon-Fibre Reinforcements with Active Forming Manipulation for the Manufacturing of Complex Shaped Composite Components*. Dissertation, Dresden, 2015.
- [171] Christ, M.; Miene, A.; Mörschel, U. Measurement and Analysis of Drapability Effects of Warp-Knit NCF with a Standardised, Automated Testing Device. *Appl Compos Mater* **2017**, *24*, 803–820. DOI: 10.1007/s10443-016-9555-7.
- [172] Mansoori, M.; Kalantar, N.; Creasy, T.; Rybkowski, Z. Adaptive Wooden Architecture. Designing a Wood Composite with Shape-Memory Behavior. In *Digital Wood Design*; Bianconi, F., Filippucci, M., Eds.; Springer International Publishing: Cham, 2019; pp 703–717.

- [173] Friedrich, K.; Hou, M.; Krebs, J. Chapter 4 Thermoforming of continuous fibre/thermoplastic composite sheets. *Composite Sheet Forming*; Elsevier, 1997; pp 91–162.
- [174] Jagpal, R.; Evangelou, E.; Butler, R.; Loukaides, E. G. Multiple ply preforming of non-crimp fabrics with distributed magnetic clamping. *Composites Communications* **2022**, *31*, 101107. DOI: 10.1016/j.coco.2022.101107.
- [175] Wilks C. E. *Characterization of the Tool/Ply interface during forming: PhD thesis*; University of Nottingham: UK, 1999.
- [176] Azzouz, R.; Allaoui, S.; Moulart, R. Composite preforming defects: a review and a classification. *Int J Mater Form* **2021**, *14*, 1259–1278. DOI: 10.1007/s12289-021-01643-7.
- [177] Lin, H.; Wang, J.; Long, A. C.; Clifford, M. J.; Harrison, P. Predictive modelling for optimization of textile composite forming. *Composites Science and Technology* **2007**, *67*, 3242–3252. DOI: 10.1016/J.COMPSCITECH.2007.03.040.
- [178] Coupé, D. Woven reinforcements for composites. *Composite Reinforcements for Optimum Performance*; Elsevier, 2021; pp 97–120.
- [179] Hermann Hammesfahr. Glass cloth or fabric.
- [180] Ghosh, A. K.; Dwivedi, M. *Processability of polymeric composites*; Springer: New Delhi, India, 2020.
- [181] Potter, K. 'But How Can We Make Something Useful Out of Black String?' The Development of Carbon Fibre Composites Manufacturing (1965–2015). In *The Structural Integrity of Carbon Fiber Composites*; Beaumont, P. W. R., Soutis, C., Hodzic, A., Eds.; Springer International Publishing: Cham, 2017; pp 29–57.
- [182] Perera, Y. S.; Muwanwella, R. M. H. W.; Fernando, P. R.; Fernando, S. K.; Jayawardana, T. S. S. Evolution of 3D weaving and 3D woven fabric structures. *Fash Text* **2021**, *8*. DOI: 10.1186/s40691-020-00240-7.
- [183] Mountasir, A.; Hoffmann, G.; Cherif, C.; Löser, M.; Mühl, A.; Großmann, K. Development of Non-Crimp Multi-Layered 3D Spacer Fabric Structures using Hybrid Yarns for Thermoplastic Composites. *Procedia Materials Science* **2013**, *2*, 10–17. DOI: 10.1016/j.mspro.2013.02.002.
- [184] Fazeli, M. *Technology development for woven node structures with complex geometry and in integral design for fiber-reinforced composite applications*; Dr. Hut: München, 2017.
- [185] Taylor, L. W.; Chen, X. Nodal three-dimensional woven textiles. *Advances in 3D Textiles*; Elsevier, 2015; pp 99–122.

- [186] Haentzsch, E.; Onggar, T.; Nocke, A.; Hund, R. D.; Cherif, C. Multi-layered sensor yarns for in situ monitoring of textile reinforced composites. *IOP Conf. Ser.: Mater. Sci. Eng.* **2017**, *254*, 42012. DOI: 10.1088/1757-899X/254/4/042012.
- [187] Weise, D. *Konstruktiv-technologische Entwicklung von Hochleistungs-Drehergeweben für Hightech-Anwendungen*; TUDpress: Dresden, 2020.
- [188] Schirmaier, F. *Experimentelle Untersuchung und Simulation des Umformverhaltens nähgewirkter unidirektionaler Kohlenstofffasergelege*, 2017.
- [189] Tsai, S. W. Double-Double: New Family of Composite Laminates. *AIAA Journal* **2021**, *59*, 4293–4305. DOI: 10.2514/1.J060659.
- [190] Spencer. *Knitting Technology: A comprehensive handbook and practical guide*, 3. ed.; Woodhead Publishing: Cambridge, 2001.
- [191] *Four Centuries of machine knitting: Commemorating William Lee's invention of the stocking frame in 1589*; Knitting International: Leicester, 1989.
- [192] Iyer, C.; Mammel, B.; Schäche, W. *Rundstricken: Theorie und Praxis der Maschentechnik*; Meisenbach: Bamberg, 2000.
- [193] Abounaim, M. S. M. Process development for the manufacturing of flat knitted innovative 3D spacer fabrics for high performance composite applications. PhD Thesis, Technische Universität Dresden.
- [194] Ray, S. C. *Fundamentals and advances in knitting technology*; Woodhead Publishing India; CRC Press: New Delhi, Boca Raton, FL, 2012.
- [195] Ma, J.; Zha, X. F.; Tao, H. B.; Ni, J. F. Testing System of Needle Selectors for Jacquard Knitting Machines. *AMM* **2013**, *397-400*, 1174–1177. DOI: 10.4028/www.scientific.net/AMM.397-400.1174.
- [196] Duhovic, M. Deformation characteristics of knitted fabric composites **2004**, *1994*, 225.
- [197] Mayer, J. *Gestricke aus Kohlenstoffasern für biokompatible Verbundwerkstoffe, dargestellt an einer homoelastischen Osteosyntheseplatte*, ETH Zurich, 1994.
- [198] Sun, B.; Hu, D.; Gu, B. Transverse impact damage and energy absorption of 3-D multi-structured knitted composite. *Composites Part B* **2009**, *40*, 572–583. DOI: 10.1016/j.compositesb.2008.12.005.
- [199] Anwar, K. O.; Callus, P. J.; Leong, K. H.; Curiskis, J. I.; Herszberg, I. The effect of architecture on the mechanical properties of knitted composites. In *11th Conf. on Comp. Mater., ICCM-11 (ed ML Scott), Goldcoast, Australia*, 1997; pp 14–18.
- [200] Hasani, H.; Ajeli, S.; Hessami, R.; Zadhoush, A. Investigation into energy absorption capacity of composites reinforced by three-dimensional-weft knitted fabrics. *Journal of Industrial Textiles* **2014**, *43*, 536–548. DOI: 10.1177/1528083712468604.

- [201] Khondker, O.; Fukui, T.; Inoda, M.; Nakai, A.; Hamada, H. Fabrication and mechanical properties of aramid/nylon plain knitted composites. *Composites Part A: Applied Science and Manufacturing* **2004**, *35*, 1195–1205. DOI: 10.1016/j.compositesa.2004.03.004.
- [202] Ramakrishna, S.; Hamada, H.; Rydin, R.; Chou, T. Impact Damage Resistance of Knitted Glass Fiber Fabric Reinforced Polypropylene Composites. *Science and Engineering of Composite Materials* **1995**, *4*, 61–72. DOI: 10.1515/SECM.1995.4.2.61.
- [203] Pandita, S. D.; Falconet, D.; Verpoest, I. Impact properties of weft knitted fabric reinforced composites. *Composites Science and Technology* **2002**, *62*, 1113–1123. DOI: 10.1016/S0266-3538(02)00057-X.
- [204] Abounaim, M.; Hoffmann, G.; Diestel, O.; Cherif, C. Thermoplastic composite from innovative flat knitted 3D multi-layer spacer fabric using hybrid yarn and the study of 2D mechanical properties. *Composites Science and Technology* **2010**, *70*, 363–370. DOI: 10.1016/j.compscitech.2009.11.008.
- [205] Rudd, C.; Owen, M.; Middleton, V. Mechanical properties of weft knit glass fibre/polyester laminates. *Composites Science and Technology* **1990**, *39*, 261–277. DOI: 10.1016/0266-3538(90)90045-7.
- [206] Leong, K. H.; Falzon, P. J.; Bannister, M. K.; Herszberg, I. An investigation of the mechanical performance of weft-knit Milano-rib glass/epoxy composites. *Composites Science and Technology* **1998**, *58*, 239–251. DOI: 10.1016/S0266-3538(97)00128-0.
- [207] Araújo, M. de; Figueiro, R.; Hong, H. Modelling and simulation of the mechanical behavior of weft-knitted fabrics for technical applications: Part II: 3D model based on the elastica theory. *Autex Res J* **2003**, *3*, 166–172.
- [208] Padaki, N. V.; Alagirusamy, R.; Sugun, B. S. Knitted Preforms for Composite Applications. *Journal of Industrial Textiles* **2006**, *35*, 295–321. DOI: 10.1177/1528083706060784.
- [209] Lau, K. W.; Dias, T. Knittability of High-modulus Yarns. *Journal of the Textile Institute* **1994**, *85*, 173–190. DOI: 10.1080/00405009408659018.
- [210] Moazzeni, N.; Hasani, H.; Shanbeh, M. Effect of material and fabric parameters on fatigue value of weft knitted fabrics **2014**.
- [211] Füller, J. *Developments in the science and technology of composite materials*; Elsevier Applied Science, 1990.
- [212] Offermann, P.; Hoffmann, G.; Engelmann, U. MEHRLAGENGESTRICK UND VERFAHREN ZU SEINER HERSTELLUNG - European Patent Office - EP 0873440 B1: MULTILAYER KNITTED STRUCTURE AND METHOD OF PRODUCING THE SAME TRICOT MULTICOUCHE ET SON PROCEDE DE PRODUCTION. PCT/DE95/01774.

- [213] Le Phuc, B. *Konstruktive und technologische Weiterentwicklung der Flachstricktechnik zur Herstellung von Multilayer-Gestriicken mit bis zu neun Verstärkungslagen*; TUDpress: Dresden, 2006.
- [214] Natalie Ishmael. Manufacturing and mechanical characterisation of 3D biaxial weft knitted preforms for composites. UoM administered thesis: Phd, The University of Manchester, Manchester, England, 2021.
- [215] Hasani, H.; Hassanzadeh, S.; Abghary, M. J.; Omrani, E. *Biaxial weft-knitted fabrics as composite reinforcements: A review*, 2017. *J Ind Text*, 46 (7).
- [216] Qi, Y.; Li, J.; Liu, L. Tensile properties of multilayer-connected biaxial weft knitted fabric reinforced composites for carbon fibers. *Materials & Design* **2014**, 54, 678–685. DOI: 10.1016/j.matdes.2013.08.051.
- [217] Demircan, Ö.; Ashibe, S.; Kosui, T.; Nakai, A. Effect of various knitting techniques on mechanical properties of biaxial weft-knitted thermoplastic composites. *Journal of Thermoplastic Composite Materials* **2015**, 28, 896–910. DOI: 10.1177/0892705713519121.
- [218] Cebulla, H.; Diestel, O.; Offermann, P. Fully fashioned biaxial weft knitted fabrics. *Autex Research Journal* **2002**, 2, 8–13.
- [219] Cherif, C.; Krzywinski, S.; Diestel, O.; Schulz, C.; Lin, H.; Klug, P.; Trümper, W. Development of a process chain for the realization of multilayer weft knitted fabrics showing complex 2D/3D geometries for composite applications. *Textile Research Journal* **2012**, 82, 1195–1210. DOI: 10.1177/0040517511429602.
- [220] Ciobanu, L. Development of 3D Knitted Fabrics for Advanced Composite Materials. In *Advances in Composite Materials - Ecodesign and Analysis*; Attaf, B., Ed.; InTech, 2011.
- [221] Schulz, C. *Entwicklung einer Technologie für die Herstellung textiler Halbzeuge für thermoplastische Verbundwerkstoffe auf Basis der Mehrlagenflachstricktechnik*; Inst. für Textilmaschinen u. Textile Hochleistungswerkstofftechnik: Dresden, 2013.
- [222] Cherif, C.; Krzywinski, S.; Lin, H.; Schulz, C.; Haasemann, G. New Process Chain for Realisation of Complex 2D/3D Weft Knitted Fabrics for Thermoplastic Composite Applications. *Procedia Materials Science* **2013**, 2, 111–129. DOI: 10.1016/j.mspro.2013.02.014.
- [223] Xu, Y.; Yuan, X.; Wang, N. Comparison of tensile properties of co-woven-knitted and multi-layered biaxial weft-knitted fabric reinforced composites. *Fibers Polym* **2013**, 14, 1006–1011. DOI: 10.1007/s12221-013-1006-6.
- [224] Xu, Y.; Yuan, X.; Wang, N.; Liu, Z. Comparison of bending properties Co-woven-knitted and Multi-layered biaxial Weft-knitted fabric reinforced composites. *Fibers Polym* **2014**, 15, 1288–1294. DOI: 10.1007/s12221-014-1288-3.

- [225] Orawattanasrikul, S. Experimentelle Analyse der Scherdeformationen biaxial verstärkter Mehrlagengestricke, Technische Universität Dresden.
- [226] Plaut, R. H. Formulas to determine fabric bending rigidity from simple tests. *Textile Research Journal* **2015**, *85*, 884–894. DOI: 10.1177/0040517514553877.
- [227] Cherif, C. *Drapierbarkeitssimulation von Verstärkungstextilien für den Einsatz in Faserverbundkunststoffen mit der Finite-Elemente-Methode*, Als Ms. gedr; Shaker: Aachen, 1999.
- [228] Sköck-Hartmann, B. A. *Prüfverfahren für das Umformen von Multiaxialgelegen für Strukturbauteile*; Shaker-Verl.: Aachen, 2013.
- [229] Schlien, K. Amerikanische Prüfgeräte zur Gewebeuntersuchung. *Das deutsche Textilegewerbe - Prüfgerät* **1951**.
- [230] Culpin, M. F. 8—THE SHEARING OF FABRICS: A NOVEL APPROACH. *Journal of the Textile Institute* **1979**, *70*, 81–88. DOI: 10.1080/00405007908631522.
- [231] Stumpf, H. *Study on the manufacture of thermoplastic composites from new textile preforms*; TUHH, 1998.
- [232] Lomov, S. V.; Willems, A.; Verpoest, I.; Zhu, Y.; Barburski, M.; Stoilova, T. Picture Frame Test of Woven Composite Reinforcements with a Full-Field Strain Registration. *Textile Research Journal* **2006**, *76*, 243–252. DOI: 10.1177/0040517506061032.
- [233] Subramaniam, V.; Chanchal, B.; Vatsala, R.; Rajendran, B. Shearing properties of fabrics - Testing methods. *Man-Made-Textile* **1983**, *6*.
- [234] Harwood, R. J.; Weedall, P. J.; Carr, C. The use of the Kawabata Evaluation System for product development and quality control. *Journal of the Society of Dyers and Colourists* **1990**, *106*, 64–68. DOI: 10.1111/j.1478-4408.1990.tb01244.x.
- [235] Boisse, P.; Hamila, N.; Guzman-Maldonado, E.; Madeo, A.; Hivet, G.; Dell'Isola, F. *The bias-extension test for the analysis of in-plane shear properties of textile composite reinforcements and preregs: a review*, 2017. *Int J Mater Form*.
- [236] Kawabata, S.; Niwa, M.; Kawai, H. 5—THE FINITE-DEFORMATION THEORY OF PLAIN-WEAVE FABRICS. PART III: THE SHEAR-DEFORMATION THEORY. *Journal of the Textile Institute* **1973**, *64*, 62–85. DOI: 10.1080/00405007308630418.
- [237] Chen, W.; Gao, C.; Zhang, D.; Wang, L.; Qiu, Z. A new biaxial tensile shear test method to measure shear behavior of coated fabrics for architectural use. *Composite Structures* **2018**. DOI: 10.1016/j.compstruct.2018.06.063.
- [238] El-Messiry, M.; Sheta, A. Measurement of fabric shearability by twisting method. *The Indian Textile Journal* **1987**, 122–129.

- [239] Rothe, S.; Wendt, E.; Krzywinski, S.; Halász, M.; Bakonyi, P.; Tamás, P.; Bojtos, A. Investigation of shear-induced deformation of reinforcing textiles by optical measurement devices. *Materials* **2019**. DOI: 10.3390/ma12071029.
- [240] Souter, B. J. Effects of fibre architecture on formability of textile preforms, University of Nottingham, 2001.
- [241] Zhu, B.; Yu, T. X.; Teng, J.; Tao, X. M. Theoretical Modeling of Large Shear Deformation and Wrinkling of Plain Woven Composite. *Journal of Composite Materials* **2009**, *43*, 125–138. DOI: 10.1177/0021998308098237.
- [242] Thijsse, R. H. W. ten; Akkerman, R. Finite element simulations of laminated composites forming processes. *Int J Mater Form* **2010**, *3*, 715–718.
- [243] Lebrun, G.; Bureau, M. N.; Denault, J. Thermoforming-Stamping of Continuous Glass Fiber/Polypropylene Composites: Interlaminar and Tool-Laminate Shear Properties. *Journal of Thermoplastic Composite Materials* **2004**, *17*, 137–165. DOI: 10.1177/0892705704035411.
- [244] Gorczyca, J. L.; Sherwood, J. A.; Liu, L.; Chen, J. Modeling of Friction and Shear in Thermoforming of Composites - Part I. *Journal of Composite Materials* **2004**, *38*, 1911–1929. DOI: 10.1177/0021998304048416.
- [245] Liu, L.; Chen, J.; Gorczyca, J. L.; Sherwood, J. A. Modeling of Friction and Shear in Thermoforming of Composites - Part II. *Journal of Composite Materials* **2004**, *38*, 1931–1947. DOI: 10.1177/0021998304048417.
- [246] Thijsse, R. ten; Akkerman, R.; Ubbink, M.; van der Meer, L. A lubrication approach to friction in thermoplastic composites forming processes. *Composites Part A: Applied Science and Manufacturing* **2011**, *42*, 950–960. DOI: 10.1016/j.compositesa.2011.03.023.
- [247] Thijsse, R. H. W. ten; Akkerman, R.; van der Meer, L.; Ubbink, M. P. Tool-ply friction in thermoplastic composite forming. *Int J Mater Form* **2008**, *1*, 953–956. DOI: 10.1007/s12289-008-0215-9.
- [248] Vanclooster, K.; van Goidsenhoven, S.; Lomov, S. V.; Verpoest, I. Optimizing the deepdrawing of multilayered woven fabric composites. *Int J Mater Form* **2009**, *2*, 153–156. DOI: 10.1007/s12289-009-0522-9.
- [249] Allaoui, S.; Hivet, G.; Wendling, A.; Ouagne, P.; Soulat, D. Influence of the dry woven fabrics meso-structure on fabric/fabric contact behavior. *Journal of Composite Materials* **2012**, *46*, 627–639. DOI: 10.1177/0021998311424627.
- [250] Hivet, G.; Allaoui, S.; Cam, B. T.; Ouagne, P.; Soulat, D. Design and Potentiality of an Apparatus for Measuring Yarn/Yarn and Fabric/Fabric Friction. *Experimental Mechanics* **2012**, *52*, 1123–1136. DOI: 10.1007/s11340-011-9566-0.

- [251] Kruse, M.; Werner, H. O.; Chen, H.; Mennecart, T.; Liebig, W. V.; Weidenmann, K. A.; Ben Khalifa, N. Investigation of the friction behavior between dry/infiltrated glass fiber fabric and metal sheet during deep drawing of fiber metal laminates. *Prod. Eng. Res. Dev.* **2022**. DOI: 10.1007/s11740-022-01141-y.
- [252] Mennecart, T.; Gies, S.; Ben Khalifa, N.; Tekkaya, A. E. Analysis of the Influence of Fibers on the Formability of Metal Blanks in Manufacturing Processes for Fiber Metal Laminates. *JMMP* **2019**, 3, 2. DOI: 10.3390/jmmp3010002.
- [253] Cornelissen, B.; Sachs, U.; Rietman, B.; Akkerman, R. Dry friction characterisation of carbon fibre tow and satin weave fabric for composite applications. *Composites Part A: Applied Science and Manufacturing* **2014**, 56. DOI: 10.1016/j.compositesa.2013.10.006.
- [254] Mulvihill, D. M.; Sutcliffe, M. P. Effect of tool surface topography on friction with carbon fibre tows for composite fabric forming. *Composites Part A: Applied Science and Manufacturing* **2017**, 93, 199–206. DOI: 10.1016/j.compositesa.2016.10.017.
- [255] Bowden, F. P.; Young, J. E. Friction of diamond, graphite, and carbon and the influence of surface films. *Proc. R. Soc. Lond. A* **1951**, 208, 444–455. DOI: 10.1098/rspa.1951.0173.
- [256] Howell, H. G.; Mazur, J. AMONTONS' LAW AND FIBRE FRICTION. *Journal of the Textile Institute Transactions* **1953**, 44, T59-T69. DOI: 10.1080/19447025308659728.
- [257] Thijsse, R. H. W. ten; Akkerman, R. Design of an experimental setup to measure tool-ply and ply-ply friction in thermoplastic laminates. *Int J Mater Form* **2009**, 2, 197–200. DOI: 10.1007/s12289-009-0638-y.
- [258] Sachs, U.; Akkerman, R.; Fetfatsidis, K.; Vidal-Sallé, E.; Schumacher, J.; Ziegmann, G.; Allaoui, S.; Hivet, G.; Maron, B.; Vanclooster, K.; *et al.* Characterization of the dynamic friction of woven fabrics: Experimental methods and benchmark results. *Composites Part A: Applied Science and Manufacturing* **2014**, 67, 289–298. DOI: 10.1016/j.compositesa.2014.08.026.
- [259] Lin, H.; Harrison, P.; K, H.; Long, A.; Akkerman, R.; Clifford, M. Investigation of tool-ply friction of viscous textile composites. *IEEE Transactions on Magnetics - IEEE TRANS MAGN* **2006**.
- [260] Veit, D. *Simulation in textile technology: Theory and applications / edited by D. Veit*; The Textile Institute: Oxford, 2012.
- [261] Padua, D.; Ghoting, A.; Gunnels, J. A.; Squillante, M. S.; Meseguer, J.; Cownie, J. H.; Roweth, D.; Adve, S. V.; Boehm, H. J.; McKee, S. A.; *et al.* Moore's Law. In *Encyclopedia of Parallel Computing*; Padua, D., Ed.; Springer US: Boston, MA, 2011; pp 1177–1184.
- [262] Barbarossa, M. V.; Fuhrmann, J.; Meinke, J. H.; Krieg, S.; Varma, H. V.; Castelletti, N.; Lippert, T. Modeling the spread of COVID-19 in Germany: Early assessment and

- possible scenarios. *PloS one* **2020**, *15*, e0238559. DOI: 10.1371/journal.pone.0238559.
- [263] Pickett, A. K.; Creech, G.; Luca, P. de. Simplified and advanced simulation methods for prediction of fabric draping. *Revue Européenne des Éléments Finis* **2005**, *14*, 677–691. DOI: 10.3166/reef.14.677-691.
- [264] Volino, P.; Thalmann, N. M. Implementing fast cloth simulation with collision response. In *Proceedings Computer Graphics International 2000*, 2000; pp 257–266.
- [265] Cordier, F.; Magnenat-Thalmann, N. Real-time Animation of Dressed Virtual Humans. *Computer Graphics Forum* **2002**, *21*, 327–335. DOI: 10.1111/1467-8659.t01-1-00592.
- [266] Potluri, P.; Sharma, S.; Ramgulam, R. Comprehensive drape modelling for moulding 3D textile preforms. *Composites Part A: Applied Science and Manufacturing* **2001**, *32*, 1415–1424. DOI: 10.1016/S1359-835X(01)00040-9.
- [267] Sharma, S. B.; Sutcliffe, M. P. F. Draping of woven fabrics: Progressive drape model. *Plastics, Rubber and Composites* **2003**, *32*, 57–64. DOI: 10.1179/146580103225009149.
- [268] Kyosev, Y. K. The finite element method (FEM) and its application to textile technology. *Simulation in Textile Technology*; Elsevier, 2012; 172-222e.
- [269] Rieg, F.; Alber-Laukant, B.; Hackenschmidt, R. *Finite element analysis for engineers: Basics and practical applications with Z88Aurora*; Hanser: München, 2014.
- [270] Belytschko, T.; Liu, W. K.; Moran, B.; Elkhodary, K. I. *Nonlinear finite elements for continua and structures*, Second edition; Wiley: Chichester, 2014.
- [271] Hughes, T.; Cottrell, J. A.; Bazilevs, Y. Isogeometric analysis: CAD, finite elements, NURBS, exact geometry and mesh refinement. *Computer Methods in Applied Mechanics and Engineering* **2005**, *194*, 4135–4195. DOI: 10.1016/j.cma.2004.10.008.
- [272] Nguyen-Thanh, N.; Valizadeh, N.; Nguyen, M. N.; Nguyen-Xuan, H.; Zhuang, X.; Areias, P.; Zi, G.; Bazilevs, Y.; Lorenzis, L. de; Rabczuk, T. An extended isogeometric thin shell analysis based on Kirchhoff–Love theory. *Computer Methods in Applied Mechanics and Engineering* **2015**, *284*, 265–291. DOI: 10.1016/j.cma.2014.08.025.
- [273] Hartmann, S.; Benson, D.; Nagy, A. Isogeometric Analysis with LS-DYNA. *J. Phys.: Conf. Ser.* **2016**, *734*, 32125. DOI: 10.1088/1742-6596/734/3/032125.
- [274] Newmark, N. M. A Method of Computation for Structural Dynamics. *J. Engrg. Mech. Div.* **1959**, *85*, 67–94. DOI: 10.1061/JMCEA3.0000098.
- [275] Wriggers, P. *Nonlinear finite element methods*; Springer: Berlin, London, 2008.
- [276] Malachowski, J.; Bukala, J.; Tomaszewski, M.; Damaziak, K. LS-DYNA CONTACT PROCEDURE ANALYSIS FOR SELECTED MECHANICAL SYSTEMS. *Journal of KONES* **2015**, *22*, 193–202. DOI: 10.5604/12314005.1161741.

- [277] Gereke, T.; Cherif, C. *A review of numerical models for 3D woven composite reinforcements*, 2019. *Composite Structures*, 209.
- [278] Bussetta, P.; Correia, N. Numerical forming of continuous fibre reinforced composite material : a review. *Composites Part A: Applied Science and Manufacturing* **2018**, 113, 12–31. DOI: 10.1016/j.compositesa.2018.07.010.
- [279] Boisse, P. Simulation of Continuous Fibre Composite Forming. In *Mechanics of Fibrous Materials and Applications*; Picu, C., Ganghoffer, J.-F., Eds.; Springer International Publishing: Cham, 2020; pp 157–193.
- [280] Boisse, P.; Hamila, N.; Madeo, A. The difficulties in modeling the mechanical behavior of textile composite reinforcements with standard continuum mechanics of Cauchy. Some possible remedies. *International Journal of Solids and Structures* **2018**, 154, 55–65. DOI: 10.1016/j.IJSOLSTR.2016.12.019.
- [281] Hsiao, S.-W.; Kikuchi, N. Numerical analysis and optimal design of composite thermoforming process. *Computer Methods in Applied Mechanics and Engineering* **1999**, 177, 1–34. DOI: 10.1016/S0045-7825(98)00273-4.
- [282] Harrison, P.; Clifford, M. J.; Long, A. C.; Rudd, C. D. Constitutive modelling of impregnated continuous fibre reinforced composites Micromechanical approach. *Plastics, Rubber and Composites* **2002**, 31, 76–86. DOI: 10.1179/146580102225001409.
- [283] Soulat, D.; Cheruet, A.; Boisse, P. Simulation of continuous fibre reinforced thermoplastic forming using a shell finite element with transverse stress. *Computers and Structures* **2006**, 84, 888–903. DOI: 10.1016/j.compstruc.2006.02.011.
- [284] Liang, B.; Colmars, J.; Boisse, P. A shell formulation for fibrous reinforcement forming simulations. *Composites Part A: Applied Science and Manufacturing* **2017**, 100, 81–96. DOI: 10.1016/j.compositesa.2017.04.024.
- [285] Döbrich, O.; Gereke, T.; Diestel, O.; Krzywinski, S.; Cherif, C. Decoupling the bending behavior and the membrane properties of finite shell elements for a correct description of the mechanical behavior of textiles with a laminate formulation. *J Ind Text* **2013**, 44, 70–84.
- [286] Nishi, M.; Hirashima, T.; Kurashiki, T.; Uenishi, K. FORMING SIMULATION OF TEXTILE COMPOSITE BY FINITE ELEMENT METHOD. In , 2015.
- [287] Wang, J.; Long, A. C.; Clifford, M. J. Experimental measurement and predictive modelling of bending behavior for viscous unidirectional composite materials. *Int J Mater Form* **2010**, 3, 1253–1266. DOI: 10.1007/s12289-009-0670-y.

- [288] Alshahrani, H.; Hojjati, M. A theoretical model with experimental verification for bending stiffness of thermosetting prepreg during forming process. *Composite Structures* **2017**, *166*, 136–145. DOI: 10.1016/j.compstruct.2017.01.030.
- [289] Sachs, U.; Akkerman, R. Viscoelastic bending model for continuous fiber-reinforced thermoplastic composites in melt. *Composites Part A: Applied Science and Manufacturing* **2017**, *100*, 333–341. DOI: 10.1016/j.compositesa.2017.05.032.
- [290] Borrvall, T. A heuristic attempt to reduce transverse shear locking in fully integrated hexahedra with poor aspect ratio. In , 2009.
- [291] Quyen Nguyen-Trong; F. N. Ferreira; Abel João Padrão Gomes. Modelling the bending behavior of plain-woven fabric using flat shell element and strain smoothing technique. In , 2013.
- [292] Ghafour, T. A.; Colmars, J.; Boisse, P. The Dahl's Model for the Inelastic Bending Behavior of Textile Composite Preforms. Analysis of its Influence in Draping Simulation. *Front. Mater.* **2021**, *8*. DOI: 10.3389/fmats.2021.728485.
- [293] Syerko, E.; Comas-Cardona, S.; Binetruy, C. Models for shear properties/behavior of dry fibrous materials at various scales: a review. *Int J Mater Form* **2015**, *8*, 1–23. DOI: 10.1007/s12289-013-1138-7.
- [294] Truesdell, C.; Noll, W. *The non-linear field theories of mechanics*, 3rd ed.; Springer: Berlin, London, 2003.
- [295] Boisse, P.; Hamila, N. Modeling composite reinforcement forming processes. *Composite Reinforcements for Optimum Performance*; Elsevier, 2021; pp 671–691.
- [296] Boisse, P.; Aimène, Y.; Dogui, A.; Dridi, S.; Gatouillat, S.; Hamila, N.; Aurangzeb Khan, M.; Mabrouki, T.; Morestin, F.; Vidal-Sallé, E. Hypoelastic, hyperelastic, discrete and semi-discrete approaches for textile composite reinforcement forming. *Int J Mater Form* **2010**, *3*, 1229–1240. DOI: 10.1007/s12289-009-0664-9.
- [297] Ferretti, M.; Madeo, A.; dell'Isola, F.; Boisse, P. Modeling the onset of shear boundary layers in fibrous composite reinforcements by second-gradient theory. *Z. Angew. Math. Phys.* **2014**, *65*, 587–612. DOI: 10.1007/s00033-013-0347-8.
- [298] Andreaus, U.; dell'Isola, F.; Giorgio, I.; Placidi, L.; Lekszycki, T.; Rizzi, N. L. Numerical simulations of classical problems in two-dimensional (non) linear second gradient elasticity. *International Journal of Engineering Science* **2016**, *108*, 34–50. DOI: 10.1016/j.ijengsci.2016.08.003.
- [299] Thije, R. ten; Akkerman, R. Solutions to intra-ply shear locking in finite element analyses of fibre reinforced materials. *Composites Part A: Applied Science and Manufacturing* **2008**, *39*, 1167–1176. DOI: 10.1016/j.compositesa.2008.03.014.

- [300] Hamila, N.; Boisse, P. Locking in simulation of composite reinforcement deformations. Analysis and treatment. *Composites Part A: Applied Science and Manufacturing* **2013**, *53*, 109–117. DOI: 10.1016/j.compositesa.2013.06.001.
- [301] Hamila, N.; Boisse, P. Tension locking in finite-element analyses of textile composite reinforcement deformation. *Comptes Rendus Mécanique* **2013**, *341*, 508–519. DOI: 10.1016/j.crme.2013.03.001.
- [302] Wriggers, P.; Schröder, J.; Auricchio, F. Finite element formulations for large strain anisotropic material with inextensible fibers. *Adv. Model. and Simul. in Eng. Sci.* **2016**, *3*. DOI: 10.1186/s40323-016-0079-3.
- [303] Sun, E. Shear Locking and Hourglassing in MSC Nastran, ABAQUS, and ANSYS **2006**.
- [304] Belytschko, T.; Ong, J. S.-J.; Liu, W. K.; Kennedy, J. M. Hourglass control in linear and nonlinear problems. *Computer Methods in Applied Mechanics and Engineering* **1984**, *43*, 251–276. DOI: 10.1016/0045-7825(84)90067-7.
- [305] Araújo, M. de; Figueiro, R.; Hong, H. Modelling and simulation of the mechanical behavior of weft-knitted fabrics for technical applications: Part III: 2D hexagonal FEA model with non-linear truss elements. *Autex Res J* **2004**, *4*, 25–32.
- [306] Hübner, M.; Staiger, E.; Küchler, K.; Gereke, T.; Cherif, C. Simulation of patched woven fabric composite structures under tensile load. *Tekstilec* **2016**, *59*, 175–181. DOI: 10.14502/Tekstilec2016.59.175-181.
- [307] Stig, F.; Hallström, S. Spatial modelling of 3D-woven textiles. *Composite Structures* **2012**, *94*, 1495–1502. DOI: 10.1016/j.compstruct.2011.12.003.
- [308] Naouar, N.; Vidal-Salle, E.; Schneider, J.; Maire, E.; Boisse, P. 3D composite reinforcement meso F.E. analyses based on X-ray computed tomography. *Composite Structures* **2015**, *132*, 1094–1104. DOI: 10.1016/j.compstruct.2015.07.005.
- [309] Wendling, A.; Daniel, J. L.; Hivet, G.; Vidal-Sallé, E.; Boisse, P. Meshing Preprocessor for the Mesoscopic 3D Finite Element Simulation of 2D and Interlock Fabric Deformation. *Appl Compos Mater* **2015**, *22*, 869–886. DOI: 10.1007/s10443-015-9441-8.
- [310] Araújo, M. de; Figueiro, R.; Hong, H. Modelling and simulation of the mechanical behavior of weft-knitted fabrics for technical applications. Part IV: 3D FEA model with a mesh of tetrahedric elements. *Autex Res J* **2004**, *4*, 72–80.
- [311] Naouar, N.; Vidal-Sallé, E.; Schneider, J.; Maire, E.; Boisse, P. Meso-scale FE analyses of textile composite reinforcement deformation based on X-ray computed tomography. *Composite Structures* **2014**, *116*, 165–176. DOI: 10.1016/j.compstruct.2014.04.026.

- [312] Nayak, S. Y.; Satish, S. B.; Sultan, M. T. H.; Kini, C. R.; Shenoy, K. R.; Samant, R.; Sarvade, P. P.; Basri, A. A.; Mustapha, F. Influence of fabric orientation and compression factor on the mechanical properties of 3D E-glass reinforced epoxy composites. *Journal of Materials Research and Technology* **2020**, *9*, 8517–8527. DOI: 10.1016/j.jmrt.2020.05.111.
- [313] Döbrich, O.; Anderegg, A.; Gort, N.; Brauner, C. Machine Vision for As-Built Modeling of Complex Draped Composite Structures. *Materials* **2021**, *14*. DOI: 10.3390/ma14030682.
- [314] Brown, L. P.; Long, A. C. Modeling the geometry of textile reinforcements for composites: TexGen. *Composite Reinforcements for Optimum Performance*; Elsevier, 2021; pp 237–265.
- [315] Lomov, S. WiseTex—A Virtual Textile Composites Software. In *Advanced Weaving Technology*; Kyosev, Y., Boussu, F., Eds.; Springer International Publishing: Cham, 2022; pp 293–318.
- [316] Kyosev, Y. *Topology-Based Modeling of Textile Structures and Their Joint Assemblies*; Springer International Publishing, 2019.
- [317] Daelemans, L.; Tomme, B.; Caglar, B.; Michaud, V.; van Stappen, J.; Cnudde, V.; Boone, M.; van Paepegem, W. Kinematic and mechanical response of dry woven fabrics in through-thickness compression: Virtual fiber modeling with mesh overlay technique and experimental validation. *Composites Science and Technology* **2021**, *207*, 108706. DOI: 10.1016/j.compscitech.2021.108706.
- [318] Döbrich, O.; Gereke, T.; Cherif, C. Modeling the mechanical properties of textile-reinforced composites with a near micro-scale approach. *Compos Struct* **2016**, *135*, 1–7. DOI: 10.1016/j.compstruct.2015.09.010.
- [319] Dinh, T.; Daelemans, L.; van Paepegem, W. Near-microscale modelling of dry woven fabrics under in-plane shear loading. In.
- [320] Thompson, A. J.; El Said, B.; Ivanov, D.; Belnoue, J. P.-H.; Hallett, S. R. High fidelity modelling of the compression behavior of 2D woven fabrics. *International Journal of Solids and Structures* **2018**, *154*, 104–113. DOI: 10.1016/j.ijsolstr.2017.06.027.
- [321] Thompson, A. J.; McFarlane, J. R.; Belnoue, J. P.; Hallett, S. R. Numerical modelling of compaction induced defects in thick 2D textile composites. *Materials and Design* **2020**, *196*, 109088. DOI: 10.1016/j.matdes.2020.109088.
- [322] Hamila, N.; Boisse, P.; Chatel, S. Finite element simulation of composite reinforcement draping using a three node semi discrete triangle. *Int J Mater Form* **2008**, *1*, 867–870. DOI: 10.1007/s12289-008-0273-z.

- [323] Luycker, E. de; Morestin, F.; Boisse, P.; Marsal, D. Simulation of 3D interlock composite preforming. *Composite Structures* **2009**, *88*, 615–623. DOI: 10.1016/j.compstruct.2008.06.005.
- [324] Gorczyca-Cole, J. L.; Sherwood, J. A.; Chen, J. A friction model for thermostamping commingled glass–polypropylene woven fabrics. *Composites Part A: Applied Science and Manufacturing* **2007**, *38*, 393–406. DOI: 10.1016/j.compositesa.2006.03.006.
- [325] Boisse, P.; Hamila, N.; Madeo, A. Analysis of Defect Developments in Composite Forming. In *The Structural Integrity of Carbon Fiber Composites*; Beaumont, P. W. R., Soutis, C., Hodzic, A., Eds.; Springer International Publishing: Cham, 2017; pp 319–337.
- [326] Boisse, P.; Hamila, N.; Madeo, A. Modelling the development of defects during composite reinforcements and prepreg forming. *Philosophical transactions. Series A, Mathematical, physical, and engineering sciences* **2016**, *374*, 20150269. DOI: 10.1098/rsta.2015.0269.
- [327] Tavana, R.; Najar, S. S.; Abadi, M. T.; Sedighi, M. Meso/macro-scale finite element model for forming process of woven fabric reinforcements. *Journal of Composite Materials* **2013**, *47*, 2075–2085. DOI: 10.1177/0021998312454034.
- [328] Hübner, M.; Rocher, J.-E.; Allaoui, S.; Hivet, G.; Gereke, T.; Cherif, C. Simulation-based investigations on the drape behavior of 3D woven fabrics made of commingled yarns. *Int J Mater Form* **2015**, *9*, 591–599.
- [329] Garnich, M. R.; Klymyshyn, N. A. Multiscale analysis of stamp forming of a woven composite. *Journal of Thermoplastic Composite Materials* **2013**, *26*, 640–662. DOI: 10.1177/0892705711428654.
- [330] Auricchio, F.; Scalet, G.; Wriggers, P. Fiber-reinforced materials: finite elements for the treatment of the inextensibility constraint. *Comput Mech* **2017**, *60*, 905–922. DOI: 10.1007/s00466-017-1437-9.
- [331] Peng, X.; Cao, J. A dual homogenization and finite element approach for material characterization of textile composites. *Composites Part B* **2002**, *33*, 45–56. DOI: 10.1016/S1359-8368(01)00052-X.
- [332] Xue, P.; Peng, X.; Cao, J. A non-orthogonal constitutive model for characterizing woven composites. *Composites Part A: Applied Science and Manufacturing* **2003**, *34*, 183–193. DOI: 10.1016/S1359-835X(02)00052-0.
- [333] Cao, J.; Xue, P.; Peng, X.; Krishnan, N. An approach in modeling the temperature effect in thermo-stamping of woven composites. *Composite Structures* **2003**, *61*, 413–420. DOI: 10.1016/S0263-8223(03)00052-7.

- [334] Lee, W.; Um, M.-K.; Byun, J.-H.; Boisse, P.; Cao, J. Numerical study on thermo-stamping of woven fabric composites based on double-dome stretch forming. *Int J Mater Form* **2010**, *3*, 1217–1227. DOI: 10.1007/s12289-009-0668-5.
- [335] Zhang, W.; Ren, H.; Liang, B.; Zeng, D.; Su, X.; Dahl, J.; Mirdamadi, M.; Zhao, Q.; Cao, J. A non-orthogonal material model of woven composites in the preforming process. *CIRP Annals* **2017**, *66*, 257–260. DOI: 10.1016/j.cirp.2017.04.112.
- [336] Chen, S.; McGregor, O.; Harper, L. T.; Endruweit, A.; Warrior, N. A. Defect formation during preforming of a bi-axial non-crimp fabric with a pillar stitch pattern. *Composites Part A: Applied Science and Manufacturing* **2016**, *91*, 156–167. DOI: 10.1016/j.compositesa.2016.09.016.
- [337] Erol, O.; Powers, B.; Keefe, M. Development of a non-orthogonal macroscale material model for advanced woven fabrics based on mesoscale structure. *Composites Part B* **2017**, *110*, 497–510. DOI: 10.1016/j.compositesb.2016.11.023.
- [338] Thije, R. ten; Akkerman, R.; Huétink, J. Large deformation simulation of anisotropic material using an updated Lagrangian finite element method. *Computer Methods in Applied Mechanics and Engineering* **2007**, *196*, 3141–3150. DOI: 10.1016/j.cma.2007.02.010.
- [339] Erol, O.; Powers, B.; Keefe, M. A novel approach to investigate the effect of meso-scale yarn structure on the in-plane mechanical response of woven monofilament textiles by numerical modeling of experiments. *Mechanics of Advanced Materials and Structures* **2018**, *25*, 548–558. DOI: 10.1080/15376494.2017.1280203.
- [340] Tran, P.; Ngo, T.; Yang, E. C.; Mendis, P.; Humphries, W. Effects of architecture on ballistic resistance of textile fabrics: Numerical study. *International Journal of Damage Mechanics* **2014**, *23*, 359–376. DOI: 10.1177/1056789513495246.
- [341] Vilfayeau, J.; Crépin, D.; Boussu, F.; Soulat, D.; Boisse, P. Kinematic modelling of the weaving process applied to 2D fabric. *Journal of Industrial Textiles* **2015**, *45*, 338–351. DOI: 10.1177/1528083714532114.
- [342] Pinkos, J.; Stempien, Z. Numerical and Experimental Comparative Analysis of Ballistic Performance of Packages Made of Biaxial and Triaxial Kevlar 29 Fabrics. *Autex Research Journal* **2020**, *20*, 203–219. DOI: 10.2478/aut-2020-0015.
- [343] Nilakantan, G.; Keefe, M.; Bogetti, T. A.; Adkinson, R.; Gillespie, J. W. On the finite element analysis of woven fabric impact using multiscale modeling techniques. *International Journal of Solids and Structures* **2010**. DOI: 10.1016/j.ijsolstr.2010.04.029.
- [344] Grujicic, M.; Bell, W. C.; Arakere, G.; He, T.; Xie, X.; Cheeseman, B. A. Development of a Meso-Scale Material Model for Ballistic Fabric and Its Use in Flexible-Armor

- Protection Systems. *Journal of Materials Engineering and Performance* **2010**, *19*, 22–39. DOI: 10.1007/s11665-009-9419-5.
- [345] Zeng, X.; Brown, L. P.; Endruweit, A.; Long, A. C. Advanced Geometry Modelling of 3D Woven Reinforcements in Polymer Composites : Processing and Performance Analysis. *Fourth World Conference on 3D Fabrics and their Applications, 10-11 Sep 2012, Aachen, Germany* **2012**, 1–10.
- [346] Vidal-Sallé, E.; Hivet, G. Mesoscopic approaches for understanding the mechanical behavior of reinforcements in composites. *Composite Reinforcements for Optimum Performance*, 2011; pp 486–528.
- [347] Lomov, S. V. *Modelling the geometry of textile reinforcements for composites: WisTex. In: Composite Reinforcements for Optimum Performance*, 2011.
- [348] Wang, L.; Zhang, S.; Gao, W. M.; Wang, X. FEM analysis of knife penetration through woven fabrics. *CMES - Computer Modeling in Engineering and Sciences* **2007**, *20*, 11–20.
- [349] Lin, H.; Brown, L. P.; Long, A. C. Modelling and Simulating Textile Structures Using TexGen. *Advanced Materials Research* **2011**, *331*, 44–47. DOI: 10.4028/www.scientific.net/AMR.331.44.
- [350] Ivanov, I.; Tabiei, A. Loosely woven fabric model with viscoelastic crimped fibres for ballistic impact simulations. *Int. J. Numer. Meth. Engng.* **2004**, *61*, 1565–1583. DOI: 10.1002/nme.1113.
- [351] Tabiei, a.; Ivanov, I. Computational micro-mechanical model of flexible woven fabric for finite element impact simulation. *Int. J. Numer. Methods Eng.* **2002**, *53*, 1259–1276. DOI: 10.1002/nme.321.
- [352] Yang, X. Dynamic simulation of 3D weaving process. Dissertation, Kansas State, USA, 2015.
- [353] Russcher, L.; Lamers, E.; Dufour, C.; Boussu, F.; Wang, P.; Soulat, D. Modelling the microstructure of multilayer woven fabrics. In *13th AUTEX World Textile Conference*, 2013.
- [354] Durville, D. Microscopic approaches for understanding the mechanical behavior of reinforcement in composites. *Composite Reinforcements for Optimum Performance*, 2011; pp 461–485.
- [355] Hans, T.; Cichosz, J.; Brand, M.; Hinterhölzl, R. Finite element simulation of the braiding process for arbitrary mandrel shapes. *Composites Part A: Applied Science and Manufacturing* **2015**, *77*, 124–132. DOI: 10.1016/j.compositesa.2015.06.003.
- [356] Pickett, A. K.; Sirtautas, J.; Erber, A. Braiding Simulation and Prediction of Mechanical Properties. *Appl Compos Mater* **2009**, *16*, 345–364. DOI: 10.1007/s10443-009-9102-x.

- [357] Gereke, T.; Döbrich, O.; Aibibu, D.; Nowotny, J.; Cherif, C. Approaches for process and structural finite element simulations of braided ligament replacements. *Journal of Industrial Textiles* **2017**. DOI: 10.1177/1528083716648765.
- [358] Wang, X.; Zhang, G.; Shi, X.; Zhang, C. Modeling method of irregular cross section annular axis braided preform based on finite element simulation. *Journal of Engineered Fibers and Fabrics* **2021**, *16*, 155892502110372. DOI: 10.1177/15589250211037243.
- [359] Shanahan, C.; Tofail, S. A.; Tiernan, P. Viscoelastic braided stent: Finite element modelling and validation of crimping behavior. *Materials & Design* **2017**, *121*, 143–153. DOI: 10.1016/j.matdes.2017.02.044.
- [360] Barry, C. P.; Olson, B. G.; Bergeron, K.; Willis, D. J.; Sherwood, J. A. Modeling Tensile Tests of a Braided Parachute Suspension Line using a Mesomechanical Finite Element Model. In *AIAA Scitech 2020 Forum*; American Institute of Aeronautics and Astronautics: Reston, Virginia, 01062020.
- [361] Yordan Kyosev, Ed. *Advances in Braiding Technology*; Woodhead Publishing, 2016.
- [362] Vu, T. D.; Durville, D.; Davies, P. Finite element simulation of the mechanical behavior of synthetic braided ropes and validation on a tensile test. *International Journal of Solids and Structures* **2015**, *58*, 106–116. DOI: 10.1016/j.ijsolstr.2014.12.022.
- [363] Ghaedsharaf, M.; Brunel, J.-E.; Lebel, L. L. Fiber-level numerical simulation of biaxial braids for mesoscopic morphology prediction validated by X-ray computed tomography scan. *Composites Part B* **2021**, *218*, 108938. DOI: 10.1016/j.compositesb.2021.108938.
- [364] Zhou, G.; Sun, X.; Wang, Y. Multi-chain digital element analysis in textile mechanics. *Composites Science and Technology* **2004**. DOI: 10.1016/S0266-3538(03)00258-6.
- [365] Dörr, D.; Schirmaier, F. J.; Henning, F.; Kärger, L. A viscoelastic approach for modeling bending behavior in finite element forming simulation of continuously fiber reinforced composites. *Composites Part A: Applied Science and Manufacturing* **2017**, *94*, 113–123. DOI: 10.1016/j.compositesa.2016.11.027.
- [366] Bardl, G.; Nocke, A.; Hübner, M.; Gereke, T.; Pooch, M.; Schulze, M.; Heuer, H.; Schiller, M.; Kupke, R.; Klein, M.; *et al.* Analysis of the 3D draping behavior of carbon fiber non-crimp fabrics with eddy current technique. *Composites Part B* **2018**, *132*, 49–60. DOI: 10.1016/j.compositesb.2017.08.007.
- [367] Yu, W.-R.; Harrison, P.; Long, A. Finite element forming simulation for non-crimp fabrics using a non-orthogonal constitutive equation. *Composites Part A: Applied Science and Manufacturing* **2005**, *36*, 1079–1093. DOI: 10.1016/j.compositesa.2005.01.007.

- [368] Mallach, A.; Härtel, F.; Heieck, F.; Fuhr, J.-P.; Middendorf, P.; Gude, M. Experimental comparison of a macroscopic draping simulation for dry non-crimp fabric preforming on a complex geometry by means of optical measurement. *Journal of Composite Materials* **2017**, *51*, 2363–2375. DOI: 10.1177/0021998316670477.
- [369] Orlik, J.; Pietsch, K.; Fassbender, A.; Sivak, O.; Steiner, K. Simulation and Experimental Validation of Spacer Fabrics Based on their Structure and Yarn's Properties. *Appl Compos Mater* **2018**, *25*, 709–724. DOI: 10.1007/s10443-018-9726-9.
- [370] Kyosev, Y.; Renkens, W. Modelling and visualization of knitted fabrics. *Modelling and predicting textile behavior*, 2009; pp 225–262.
- [371] Kyosev, Y. Topological Modelling of Knitted Structures. In *Topology-Based Modeling of Textile Structures and Their Joint Assemblies*; Kyosev, Y., Ed.; Springer International Publishing: Cham, 2019; pp 91–129.
- [372] F Robitaille; B R Clayton; A C Long; B J Souter; C D Rudd. Geometric modelling of industrial preforms: Warp-knitted textiles. *Proceedings of the Institution of Mechanical Engineers, Part L: Journal of Materials: Design and Applications* **2000**, *214*, 71–90. DOI: 10.1177/146442070021400203.
- [373] Colin, D.; Bel, S.; Hans, T.; Hartmann, M.; Drechsler, K. Virtual Description of Non-Crimp Fabrics at the Scale of Filaments Including Orientation Variability in the Fibrous Layers. *Appl Compos Mater* **2020**, *27*, 337–355. DOI: 10.1007/s10443-020-09819-1.
- [374] Döbrich, O.; Gereke, T.; Cherif, C.; Krzywinski, S. Analysis and finite element simulation of the draping process of multilayer knit structures and the effects of a localized fixation. *Advanced Composite Materials* **2013**, *22*, 175–189. DOI: 10.1080/09243046.2013.791239.
- [375] Ru, X.; Wang, J. C.; Peng, L.; Shi, W.; Hu, X. Modeling and deformation simulation of weft knitted fabric at yarn level. *Textile Research Journal* **2022**, 004051752211349. DOI: 10.1177/00405175221134934.
- [376] Maron, B. Beitrag zur Modellierung und Simulation des Thermoformprozesses von textilverstärkten Thermoplastverbunden. Dissertation, Technische Universität Dresden, Dresden, 2016.
- [377] Duhovic, M.; Bhattacharyya, D. Simulating the deformation mechanisms of knitted fabric composites. *Compos Part A-Appl S* **2006**, *37*, 1897–1915. DOI: 10.1016/J.COMPOSITESA.2005.12.029.
- [378] *Handbuch Faserverbundkunststoffe/Composites*; Springer Fachmedien Wiesbaden: Wiesbaden, 2013.
- [379] Alger, M. S. M. *Polymer science dictionary*; Chapman & Hall: London, 1997.

- [380] Askeland, D. R.; Fulay, P. P.; Wright, W. J. *The science and engineering of materials*, 6th ed.; Cengage Learning: Stamford CT, 2011.
- [381] Puck, A. *Zur Beanspruchung und Verformung von GFK-Mehrschichtenverbund-Bauelementen: T. 1. Grundlagen d. Spannungs- u. Verformungsanalyse. T. 2. Spannungs- u. Verformungsanalyse an GFK-Wickelrohren unter Überdruck. T. 3. Versuche an Mehrschichtenverbunden Gekürzte Fassg*; Hanser, 1967.
- [382] Bauchau, O. A.; Craig, J. I. Kirchhoff plate theory. In *Structural Analysis*; Gladwell, G. M. L., Bauchau, O. A., Craig, J. I., Eds.; Springer Netherlands: Dordrecht, 2009; pp 819–914.
- [383] Augustus Edward Hough Love. XVI. The small free vibrations and deformation of a thin elastic shell. *Phil. Trans. R. Soc. Lond. A* **1888**, 179, 491–546. DOI: 10.1098/rsta.1888.0016.
- [384] Timoshenko, S. *Theory of Plates and Shells*, 2nd ed + International Student, 1970 (1982).
- [385] Schürmann, H. *Konstruieren mit Faser-Kunststoff-Verbunden, 2.*, bearbeitete und erw. Aufl.; Springer-Verlag Berlin Heidelberg: Berlin, Heidelberg, 2007.
- [386] Chou, P. C.; Carleone, J.; Hsu, C. M. Elastic Constants of Layered Media. *Journal of Composite Materials* **1972**, 6, 80–93. DOI: 10.1177/002199837200600107.
- [387] Mindlin, R. D. Influence of Rotatory Inertia and Shear on Flexural Motions of Isotropic, Elastic Plates. *J.Appl. Mech* **1951**, 18, 31–38. DOI: 10.1115/1.4010217.
- [388] Reissner, E. The Effect of Transverse Shear Deformation on the Bending of Elastic Plates. *J.Appl. Mech* **1945**, 12, A69-A77. DOI: 10.1115/1.4009435.
- [389] Bhaskar, K.; Varadan, T. K. *Plates*; Springer International Publishing: Cham, 2021.
- [390] Roufaeil, O. L.; Tran-Cong, T. Finite strip elements for laminated composite plates with transverse shear strain discontinuities. *Composite Structures* **2002**, 56, 249–258. DOI: 10.1016/S0263-8223(02)00010-7.
- [391] Jweeg, M. J.; Al-Waily, M.; Resan, K. K. Higher-order isoparametric formulation. *Energy Methods and Finite Element Techniques*; Elsevier, 2022; e633-e676.
- [392] Whitney, J. M. Analysis of Interlaminar Mode II Bending Specimens Using a Higher Order Beam Theory. *Journal of Reinforced Plastics and Composites* **1990**, 9, 522–536. DOI: 10.1177/073168449000900601.
- [393] Pagano, N. J. Erratum to: Exact Solutions for Composite Laminates in Cylindrical Bending. In *Mechanics of Composite Materials*; Gladwell, G. M. L., Reddy, J. N., Eds.; Springer Netherlands: Dordrecht, 1994; p 449.
- [394] Tang, S. A Boundary Layer Theory - Part I: Laminated Composites in Plane Stress. *Journal of Composite Materials* **1975**, 9, 33–41. DOI: 10.1177/002199837500900104.

- [395] Hsu, P. W.; Herakovich, C. T. Edge Effects in Angle-Ply Composite Laminates*. *Journal of Composite Materials* **1977**, *11*, 422–428. DOI: 10.1177/002199837701100405.
- [396] Pipes, B. "Interlaminar Stresses in Composite Laminates - An Approximate Elasticity Solution," *Journal of Applied Mechanics*, Vol. 41, No. 3, (1974), pp. 668-672. Pipes, R. B., and Pagano, N. J., **2018**.
- [397] Wang, S. S.; Choi, I. *Boundary Layer Thermal Stresses in Angle-ply Composite Laminates*; National Aeronautics and Space Administration, 1981.
- [398] Ambartsumyan, S. A.; Kunin, I. *Theory of anisotropic plates: Strength, stability, and vibrations / S.A. Ambartsumyan ; English edition editor Isaak Kunin*, 2nd ed., 1991.
- [399] Reddy, J. N.; Phan, N. D. Stability and vibration of isotropic, orthotropic and laminated plates according to a higher-order shear deformation theory. *Journal of Sound and Vibration* **1985**, *98*, 157–170. DOI: 10.1016/0022-460X(85)90383-9.
- [400] Matsunaga, H. Vibration and stability of cross-ply laminated composite plates according to a global higher-order plate theory. *Composite Structures* **2000**, *48*, 231–244. DOI: 10.1016/S0263-8223(99)00110-5.
- [401] Mantari, J. L.; Guedes Soares, C. Analysis of isotropic and multilayered plates and shells by using a generalized higher-order shear deformation theory. *Composite Structures* **2012**, *94*, 2640–2656. DOI: 10.1016/j.compstruct.2012.03.018.
- [402] Touratier, M. An efficient standard plate theory. *International Journal of Engineering Science* **1991**, *29*, 901–916. DOI: 10.1016/0020-7225(91)90165-Y.
- [403] Stein, M.; Jegley, D. C. Effects of transverse shearing on cylindrical bending, vibration, and buckling of laminated plates. *AIAA Journal* **1987**, *25*, 123–129. DOI: 10.2514/3.9590.
- [404] Soldatos, K. P. A transverse shear deformation theory for homogeneous monoclinic plates. *Acta Mechanica* **1992**, *94*, 195–220. DOI: 10.1007/BF01176650.
- [405] RAMALINGESWARA RAO, S.; GANESAN, N. INTERLAMINAR STRESSES IN SHELLS OF REVOLUTION. *Mechanics of Composite Materials and Structures* **1996**, *3*, 321–339. DOI: 10.1080/10759419608945870.
- [406] Carrera, E. Historical review of zig-zag theories for multilayered plates and shells. *Appl. Mech. Rev.* **2003**, *56*, 287–308.
- [407] Pagano, N. J. Exact Solutions for Rectangular Bidirectional Composites and Sandwich Plates. *Journal of Composite Materials* **1970**, *4*, 20–34. DOI: 10.1177/002199837000400102.
- [408] Reddy, J. N. *Mechanics of laminated composite plates- Theory and analysis*(Book). Boca Raton, FL: CRC Press, 1997 **1997**.

- [409] Plagianakos, T. S.; Saravanos, D. A. Higher-order layerwise laminate theory for the prediction of interlaminar shear stresses in thick composite and sandwich composite plates. *Composite Structures* **2009**, *87*, 23–35. DOI: 10.1016/j.compstruct.2007.12.002.
- [410] Noor, A. K.; Burton, W. S.; Bert, C. W. Computational Models for Sandwich Panels and Shells. *Applied Mechanics Reviews* **1996**, *49*, 155–199. DOI: 10.1115/1.3101923.
- [411] Barbero, E. J.; Reddy, J. N.; Teply, J. L. General two-dimensional theory of laminated cylindrical shells. *AIAA Journal* **1990**, *28*, 544–553. DOI: 10.2514/3.10426.
- [412] Heyliger, P.; Pei, K. C.; Saravanos, D. Layerwise mechanics and finite element model for laminated piezoelectric shells. *AIAA Journal* **1996**, *34*, 2353–2360. DOI: 10.2514/3.13401.
- [413] Averill, R. C.; Yip, Y. C. Thick beam theory and finite element model with zig-zag sublaminar approximations. *AIAA Journal* **1996**, *34*, 1627–1632. DOI: 10.2514/3.13281.
- [414] Hinton, M.; Soden, P. D.; Kaddour, A.-S. *Failure criteria in fibre reinforced polymer composites: the world-wide failure exercise*; Elsevier, 2004.
- [415] Daniel, I. M. Failure of Composite Materials. In *Fracture of Nano and Engineering Materials and Structures*; Gdoutos, E. E., Ed.; Springer Netherlands: Dordrecht, 2006; pp 11–12.
- [416] Zinoviev, P. A.; Lebedeva, O. V.; Tairova, L. P. A coupled analysis of experimental and theoretical results on the deformation and failure of composite laminates under a state of plane stress. *Composites Science and Technology* **2002**, *62*, 1711–1723.
- [417] Bogetti, T. A.; Hoppel, C. P.; Harik, V. M.; Newill, J. F.; Burns, B. P. Predicting the nonlinear response and progressive failure of composite laminates. *Composites Science and Technology* **2004**, *64*, 329–342. DOI: 10.1016/S0266-3538(03)00217-3.
- [418] Hart-Smith, L. Predictions of a generalized maximum-shear-stress failure criterion for certain fibrous composite laminates. *Composites Science and Technology* **1998**, *58*, 1179–1208. DOI: 10.1016/S0266-3538(97)00193-0.
- [419] Tsai, S. W. Strength theories of filamentary structure. *Fundamental aspects of fiber reinforced plastic composites* **1968**.
- [420] Tsai, S. W.; Wu, E. M. A General Theory of Strength for Anisotropic Materials. *Journal of Composite Materials* **1971**, *5*, 58–80. DOI: 10.1177/002199837100500106.
- [421] Hashin, Z. Failure Criteria for Unidirectional Fiber Composites. *J. Appl. Mech* **1980**, *47*, 329–334. DOI: 10.1115/1.3153664.
- [422] Rotem, A. Prediction of laminate failure with the Rotem failure criterion. *Failure Criteria in Fibre-Reinforced-Polymer Composites*; Elsevier, 2004; pp 298–315.

- [423] Cuntze, R. G.; Freund, A. The predictive capability of failure mode concept-based strength criteria for multidirectional laminates. *Composites Science and Technology* **2004**, *64*, 343–377. DOI: 10.1016/S0266-3538(03)00218-5.
- [424] SUN, C. T. Strength Analysis of Unidirectional Composites and Laminates. *Comprehensive Composite Materials*; Elsevier, 2000; pp 641–666.
- [425] McCartney, L. N. Predicting Properties of Undamaged and Damaged Carbon Fibre Reinforced Composites. In *The Structural Integrity of Carbon Fiber Composites*; Beaumont, P. W. R., Soutis, C., Hodzic, A., Eds.; Springer International Publishing: Cham, 2017; pp 425–467.
- [426] Edge, E. A comparison of theory and experiment for the stress-based Grant-Sanders method. *Composites Science and Technology* **2002**, *62*, 1571–1589. DOI: 10.1016/S0266-3538(01)00209-3.
- [427] Chamis, C. C.; Smith, G. T. Codstran: Composite Durability Structural Analysis. In *Fibrous Composites in Structural Design*; Lenoe, E. M., Oplinger, D. W., Burke, J. J., Eds.; Springer US: Boston, MA, 1980; pp 771–780.
- [428] Gotsis, P. K.; Chamis, C. C.; Minnetyan, L. Prediction of composite laminate fracture. *Failure Criteria in Fibre-Reinforced-Polymer Composites*; Elsevier, 2004; pp 98–120.
- [429] Daniel, I. M.; Daniel, S. M.; Fenner, J. S. A new yield and failure theory for composite materials under static and dynamic loading. *International Journal of Solids and Structures* **2018**, *148-149*, 79–93. DOI: 10.1016/j.ijsolstr.2017.08.036.
- [430] Huang, Z.-M. A bridging model prediction of the ultimate strength of composite laminates subjected to biaxial loads. *Composites Science and Technology* **2004**, *64*, 395–448. DOI: 10.1016/S0266-3538(03)00220-3.
- [431] Mayes, J.; Hansen, A. C. Composite laminate failure analysis using multicontinuum theory. *Composites Science and Technology* **2004**, *64*, 379–394. DOI: 10.1016/S0266-3538(03)00219-7.
- [432] Butalia, T. S.; Wolfe, W. E. A strain-energy-based non-linear failure criterion: comparison of numerical predictions and experimental observations for symmetric composite laminates. *Composites Science and Technology* **2002**, *62*, 1697–1710.
- [433] Doudican, B. M.; Zand, B.; Amaya, P.; Butalia, T. S.; Wolfe, W. E.; Schoeppner, G. A. Strain energy based failure criterion: Comparison of numerical predictions and experimental observations for symmetric composite laminates subjected to triaxial loading. *Journal of Composite Materials* **2013**, *47*, 847–866. DOI: 10.1177/0021998312462617.
- [434] Mast, P. W.; Nash, G. E.; Michopoulos, J. G.; Thomas, R.; Badaliane, R.; Wolock, I. Characterization of strain-induced damage in composites based on the dissipated

- energy density part I. Basic scheme and formulation. *Theoretical and Applied Fracture Mechanics* **1995**, 22, 71–96. DOI: 10.1016/0167-8442(94)00050-B.
- [435] Li, S.; Reid, S. R.; Soden, P. D. A continuum damage model for transverse matrix cracking in laminated fibre-reinforced composites. *Philosophical Transactions of the Royal Society of London. Series A: Mathematical, Physical and Engineering Sciences* **1998**, 356, 2379–2412. DOI: 10.1098/rsta.1998.0278.
- [436] Ramesh Talreja. A continuum mechanics characterization of damage in composite materials. *Proc. R. Soc. Lond. A* **1985**, 399, 195–216. DOI: 10.1098/rspa.1985.0055.
- [437] Hart-Smith, L. J. Expanding the capabilities of the Ten-Percent Rule for predicting the strength of fibre-polymer composites. *Composites Science and Technology* **2002**, 62, 1515–1544. DOI: 10.1016/S0266-3538(02)00092-1.
- [438] Hart-Smith, L. J. The ten-percent rule for preliminary sizing of fibrous composite structures. *Weight Engineering* **1992**, 52, 29–45.
- [439] Talreja, R. On Failure Theories for Composite Materials. In *Advanced Methods of Continuum Mechanics for Materials and Structures*; Naumenko, K., Aßmus, M., Eds.; Springer Singapore: Singapore, 2016; pp 379–388.
- [440] Kaddour, A. S.; Hinton, M. J.; Soden, P. D. Predictive capabilities of nineteen failure theories and design methodologies for polymer composite laminates. Part B. *Failure Criteria in Fibre-Reinforced-Polymer Composites*; Elsevier, 2004; pp 1073–1221.
- [441] Soden, P. D.; Kaddour, A. S.; Hinton, M. J. Recommendations for designers and researchers resulting from the world-wide failure exercise. *Failure Criteria in Fibre-Reinforced-Polymer Composites*; Elsevier, 2004; pp 1223–1251.
- [442] LLorca, J.; González, C.; Molina-Aldareguía, J. M.; Segurado, J.; Seltzer, R.; Sket, F.; Rodríguez, M.; Sádaba, S.; Muñoz, R.; Canal, L. P. Multiscale modeling of composite materials: a roadmap towards virtual testing. *Advanced materials (Deerfield Beach, Fla.)* **2011**, 23, 5130–5147. DOI: 10.1002/adma.201101683.
- [443] Pindera, M.-J.; Khatam, H.; Drago, A. S.; Bansal, Y. Micromechanics of spatially uniform heterogeneous media: A critical review and emerging approaches. *Compos Part B-Eng* **2009**, 40, 349–378. DOI: 10.1016/j.compositesb.2009.03.007.
- [444] Swolfs, Y.; Fazlali, B.; Melnikov, A.; Mesquita, F.; Feyen, V.; Breite, C.; Gorbatiikh, L.; Lomov, S. V. State-of-the-art models for mechanical performance of carbon-glass hybrid composites in wind turbine blades. *IOP Conf. Ser.: Mater. Sci. Eng.* **2020**, 942, 12005. DOI: 10.1088/1757-899X/942/1/012005.
- [445] Bunsell, A.; Gorbatiikh, L.; Morton, H.; Pimenta, S.; Sinclair, I.; Spearing, M.; Swolfs, Y.; Thionnet, A. Benchmarking of strength models for unidirectional composites

- under longitudinal tension. *Composites Part A: Applied Science and Manufacturing* **2018**, *111*, 138–150. DOI: 10.1016/j.compositesa.2018.03.016.
- [446] Totry, E.; González, C.; LLorca, J. Prediction of the failure locus of C/PEEK composites under transverse compression and longitudinal shear through computational micromechanics. *Composites Science and Technology* **2008**, *68*, 3128–3136. DOI: 10.1016/j.compscitech.2008.07.011.
- [447] Canal, L. P.; Segurado, J.; LLorca, J. Failure surface of epoxy-modified fiber-reinforced composites under transverse tension and out-of-plane shear. *International Journal of Solids and Structures* **2009**, *46*, 2265–2274. DOI: 10.1016/j.ijsolstr.2009.01.014.
- [448] Totry, E.; Molina-Aldareguía, J. M.; González, C.; LLorca, J. Effect of fiber, matrix and interface properties on the in-plane shear deformation of carbon-fiber reinforced composites. *Composites Science and Technology* **2010**, *70*, 970–980. DOI: 10.1016/j.compscitech.2010.02.014.
- [449] Döbrich, O.; Gereke, T.; Cherif, C. Modelling of fibre-reinforced composites on a near micro scale: Possibilities and benefits. In *10th European LS-DYNA Conference*, 2015.
- [450] Liu, C.; Xie, J.; Sun, Y.; Chen, L. Micro-scale modeling of textile composites based on the virtual fiber embedded models. *Compos Struct* **2019**, *230*, 111552. DOI: 10.1016/j.compstruct.2019.111552.
- [451] Lomov, S.; IVANOV, D.; Verpoest, I.; ZAKO, M.; KURASHIKI, T.; NAKAI, H.; HIROSAWA, S. Meso-FE modelling of textile composites: Road map, data flow and algorithms. *Composites Science and Technology* **2007**, *67*, 1870–1891. DOI: 10.1016/j.compscitech.2006.10.017.
- [452] Verpoest, I.; Lomov, S. V. Virtual textile composites software WiseTex: Integration with micro-mechanical, permeability and structural analysis. *Composites Science and Technology* **2005**, *65*, 2563–2574. DOI: 10.1016/j.compscitech.2005.05.031.
- [453] Hallett, S. R.; Wisnom, M. R. Numerical Investigation of Progressive Damage and the Effect of Layup in Notched Tensile Tests. *Journal of Composite Materials* **2006**, *40*, 1229–1245. DOI: 10.1177/0021998305057432.
- [454] Meer, F. P.; Sluys, L. J. A phantom node formulation with mixed mode cohesive law for splitting in laminates. *Int J Fract* **2009**, *158*, 107–124. DOI: 10.1007/s10704-009-9344-5.
- [455] Greve, L.; Pickett, A. K. Delamination testing and modelling for composite crash simulation. *Composites Science and Technology* **2006**, *66*, 816–826. DOI: 10.1016/j.compscitech.2004.12.042.

- [456] Camanho, P. P.; Hallett, S. R. *Numerical modelling of failure in advanced composite materials*; Elsevier Inc, 2015.
- [457] Raju, K.; Tay, T.-E.; Tan, V. B. C. A review of the FE2 method for composites. *Multiscale and Multidiscip. Model. Exp. and Des.* **2021**, *4*, 1–24. DOI: 10.1007/s41939-020-00087-x.
- [458] Tabiei, a.; Jiang, Y. Woven fabric composite material model with material nonlinearity for nonlinear finite element simulation. *International Journal of Solids and Structures* **1999**, *36*, 2757–2771.
- [459] Whitcomb, J.; Noh, J.; Chapman, C. Evaluation of Various Approximate Analyses for Plain Weave Composites. *Journal of Composite Materials* **1999**, *33*, 1958–1980. DOI: 10.1177/002199839903302101.
- [460] Woo, K.; Whitcomb, J. Global/Local Finite Element Analysis for Textile Composites. *Journal of Composite Materials* **1994**, *28*, 1305–1321. DOI: 10.1177/002199839402801402.
- [461] Fujita, A.; HAMADA, H.; Maekawa, Z. Tensile Properties of Carbon Fiber Triaxial Woven Fabric Composites. *Journal of Composite Materials* **1993**, *27*, 1428–1442. DOI: 10.1177/002199839302701501.
- [462] Johnson, W. S.; Masters, J. E.; Raju, I. S.; Wang, J. T. Classical Laminate Theory Models for Woven Fabric Composites. *J. Compos. Technol. Res.* **1994**, *16*, 289. DOI: 10.1520/CTR10589].
- [463] Ishikawa, T.; Chou, T.-W. One-dimensional micromechanical analysis of woven fabric composites. *AIAA Journal* **1983**, *21*, 1714–1721. DOI: 10.2514/3.8314.
- [464] Hahn, H. T.; Pandey, R. A Micromechanics Model for Thermoelastic Properties of Plain Weave Fabric Composites. *Journal of Engineering Materials and Technology* **1994**, *116*, 517–523. DOI: 10.1115/1.2904322.
- [465] Zhang, Y. C.; Harding, J. A numerical micromechanics analysis of the mechanical properties of a plain weave composite. *Computers and Structures* **1990**, *36*, 839–844. DOI: 10.1016/0045-7949(90)90154-T.
- [466] Naik, N. K.; Ganesh, V. K. An analytical method for plain weave fabric composites. *00104361* **1995**, *26*, 281–289. DOI: 10.1016/0010-4361(95)93671-6.
- [467] Soykasap, Ö. Analysis of plain-weave composites. *Mech Compos Mater* **2011**, *47*, 161–176. DOI: 10.1007/s11029-011-9195-9.
- [468] Stig, F.; Hallström, S. A modelling framework for composites containing 3D reinforcement. *Composite Structures* **2012**, *94*, 2895–2901. DOI: 10.1016/j.compstruct.2012.03.009.

- [469] Wang, Y.; Soutis, C. A Finite Element and Experimental Analysis of Composite T-Joints Used in Wind Turbine Blades. *Appl Compos Mater* **2018**, *25*, 953–964. DOI: 10.1007/s10443-018-9711-3.
- [470] Le Page, B. H.; Guild, F. J.; Ogin, S. L.; Smith, P. A. Finite element simulation of woven fabric composites. *Composites Part A: Applied Science and Manufacturing* **2004**, *35*, 861–872. DOI: 10.1016/j.compositesa.2004.01.017.
- [471] Barbero, E. J.; Lonetti, P.; Sikkil, K. K. Finite element continuum damage modeling of plain weave reinforced composites. *Composites Part B* **2005**, *37*, 137–147. DOI: 10.1016/j.compositesb.2005.06.001.
- [472] Daggumati, S.; van Paepegem, W.; Degrieck, J.; Xu, J.; Lomov, S. V.; Verpoest, I. Local damage in a 5-harness satin weave composite under static tension: Part II – Meso-FE modelling. *Composites Science and Technology* **2010**, *70*, 1934–1941. DOI: 10.1016/j.compscitech.2010.07.002.
- [473] Yu, S.; Zhang, D.; Qian, K. Numerical Analysis of Macro-Scale Mechanical Behaviors of 3D Orthogonal Woven Composites using a Voxel-Based Finite Element Model. *Appl Compos Mater* **2019**, *26*, 65–83. DOI: 10.1007/s10443-018-9707-z.
- [474] Cox, B. N.; Carter, W. C.; Fleck, N. A. A binary model of textile composites—I. Formulation. *Acta Metallurgica et Materialia* **1994**, *42*, 3463–3479. DOI: 10.1016/0956-7151(94)90479-0.
- [475] Cox, B. N.; Dadkhah, M. S. The Macroscopic Elasticity of 3D Woven Composites. *Journal of Composite Materials* **1995**, *29*, 785–819. DOI: 10.1177/002199839502900606.
- [476] Cichosz, J. A. *Experimental characterization and numerical modeling of the mechanical response for biaxial braided composites*, 1. Auflage; Verlag Dr. Hut: München, 2016.
- [477] Blinzler, B.; Goldberg, R.; Binienda, W. Macro Scale Independently Homogenized Subcells for Modeling Braided Composites. In *52nd AIAA/ASME/ASCE/AHS/ASC Structures, Structural Dynamics and Materials Conference*; American Institute of Aeronautics and Astronautics: Reston, Virginia, 04042011.
- [478] Mathieu Vinot; Martin Holzapfel; Christian Liebold. A multiscale strategy for the simulation of braided composites with ENVYO. In *Deutsches LS-DYNA Forum 2018*, 2018; pp 138–140.
- [479] Li, D.; Fang, D.; Jiang, N.; Xuefeng, Y. Finite element modeling of mechanical properties of 3D five-directional rectangular braided composites. *Composites Part B* **2011**, *42*, 1373–1385. DOI: 10.1016/j.compositesb.2011.05.042.
- [480] Zhang, C.; Curiel-Sosa, J. L.; Bui, T. Q. Meso-scale finite element analysis of mechanical behavior of 3D braided composites subjected to biaxial tension loadings. *Appl Compos Mater* **2019**, *26*, 139–157. DOI: 10.1007/s10443-018-9686-0.

- [481] LIU, Z.; HOU, Y.; ZHAO, Q.; LI, C. A novel surrogate modeling strategy of the mechanical properties of 3D braided composites. *Chinese Journal of Aeronautics* **2020**, *33*, 2589–2601. DOI: 10.1016/j.cja.2020.05.017.
- [482] Gholami, A.; Melenka, G. W. Finite element analysis of 2-D tubular braided composite based on geometrical models to study mechanical performances. *Mechanics of Advanced Materials and Structures* **2021**, 1–17. DOI: 10.1080/15376494.2021.2001879.
- [483] Gu, B. A microstructure model for finite-element simulation of 3D rectangular braided composite under ballistic penetration. *Philosophical Magazine* **2007**, *87*, 4643–4669. DOI: 10.1080/14786430701573362.
- [484] Dhimole, V. K.; Chen, Y.; Cho, C. Modeling and Two-Step Homogenization of Aperiodic Heterogenous 3D Four-Directional Braided Composites. *J. Compos. Sci.* **2020**, *4*, 179. DOI: 10.3390/jcs4040179.
- [485] Li, X.; Binienda, W. K.; Goldberg, R. K. Finite-Element Model for Failure Study of Two-Dimensional Triaxially Braided Composite. *J. Aerosp. Eng.* **2011**, *24*, 170–180. DOI: 10.1061/(ASCE)AS.1943-5525.0000029.
- [486] Zheng, H.; Zhou, C.; Yuan, Y. Meso-scale finite element modeling of moisture diffusion in 3D braided composite. *International Journal of Heat and Mass Transfer* **2019**, *129*, 862–872. DOI: 10.1016/j.ijheatmasstransfer.2018.10.020.
- [487] Xu, K.; Qian, X.; Huang, R. An FEM Analysis with Consideration of Random Void Defects for Predicting the Mechanical Properties of 3D Braided Composites. *Advances in Materials Science and Engineering* **2014**, *2014*, 439819. DOI: 10.1155/2014/439819.
- [488] Yamamoto, T.; Imaoku, A.; Sakakibara, T.; Zako, M. A proposal of conventional FE-modeling for layered braided composites: comparison of numerical results with experimental results. *IOP Conf. Ser.: Mater. Sci. Eng.* **2018**, *406*, 12031. DOI: 10.1088/1757-899X/406/1/012031.
- [489] Song, S.; Waas, A. M.; Shahwan, K. W.; Xiao, X.; Faruque, O. Braided textile composites under compressive loads: Modeling the response, strength and degradation. *Composites Science and Technology* **2007**, *67*, 3059–3070. DOI: 10.1016/j.compscitech.2007.06.008.
- [490] Song, S.; Waas, A. M.; Shahwan, K. W.; Faruque, O.; Xiao, X. Compression Response of 2D Braided Textile Composites: Single Cell and Multiple Cell Micromechanics Based Strength Predictions. *Journal of Composite Materials* **2008**, *42*, 2461–2482. DOI: 10.1177/0021998308096500.
- [491] Fang, G.; Wang, B.; Liang, J. A coupled FE-FFT multiscale method for progressive damage analysis of 3D braided composite beam under bending load. *Composites*

- Science and Technology* **2019**, *181*, 107691. DOI: 10.1016/j.compscitech.2019.107691.
- [492] Mattsson, D.; Joffe, R.; Varna, J. Damage in NCF composites under tension: Effect of layer stacking sequence. *Engineering Fracture Mechanics* **2008**, *75*, 2666–2682. DOI: 10.1016/j.engfracmech.2007.03.014.
- [493] Drapier, S.; Wisnom, M. R. Finite-element investigation of the compressive strength of non-crimp-fabric-based composites. *Composites Science and Technology* **1999**, *59*, 1287–1297. DOI: 10.1016/S0266-3538(98)00165-1.
- [494] Yin, H.; Li, Q.; Iannucci, L. Meso-scale finite element (FE) modelling of biaxial carbon fibre non-crimp-fabric (NCF) based composites under uniaxial tension and in-plane shear. *Compos Struct* **2022**, *290*, 115538. DOI: 10.1016/j.compstruct.2022.115538.
- [495] Carvelli, V.; Chi, T. T.; Larosa, M. S.; Lomov, S. V.; Poggi, C.; Angulo, D. R.; Verpoest, I. Experimental and numerical determination of the mechanical properties of multi-axial multi-ply composites. *Proceeding of the 11 ECCM* **2004**, 31-05.
- [496] Ferreira, L. M.; Graciani, E.; París, F. Predicting failure load of a non-crimp fabric composite by means of a 3D finite element model including progressive damage. *Composite Structures* **2019**, *225*, 111115. DOI: 10.1016/j.compstruct.2019.111115.
- [497] González, A.; Graciani, E.; París, F. Prediction of in-plane stiffness properties of non-crimp fabric laminates by means of 3D finite element analysis. *Composites Science and Technology* **2008**, *68*, 121–131. DOI: 10.1016/j.compscitech.2007.05.026.
- [498] Mikhaluk, D. S.; Truong, T. C.; Borovkov, A. I.; Lomov, S. V.; Verpoest, I. Experimental observations and finite element modelling of damage initiation and evolution in carbon/epoxy non-crimp fabric composites. *Engineering Fracture Mechanics* **2008**, *75*, 2751–2766. DOI: 10.1016/j.engfracmech.2007.03.010.
- [499] Haasemann, G.; Ulbricht, V.; Brummund, J. Modelling the mechanical properties of biaxial weft-knitted fabric reinforced. *Proc. Appl. Math. Mech.* **2004**, *4*, 193–194. DOI: 10.1002/pamm.200410078.
- [500] Ravandi, M.; Ahlquist, S.; Banu, M. Numerical modelling of mechanical behavior of weft-knitted carbon fiber composites. In *8th European Conference for Aeronautics and Space Sciences (EUCASS)*, 2019.
- [501] Ionesi, S. D.; Ciobanu, L.; Dumitras, C.; Avadanei, M.; Dulgheriu, I.; Ionescu, I.; Loghin, M. C. FEM Analysis of Textile Reinforced Composite Materials Impact Behavior. *Materials* **2021**, *14*. DOI: 10.3390/ma14237380.
- [502] Hamedi, S.; Hasani, H.; Dibajian, S. H. Numerical simulating the flexural properties of 3D weft-knitted spacer fabric reinforced composites. *Journal of Composite Materials* **2017**, *51*, 1887–1899. DOI: 10.1177/0021998316665240.

- [503] Haasemann, G.; Kästner, M.; Prüger, S.; Ulbricht, V. Simulation and Modeling the Mechanical Behavior of Textile Reinforced Composites by Combining the Binary Model and X-FEM. *Proc. Appl. Math. Mech.* **2008**, *8*, 10563–10564. DOI: 10.1002/pamm.200810563.
- [504] Zanoaga, M.; Tanasa, F. Complex textile structures as reinforcement for advanced composite materials. *INTERNATIONAL SCIENTIFIC COMMITTEE* **2014**, 267.
- [505] Reumann, R.-D.; Hempel, P.; Haase, J. Flächengebildeprüfungen. *Prüfverfahren in der Textil- und Bekleidungstechnik*, 2011; pp 379–491.
- [506] Bilbao, E. de; Soulat, D.; Hivet, G.; Gasser, A. Experimental Study of Bending Behavior of Reinforcements. *Experimental Mechanics* **2010**. DOI: 10.1007/s11340-009-9234-9.
- [507] Harrison, P.; Alvarez, M. F.; Anderson, D. *Towards comprehensive characterisation and modelling of the forming and wrinkling mechanics of engineering fabrics*, 2018. *International Journal of Solids and Structures*.
- [508] Wendt, E.; Rothe, S.; Krzywinski, S., Eds. *Neuartige optische Erfassung des Scherverhaltens textiler Verstärkungshalbzeuge für die realitätsnahe Drapiersimulation*, 2018.
- [509] Boisse, P.; Colmars, J.; Hamila, N.; Naouar, N.; Steer, Q. Bending and wrinkling of composite fiber preforms and prepregs . A review and new developments in the draping simulations. *Composites Part B* **2018**, *141*, 234–249. DOI: 10.1016/j.compositesb.2017.12.061.
- [510] Townsend, M. W. H. WEFT TENSION IN WEAVING. *Journal of the Textile Institute Proceedings* **1955**, *46*, P699-P712. DOI: 10.1080/19447015508665132.
- [511] Hancock, S. G.; Potter, K. D. The use of kinematic drape modelling to inform the hand lay-up of complex composite components using woven reinforcements. *Composites Part A: Applied Science and Manufacturing* **2006**. DOI: 10.1016/j.compositesa.2005.05.044.
- [512] Tri-D Technologies. 3D to 2D Digital Patterning For Transportation Interiors: White paper. <https://www.exactflat.com/> (accessed January 27, 2022).
- [513] Bathe, K.-J. *Finite element procedures*; Prentice Hall: Englewood Cliffs, N.J., 2006.
- [514] Lima, M. V. A.; Lima, J. M. F.; Lima, P. R. L. Finite Difference Energy Method for nonlinear numerical analysis of reinforced concrete slab using simplified isotropic damage model. *Rev. IBRACON Estrut. Mater.* **2014**, *7*, 940–964. DOI: 10.1590/S1983-41952014000600004.
- [515] Bischoff, M. *Theorie und Numerik einer dreidimensionalen Schalenformulierung*, 1999.
- [516] Yousaf, Z.; Potluri, P.; Withers, P. J.; Mollenhauer, D.; Zhou, E.; Duning, S. Digital element simulation of aligned tows during compaction validated by computed

- tomography (CT). *International Journal of Solids and Structures* **2018**, 154, 78–87. DOI: 10.1016/j.ijsolstr.2017.05.044.
- [517] Wang, Y.; Sun, X. Digital-element simulation of textile processes. *Composites Science and Technology* **2001**. DOI: 10.1016/S0266-3538(00)00223-2.
- [518] Livermore software technology corporation. *LS-DYNA Keyword user's manual Volume I*; USA, California: Livermore software technology corporation, 2017.
- [519] Pham, M. Q.; Döbrich, O.; Mersch, J.; Gereke, T.; Cherif, C. Meso-scale model for the forming process of biaxial reinforced weft-knitted fabrics. *IOP Conf Ser-Mat Sci*, 406. DOI: 10.1088/1757-899X/406/1/012026.
- [520] Pham, M. Q.; Döbrich, O.; Trümper, W.; Gereke, T.; Cherif, C. Numerical modelling of the mechanical behavior of biaxial weft-knitted fabrics on different length scales. *Materials* **2019**, 12. DOI: 10.3390/ma12223693.
- [521] Hughes, T. J. R.; Liu, W. K. Implicit-Explicit Finite Elements in Transient Analysis: Stability Theory. *J.Appl. Mech* **1978**, 45, 371. DOI: 10.1115/1.3424304.
- [522] Hughes, T. J.; Carnoy, E. Nonlinear finite element shell formulation accounting for large membrane strains. In *American Society of Mechanical Engineers, Applied Mechanics Division, AMD*, 1981.
- [523] Hughes, T. J.; Carnoy, E. Nonlinear finite element shell formulation accounting for large membrane strains. *Computer Methods in Applied Mechanics and Engineering* **1983**. DOI: 10.1016/0045-7825(83)90074-9.
- [524] Ahmad, S.; Irons, B. M.; Zienkiewicz, O. C. Analysis of thick and thin shell structures by curved finite elements. *International Journal for Numerical Methods in Engineering* **1970**. DOI: 10.1002/nme.1620020310.
- [525] Hallquist, J. *LS-DYNA Theory manual*, 2006.
- [526] Choi, K. F.; Lo, T. Y. An Energy Model of Plain Knitted Fabric. *Textile Research Journal* **2003**, 73, 739–748. DOI: 10.1177/004051750307300813.
- [527] Maik Gude. *AMARETO - Sächsische Allianz für MAterial- und RessourcenEffiziente TechnOlogien: Sachbericht - Teilthema Smart Design - Teilprojekt TU Dresden; Forschungsprojekte im Bereich anwendungsnaher öffentlicher Forschung (RL Forschung InfraPro) Antragsnummer: 100291445 - Clusternummer: 3413; Dresden, 2021.*
- [528] SUN, C. T.; Vaidya, R. S. Prediction of composite properties from a representative volume element. *Composites Science and Technology* **1996**, 56, 171–179. DOI: 10.1016/0266-3538(95)00141-7.
- [529] Liebold, C.; Haufe, A. Mapping – Übertragung der Ergebnisse der Prozesssimulation auf die Struktursimulation. In *Der digitale Prototyp*; Dittmann, J.,

- Middendorf, P., Eds.; Springer Berlin Heidelberg: Berlin, Heidelberg, 2019; pp 83–93.
- [530] Liebold, C.; Zerbst, D.; Gereke, T.; Clauss, S. A gray-scale mapping method to consider locally varying properties for wood forming simulations. In , 2021.
- [531] Schweizerhof, K.; Weimar, K.; Münz, T. Simulations LS-DYNA Composite Materials for Shell Analysis in Crashworthiness Situations - Merits and Limits. In , 2003.
- [532] Jiang, W.-G.; Hallett, S. R.; Wisnom, M. R. Development of Domain Superposition Technique for the Modelling of Woven Fabric Composites. In *Mechanical Response of Composites*; Oñate, E., Camanho, P. P., Dávila, C. G., Pinho, S. T., Remmers, J. J. C., Eds.; Springer Netherlands: Dordrecht, 2008; pp 281–291.
- [533] Malik, S. A.; Gereke, T.; Farooq, A.; Aibibu, D.; Cherif, C. Prediction of yarn crimp in PES multifilament woven barrier fabrics using artificial neural network. *Journal of the Textile Institute* **2018**, *109*. DOI: 10.1080/00405000.2017.1393786.

LIST OF FIGURES

Figure 1-1: Industry accepted additional cost for lightweight construction in € per kilogram according to Klein [8].....	3
Figure 1-2: Design of a composite 8' x 20' aircraft blade stiffened panels [34]	3
Figure 1-3: Estimated cost summary for a composite 8' x 20' aircraft blade stiffened panels by various fabrication processes (in thousand USD) [34].....	3
Figure 2-1: Tensile behavior of biaxial reinforced FRP vs. metal	6
Figure 2-2: FRP production process with “multi-step” forming.....	14
Figure 2-3: Loss of tensile strength in dependence of angle between fibers and stress (adapted from Bagherpour [160]).....	17
Figure 2-4: Illustrations of fiber deformation mechanisms (adapted from Creech and Pickett [163]).....	18
Figure 2-5: Drapability test according to DIN EN ISO 9073.....	19
Figure 2-6: Influence of in-plane tensile stress on shear behavior (adapted from Thor [157]).....	20
Figure 2-7: Sliding between fiber layers during textile bending	20
Figure 2-8: Surface typology and principal curvature (adapted from Mansoori [172])...21	
Figure 2-9: Plain woven glass fabric from GF 1200 tex: a) weave pattern, b) fabric appearance and c) cross-section	23
Figure 2-10: ORT plain weave: a) weave pattern and 3D illustration by TexGen, b) top appearance, c) cross-section in the warp direction.....	24
Figure 2-11: Comparison of loop structure and loop formation with bearded needle between weft and warp knitting according to Spencer [190]	26
Figure 2-12: An example of non-crimp fabrics construction (© SAERTEX GmbH & Co.KG)	26
Figure 2-13: Single jersey stitch formation by hand knitting using: (a) pins and (b) by knitting machine with latch needle and cam according to Spencer [190]	28
Figure 2-14: Structural element by flat knitting according to Abounaim [193]	29
Figure 2-15: Dependence of tensile behavior on structure of BWKF (in weft direction) according to Trümper [125]	29
Figure 2-16: Construction of the knitting zone of: (a) asymmetric 2- and (b) 4-layer BWKF [193].....	31
Figure 2-17: Construction of the knitting zone of: (a) symmetric 5-; (b) 9-layer BWKF and (c) symmetric 5-layer MWKF [219].....	31
Figure 2-18: Fully fashioned near-net shape BWKF preforms [218]	32

Figure 2-19: 3D spacer BWKF preforms [193]	32
Figure 2-20: MWKF knitting machine and the orientation of the reinforcing yarns in MWKF [125].....	32
Figure 2-21: 3D complex BWKF preform of a truck corner connection [219].....	33
Figure 2-22: Production of 3D BWKF preforms for cabin carrier on flat knitting machine with active segmented take-down system [222].....	33
Figure 2-23: Tubular and shell-rib BWKF preforms [37]	34
Figure 2-24: Structural geometry and surface of CWK fabric [223].....	34
Figure 2-25: Dependence of shear behavior of BWKF on stitch length according to Trümper [125]	35
Figure 2-26: Testing principle of vibration method and the FAVIMAT+ test machine	36
Figure 2-27: Deformation controlled test methods for bending stiffness	38
Figure 2-28: Schematic of shear principle adapted from Orawattanasrikul [225].....	39
Figure 2-29: Simple illustration of test principles for shear behavior of fabrics (adapted from Orawattanasrikul [225] with supplement)	40
Figure 2-30: Estimation method for critical shear angle according to: (a) Souter [240] and (b) Cherif [227] - Zhu [241] (adapted from Rothe [239])	41
Figure 2-31: Some test principles of fabric/metal surface friction	43
Figure 3-1: (a) Wood versus Waves experiment by Deltares and (b) Fluid-Structure Interaction simulation with LS-DYNA.....	46
Figure 3-2: Kinematic analysis of a thin-walled T-cup component with ExactFlat	47
Figure 3-3: FEM explanation for simple static case (Equation (3-1)) by T. Gereke	49
Figure 3-4: A two nodes 1D-continua with 6 DOF of each node	50
Figure 3-5: A four nodes 2D-continua with six DOF at each node.....	51
Figure 3-6: Typical 3D-continua: (a) tetrahedron, (b) pentahedron and (c) hexahedron..	51
Figure 3-7: Multi-scale modelling of textile structures.....	57
Figure 3-8: Topological model of BWKF by Kyosev [371], implemented in Matlab: (a) Relaxation state, (b) Shear state and (c) Jammed state (© Kyosev).....	60
Figure 3-9: Meso FEM model of BWKF by Macron [376] and its description of non-linear tensile behavior of BWKF.....	61
Figure 3-10: Typical failure modes of FRP adapted from AVK [378] with modification.....	62
Figure 3-11: Qualitative stress-strain diagram of a single layer UD composite according to AVK [378].....	62
Figure 5-1: Overview of the representative fabrics and their cross-sections (microscopy photos along warp direction): (a) BWKF CF/PA 2-layer V1 and (b) BWKF GF 2-layer	74
Figure 5-2: Preforming of integral BWKF from 2D to 3D: a) illustration of the principle, b) flat fabric, c) clamp and yarn pull out and d) 3D integral BWKF	74

Figure 5-3: Force-strain-curve of fiber tensile test (average value).....	76
Figure 5-4: Force-strain-curves of homogeneous yarns	78
Figure 5-5: Tensile force-strain-curves of commingling CF/PA 6.6 hybrid yarns produced by different air jet pressure	79
Figure 5-6: Tensile test of BWKF CF/PA 2-layer V1 on a Zwick Z100 machine	81
Figure 5-7: Force-strain curves of textile stripe tensile tests for BWKF GF 2-layer and 4-layer	82
Figure 5-8: Force-strain curves of textile stripe tensile tests for BWKF CF/PA 2-layer (V1 & V2) and 4-layer	83
Figure 5-9: Force-strain curves of textile stripe tensile tests for plain-woven fabrics W GF	84
Figure 5-10: Cantilever test principle according to DIN 53362 and the test machine ACPM 200	84
Figure 5-11: (a) Working principle of picture-frame-test and (b) Test of biaxial BWKF CF/PA 2-layer V1 on Zwick 2.5kN tensile test machine	87
Figure 5-12: Shear force - shear angle curves of (a) BWKF GF 2-layer and (b) BWKF GF 4-layer	89
Figure 5-13: Shear force - shear angle curves of plain-woven fabrics W GF.....	90
Figure 5-14: Shear force - shear angle curves of BWKF CF/PA: (a) 2-layer V1, (b) 2-layer V2 and (c) 4-layer	90
Figure 5-15: Scan data of wrinkle formation at different shear angles during the picture frame test of BWKF CF/PA 2-layer V1 and W GF.....	91
Figure 5-16: Force-displacement curve during friction test of fabrics at defined normal pressure	92
Figure 5-17: Friction coefficient CoF of fabrics under different pressure	93
Figure 5-18: Yarn pull-out test for BWKF CF/PA 2-layer V1 in warp direction.....	94
Figure 5-19: Force-displace-curves of yarn pull-out test.....	94
Figure 5-20: CAD model of T-cup shell-like forming tools and the installation of the developed tools on a RUCKS laboratory press at ILK © D. Weck	96
Figure 5-21: Parameter for thermo-pressing of T cup thin-walled composite part on the COLLIN P300 PV laboratory press © D. Weck.....	97
Figure 5-22: T cup thin-walled composite part produced from BWKF CF/PA 2-layer V1... ..	97
Figure 5-23: Construction of 8-layer BWKF preforms for T-shaped FRP: (a) with 4 x 2-layer BWKF (FRP-T1), (b) with 2 x 4-layer BWKF (FRP-T2) and (c) with integral layer (FRP-T3)..	100
Figure 5-24: Production of T-shaped FRP samples with VARI process	100
Figure 5-25: Tensile test of FRP coupon specimens on Zwick Z100 tensile machine	103

Figure 5-26: Force-strain curves of tensile test for UD FRP made from hybrid commingling yarn CF/PA 6.6 under different air pressure.....	104
Figure 5-27: Force-strain curves of tensile test for FRP-C0.....	105
Figure 5-28: Force-strain curves of tensile test for FRP made of BWKF GF.....	106
Figure 5-29: Four-point bending test of FRP coupon specimens on Zwick Z100 tensile machine.....	107
Figure 5-30: Force-deformation curves of four-point bending test for FRP-C0.....	108
Figure 5-31: Force-deformation curves of four-point bending test for FRP-C1, -C2 and -C3	109
Figure 5-32: ILSS test of FRP coupon specimens on a Zwick Zmart.Pro tensile machine	110
Figure 5-33: Force-deformation curves of ILSS test for FRP-C1, -C2 and -C3.....	112
Figure 5-34: Three-point bending tests according to DIN 14125 (method A) of T shaped rib-stiffened FRP.....	113
Figure 5-35: Failure modes of T-shaped FRP samples with different rib heights: a) variant T120-0, construction FRP-T1, b) T120-33 (3 variants), and c) T300-33, FRP-T1, H = 32.1 mm	114
Figure 5-36: Force-deformation-curves from 3-point bending test of FRP T120-0 (no rib) with different construction of BWKF preforms	115
Figure 5-37: Force-deformation curves from 3-point bending tests of FRP T120-33 with different constructions of the preforms	115
Figure 5-38: Force-deformation curves from three-point bending tests of long T-shaped FRP samples with 300 mm and 400 mm length, configuration FRP-T1 (rib height H = 32 mm, failure of yarn in rib).....	116
Figure 6-1: State of strain and translation of a 4-node shell element (adapted from [166])	118
Figure 6-2: Example of a laminate design with three integration layers (adapted from [285]).....	121
Figure 6-3: Hughes-Liu beam [525].....	125
Figure 6-4: Round cross-section of a beam element with 8 arbitrary integration point position.....	127
Figure 6-5: Single jersey weft-knitting structure according to Choi and Lo [526] (created with TexGen).....	128
Figure 6-6: Decrease of the curvature of the beam element chain by increasing the length of beam elements.....	129

Figure 6-7: Model of a unit cell 4 x 4 of BWKF CF/PA V1 with beam elements: (a) isometric view, (b) top view and (c) side view along warp direction and (d) side view along weft direction	130
Figure 6-8: Model of a unit cell 4 x 4 of plain woven with beam elements: (a) isometric view, (b) top view and (c) side view	130
Figure 6-9: Comparison of (a) real cross-section of woven fabrics with (b) meso-model with 4 shell segments and (c) 8 shell segments.....	131
Figure 6-10: Model of a unit cell 3 x 3 of BWKF 2-layer asymmetric with shell and beam elements generated by process-like simulation: (a) initial state, (b) generated structure, (c) right side, (d) left side, (e) side view along warp direction.....	133
Figure 6-11: Further models of a unit cell 3 x 3 of BWKF with shell and beam elements generated by process-like simulation.....	133
Figure 6-12: (a) Process-like weaving simulation of a unit cell of 4 warp x 4 weft yarns, (b) top view of the generated structure and (c) side view of the generated structure	134
Figure 6-13: Comparison of tensile force - strain curve between simulation and experiment	136
Figure 6-14: Tensile test simulation of BWKF CF/PA 2-layer V1 and W GF (warp direction)	137
Figure 6-15: Comparison of tensile force - strain curves between experiment and simulation	138
Figure 6-16: Cantilever test simulation of BWKF CF/PA 2-layer V1 and W GF (warp direction)	139
Figure 6-17: Comparison of cantilever test simulation of three types of model.....	140
Figure 6-18: Picture frame test simulation with macro model	141
Figure 6-19: Explanation of the keyword CONSTRAINED_NODE_SET [518].....	141
Figure 6-20: Picture frame test simulation with meso beam model.....	141
Figure 6-21: Shear test simulation with meso beam model by periodic boundary conditions	142
Figure 6-22: Displacement in thickness direction (z direction) of textile FEM models at 40° shear angle	143
Figure 6-23: Comparison of shear force - shear angle curves between experiment and simulation	144
Figure 6-24: Penetration between shell/shell and shell/beam elements during shear test simulation	145
Figure 6-25: Comparison of max. z displacement - shear angle curves between experiment and simulation	145
Figure 6-26: Friction test simulation	146

Figure 6-27: Comparison of force - displacement curves of friction test between experiment and simulation.....	146
Figure 7-1: Forming of BWKF GF 2-layer with hemisphere draping machine with blank holder	149
Figure 7-2: 3D preforms at different setting of blank holder pressure (right after forming)	149
Figure 7-3: Force - displacement curves of stamp during forming process at different air pressure settings	150
Figure 7-4: FEM model of hemisphere draping machine with macro model of fabric ...	151
Figure 7-5: FEM forming simulation results with hemisphere tools with macro model of fabric.....	151
Figure 7-6: FEM forming simulation results with hemisphere tools with meso beam model of fabric	152
Figure 7-7: FEM forming simulation results with hemisphere tools with meso shell model of fabric	152
Figure 7-8: Comparison of the force - displacement curves of stamp during forming process between experiment and simulation.....	154
Figure 7-9: Shear force - shear angle curves of BWKF GF 2-layer with different SCD	156
Figure 7-10: Simulative analysis of the influence of SCD on 3D preform quality (BWKF GF 2-layer).....	157
Figure 7-11: Yarn pull-out simulation for BWKF CF/PA 2-layer V1 with meso shell model	158
Figure 7-12: Comparison of yarn pull-out force between experiment and simulation of BWKF CF/PA 2-layer V1 (Friction coefficient CoF = 0.15)	159
Figure 7-13: Influence of yarn sliding resistance on shear behavior	159
Figure 7-14: Comparison of max. z displacement - shear angle curves between simulation with different stitch yarn material.....	160
Figure 7-15: Displacement in thickness direction (z direction) of textile FEM models with different stitch yarn material at 40° shear angle	161
Figure 7-16: Simulative analysis of the influence of weft yarn density on 3D preform quality (BWKF CF/PA 2-layer).....	162
Figure 7-17: Simulative analysis of the influence 3D preform quality by forming BWKF 4-layer	163
Figure 7-18: 3D preform of BWKF CF/PA 4-layer at 2 bar setting of blank holder pressure (right after forming).....	163
Figure 7-19: Comparison of the force - displacement curves of stamp during forming process between experiment and simulation for BWKF CF/PA 4-layer.....	164

Figure 7-20: Overview of the L-profile draping machine	165
Figure 7-21: Origin of the L-profile geometry © Nezami [170]	165
Figure 7-22: 3D preforms of BWKF CF/PA 2-layer V1 with homogenous blank holder pressure on the L-profile draping machine at 0°/90° orientation (overview)	166
Figure 7-23: 3D preforms with homogenous blank holder pressure on the L-profile draping machine at different textile orientation (detail view)	166
Figure 7-24: (a) Forming tool with L-profile and (b) FEM model	167
Figure 7-25: Lay-up of the W GF models in the forming simulation model: (a) meso beam model 0°/90°, (b) meso beam model +45°/-45°, (c) meso shell model 0°/90° and (d) meso shell model +45°/-45°	168
Figure 7-26: Lay-up of the BWKF CF/PA 2-layer V1 model in the forming simulation: (a) beam model 0°/90°, (b) beam model +45°/-45°, (c) shell model 0°/90° and (d) shell model +45°/-45°	168
Figure 7-27: 3D preforms results from simulation with macro models	169
Figure 7-28: 3D preforms results from simulation with meso beam models	170
Figure 7-29: 3D preforms results from simulation with meso shell models	171
Figure 7-30: Gap formation of the 3D preform due to yarn sliding by forming BWKF CF/PA 2-layer V1 with orientation 0°/90° of textile	172
Figure 7-31: Gap formation of the 3D preform due to yarn sliding by forming W GF with orientation 0°/90° of textile.....	173
Figure 7-32: Measurement of the fiber orientation for meso shell model of BWKF CF/PA 2-layer V1 with orientation +45°/-45° at the upper left corner	174
Figure 7-33: Orientation of yarns on the top side of L-profile 3D preforms from BWKF CF/PA 2-layer V1 in the experiment and prediction with the meso-scale models.....	174
Figure 7-34: Orientation of yarns on the top side of L-profile 3D preforms from W GF in the experiment and prediction with the meso-scale models	175
Figure 7-35: Effective stress (in MPa) of macro and meso shell model; axial force (in N) of meso beam model of BWKF CF/PA 2-layer V1 with 0°/90° lay-up	176
Figure 7-36: Model of the forming tool with T-shape geometry (arrow showing movement of the stamp)	177
Figure 7-37: Results of forming simulation of BWKF CF/PA 2-layer V1 with conceptual T-cup tools with macro and meso beam models at different blank holder forces.....	178
Figure 7-38: FEM model of final forming tools for T-cup and the 3D preform BWKF CF/PA 2-layer V1 predicted with meso shell model	178
Figure 7-39: Computational cost of forming process simulation with L-profile tool for BWKF CF/PA 2-layer V1 with different models	179

Figure 8-1: Twin digital FRP production chain process including forming simulation and structural analysis with the help of ENVYO	181
Figure 8-2: Mapping result with orientation of source mesh in 0°/90° orientation	182
Figure 8-3: Mapping result with orientation of source mesh in +45°/-45° orientation...	183
Figure 8-4: Test simulation of thermoplastic FRP on the macro scale.....	184
Figure 8-5: Smooth surface failure criterion (FS=1.0) [531]	184
Figure 8-6: Comparison of force-strain curves of tensile test for FRP-C0 between experiment and simulation	185
Figure 8-7: Comparison of force-strain curves of 4-point bending test for FRP-C0 between experiment and simulation	185
Figure 8-8: Loading scenarios on T-cup component	186
Figure 8-9: Force - deformation curves by different loading scenarios.....	187
Figure 8-10: Effective stress (MPa) in T-cup component by tensile loading at different deformation.....	187
Figure 8-11: Effective stress (MPa) in T-cup component by compression loading at 20 mm deformation.....	188
Figure 8-12: Some typical designs of shell-rib structures	189
Figure 8-13: View of the cross-sections along the weft direction of FRP models.....	190
Figure 8-14: Modelling FRP with a meso-scale fabric model and Domain Superposition Technique	191
Figure 8-15: FEM model of T-shaped FRP from 2-layer/4-layer/2-layer BWKF preform..	192
Figure 8-16: Tensile test simulations with meso-scale model of FRP-C1 made from 4 x BWKF GF 2-layer	193
Figure 8-17: Tensile test simulation results and experimental results of FRP samples..	194
Figure 8-18: Comparison of force-deformation-curves from 3-point bending test of FRP T120-0 (no rib) with different construction of BWKF preforms	195
Figure 8-19: 3-point bending test of T-shaped FRP variant T120-33 simulation with support length of 90 mm for FRP specimen with length of 120 mm (failure due to delamination) at deformation of 3 mm.....	196
Figure 8-20: Comparison of force-deformation curves from 3-point bending tests of FRP T120-33 with different constructions of the preforms.....	197
Figure 8-21: Comparison between experiment and simulation of three-point bending tests of long T-shaped FRP samples with 300 mm and 400 mm length, configuration FRP-T1 (rib height H = 32 mm, NFLS = 18, failure of yarn in rib).....	198
Figure 8-22: Detail yarn path in a real preform and in the FEM model of variant 3 (45°)	199

Figure 8-23: Detail yarn path on actual 3D preform and in FEM model of variant 4 (0°/90°) 199

Figure 8-24: Predicted force-deformation-curves of FRP during 3-point bending test for all typical designs of rib with chosen dimension by max deformation of 10 mm200

Figure 8-25: Crack opening of matrix in the diagonal rib in variant 5200

Figure 8-26: Crack opening of matrix in variant 7.....201

Figure 9-1: Possibilities of a hybrid textile FEM model for BWKF forming simulation with L-profile tools.....203

LIST OF TABLES

Table 2-1: Typical properties of some metallic materials and FRPs according to Bunsell [39]	6
Table 2-2: Overview of typical reinforcing fiber given by Bunsell [39].....	7
Table 2-3: Overview of typical glass fiber by Freudenberg [42].....	9
Table 2-4: Qualitative comparison between thermoset and thermoplastic matrix	14
Table 2-5: Value of n for each type of contact.....	42
Table 3-1: Overview of basic 1D-continua with different DOF.....	50
Table 3-2: Overview of basic 2D-continua with different DOF.....	51
Table 3-3: Overview of representative FEM models of selected textile structures.....	59
Table 3-4: Overview of FEM models of FRP made from selected textile structures	68
Table 5-1: Fabric configurations	73
Table 5-2: Test results of GF, CF and PA 6.6 fiber (deviation).....	76
Table 5-3: Homogeneous yarn properties given as mean value (standard deviation)	77
Table 5-4: Hybrid yarn properties given as mean value (standard deviation).....	79
Table 5-5: Basic properties of fabrics given as mean value (standard deviation).....	80
Table 5-6: Overview of the tensile test results of fabrics.....	82
Table 5-7: Test results of cantilever test (deviation).....	86
Table 5-8: Estimated critical shear angle of fabrics	89
Table 5-9: Average of friction coefficient CoF under different normal loads	93
Table 5-10: Parameter of the COLLIN P300 PV laboratory press for the production of UD FRP according to Hasan [70]	95
Table 5-11: Parameter for FRP test specimen production from BWMF CF/PA 2-layer V1 according to D. Rabe	96
Table 5-12: Material properties of unreinforced epoxy matrix given by Hexion Specialty Chemicals.....	98
Table 5-13: Configuration of FRP samples for composite characterisation on coupon level made from BWKF GF	99
Table 5-14: Nominal dimensions of T-shaped FRP samples for structural bending tests	101
Table 5-15: Quantity of produced T-shaped FRP samples per variant and per construction, in parentheses: average of actual rib height H in mm.....	101
Table 5-16: Fiber volume content of FRP of selected textile material	102
Table 5-17: FRP characterization results as mean value (standard deviation).....	104
Table 5-18: Four-point bending test results of FRP	107

Table 5-19: ILSS test results for FRP-C1, -C2 and -C3..... 111

Table 5-20: Test results of 3-point bending of T-shaped FRP samples as mean value (standard deviation), max. F is standardised to rib height of 33 mm..... 114